STOCHASTIC ORBIT PREDICTION USING KAM TORI

THESIS

Max William Yates, Captain, USAF

AFIT/GA/ENY/11-M15

DEPARTMENT OF THE AIR FORCE
AIR UNIVERSITY

AIR FORCE INSTITUTE OF TECHNOLOGY

Wright-Patterson Air Force Base, Ohio

AFIT/GA/ENY/11-M15

STOCHASTIC ORBIT PREDICTION USING KAM TORI

THESIS

Presented to the Faculty

Department of Aeronautics and Astronautics

Graduate School of Engineering and Management

Air Force Institute of Technology

Air University

Air Education and Training Command

In Partial Fulfillment of the Requirements for the

Degree of Master of Science in Astronautical Engineering

Max William Yates, B.S.

Captain, USAF

March 2011

AFIT/GA/ENY/11-M15

STOCHASTIC ORBIT PREDICTION USING KAM TORI

Max William Yates, B.S.
Captain, USAF

Approved:

William E. Wiesel, PhD (Chairman)	16 Mar 2011 Date
Eric D. Swenson, PhD (Member)	15 Mar 2011 Date
Lt. Col. Carl R. Hartsfield, PhD (Member)	16 Mar 2011 Date

Abstract

Kolmogorov-Arnold-Moser (KAM) Theory states that a lightly perturbed, conservative, dynamical system will exhibit lasting quasi-periodic motion on an invariant torus. Its application to purely deterministic orbits has revealed exquisite accuracy limited only by machine precision. The theory is extended with new mathematical techniques for determining and predicting stochastic orbits for Earth satellite systems. The linearized equations of motion are developed and a least squares estimating environment is pioneered to fit observation data from the International Space Station to a phase space trajectory that exhibits drifting toroidal motion over a dense continuum of adjacent tori. The dynamics near the reference torus can be modeled with time-varying torus parameters that preserve both deterministic and stochastic effects. These parameters were shown to predict orbits for days into the future without tracking updates—a vast improvement over classical methods of orbit propagation that require routine updates.

To the oppressed who persist—
to gay servicemembers everywhere.

Acknowledgments

I would like to take this opportunity to thank all of the incredible people that have helped me see the fruition of this study and those who have supported me throughout my life in my educational and professional pursuits.

I am forever indebted to my academic and thesis advisor, Dr. William Wiesel, for his extensive guidance and acumen in orbital dynamics and his wisdom on life. Even as I share his insatiable appetite for knowledge, insight and innovation, occasionally I got burned out. I started to feel like the envelope had reached its limit. Without fail, Dr. Wiesel proved me wrong. He would say something that triggered a new way of thinking and discovery. To future students reading this, I offer one piece of advice: check your paradigm at his door. Dr. Wiesel is a visionary who operates on the cutting edge where traditional modes of thinking simply won't do. He is also quick to dismiss such a compliment which displays a genuine humility from which I've learned and valued.

When our conversations about technical matters occasionally evolved into conversations about current events, I also discovered new perspectives. His most powerful lesson to me is that any advancement for society will not be won by raw science and technology alone, but at their nexus with the human condition—the greater confluence of social sciences, conscience and consensus. In this way, civic engagement and interdisciplinary backgrounds in social science are a vital compliment to technical talent for solving some of the greatest challenges of our time—both as innovators and as humanitarians.

To all of the members of my board, I am grateful for their constructive feedback and the sheer time they put into the review of this thesis. None of this would have been possible without their outstanding courses in astrodynamics which prepared me so well for the undertakings of this research and challenged me every day of this journey.

AFIT has a habit of routinely humbling and intimidating me, especially on day one when I first encountered nearly 250 of the Air Force's best and brightest who would become my interlocutors, my friends to lean on, my testing ground for crazy theories—my classmates! I would be remiss not to thank them for enriching my experience. To my section, thank you for providing structure, stability, a cadre of wingmen, and friendships that will last forever.

Among them, I'd like to thank Dr. Wiesel's other master students, Capt. Gregory Frey and Capt. Luke Hagen, with whom I routinely brainstormed ideas and collaborated when possible. Thank you also to Lt. Col. Ralph Bordner, one of Dr. Wiesel's most recent Ph.D. students, who mentored me early in the process. We will always share a special bond in our work to advance KAM theory for earth orbits.

My friends and colleagues at NASA Johnson Space Center were also instrumental to the success of this study, particularly by providing observation data. Edgar Medina, with whom I worked on the Orion Launch Abort Flight Test Program, helped identify resources and points of contact in the Mission Operations Directorate, ISS Trajectory Operations and Planning Branch (DM33). Peter Ewan, the Trajectory Operations Officer, was indispensible to me. He provided multiple options for gathering ISS observation data and dedicated members of his team to work closely with me throughout this project.

Those members include Ryan East and Daniel Beltz whom routinely impressed me by their professionalism, knowledge and responsiveness.

It is important that I also recognize those folks in my life that looked out for my personal wellbeing during this time. Shortly after arriving at AFIT, I overcame a very personal struggle. To the classmate who helped me through that difficult time and made me realize that after the hurricane comes a rainbow, we will always share a special bond. You know who you are. Thank you!

Most importantly, I couldn't have done this without my family. Their support has been and always will be the secret ingredient to my success. I wish to thank them for so much patience, for encouraging me when I felt overwhelmed, for inspiring me to be a better person, and for never letting me give up. Through all of the ups and downs, all of the surprises along the way, my parents, my awesome siblings and their spouses showed me that a loving family can endure anything.

To all of you, thank you!

M. Yates

Table of Contents

Page

List of Figures

Figure Page

List of Tables

Table Page

List of Symbols

a	Semimajor axis
b	Semiminor axis
$\vec{\boldsymbol{B}}$	Laplace vector
$\vec{\boldsymbol{C}}_{\boldsymbol{j}}$	Fourier series real coefficient vector
C_{nm}	Dimensionless geopotential coefficient
δ	Geocentric latitude
δf	Virtual displacement
δP	Torus momenta offset
δQ	Torus coordinate offset
δV	Virtual potential
$\overline{\delta W}$	Virtual work
$\overrightarrow{\boldsymbol{\delta Y}}$	Torus distortion vector
G	Gravitational constant
$\vec{\boldsymbol{e}}$	Eccentricity vector
E	Eccentric anomaly
ε	Specific mechanical energy
$\vec{\boldsymbol{F}}$	Force vector
$\mathcal{F}$	Fourier transform
$\vec{\boldsymbol{h}}$	Angular momentum vector
H	Hamiltonian function

$\boldsymbol{H}$	Observer matrix
i	Inclination
$\Im$	Imaginary part of complex number
$\vec{\boldsymbol{j}}$	Fourier series index summation vector
J_2	Zonal harmonic given by $m = 0$ and $n = 2$
$\mathcal{K}$	Hamiltonian function
L	Lagrangian function
λ	East longitude
m	Order of geopotential expansion
m_i	Mass of i^{th} body
M	Mean anomaly
μ	Gravitational parameter
n	Degree of geopotential expansion
$\vec{\boldsymbol{n}}$	Nodal vector
Ω	Right ascension of the ascending node
$\vec{\boldsymbol{\Omega}}$	Fundamental basis frequency vector
p	Semilatus rectum
$\vec{\boldsymbol{p}}$	Generalized native momenta
P	Orbital period
$\boldsymbol{P}$	Covariance matrix
$\vec{\boldsymbol{P}}$	Torus or transformed momenta
P_n^m	Legendre polynomial

$\mathcal{P}$	Spectral power
$\vec{\boldsymbol{q}}$	Cartesian or generalized native coordinates
$\boldsymbol{Q}$	Instrument covariance matrix
$\vec{\boldsymbol{Q}}$	Torus angle variables or transformed coordinates
$\vec{\boldsymbol{r}}$	Position vector
R_2	Disturbing function approximated by J_2
$R_\oplus$	Equatorial radius of Earth
$\Re$	Real part of complex number
$\vec{\boldsymbol{S}}_{\boldsymbol{j}}$	Fourier series imaginary coefficient vector
S_{nm}	Dimensionless geopotential coefficient
t	Time
T	Time of periapsis passage
$\boldsymbol{T}$	Observation partial derivative matrix
u	Argument of latitude
ϕ	Geocentric longitude
$\boldsymbol{\Phi}$	State transition matrix
$\vec{\boldsymbol{v}}$	Velocity vector
ν	True anomaly or cycle frequency
V	Geopotential function
ω	Argument of perigee or angular frequency
$\omega_\oplus$	Rotation rate of Earth

$\vec{\boldsymbol{X}}$	Cartesian state vector
$\mathcal{X}_p$	Hanning window of order p
$\vec{\boldsymbol{Y}}$	Torus state vector
$\vec{\boldsymbol{Z}}$	Classical orbital elements or observation vector

List of Abbreviations

ACA	Active Collision Avoidance
AFIT	Air Force Institute of Technology
ATCS	Active Thermal Control System
CAPCOM	Capsule Communicator
CEP	Celestial Ephemeris Pole
CME	Coronal Mass Ejection
COE	Classical Orbital Element
DSST	Draper Semianalytic Satellite Theory
DU	Distance Unit
ECEF	Earth-Centered Earth-Fixed
ECI	Earth Centered Inertial
EFG	Earth-Fixed Greenwich
EGM	Earth Gravity Model
GAST	Greenwich Apparent Sidereal Time
GEO	Geosynchronous Earth Orbit
GMST	Greenwich Mean Sidereal Time
GMT	Greenwich Mean Time
GRACE	Gravity Recovery and Climate Experiment
IRP	International Reference Pole
ISS	International Space Station
ITRF	International Terrestrial Reference Frame

KAM	Kolmogorov Arnold Moser
LEGEND	LEO-to-GEO Environment Debris
LEO	Low Earth Orbit
LST	Local Sidereal Time
MCC	Mission Control Center
MRM	Mini Research Module
NAFF	Numerical Algorithm of the Fundamental Frequency
NASA	National Aeronautics and Space Administration
NLS	Nonlinear Least Squares
NOAA	National Oceanic and Atmospheric Administration
PAM	Payload Assist Module
PSD	Power Spectral Density
RAAN	Right Ascension of the Ascending Node
RMS	Root Mean Square
SGP	Simplified General Perturbations
SSN	Space Surveillance Network
TCFT	Truncated Continuous Fourier Transform
TDR	True of Date Rotating
TOD	True of Date
TT	Terrestrial Time
TU	Time Unit

USAF	United States Air Force
UTC	Coordinated Universal Time
VOP	Variation of Parameters
XVV	X-axis in the velocity vector

STOCHASTIC ORBIT PREDICTION USING KAM TORI

I. Introduction

1.1 A Silent Crisis

Students from the Sewickley Academy packed tightly into a small room at the Carnegie Science Center in Pittsburg on the morning of March 12, 2009, for an amateur radio downlink from the International Space Station (ISS). One of the students waited with nervous excitement to ask about "new objects being sent into space to be attached to the ISS," but ironically he was about to get a rapid lesson about objects sent into space that aren't attached to anything useful at all, i.e. frangible nut fragments, drifting tool bags, defunct satellites, loitering rocket stages the size of school buses – junk in general [1; 2].

Just moments before the scheduled downlink, Mission Control Center (MCC) Houston's Capsule Communicator (CAPCOM) Kathy Bolt delivered a chilling message to Expedition 18 Commander Michael Fincke:

> *We have information about a RED conjunction. The information came in late and with the uncertainty of it, we are wanting to take a conservative approach. It's a low probability of a hit; however, the object is rather large based on what we can track and if it does happen to hit the ISS, we're talking about only a 10 minute reserve time.* [3]

The 13-cm diameter object, cataloged as “25090 PAM-D,” was a tumbling yo weight that unwound from a spent payload assist module (PAM-D) during the launch of Navstar 2A-11 in 1993 [4; 5].

As a precaution against depressurization from a collision, the three person crew took refuge in the Russian Soyuz “lifeboat” shown in Figure 1. Lucky for them, the object passed without incident, but this was a close call that could have been avoided. Normally the ISS is maneuvered out of harm’s way. In the eight years prior to this event, the ISS maneuvered eight times to avoid space debris [6]. No maneuver was coordinated this time because 25090 PAM-D was classified as a low concern 42 hours prior to the time of closest approach. NASA claimed to have “good tracking and a miss outside the notification box” [4], but after the maneuver window passed, it was discovered that the solar radiation pressure in the tracking model was wrong due to the low perigee of the object. This resulted in a smaller radial miss distance. NASA scrambled to obtain a higher certainty of the object’s path, but the highly elliptical and low perigee orbit made it difficult to get a good track. The best models showed a stable and well-behaved covariance, but it was much larger than typically observed near the time of conjunction [4].

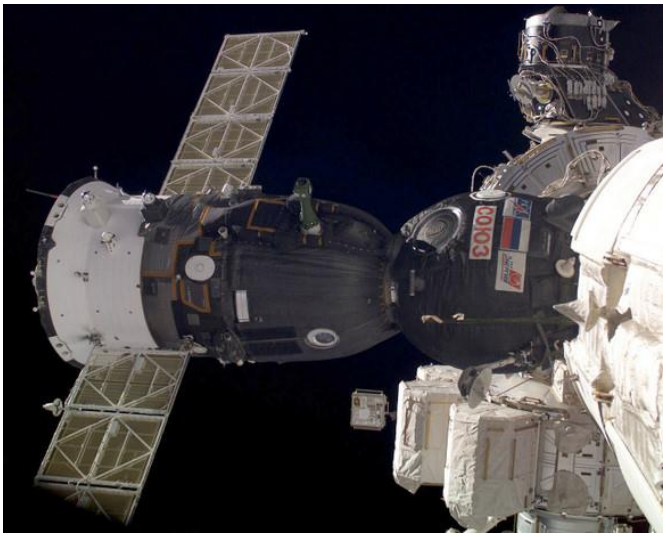

Figure 1. Russian Soyuz docked to the ISS. *Credit: NASA*

This wasn't the first time NASA encountered such shortcomings, nor would it be the last. Just eleven days later, the ISS had to be maneuvered to avoid object 26264, part of a Chinese CZ-4 rocket launched in 1999 that broke up in March 2000 [7]. These close calls were warning shots fired across the bow of the ISS. It made painstakingly clear the limitations of our tracking resources, capabilities, and the certainty of orbit predictions, all of which will habitually haunt us in the absence of immediate and pervasive innovations to the way we conduct business.

1.2 Purpose

The subject of this thesis will explore a new method for predicting orbits that may improve our space situational awareness and allow us to track more objects with greater accuracy than we can today. Doing so would potentially enhance space operations to more easily avoid debris headed our way. Unfortunately, even the most accurate method of orbit determination cannot eliminate the excessive catalogue of junk orbiting the earth. That makes it all the more essential that we have the best orbit predictions possible to forecast collisions and take whatever actions are available to reduce the impact on other operations.

1.3 Implications

Since the dawn of the space age, the United States and other space faring nations have lobbed manmade objects into orbit under the premise that space is so big, it is highly unlikely that two random objects will collide in a limited time span. This paradigm – called the Big Sky Theory – had left us more concerned about junk falling out of the sky. Routine encounters with space junk reentering the atmosphere supported this early

outlook. Take for example the Lan Chile Airbus A340 which was travelling between Santiago, Chile, and Auckland, New Zealand on March 27, 2007 [8]. The pilot was enjoying the calm night air over the South Pacific Ocean when, out of nowhere, flaming balls of space junk went hurtling past the plane. The debris was later identified as a reentering Russian Progress 23P cargo freighter for the ISS. Similar incidents had a more direct "impact" on our psyche. Skylab's premature reentry in 1979 wiped out a cow in the Australian Outback and in 1997 an Oklahoma woman was struck in the shoulder by charred material from a Delta II rocket that the U.S. Air Force launched the previous year.

With the threat of space debris coming from all directions, U.S. Space Command's Space Surveillance Network (SSN) today tracks over 19,000 objects in earth orbit roughly the size of a baseball or larger. Even as they prioritize tracking assets to protect human spaceflight missions and high priority military and civilian satellites, prediction accuracy is limited and hundreds of thousands of smaller artificial debris, from paint flecks to solid rocket fuel slag, are untracked. The smaller objects can pose just as serious of a threat in the space environment, but their sheer number and size make tracking these objects very difficult. With a lower mass-to-area ratio, air drag is a more dominant force, tending to degrade the orbit much too rapidly for sustainable predictions.

As the population density of satellites and debris increases, the finite probability of two objects colliding also increases. When probability becomes reality, the density skyrockets further with the production of new fragments that pose new threats to existing satellites. For example, in February 2009 when the Russian Cosmos 2251 collided with a

U.S. Iridium satellite 500 miles above Siberia, it resulted in a vast cloud of debris adding to the already crowded low-altitude orbital catalogue. More than 2,000 objects being tracked today are a result of the Cosmos-Iridium collision alone.

In 1978, NASA scientists Donald Kessler and Burton Cour-Palais predicted that a continued population growth of satellites coupled with seed collisions, like the one described above, would fuel a cascade of collisions. "The result would be an exponential increase in the number of objects with time, creating a belt of debris around the earth [9]." This is very much like the natural planet forming process that relies on a cascade of collisions beginning with larger objects and, over time, shifting to smaller objects that are greater in number. With every collision, the smashed remnants lose their inclination and eccentricity until eventually a cloud of dust orbits in a ring about the equator of the central body (like the rings of Saturn), or coalesce into a moon or planet. Hannes Alfvén famously described this coalescing of debris using apples in a spacecraft [10].

Later studies done by Kessler identified critical population densities for unstable and runaway environments in which collisional cascading occurs [11; 12]. He surmised that a threshold value for instability exists in an environment in which the fragment population will inevitably increase as a result of random collisions dominated by overpopulated "intact" objects. Given enough time and no additions to the intact population (only subtractions by way of collision), equilibrium will be achieved in which the number of fragments generated by random collisions matches the number of fragments eliminated by natural processes (like air drag). Increasing the intact orbital population beyond its final state at equilibrium would upset the system and the production rate of debris would

exceed the decay rate of debris. Under the scenario that the intact population is continually increased or held steady above the equilibrium threshold, the number of fragments would increase toward infinity. Kessler describes this as a "runaway environment" [13].

The NASA Orbital Debris Program Office's LEGEND model for studying the orbital debris environment between 200 and 50,000 km altitude currently shows regions between 600 and 1,700 km altitude that are already beyond the critical density [14]. Figure 2 shows a 200 year forecast for the altitude band between 900 and 1,000 km. With no new launches contributing to the current intact population of roughly 500 objects in that band, the prediction shows a runaway environment. Similar conditions are found near 1,400 km [13].

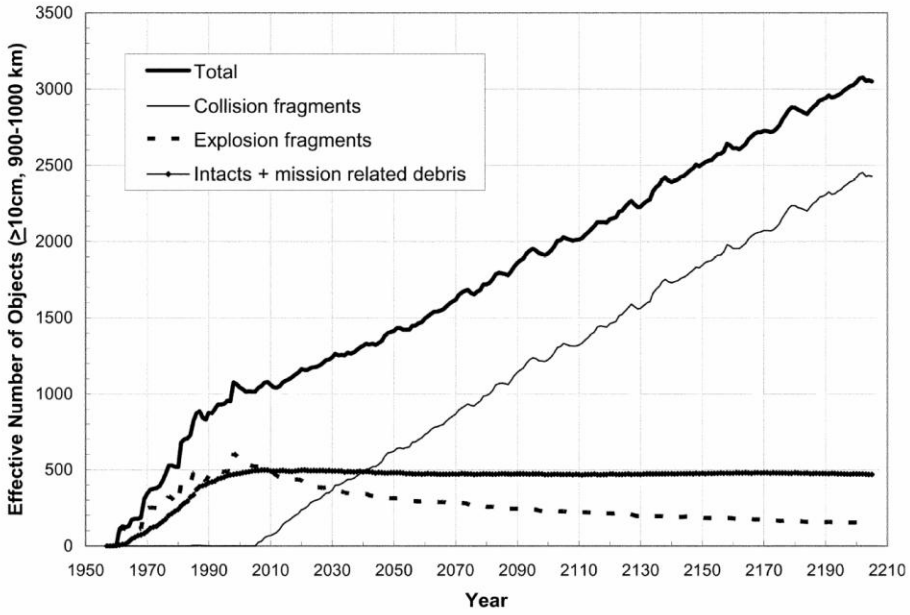

Figure 2. LEGEND prediction shows runaway environment between 900 and 1,000 km assuming no new additions to the intact population after 2004.

Earlier last year, Kessler warned that if the aerospace community continues to conduct business as usual—without international adherence to post mission disposal guidelines—and if we refuse to innovate with active debris removal programs, catastrophic collisions will become more frequent. This could wreak havoc on the global economy by disrupting commerce, communications, agriculture, transportation, health services, education, energy, and the environment, all of which have become dependent on a diverse network of space-based systems that detect and transmit information. Just as importantly, it could impair the United States' ability to defend its interests at home and abroad.

With so much at stake, Congress established the largest study ever conducted on U.S. space management and operations in the National Defense Authorization Act for Fiscal Year 2000. The *Commission to Assess United States National Security Space Management and Organization*, chaired by the Honorable Donald H. Rumsfeld, released its findings on January 11, 2001, with a slew of warnings about space situational awareness. "To use space effectively and to protect against threats that may originate from it, the U.S. must be able to identify and track much smaller objects in space than it can track today" [15:31]. The report specifically recommended technological improvements to the Space Surveillance Network by means of electro-optical and radar systems, but beyond hardware solutions that unveil what is happening *this instant*, the U.S. strategy must also include proactive measures to avoid *future* threats. That is to say, observing precisely what struck the ISS or a critical satellite is less important than forecasting that something *will* strike the ISS or a critical satellite.

As we saw earlier with the close call at the ISS, uncertainty about the debris path left NASA scrambling for better tracking data to corroborate the accuracy of already limited predictions. If we can predict orbits with greater accuracy, active collision avoidance (ACA) systems can serve as a partial solution for those objects that have the means to maneuver, such as the ISS. But even for those that do not, there are still benefits to be had by targeting objects for new disposal initiatives that seek to remove the most dangerous debris from LEO. If nothing else, an expanded catalogue of improved predictions provides a crucial level of situational awareness and gives us the ability to plan rather than react and potentially avert a silent crisis.

1.4 State-of-the-Art

The current state-of-the-art for orbit propagation can be divided into three main branches: numerical (also called special perturbations), analytical (also called general perturbations), and semianalytical techniques (a combination of the other two). The most accurate method is the numerical technique—generally known as Cowell's method—that performs a direct numerical integration of the equations of motion with expanded, high-order disturbing forces. The problem with this method is that it requires very small time steps to benefit from the precision of high order models and is therefore computationally expensive. Even as computer resources have become pervasive, the sheer number of objects that must be tracked makes this method difficult at this time. The analytical techniques which include Simplified General Perturbations (SGP), its popular variant SGP4, and Brouwer-Lyddane use truncated force models and averaging techniques to simplify the calculations. The benefit of analytical techniques is their speed, but they

suffer from immediate errors at epoch on the order of 1 km due to the simplifications [16]. Semianalytical techniques such as Draper Semianalytic Satellite Theory (DSST) are hybrid variants of the previous techniques for relatively fast and accurate results. Unfortunately, all three methods leave a lot to be desired since even the most accurate Cowell's method can become suspect for low earth orbits within a 24 hour period. This lack of accuracy keeps the Space Surveillance Network (SSN) overly tasked detecting, tracking and cataloging as many objects as possible – barely 20,000 objects out of hundreds of thousands.

Here lies the inspiration for this thesis: what new, innovative orbital prediction techniques can we validate and apply to accurately track more objects faster, cheaper and better?

1.5 Problem Statement and Approach

This thesis will introduce new mathematical techniques for determining and predicting stochastic orbits based on the work of William Wiesel [17; 18; 19] using Kolmogorov-Arnold-Moser (KAM) Theory in a least squares estimation environment. KAM theory eliminates special and general perturbation paradigms by representing orbits on tori in 6-dimensional phase space rather than the standard rectangular, inertial coordinates. Wiesel previously showed that, when perturbed only by conserved forces from a 20x20 EGM96 gravity field, KAM tori predict orbits to within meters of numerically integrated orbits for up to a decade [20].

With such high accuracy as the baseline for deterministic orbits, the only remaining hurdle for KAM theory's application to low earth orbits are stochastic effects (air drag,

lunar/solar point mass effects, and other non-conservative perturbations). Typically for low earth orbits, the state-of-the-art numerical methods diverge from the actual orbit within a couple days and must be recomputed from new initial conditions, whereas this author claims that the baseline KAM torus can be used to predict the actual orbit for a much longer period so long as it contains routine phase angle updates and stochastic offsets to the reference torus (performed in this research at every time-step). The duration and level of accuracy of this so-called "motion near a reference torus" is the topic of this research.

Previous work by Little attempted to fit actual observation data from NASA's oceanography satellite, Jason-1, and the Gravity Recovery and Climate Experiment (GRACE) satellite to reference tori that he constructed from purely deterministic orbits [21]. His results for Jason-1 produced residuals constrained to less than 1 km for 30 days which is not surprising. KAM theory states that a lightly perturbed, nearly-integrable Hamiltonian system will lie on a quasi-periodic trajectory in the phase space of a torus. Since the height of perigee for Jason-1 is near 1,330 km—where air drag no longer dominates among perturbing agencies in low earth orbit (LEO) [22:271]—the system is only lightly perturbed and is governed mostly according to KAM theory. However, the results from GRACE depicted a much worse correlation between the observation data and the reference torus with residuals as large as 90 km. This is due to frequent thruster firings and air drag which is more prominent than that experienced by Jason-1 since GRACE's nearly circular polar orbit has a height of less than 500 km. The larger perturbations cause the satellite to wander off the reference torus, but since the residuals

were limited, it is logical to suppose the satellite was constrained to motion *near* the reference torus.

Contingent that a reference torus does exist for a non-chaotic orbit, Wiesel and this author are investigating the possibility that a dense continuum of flexing, persisting tori will also exist nearby, such that the satellite may drift off the initial reference torus (generated only by Earth's gravity field) and circumnavigate neighboring tori when stochastic perturbations exceed a threshold value. This must be true for KAM theory to accurately apply to all LEO orbits, especially those where air drag is most prevalent.

1.6 Research Focus

To explore the concept of motion near a reference torus, the following questions and issues will be addressed:

1) What are the linearized equations of motion near the reference torus?

2) What classical estimation techniques can be applied to fit observation data to a continuum of tori near the reference torus?

3) Given a good fit from the previous question, can the torus be used to generate stochastic predictions and for how long?

1.7 Preview

All three research focuses will be successfully answered in this document. Using the ISS orbit as a test case, it will be shown that a single "flexing" torus can provide stochastic predictions with constrained residuals for a yet-to-be-determined time limit (currently more than 18 days). The low eccentricity of the ISS orbit will induce obstacles that limit the accuracy of these predictions to RMS residuals near 2 km. It will also be

shown that the torus is very sensitive to drag changes in LEO orbits and, in fact, can be used to identify weak variations in the thermosphere density due to geomagnetic activity.

II. Background

The technical merits of KAM theory are anchored firmly in Hamiltonian physics which necessitates a review of relevant analytical mechanics in this chapter. However, as LEO orbits are explored in this research, Keplarian motion (anchored squarely in Newtonian physics) must be relied upon more heavily for understanding motion near a KAM torus. This necessitates a modest review of orbital mechanics up front. Of course, most fundamental to this research is KAM theory, itself. Thus, we conclude this chapter with a look at the most fundamental work of Kolmogorov, Arnold and Moser.

2.1 Orbital Mechanics

This paper is intended to be comprehensive enough to avoid routine cross-references, but in order to stand alone, a significant review and derivation of the two-body problem is necessitated here. The two-body problem is required to linearize the dynamics of motion near Earth satellite KAM tori as will be discussed in §3.2. In addition to deriving the classical orbital elements, a number of other related topics are discussed in this section, including coordinate systems, perturbations, and Lagrange's Planetary Equations—all of which are relevant or essential to the science of orbit determination using KAM tori.

2.1.1 Keplerian Motion

In 1687, Sir. Isaac Newton published *The Mathematical Principles of Natural Philosophy*, more commonly known as the *Principia*, which not only introduced his famous three laws of motion, but also the law of universal gravitation. He stated that any two bodies in a system attract one another with a force proportional to the product of their

masses and inversely proportional to the square of the distance between them [23:4]. For a system of n particles given by m_1, m_2, …, m_n, the vector force acting on m_i by each particle is expressed as [23:7]:

$$\vec{\boldsymbol{F}}_i = -Gm_i \sum_{\substack{j=1 \\ j \neq i}}^{n} \frac{m_j}{r_{ji}^3} \vec{\boldsymbol{r}}_{ji} \tag{1}$$

where G is the universal gravitational constant approximated as $6.672 \times 10^{-11}\,\mathrm{Nm^2/kg^2}$.

The position and velocity vectors for the center of mass of each particle is given by:

$$\vec{\boldsymbol{r}}_i = \begin{bmatrix} x_i \\ y_i \\ z_i \end{bmatrix} \tag{2}$$

$$\vec{\boldsymbol{v}}_i = \begin{bmatrix} dx_i/dt \\ dy_i/dt \\ dz_i/dt \end{bmatrix} \tag{3}$$

The force acts along the vector [23:7],

$$\vec{\boldsymbol{r}}_{ji} = \vec{\boldsymbol{r}}_i - \vec{\boldsymbol{r}}_j \tag{4}$$

and its magnitude is expressed as:

$$r_{ji} = \left|\vec{\boldsymbol{r}}_{ji}\right| = \sqrt{\left(\vec{\boldsymbol{r}}_i - \vec{\boldsymbol{r}}_j\right) \cdot \left(\vec{\boldsymbol{r}}_i - \vec{\boldsymbol{r}}_j\right)} \tag{5}$$

For a simplified case with no external forces such as drag, thrust, solar radiation pressure, or other perturbations, the gravitational force can also be formulated in the inertial frame using Newton's second law of motion [23:8].

$$\vec{\boldsymbol{F}}_i = \frac{d}{dt}\left(m_i \vec{\boldsymbol{v}}_i\right) = m_i \frac{d\vec{\boldsymbol{v}}_i}{dt} + \vec{\boldsymbol{v}}_i \frac{dm_i}{dt} \tag{6}$$

Since we assume the body is not expelling mass to generate thrust, the last term in (6) is zero.

Setting (6) equal to (1) and dividing both sides by m_i gives the general equation of motion for the i^{th} body. A total of n second-order vector differential equations can be formed according to [23:9]:

$$\frac{d^2\vec{\boldsymbol{r}}_i}{dt^2} = -G\sum_{\substack{j=1 \\ j\neq i}}^{n} \frac{m_j}{r_{ji}^3}\vec{\boldsymbol{r}}_{ji} \tag{7}$$

In a simplified two-body system, the two resulting second order differential equations are [23:9]:

$$\frac{d^2\vec{\boldsymbol{r}}_1}{dt^2} = G\frac{m_2}{r_{21}^3}(\vec{\boldsymbol{r}}_2 - \vec{\boldsymbol{r}}_1) \tag{8a}$$

$$\frac{d^2\vec{\boldsymbol{r}}_2}{dt^2} = G\frac{m_1}{r_{12}^3}(\vec{\boldsymbol{r}}_1 - \vec{\boldsymbol{r}}_2) \tag{8b}$$

From (4) we know that [23:10]:

$$\frac{d^2\vec{\boldsymbol{r}}_{12}}{dt^2} = \frac{d^2\vec{\boldsymbol{r}}_2}{dt^2} - \frac{d^2\vec{\boldsymbol{r}}_1}{dt^2} \tag{9}$$

Substituting (8a) and (8b) into (9), produces the simplified Keplerian (two-body) equation of motion that describes the acceleration of one body *relative* to the other (since it is relative motion, a non-inertial, non-rotating coordinate system may be used with its origin in the central body) [23:14]:

$$\frac{d^2\vec{\boldsymbol{r}}}{dt^2} + \frac{\mu}{r^3}\vec{\boldsymbol{r}} = 0 \tag{10}$$

where μ is a gravitational parameter equivalent to $G(m_1+m_2)$. This value varies based on the attracting bodies. When the mass of the central body (m_1) is significantly larger than

its satellite (m_2), the satellite's mass can be ignored and μ is simply $G(m_1)$. For earth this value is approximated as $3.986012\times10^5\ \text{km}^3/\text{s}^2$ [23:429].

The two-body equation is a useful tool for a quick approximation of more complex systems, but its accuracy is limited by the assumptions used for its derivation. It assumes the bodies are perfectly spherical and symmetric in composition so that they may be treated as simple point masses in the analysis [23:11]. In reality, the nonspherical shape of each body introduces variations in gravitational forces. The two-body equation further assumes that the only force present on each body is a gravitational force acting along a line joining the centers of each body [23:12]. This discounts the effects of perturbations such as drag, solar radiation pressure, the gravitational influence of additional bodies, etc. Each of these perturbations must be accounted for if a higher accuracy solution is desired.

2.1.2 Integrals (Constants) of Motion

The solution to the two body problem, like any differential equation, requires constants of integration known as integrals of motion, or more simply, just integrals. Since the two-body problem consists of three second order differential equations for each body, the order of the system or degrees of freedom are 12 [given by (3x2) x 2 bodies] [24:37]. To reduce the order to zero, 12 integrals are needed.

We can start by reducing the system to three second-order differential equations using conservation of linear momentum to provide the first six constants from the initial position and velocity components of the system's center of mass [24:37]. This transforms the origin to the barycenter of the central body since we assume the satellite's mass is negligible [24:37]. The remaining six are used to define the shape and size of the

satellite's orbit about the central body, the orientation of the orbit using Euler angles, and the position of the satellite on the orbit [25:208]. Since angular momentum is conserved, three constants come from the components of the angular momentum vector, $\vec{\boldsymbol{h}}$ [25:80]. Three more constants come from Kepler's first law which gives the constant eccentricity vector, $\vec{\boldsymbol{e}}$. Since $\vec{\boldsymbol{h}}$ is defined perpendicular to $\vec{\boldsymbol{e}}$, the constraint of $\vec{\boldsymbol{h}} \cdot \vec{\boldsymbol{e}} = 0$ means the components of angular momentum and eccentricity only contribute five independent constants of integration [25:208]. Kepler's second law can be used with the polar component of the angular momentum vector to provide the final constant of integration – the time of perigee passage [24:37]. The conservation of energy also provides a constant of integration [24:37], but it is not independent of angular momentum and eccentricity.

Given the final six integrals, the satellite's orbit can be completely specified in space with six orbital elements. The eccentricity and angular momentum scalar quantities define the orbit in the plane [25:208]. The inclination, right ascension of the ascending node and argument of perigee are the three Euler angles that define the orientation of the orbit. The first two are directly mapped from the angular momentum vector while the latter can be mapped from both the angular momentum vector and eccentricity vector. Finally, a point in the orbit is defined by the true anomaly which leads to the time since perigee passage.

For *n*-body problems, $n \geq 3$, the solution requires $6n$ integrals of motion [24:37]. Six are given by the conservation of linear momentum, one is given by the conservation of energy, and three more are given by conservation of angular momentum, for a total of ten constants [24:37]. The additional integrals obtained with Kepler's laws in the two-body

problem are not applicable for $n \geq 3$, so the system can only be reduced to order $6n - 10$ [24:37]. Thus a closed form solution for systems greater than two bodies is not possible, but simplifications to the general problem have yielded analytical solutions such as the *restricted three-body problem* (not discussed here).

2.1.2.1 Specific Angular Momentum

In a Keplerian system, the only force acting on an orbiting satellite is the gravitational force directed radially toward the larger central body. Without other tangential forces to alter the rotational motion, angular momentum is conserved. A constant called the specific angular momentum can be derived independent of mass by first cross multiplying the two-body equation with the position vector [24:24]:

$$\vec{\boldsymbol{r}} \times \ddot{\vec{\boldsymbol{r}}} + \vec{\boldsymbol{r}} \times \frac{\mu}{r^3}\vec{\boldsymbol{r}} = 0 \tag{11}$$

The second term vanishes since $\vec{\boldsymbol{r}} \times \vec{\boldsymbol{r}} = 0$ and the first term is just the differential [24:24]:

$$\frac{d}{dt}\left(\vec{\boldsymbol{r}} \times \dot{\vec{\boldsymbol{r}}}\right) = \dot{\vec{\boldsymbol{r}}} \times \dot{\vec{\boldsymbol{r}}} + \vec{\boldsymbol{r}} \times \ddot{\vec{\boldsymbol{r}}} = \vec{\boldsymbol{r}} \times \ddot{\vec{\boldsymbol{r}}} \tag{12}$$

Substituting (12) back into (11) and integrating yields a vector constant of integration, namely constant specific angular momentum where "specific" signifies the mass independence of the equation.

$$\vec{\boldsymbol{h}} = \vec{\boldsymbol{r}} \times \vec{\boldsymbol{v}} = \begin{bmatrix} yv_z - zv_y \\ zv_x - xv_z \\ xv_y - yv_x \end{bmatrix} = constant \tag{13}$$

Since $\vec{\boldsymbol{h}}$ is a constant vector perpendicular to $\vec{\boldsymbol{r}}$ and $\vec{\boldsymbol{v}}$, the satellite's motion is fixed in the plane containing $\vec{\boldsymbol{r}}$ and $\vec{\boldsymbol{v}}$ called the orbital plane [23:17].

2.1.2.2 Kepler's First Law, the Trajectory Equation, and Eccentricity

Kepler's first law states that planets follow elliptical paths with the sun at one focus [24:10]. This statement can be extended to include all conic sections: circles, ellipses, parabolas and hyperbolas [24:29]. The mathematical representation of Kepler's first law describing orbital motion on a conic section is called the trajectory equation.

To derive the trajectory equation, start by cross multiplying the two-body equation into the specific angular momentum vector [24:27]:

$$\ddot{\vec{\boldsymbol{r}}} \times \vec{\boldsymbol{h}} + \frac{\mu}{r^3}\vec{\boldsymbol{r}} \times \vec{\boldsymbol{h}} = 0 \tag{14}$$

Since angular momentum is constant ($\dot{\vec{\boldsymbol{h}}} = \mathbf{0}$), the first term can be written [24:27]:

$$\frac{d}{dt}\left(\dot{\vec{\boldsymbol{r}}} \times \vec{\boldsymbol{h}}\right) = \ddot{\vec{\boldsymbol{r}}} \times \vec{\boldsymbol{h}} + \dot{\vec{\boldsymbol{r}}} \times \dot{\vec{\boldsymbol{h}}} = \ddot{\vec{\boldsymbol{r}}} \times \vec{\boldsymbol{h}} \tag{15}$$

Substituting the definition of angular momentum, (13), into the second term in (14) [24:28]:

$$\frac{\mu}{r^3}\vec{\boldsymbol{r}} \times \vec{\boldsymbol{h}} = \frac{\mu}{r^3}\left[\vec{\boldsymbol{r}} \times \left(\vec{\boldsymbol{r}} \times \dot{\vec{\boldsymbol{r}}}\right)\right] \tag{16}$$

Using the "bac – cab" rule for the cross-products [24:28]:

$$\frac{\mu}{r^3}\vec{\boldsymbol{r}} \times \vec{\boldsymbol{h}} = \frac{\mu}{r^3}\left[\vec{\boldsymbol{r}}\left(\vec{\boldsymbol{r}} \cdot \dot{\vec{\boldsymbol{r}}}\right) - \dot{\vec{\boldsymbol{r}}}\left(\vec{\boldsymbol{r}} \cdot \vec{\boldsymbol{r}}\right)\right] \tag{17}$$

Further simplification with the important identities $\vec{\boldsymbol{r}} \cdot \dot{\vec{\boldsymbol{r}}} = r\dot{r}$ and $\vec{\boldsymbol{r}} \cdot \vec{\boldsymbol{r}} = r^2$ yields [24:28]:

$$\frac{\mu}{r^3}\vec{\boldsymbol{r}} \times \vec{\boldsymbol{h}} = \frac{\mu}{r^3}\left[\vec{\boldsymbol{r}}(r\dot{r}) - \dot{\vec{\boldsymbol{r}}}(r^2)\right] = \frac{\mu}{r^2}\dot{r}\vec{\boldsymbol{r}} - \frac{\mu}{r}\vec{\boldsymbol{v}} \tag{18}$$

Recognizing this as the time derivative [24:28]:

$$-\mu\frac{d}{dt}\left(\frac{\vec{\boldsymbol{r}}}{r}\right) = -\mu\frac{r\dot{\vec{\boldsymbol{r}}} - \vec{\boldsymbol{r}}\dot{r}}{r^2} = \frac{\mu}{r^2}\dot{r}\vec{\boldsymbol{r}} - \frac{\mu}{r}\vec{\boldsymbol{v}} \tag{19}$$

Substituting (15) and (19) back into (14) and rearranging [24:28]:

$$\frac{d}{dt}\left(\dot{\vec{\boldsymbol{r}}} \times \vec{\boldsymbol{h}} - \mu\frac{\vec{\boldsymbol{r}}}{r}\right) = 0 \tag{20}$$

Integrating [24:28]:

$$\dot{\vec{\boldsymbol{r}}} \times \vec{\boldsymbol{h}} = \mu\frac{\vec{\boldsymbol{r}}}{r} + \vec{\boldsymbol{B}} \tag{21}$$

$\vec{\boldsymbol{B}}$ is the vector constant of integration, sometimes referred to as the Laplace vector (named after French mathematician Pierre-Simon Laplace) [25:78], which is directed toward the closest point to the central body called periapsis.

To get a scalar relation for (21), dot multiply both sides by $\vec{\boldsymbol{r}}$ [24:28]:

$$\vec{\boldsymbol{r}} \cdot \left(\dot{\vec{\boldsymbol{r}}} \times \vec{\boldsymbol{h}}\right) = \vec{\boldsymbol{r}} \cdot \left(\mu\frac{\vec{\boldsymbol{r}}}{r} + \vec{\boldsymbol{B}}\right) \tag{22}$$

The left-side is simplified using the vector identity $\vec{\boldsymbol{A}} \cdot \left(\vec{\boldsymbol{B}} \times \vec{\boldsymbol{C}}\right) = \left(\vec{\boldsymbol{A}} \times \vec{\boldsymbol{B}}\right) \cdot \vec{\boldsymbol{C}}$ from which we obtain:

$$\vec{\boldsymbol{r}} \cdot \left(\dot{\vec{\boldsymbol{r}}} \times \vec{\boldsymbol{h}}\right) = \left(\vec{\boldsymbol{r}} \times \dot{\vec{\boldsymbol{r}}}\right) \cdot \vec{\boldsymbol{h}} = \vec{\boldsymbol{h}} \cdot \vec{\boldsymbol{h}} = h^2 \tag{23}$$

Substituting this expression and expanding the right side:

$$h^2 = \mu\frac{(\vec{\boldsymbol{r}} \cdot \vec{\boldsymbol{r}})}{r} + \vec{\boldsymbol{r}} \cdot \vec{\boldsymbol{B}} \tag{24}$$

From the definition of the dot product, $\vec{\boldsymbol{r}} \cdot \vec{\boldsymbol{r}} = r^2$ and $\vec{\boldsymbol{r}} \cdot \vec{\boldsymbol{B}} = rB\,cos(\theta)$ where θ is the angle between the fixed vector $\vec{\boldsymbol{B}}$ and the variable position vector $\vec{\boldsymbol{r}}$. Substituting:

$$h^2 = \mu r + rB\,cos(\theta) \tag{25}$$

Solving for position:

$$r = \frac{\frac{h^2}{\mu}}{1 + \frac{B}{\mu}\, cos(\theta)} \tag{26}$$

This expression is identical to the polar equation of a conic section:

$$r = \frac{p}{1 + e\, cos(\nu)} \tag{27}$$

Three important observations between equations (26) and (27) are that eccentricity, *e*, is equal to B/μ, the parameter or semilatus rectum, *p*, is h^2/μ, and the angle ν, called true anomaly, represents the angle from periapsis to the current location on the orbit. The expression given by (27) is known as the trajectory equation or orbit equation.

Given the relationship between eccentricity and the Laplace vector in the trajectory equation, we can rewrite (21) as the eccentricity vector – a constant of integration:

$$\vec{\boldsymbol{e}} = \frac{\vec{\boldsymbol{v}} \times \vec{\boldsymbol{h}}}{\mu} - \frac{\vec{\boldsymbol{r}}}{r} \tag{28}$$

Like the Laplace vector, the eccentricity vector points toward periapsis and its magnitude reveals the shape of the Keplerian orbit. The latter property will be discussed more in section 2.1.3.

2.1.2.3 Kepler's Second and Third Laws

Kepler's second law states that the line joining the planet to the sun sweeps out equal areas of the orbit in equal time [24:10]. The mathematical representation of this over a differential element of area along the conic section is given by [24:30],

$$dt = \frac{dA}{h/2} \tag{29}$$

where $h/2$ is the areal velocity. Integrating over 2π radians of v yields the period of one orbit – another constant of motion:

$$P = \frac{2\pi ab}{h} \tag{30}$$

Notice the area of an ellipse is given by πab where a is the semimajor axis and b is the semiminor axis. If the orbit was circular, it would be πa^2. The period for a parabolic or hyperbolic orbit must be derived separately.

It is much more insightful to alter the form of (30) by substituting the relation for the semiminor axis, $b = a\sqrt{1-e^2} = \sqrt{ap}$, where the semilatus rectum, p, is h^2/μ:

$$P = 2\pi\sqrt{\frac{a^3}{\mu}} \tag{31}$$

This is precisely the expression of Kepler's third law: "The square of the period of a planet is proportional to the cube of its mean distance to the Sun [24:10]."

Kepler used the previous result to define the mean angular rate of a planet about the Sun in units of radians per unit time as:

$$n = \frac{2\pi}{P} = \sqrt{\frac{\mu}{a^3}} \tag{32}$$

The constant gravitational parameter, μ, can be solved to reveal the correlation:

$$n^2a^3 = \mu = G(m_1 + m_2) \tag{33}$$

2.1.2.4 Specific Mechanical Energy or Vis-Viva Equation

A satellite's total mechanical energy – the sum of its kinetic and potential energy – is conserved in a gravitational field void of external energy sources and sinks. As the satellite orbits a central body it continually exchanges one form of energy for the other. A

constant called the specific mechanical energy can be derived independent of mass by first dot multiplying the two-body equation with the velocity vector [24:26]:

$$\vec{\boldsymbol{v}} \cdot \dot{\vec{\boldsymbol{v}}} + \vec{\boldsymbol{v}} \cdot \frac{\mu}{r^3}\vec{\boldsymbol{r}} = 0 \tag{34}$$

The vectors can be eliminated by recognizing the general form of the dot product $\vec{\boldsymbol{r}} \cdot \vec{\boldsymbol{v}} = rv\cos\theta$ and realizing that the radial component of velocity, not to be confused with the magnitude of velocity, is $\dot{r} = v\cos\theta$ [24:26]:

$$v\dot{v} + \dot{r}\frac{\mu}{r^3}r = 0 \tag{35}$$

Noticing the presence of the following time derivatives [24:26]:

$$\frac{d}{dt}\left(\frac{v^2}{2}\right) = v\dot{v} \tag{36a}$$

$$\frac{d}{dt}\left(-\frac{\mu}{r}\right) = \dot{r}\frac{\mu}{r^2} \tag{36b}$$

Substituting into (35) yields [24:26]:

$$\frac{d}{dt}\left(\frac{v^2}{2}\right) + \frac{d}{dt}\left(-\frac{\mu}{r}\right) = 0 \tag{37}$$

Integrating both sides produces the *energy integral* or *vis-viva* ("living force") *equation* [24:26]:

$$\varepsilon = \frac{v^2}{2} - \frac{\mu}{r} + c \tag{38}$$

The first term is the kinetic energy. The second term is potential energy. The constant c is arbitrary and defined by the physics community as $\mu/R_{\oplus}$, but in astrodynamics it is defined as zero [24:26].

For elliptical orbits that include rectilinear ellipses, another form of the energy equation can be formed in terms of the semimajor axis, *a*. Start by dot multiplying the eccentricity vector by itself [26:116]:

$$e^2 = \vec{\boldsymbol{e}} \cdot \vec{\boldsymbol{e}} = \frac{1}{\mu^2}\left(\vec{\boldsymbol{v}} \times \vec{\boldsymbol{h}}\right) \cdot \left(\vec{\boldsymbol{v}} \times \vec{\boldsymbol{h}}\right) - \frac{2}{\mu r}\vec{\boldsymbol{r}} \cdot \left(\vec{\boldsymbol{v}} \times \vec{\boldsymbol{h}}\right) + 1 \tag{39}$$

Simplification yields [26:116]:

$$1 - e^2 = \frac{h^2}{\mu}\left(\frac{2}{r} - \frac{v^2}{\mu}\right) \tag{40}$$

Recognizing the semilatus rectum, $p = h^2/\mu$, and knowing from the geometry of an ellipse that $p = a(1 - e^2)$, the second term on the right-hand side is the inverse of the semimajor axis, *a* [26:116]:

$$a = \left(\frac{2}{r} - \frac{v^2}{\mu}\right)^{-1} \tag{41}$$

This can be rearranged to match the right-hand side of the energy equation from (38):

$$-\frac{\mu}{2a} = \frac{v^2}{2} - \frac{\mu}{r} \tag{42}$$

Plugging (42) into (38) gives the alternate form of the energy equation [24:27],

$$\varepsilon = -\frac{\mu}{2a} \tag{43}$$

which can also be rearranged to describe the semimajor axis:

$$a = -\frac{\mu}{2\varepsilon} \tag{44}$$

The traditional form of the *vis-viva equation* is given by solving (42) for v^2 [24:27]:

$$v^2 = \mu\left(\frac{2}{r} - \frac{1}{a}\right) \tag{45}$$

2.1.3 Kepler's Equation

The final constant of motion mentioned previously as the time of periapsis passage, *T*, is defined once every orbital period when the satellite passes closest to the central body. Alone, it is merely a point in time, but its combination with the current time, the time since periapsis passage, represented by $t - T$, can be used to identify the satellite's location along the orbit. Kepler sought a method that relates this change in time with the angular displacement in an orbit. His second law states that equal areas are swept out in equal times, so he resolved that all time-to-area ratios can be equated to the ratio for one complete orbit [24:51]:

$$\frac{t - T}{A_1} = \frac{P}{\pi ab} \tag{46}$$

The unknown area, A_1, is determined from geometry by encompassing an ellipse with an auxiliary circle shown in Figure 3. First, visually define the area, A_1 [24:52]:

$$A_1 = Area\ PCB - A_2 \tag{47}$$

Triangle A_2 is determined by substituting trigonometric relations into the familiar geometric area of a triangle, $base * height/2$ [24:52]:

$$A_2 = \frac{1}{2}(ae - a\cos(E))\left(\frac{b}{a}a\sin(E)\right) = \frac{ab}{2}(e\sin(E) - \cos(E)\sin(E)) \tag{48}$$

The area of the ellipse inside points PCB is determined by scaling down the similar area of the auxiliary circle inside points PCB' by *b/a* (the relationship between vertical distance on an ellipse and a circle – see [25:183]). The area of PCB' is merely the circular area of POB' minus the triangular area OB'C.

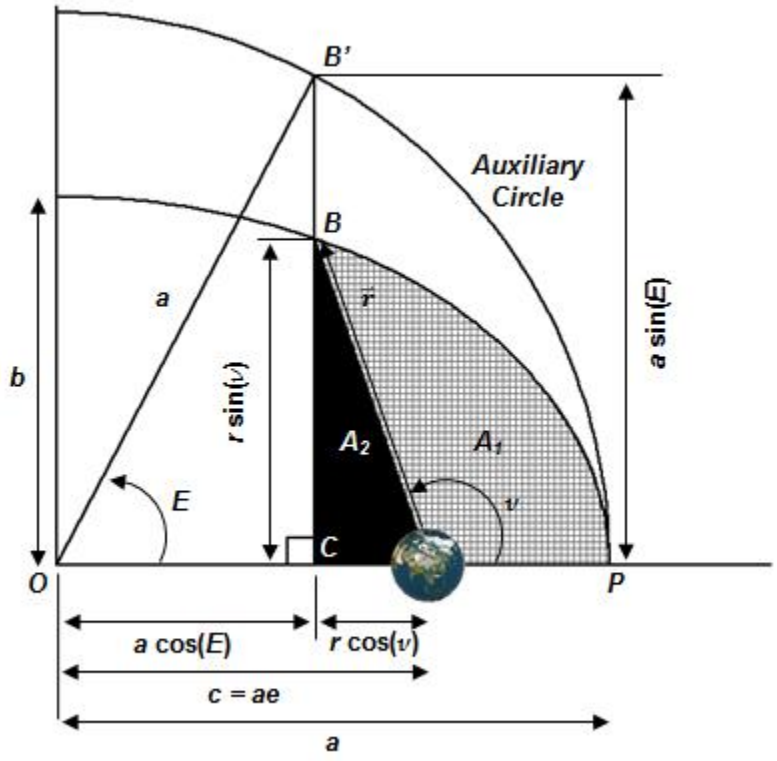

Figure 3. Ellipse circumscribed in a circle to provide geometry for Kepler's Equation.

Together, this yields [24:53]:

$$Area\ PCB = \left[\frac{a^2E}{2} - \frac{1}{2}(a\cos(E))(a\sin(E))\right]\frac{b}{a} = \frac{ab}{2}[E - \cos(E)\sin(E)] \quad (49)$$

Substituting (48) and (49) into (47) [24:53]:

$$A_1 = \frac{ab}{2}[E - e\sin(E)] \quad (50)$$

Plugging this result into (46) and rearranging gives [24:53]:

$$P = \frac{2\pi(t-T)}{E - e\sin(E)} \quad (51)$$

Equating the two expressions for the period of a satellite given by (31) and (51) yields *Kepler's equation* – a powerful tool for determining time since periapsis passage from the eccentric anomaly, semimajor axis and eccentricity [24:53]:

$$\sqrt{\frac{a^3}{\mu}} = \frac{(t-T)}{E - e\sin(E)} \tag{52}$$

Kepler rearranged (52) to define a parameter called the mean anomaly, *M*, which represents the theoretical angle swept out by a satellite travelling at its mean angular velocity on a circular orbit of radius *a* [24:53]:

$$M = E - e\sin(E) = \sqrt{\frac{\mu}{a^3}}(t-T) \tag{53}$$

The mean anomaly has no physical significance, but its importance comes from relating the eccentric anomaly with time [24:54]. First calculate mean anomaly from time and the semimajor axis. Then solve the eccentric anomaly from the mean anomaly's transcendental form. Once *E* is solved using graphical or numerical methods, it can be related to its corresponding true anomaly. Start by defining the eccentric anomaly as a function of true anomaly using the auxiliary circle from Figure 3 [24:55]:

$$\sin(E) = \frac{r\sin(\upsilon)}{a\sqrt{1-e^2}} \tag{54}$$

$$\cos(E) = \frac{ae + r\cos(\upsilon)}{a} \tag{55}$$

The trajectory equation (27) can be substituted for the position r to give [24:55]:

$$\sin(E) = \frac{a(1-e^2)\sin(\upsilon)}{a(1+e\cos(\upsilon))\sqrt{1-e^2}} = \frac{\sin(\upsilon)\sqrt{1-e^2}}{1+e\cos(\upsilon)} \tag{56}$$

$$\cos(E) = e + \frac{\frac{a(1-e^2)}{(1+e\cos(v))}\cos(v)}{a} = \frac{e+\cos(v)}{1+e\cos(v)} \tag{57}$$

Solving (57) for $\cos(v)$ [24:55]:

$$\cos(v) = \frac{\cos(E)-e}{1-e\cos(E)} \tag{58}$$

Next determine an expression for position as a function of semimajor axis and eccentricity by rearranging (55) [24:55]:

$$r = \frac{a\cos(E)-ae}{\cos(v)} \tag{59}$$

Plug (58) into (59) to eliminate true anomaly [24:56]:

$$r = \frac{a\cos(E)-ae}{\frac{\cos(E)-e}{1-e\cos(E)}} = a(1-e\cos(E)) \tag{60}$$

Solve (54) for $\sin(v)$ [24:56]:

$$\sin(v) = \frac{a\sin(E)\sqrt{1-e^2}}{r} \tag{61}$$

Plug (60) into (61) to solve true anomaly in terms of *e* and *E* [24:56]:

$$\sin(v) = \frac{\sin(E)\sqrt{1-e^2}}{1-e\cos(E)} \tag{62}$$

Now (58) and (62) can be substituted into the half-angle identity for tangents and simplified as [24:56]:

$$\tan\left(\frac{v}{2}\right) = \frac{\frac{\sin(E)\sqrt{1-e^2}}{1-e\cos(E)}}{\frac{\cos(E)-e}{1-e\cos(E)}+1} = \frac{\sin(E)\sqrt{1-e^2}}{\cos(E)-e+1-e\cos(E)} \tag{63}$$

The denominator in (63) is simply the product of $(1-e)(\cos(E)+1)$ [24:56]:

$$\tan\left(\frac{\upsilon}{2}\right) = \frac{\sin(E)\sqrt{1-e^2}}{(1-e)(\cos(E)+1)} \tag{64}$$

Again the tangent half angle can be used for the eccentric anomaly components to simplify (64) [24:56]:

$$\tan\left(\frac{\upsilon}{2}\right) = \sqrt{\frac{1+e}{1-e}}\tan\left(\frac{E}{2}\right) \tag{65}$$

Upon rearrangement, the eccentric anomaly is then just:

$$E = 2\tan^{-1}\left(\sqrt{\frac{1-e}{1+e}}\tan\left(\frac{\upsilon}{2}\right)\right) \tag{66}$$

2.1.4 State Representation

The state of a satellite can be completely specified in time by just six quantities. In a standard Cartesian reference frame, these are given by the position and velocity vectors. Additionally, an *element set* can be used that consists of scalar magnitudes and angles. The most commonly used one is referred to as *classical* or *Keplarian orbital elements*. Its canonical counterpart is known as the *Delaunay elements*. Although the classical orbital elements (COEs) are more intuitive to envision than a Cartesian set, they do suffer from some orbital geometry challenges. To bypass these difficulties, variations of the COEs exist, such as the *equinoctial elements* and their canonical counterparts known as *Poincare elements*. Nevertheless, the complete bill of fare is beyond the purview of this study, so we restrict ourselves to a review of the COEs and their Delaunay elements.

2.1.4.1 Classical Orbital Elements

The state vector typically used to identify a two-body orbit in space is given by a set of six elements called the COEs or Keplarian elements which include the semi major axis, *a*, the eccentricity, *e*, the inclination, *i*, argument of perigee, *ω*, right ascension of the ascending node, *Ω*, and true anomaly, *v* [24:104]. The COEs are the initial conditions required to solve the initial value problem for two-body orbital motion [24:103]. The COEs can be formulated from the position and velocity vectors in rectangular coordinates typically obtained from observation or measurement.

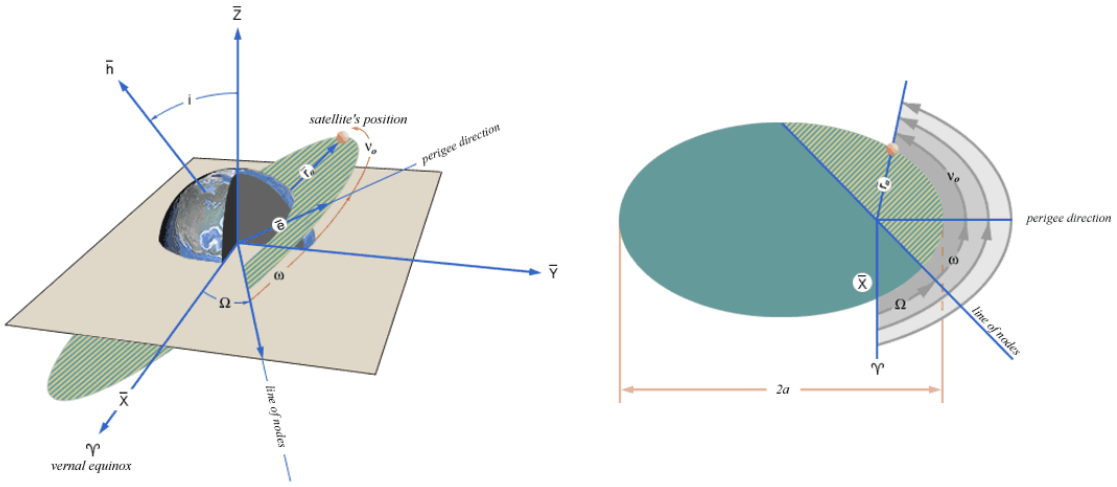

Figure 4. Classical orbital elements. *Credit: NASA*

The first element – the semimajor axis, *a* – defines the size of the orbit [24:104]. Some texts supplant this element with specific angular momentum, h, or the semilatus rectum, p, since the semimajor axis is infinite for parabolic orbits [25:209]. Derived from the semimajor axis, the mean motion, n, can also be used to define the shape of any orbit

except for parabolic orbits [24:105]. For non-parabolic orbits, the semimajor axis is most easily calculated from the energy equation or more expressly (41).

The second element – the eccentricity, e – defines the shape of the orbit and is the magnitude of the eccentricity vector [24:105]. Start by expanding the vector triple cross product from (28) to get [24:106]:

$$\vec{\boldsymbol{e}} = \frac{(\vec{\boldsymbol{v}} \cdot \vec{\boldsymbol{v}})\vec{\boldsymbol{r}} - (\vec{\boldsymbol{r}} \cdot \vec{\boldsymbol{v}})\vec{\boldsymbol{v}}}{\mu} - \frac{\vec{\boldsymbol{r}}}{r} \tag{67}$$

Simplifying the dot product of the velocity vectors and combining position vector terms yields the final equation [24:106]:

$$\vec{\boldsymbol{e}} = \frac{\left(v^2 - \frac{\mu}{r}\right)\vec{\boldsymbol{r}} - (\vec{\boldsymbol{r}} \cdot \vec{\boldsymbol{v}})\vec{\boldsymbol{v}}}{\mu} \tag{68}$$

The magnitude of the eccentricity vector is simply:

$$\|\vec{\boldsymbol{e}}\| = \sqrt{e_i^2 + e_j^2 + e_k^2} \tag{69}$$

For non-parabolic orbits the eccentricity can also be determined by [24:106]:

$$e = \sqrt{1 - \frac{p}{a}} \tag{70}$$

When the magnitude of eccentricity is zero, the orbit is circular. For $0 < e < 1$, the orbit is elliptic. When its magnitude is one, the orbit is parabolic and for $e > 1$, the orbit is hyperbolic.

The third element – inclination, i – defines the tilt of the orbit plane or, more specifically, the angle between the inertial $\widehat{\boldsymbol{K}}$ axis and the angular momentum vector, $\vec{\boldsymbol{h}}$ [24:107]. It is also helpful to think of it as the angle between the orbit plane and the

equatorial plane ($\hat{\boldsymbol{I}}\hat{\boldsymbol{J}}$ plane) of the central body. The inclination is defined without quadrant ambiguity (since *i* is always in the range of 0° to 180°) as [24:107],

$$i = \cos^{-1}\left(\frac{\hat{\boldsymbol{K}} \cdot \vec{\boldsymbol{h}}}{\|\hat{\boldsymbol{K}}\|\|\vec{\boldsymbol{h}}\|}\right) = \cos^{-1}\left(\frac{h_k}{h}\right) \tag{71}$$

where $\vec{\boldsymbol{h}}$ is given by (13).

The fourth element – right ascension of the ascending node (RAAN), Ω – defines the angle from the inertial $\hat{\boldsymbol{I}}$ axis to the point on the equatorial plane where the satellite crosses from the southern hemisphere into the northern hemisphere [24:107]. This point is called the ascending node and it is located in the direction of the nodal vector given by [24:107]:

$$\vec{\boldsymbol{n}} = \hat{\boldsymbol{K}} \times \vec{\boldsymbol{h}} = \begin{bmatrix} -h_j \\ h_i \\ 0 \end{bmatrix} \tag{72}$$

The RAAN is then defined as [24:107]:

$$\Omega = \cos^{-1}\left(\frac{\hat{\boldsymbol{I}} \cdot \vec{\boldsymbol{n}}}{\|\hat{\boldsymbol{I}}\|\|\vec{\boldsymbol{n}}\|}\right) = \cos^{-1}\left(\frac{-h_j}{\sqrt{h_i^2 + h_j^2}}\right) \tag{73}$$

A quadrant check is necessitated for (73). The RAAN will range from $0° \leq \Omega < 180°$ if the ascending node is on the positive side of the $\hat{\boldsymbol{I}}\hat{\boldsymbol{K}}$ plane, meaning the $\hat{\boldsymbol{J}}$ component of the nodal vector is greater than zero, $n_j > 0$. If the ascending node is on the negative side of the $\hat{\boldsymbol{I}}\hat{\boldsymbol{K}}$ plane, meaning $n_j < 0$, then the correct angle and quadrant are given by $\Omega = 360° - \Omega$ so that RAAN will range from $180° \leq \Omega < 360°$ [24:107].

We could have also defined RAAN as:

$$\Omega = \sin^{-1}\left(\frac{\hat{\boldsymbol{J}} \cdot \vec{\boldsymbol{n}}}{\|\hat{\boldsymbol{J}}\|\|\vec{\boldsymbol{n}}\|}\right) = \sin^{-1}\left(\frac{h_i}{\sqrt{h_i^2 + h_j^2}}\right) \tag{74}$$

Combining (73) and (74), we can define RAAN with an `ATAN2` function to avoid quadrant ambiguity altogether:

$$\Omega = \tan^{-1}\left(\frac{n_j}{n_i}\right) = \tan^{-1}\left(-\frac{h_i}{h_j}\right) \tag{75}$$

The fifth element – argument of perigee, ω – measures the angle from the ascending node to periapsis. Since the eccentricity vector points to periapsis, the argument of perigee is simply:

$$\omega = \cos^{-1}\left(\frac{\vec{\boldsymbol{n}} \cdot \vec{\boldsymbol{e}}}{\|\vec{\boldsymbol{n}}\|\|\vec{\boldsymbol{e}}\|}\right) = \cos^{-1}\left(\frac{h_i e_j - h_j e_i}{e\sqrt{h_i^2 + h_j^2}}\right) \tag{76}$$

A quadrant check is needed since ω can range from 0° to 360°. If periapsis lies below the equatorial plane, i.e. the "k" component of the eccentricity vector is less than zero, $e_k < 0$, the correct angle and quadrant are given by $\omega = 360° - \omega$ [24:108].

The sixth element – true anomaly, υ – measures the angle between periapsis and the position vector which indicates the current location of the satellite in the orbit, so:

$$\upsilon = \cos^{-1}\left(\frac{\vec{\boldsymbol{e}} \cdot \vec{\boldsymbol{r}}}{\|\vec{\boldsymbol{e}}\|\|\vec{\boldsymbol{r}}\|}\right) \tag{77}$$

A quadrant check is needed since υ can range from 0° to 360°. If the satellite is moving toward periapsis (away from apoapsis), indicated when $\vec{\boldsymbol{r}} \cdot \vec{\boldsymbol{v}} < 0$, then the correct angle and quadrant are given by $\upsilon = 360° - \upsilon$ [24:108].

Degeneracies result from the standard six elements when the orbit is equatorial, circular or both. Under these geometric conditions, alternate elements must be used to define the orbit.

For elliptical equatorial orbits where i = 0° or 180°, the nodal vector is undefined causing the RAAN to exhibit a singularity. The solution is to replace the RAAN with the *true longitude of periapsis*, $\tilde{\omega}_{true}$, which is the angle measured positive eastward from the vernal equinox to the eccentricity vector [24:109]. Mathematically this is defined as:

$$\tilde{\omega}_{true} = \cos^{-1}\left(\frac{\hat{\boldsymbol{I}} \cdot \vec{\boldsymbol{e}}}{\|\hat{\boldsymbol{I}}\|\|\vec{\boldsymbol{e}}\|}\right) \tag{78}$$

A quadrant check is necessitated since $\tilde{\omega}_{true}$ values range from 180° to 360° (or similarly -180° to 0°). If the "j" component of the eccentricity vector is less than zero, $e_j < 0$, then the correct angle and quadrant are given by $\tilde{\omega}_{true} = 360° - \tilde{\omega}_{true}$.

A note is warranted on the difference between *true longitude of periapsis*, $\tilde{\omega}_{true}$, and a similar quantity called *longitude of periapsis*, $\tilde{\omega}$, given by [24:109]:

$$\tilde{\omega} = \Omega + \omega \tag{79}$$

Longitude of periapsis defines the angle from the primary axis to periapsis by summing two angles in different planes, whereas true longitude of periapsis is a measure of the angle between the primary axis and the eccentricity vector [24:109]. At small inclinations they are similar, but as inclination increases the difference grows [24:110].

For circular inclined orbits, the eccentricity vector is undefined and a singularity results when trying to determine argument of perigee and true anomaly. The angle used instead is the *argument of latitude*, u, which is measured positive from the ascending node to the satellite's position:

$$u = \cos^{-1}\left(\frac{\vec{\boldsymbol{n}} \cdot \vec{\boldsymbol{r}}}{\|\vec{\boldsymbol{n}}\|\|\vec{\boldsymbol{r}}\|}\right) = \cos^{-1}\left(\frac{h_x y - h_y x}{r\sqrt{h_x^2 + h_y^2}}\right) \tag{80}$$

A quadrant check is needed since *u* can range from 0° to 360°. If the satellite is south of the equatorial plane, indicated when $r_k < 0$, then the correct angle and quadrant are given by $u = 360° - u$ [24:108].

When argument of perigee and true anomaly are defined for non-degenerate cases, the argument of latitude is just:

$$u = \omega + \upsilon \tag{81}$$

The last degenerate case occurs when an orbit is circular and equatorial [24:111]. In this case, the ascending node vector and eccentricity vector are undefined causing singularities in RAAN, argument of perigee and true anomaly. The angle used instead is the *true longitude*, λ_{true}, measured eastward from the primary axis to the satellite's current position [24:111]:

$$\lambda_{true} = \cos^{-1}\left(\frac{\hat{\boldsymbol{I}} \cdot \vec{\boldsymbol{r}}}{\|\hat{\boldsymbol{I}}\|\|\vec{\boldsymbol{r}}\|}\right) \tag{82}$$

A quadrant check is needed since λ_{true} can range from 0° to 360°. If the "j" component of the position vector is less than zero, $r_j < 0$, then the correct angle and quadrant are given by $\lambda_{true} = 360° - \lambda_{true}$ [24:111].

For non-degenerate cases, the true longitude can be approximated as [24:111]:

$$\lambda_{true} \approx \Omega + \omega + \upsilon \tag{83}$$

It is only approximate since RAAN is in a different plane than argument of perigee and true anomaly in an inclined orbit [24:111].

2.1.4.2 Delaunay Elements

The classical orbital elements have the benefit of being a relatively intuitive way of viewing an orbit, but they make the equations of motion more difficult to solve than another choice of variables. Their canonical equivalent—one which satisfies Hamilton's equations (discussed in §2.2.2)—renders more trivial equations of motion with its use of generalized coordinates and conjugate momenta. For their simplicity, these so-called Delaunay elements are routinely used in perturbation theory. Their derivation is left to reference textbooks such as Wiesel [27:62]; however, the result is given here in which the capitals denote the momenta:

$$L = \sqrt{\mu a} \tag{84}$$

$$G = L\sqrt{1 - e^2} \tag{85}$$

$$H = G\cos i \tag{86}$$

$$l = M \tag{87}$$

$$g = \omega \tag{88}$$

$$h = \Omega \tag{89}$$

It should be noted that the Delaunay elements suffer from the same degeneracies when the eccentricity and inclination approach zero.

2.1.4.3 Coordinate Systems

The differential equations of motion in both Newtonian and Hamiltonian systems require an inertial celestial reference frame for their solution. The closest realization of this in our neighborhood of the universe is the extra-galactic coordinate system anchored at the center of the Milky Way Galaxy. Unfortunately, it is not perfectly inertial, nor is it

realistic for Earth orbiting satellites. A *sufficiently* inertial reference frame can be used that places the origin at the Earth's center at any epoch of interest, directs the z-axis along the Earth's axis of rotation in the right-handed sense, and directs the x-axis toward the vernal equinox in the equator of epoch. This is known as a true of date (TOD) frame as shown in Figure 5. It changes very slowly over time due to planetary precession, luni-solar precession, and nutation from the Sun and the moon; however, the collective precessional period relative to the fixed stars takes nearly 26,000 years [24:207]. As such, the apparent diurnal motion of the vernal equinox is very close to the apparent motion of the fixed stars. This makes the vernal equinox a good reference point for a sufficiently inertial frame.

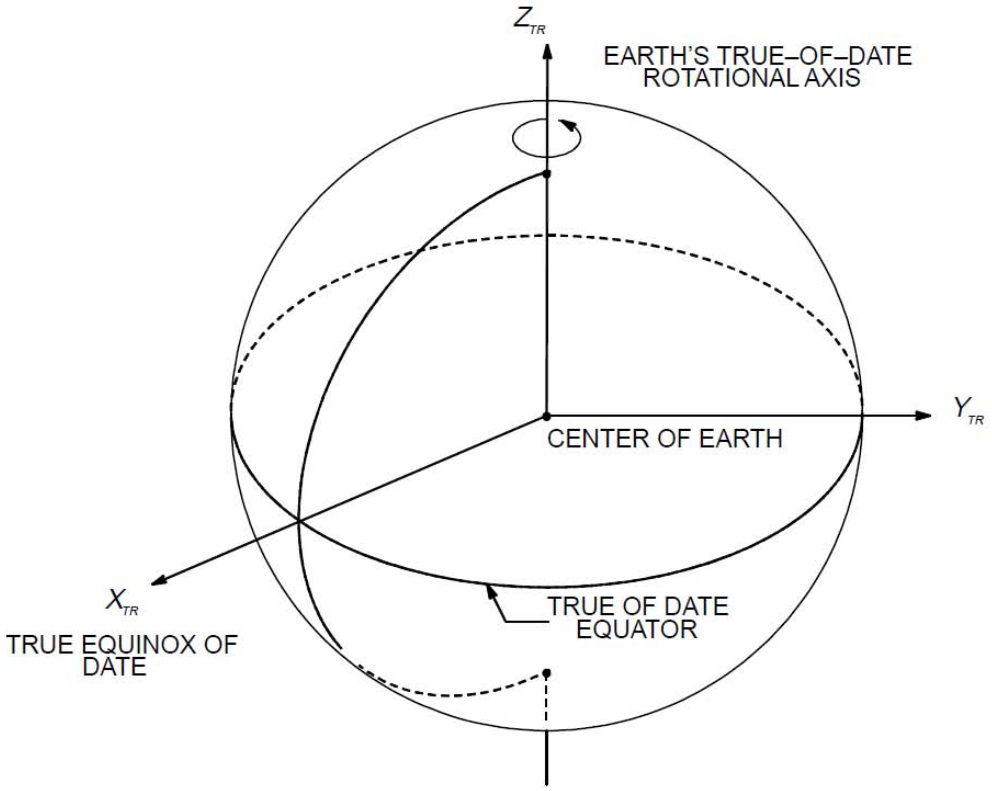

Figure 5. True of Date (TOD) Cartesian coordinate system. *Credit: NASA*

Earth orientation models are used to determine the *true of date equator* (current position of the equatorial plane) and the *true equinox of date* (intersection of the current equatorial plane and ecliptic). The latest of these, published in 2003, is known as IAU 2000, but the classical Fundamental Katalog 5 (FK5) theory will be exclusively covered here since it is used for the ISS—the source of data for this study.

2.1.4.3.1 Pseudo-Inertial J2000 Frame

The TOD frame just introduced is not a good tool for comparing data over a long period of time since the frame is constantly changing (due to the Earth's precession and nutation), albeit very slightly. The solution for high precision comparisons is to transform all data into a TOD frame at a reference epoch. The J2000 coordinate frame in FK5 theory does this by establishing a standardized Earth-centered inertial (ECI) frame at epoch January 1, 2000, noon TT. It places the origin at the Earth's center with the xy-plane in the Earth's *true of date* (TOD) equator at epoch J2000, the x-axis directed toward the true of date equinox at epoch J2000, and the z-axis pointed North along the Earth's rotational axis.

2.1.4.3.2 True of Date Rotating (Earth-Fixed Greenwich) Frame

In addition to celestial-based inertial reference frames, observations of satellites require terrestrial-based coordinate frames fixed to the rotating Earth. These come in the form of geocentric, barycentric and topocentric, but only geocentric is covered here. The geocentric version is routinely called the Earth-centered, Earth-fixed (ECEF) frame which means that its orientation remains unchanged with respect to the Earth's crust. A

strict definition of the ECEF frame must account for *polar motion*—the difference between the present axis of rotation called the Celestial Ephemeris Pole (CEP) and the International Reference Pole (IRP) which was agreed upon in 1900 and 1905 [24:207]. The resulting coordinate system is called the International Terrestrial Reference Frame (ITRF), which U.S. Air Force Space Command calls the Earth-centered rotating (ECR) frame [24:158]. While the ITRF/ECR is great for surveys or navigation, it is not conducive for satellite observations since it is not referenced to the CEP.

The ideal frame for observations which *is* referenced to the CEP is simply a rotating version of the TOD frame. NASA calls this the true of date rotating (TDR) frame, whereas the U.S. Air Force Space Command calls it the Earth-fixed Greenwich (EFG) frame [24:158]. Just like the TOD frame, the origin of the TDR frame is fixed to the center of the Earth, but the x-axis of the TDR frame is fixed to a local meridian at the true equator of date instead of pointing toward the true equinox of date. Generally, the prime meridian is used and the z-axis is the same as the TOD frame. See Figure 6 for its depiction. The only difference between the TDR frame and the ITRF/ECR frame is the correction for polar motion which is *very* small since the maximum variations between the CEP and IRP are approximately 9 meters [24:208].

Converting from TOD to TDR and viceversa requires knowledge of Earth's rotation relative to the vernal equinox—a concept known as sidereal time. Viewed from the North Pole, the Local Sidereal Time, θ_{LST}, is the angle measured counterclockwise from the vernal equinox (defined at the equator) to the local meridian. When the prime meridian (0° longitude) at Greenwich is used, there are two forms of the sidereal time: Greenwich

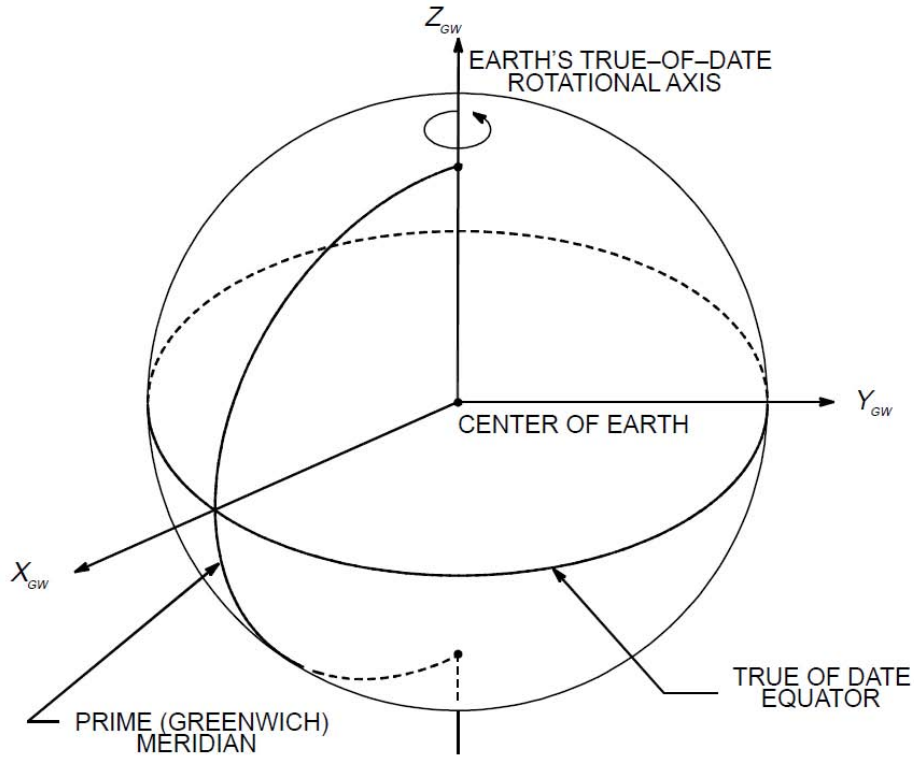

Figure 6. True of Date Rotating (TDR) Cartesian coordinate system. *Credit: NASA*

mean sidereal time, θ_{GMST}, and Greenwich apparent sidereal time, θ_{GAST}. The mean sidereal time is measured along the true equator from the *mean equinox* to the Greenwich meridian, whereas the apparent sidereal time is measured along the true equator from the *true equinox* to the Greenwich meridian. In other words, the apparent sidereal time includes the secular precession of the equinox and the periodic nutation effects, whereas the mean sidereal time *only* includes the secular precession of the equinox. This difference amounts to the equation of the equinoxes [24:223],

$$EQ_{equinox} = \Delta\Psi \cos(\bar{\epsilon}) + 0.00264'' \sin(\Omega_{moon}) + 0.000063 \sin(2\Omega_{moon}) \quad (90)$$

where $\Delta\Psi$ is the nutation in longitude, $\bar{\epsilon}$ is the mean obliquity of the ecliptic, and Ω_{moon} is the RAAN of the mean lunar orbit. The general expression for Greenwich apparent sidereal time is then:

$$\theta_{GAST} = \theta_{GMST} + EQ_{equinox} \tag{91}$$

There are a number of ways for calculating the Greewich mean sidereal time, but a convenient method for computers is given by [24:191],

$$\begin{aligned}\theta_{GMST} = 67310.54841^{s} + (876600^{h} + 8640184.812866^{s})T_{UT1} \\ + 0.093104T_{UT1}^{2} - 6.2 \times 10^{-6}T_{UT1}^{3}\end{aligned} \tag{92}$$

where T_{UT1} is the number of Julian centuries since epoch J2000.

Since the contribution from the equation of the equinoxes is on the order of a thousandth of a degree, the apparent sidereal time is approximately equal to the mean sidereal time. For many applications, the mean sidereal time is close enough; however, this author will incur the extra complications to have that precision.

Given the apparent sidereal time, a simple rotation about the z-axis is required to convert from TOD to TDR:

$$\vec{\boldsymbol{r}}_{TDR} = R_3[\theta_{GAST}]\vec{\boldsymbol{r}}_{TOD} \tag{93}$$

$$\vec{\boldsymbol{v}}_{TDR} = R_3[\theta_{GAST}]\vec{\boldsymbol{v}}_{TOD} - \vec{\boldsymbol{\omega}}_{\oplus} \times \vec{\boldsymbol{r}}_{TDR} \tag{94}$$

2.1.5 Orbit Perturbations

In the Earth system, the primary perturbing forces include gradients in the Earth's gravity field, atmospheric drag, solar radiation, and gravitational effects from the sun and the moon. Atmospheric drag (a nonconservative force) decreases exponentially with altitude, yet dominates at altitudes below ~315 km, while third-body effects

(conservative) and solar radiation (nonconservative) dominate at altitudes above ~19,950 km [22:271]. In between these altitudes, the gravity gradient (conservative) is the largest of the perturbations. It is this region upon which the author will primarily focus since the ISS is maintained at altitudes near 350 km. As such, third-body effects and solar radiation will not be discussed here.

2.1.5.1 Nonspherical Earth

Kepler's equations were derived with the assumption that the central body is a Newtonian point mass. For the Earth to have this property it would have to be a perfect sphere with uniform mass distribution or the radius would have to be large enough for the Keplarian term to dominate. In reality, the Earth is bulged at the equator, has a slight pear shape, and is flattened at the poles [28:142]. Geographical features also contribute to anomalies in the gravitational field compared to a uniform featureless surface. Large concentrations of mass such as mountain ranges add to the gravity field whereas ocean trenches and depressed landmasses reduce the gravity field.

Even with all of these complexities, the Earth's geopotential can be modeled with extraordinary accuracy and precision with a spherical harmonic expansion given by [27:108]:

$$V(r,\theta,\phi) = -\frac{\mu}{r}\sum_{n=0}^{\infty}\sum_{m=0}^{n}\left(\frac{r}{R_{\oplus}}\right)^{-n} P_n^m(\cos\theta) \times [C_{nm}\cos(m\phi) + S_{nm}\sin(m\phi)] \tag{95}$$

μ is the Earth's gravitational constant, r is the radius from the Earth's center to the satellite, $R_{\oplus}$ is the equatorial radius of the Earth, n is the degree of the expansion, m is the

order of the expansion, P_n^m are the Legendre polynomials, C_{nm} and S_{nm} are dimensionless geopotential coefficients, θ is the colatitude and ϕ is the geocentric longitude.

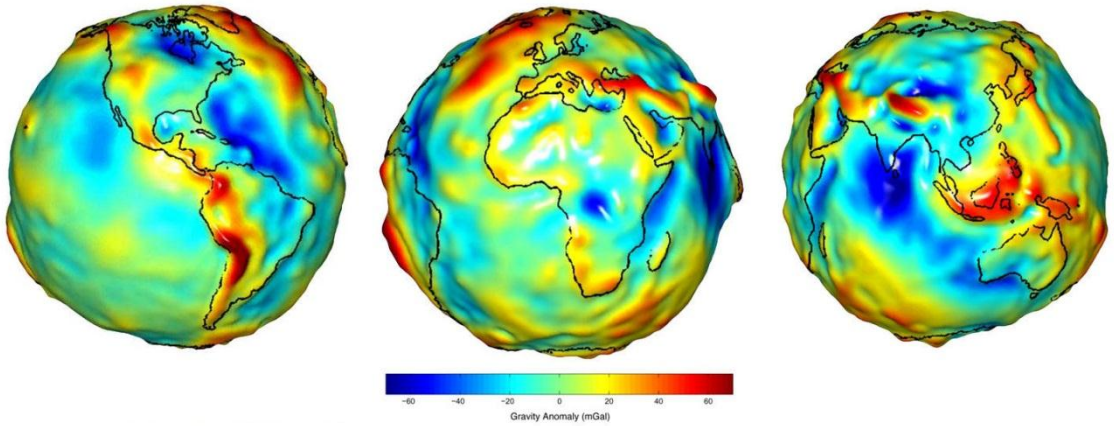

Figure 7. GRACE gravity map depicting gravity anomalies on Earth. *Credit: University of Texas Center for Space Research and NASA*

The coefficients can be divided into three classes. The coefficients for degree $m = 0$ are called zonal harmonics and depend only on latitude [27:113]. The coefficients for which $n = m$ are called sectoral harmonics and depend only on longitude [27:114]. Finally, the coefficients remaining when $m \neq 0$ and $n \neq m$ are called tesseral harmonics and depend on both longitude and latitude [27:115]. The last form appears as a "checkerboard pattern of regions that alternatively add to and subtract from the two-body potential" [28:143]. The coefficients are determined experimentally and placed in a gravity model matrix such as NASA's Earth Gravity Model 1996 (EGM96) or, more recently, models produced from the Gravity Recovery and Climate Experiment (GRACE).

2.1.5.2 Atmospheric Drag

The basic equation for atmospheric drag is given as a specific force or acceleration [24:525],

$$\vec{\boldsymbol{a}}_{drag} = -\frac{1}{2}\frac{c_D A}{m}\rho v_{rel}^2 \frac{\vec{\boldsymbol{v}}_{rel}}{|\vec{\boldsymbol{v}}_{rel}|} \tag{96}$$

where c_D is the drag coefficient, A is the cross-sectional area perpendicular to the velocity vector, m is the satellite's mass, ρ is the atmospheric density, and $\vec{\boldsymbol{v}}_{rel}$ is the velocity vector relative to the rotating atmosphere, or simply [24:526]:

$$\vec{\boldsymbol{v}}_{rel} = \frac{d\vec{\boldsymbol{r}}}{dt} - \vec{\boldsymbol{\omega}}_{\oplus} \times \vec{\boldsymbol{r}} = \left[\frac{dx}{dt} + \omega_{\oplus} y\,, \frac{dy}{dt} - \omega_{\oplus} x\,, \frac{dz}{dt}\right]^T \tag{97}$$

When working in the hypersonic realm it is generally common to characterize the susceptibility to drag with the so-called ballistic coefficient (BC) which is simply an inverse of the second fraction in (96) [24:525]:

$$BC = \frac{m}{c_D A} \tag{98}$$

A satellite with a larger surface area and larger drag coefficient will have the effect of decreasing the BC and increasing the overall drag. Thus, the BC has an inverse relationship with drag.

Drag is, perhaps, the most difficult perturbation to model because it necessitates knowledge of precise attitudes for area calculations and requires a good understanding of the atmospheric density which can fluctuate wildly due to solar flux, geomagnetic variations, and the molecular structure of the atmosphere [24:526]. Changes in extreme ultraviolet radiation (EUV) from incident solar flux cause instantaneous heating of the atmosphere. This, in turn, causes density changes at altitudes above the level heated due

to increased particle collisions. Geomagnetic storms have the same impact, but exhibit delayed heating with density variations persisting for 8 to 24 hours after ground-based magnetometers indicate the storm has ended [29:137].

Tascione shows that for a minor geomagnetic storm identified by the planetary Kp index of 3, a satellite's in-track displacement (compared to predictions) grew to 5 nautical miles in just over 12 hours. For a severe storm identified by Kp = 8, a satellite's in-track displacement grew to 50 nautical miles over the same time period. Of course, polar orbiting satellites will experience the most severe orbit degradation due to more prevalent atmospheric heating near the poles, but density changes can pervade deep into lower latitudes and influence all satellite orbits. Skylab was a perfect example of this. Even with a 50 degree inclination, its orbit quickly deteriorated due to increased solar activity at the beginning of Solar Cycle 21.

2.1.6 Variation of Parameters (VOP)

The six classical orbital elements $(a, e, i, \Omega, \omega, \mathrm{T}_0)$ were shown to be constants of motion in a Keplarian system. With the addition of time as a seventh parameter, a satellite's position and velocity could be precisely determined. In reality, all of these constants are changing, some faster than others. This is due to perturbations from forces other than the central body's gravity. These additional forces alter the two-body equations of motion given by (10) to yield [24:578]:

$$\frac{d^2\vec{\boldsymbol{r}}}{dt^2} = -\frac{\mu}{r^3}\vec{\boldsymbol{r}} + \vec{\boldsymbol{a}}_{pert} \tag{99}$$

One method for solving the perturbed orbit is called *variation of parameters*. VOP makes the assumption that the perturbations are small enough that the solution to the unperturbed two-body system will suffice for the perturbed system. Another assumption is that the constants of motion from the unperturbed system can be represented as time varying in the perturbed system. So instead of integrating the rectangular coordinates in (99) as would be done for the special perturbation technique (Cowell's method), VOP consists of six first-order differential equations describing the time rate of change of the osculating elements $(a, e, i, \Omega, \omega, \mathrm{M})$. The term osculating is used because the elements are no longer constant. They represent the satellite's position at one instant in time since they are continuously altered by perturbations. Nevertheless, once the osculating elements are solved via the differential equations, they may be resolved into a position and velocity vector using the two-body problem solution. This process repeats itself for each point in time.

There are two well-known techniques for VOP; one was developed by Lagrange and the other by Carl Friedrich Gauss. Lagrange's version applies to conservative forces while Gauss' also works for non-conservative forces [24:577]. Both are used as a foundation for general perturbation theory which is of limited interest to the present study. However, Lagrange's version will be developed here to derive *Lagrange's Planetary Equations of Motion* which contribute a set of secular rates to the basis frequencies needed for spectral analysis.

2.1.6.1 Lagrange Planetary Equations – Potential Form

Two different forms of Lagrange's Planetary equations can be derived: one arises in an acceleration component form and the other in a potential form. Since the author's motivation is merely to come up with a set of secular rates from the J_2 disturbing function, only the potential form will be shown here. The most commonly cited derivations of Lagrange's Planetary Equations use Poisson and Lagrange brackets (see Brouwer and Clemence), but Wiesel uses a simpler method using the Delaunay elements [27:94]. Avoiding the temptation to re-derive the equations, the final disturbing function form is presented as [27:98]:

$$\frac{da}{dt} = \frac{2}{na}\frac{\partial R}{\partial M_o} \tag{100}$$

$$\frac{de}{dt} = \frac{1-e^2}{na^2e}\frac{\partial R}{\partial M_o} - \frac{\sqrt{1-e^2}}{na^2e}\frac{\partial R}{\partial \omega} \tag{101}$$

$$\frac{di}{dt} = \frac{\cot i}{na^2\sqrt{1-e^2}}\frac{\partial R}{\partial \omega} - \frac{1}{na^2\sqrt{1-e^2}\sin i}\frac{\partial R}{\partial \Omega} \tag{102}$$

$$\frac{d\Omega}{dt} = \frac{1}{na^2\sqrt{1-e^2}\sin i}\frac{\partial R}{\partial i} \tag{103}$$

$$\frac{d\omega}{dt} = \frac{\sqrt{1-e^2}}{na^2e}\frac{\partial R}{\partial e} - \frac{\cot i}{na^2\sqrt{1-e^2}}\frac{\partial R}{\partial i} \tag{104}$$

$$\frac{dM_o}{dt} = -\frac{2}{na}\frac{\partial R}{\partial a} - \frac{1-e^2}{na^2e}\frac{\partial R}{\partial e} \tag{105}$$

The disturbing function is given by R in the planetary equations. Since the gravity gradient is the largest source of perturbations in the altitude band of concern in this study, we can limit the disturbance function to the geopotential. The zonal harmonic given by $m = 0$ and $n = 2$, also known as the J_2 term, has the single largest contribution to the

geopotential by at least three orders of magnitude [27:137]. Therefore, the disturbing function, R_2, is approximated by the J_2 term alone. See Wiesel [27:137] for its full glorious form. After eliminating periodic terms from R_2, its secular form, containing only a, e, and i is:

$$R_{2_{sec}} = -\frac{\mu R_{\oplus}^2 J_2}{2a^3(1-e^2)^{3/2}}\left(\frac{3}{2}\sin^2(i) - 1\right) \tag{106}$$

Three of Lagrange's planetary equations contain only secular terms: (103), (104), and (105). Upon substituting the partial derivatives of $R_{2_{sec}}$ in each of these, the resulting expressions show the approximate contributions from the J_2 disturbing function on the fundamental basis frequencies of a satellite orbiting Earth (given in the ECI frame) [27:141]:

$$\dot{\omega} = -\frac{3\sqrt{\mu}J_2 R_{\oplus}^2}{2a^{7/2}(1-e^2)^2}\left(\frac{5}{2}\sin^2(i) - 2\right) \tag{107}$$

$$\dot{\Omega} = -\frac{3\sqrt{\mu}J_2 R_{\oplus}^2}{2a^{7/2}(1-e^2)^2}\cos i \tag{108}$$

$$\dot{\mathrm{M}}_o = -\frac{3\sqrt{\mu}J_2 R_{\oplus}^2}{2a^{7/2}(1-e^2)^{3/2}}\left(\frac{3}{2}\sin^2(i) - 1\right) \tag{109}$$

2.2 Analytical Mechanics

The previous discussion of Keplarian motion relied entirely on Newtonian mechanics in which the motion of individual bodies was governed by vector quantities such as momentum and external forces. Analytical mechanics offers an alternative approach to formulate equations of motion by way of the whole system's kinetic energy and potential energy [30:45]. Since these two fundamental quantities are scalars, component-by-

component analysis with vector quantities is not required in analytical mechanics. This departure from geometrical or physical coordinates frees us from a particular coordinate system so that generalized coordinates, *q*, can be used. If the system is characterized by *n* generalized coordinates and *k* constraints, the system's degrees of freedom is given by *n* – *k* [31:31].

Two branches of analytical mechanics discussed in the proceeding sections are Lagrangian Dynamics and Hamiltonian Dynamics. The latter will be used to generate the equations of motion for the topic of this paper, but it cannot be done without first wading into Lagrangian Dynamics from which it is formed. The primary distinction between the two branches is that Lagrangian Dynamics provides *n* second-order differential equations containing generalized coordinates $q_i(i = 1,2, \dots, n)$ and their velocities $\dot{q}_i(i = 1,2, \dots, n)$, while Hamiltonian Dynamics provides 2*n* first-order differential equations containing generalized coordinates $q_i(i = 1,2, \dots, n)$ and their momenta $p_i(i = 1,2, \dots, n)$ [30:172].

2.2.1 Lagrangian Dynamics

In 1788, Italian mathematician Joseph Louis Lagrange published his seminal work, *Méchanique Analytique*, which contained the generalized *Lagrange Equations of Motion* for a mechanical body [32:226]. His famous equations were largely influenced by his work with Swiss mathematician Leonhard Euler to find an analytical solution to the tautochrone problem. Their use of calculus of variations to find the stationary value of a definite integral resulted in the *Euler-Lagrange differential equation* [30:57]. Not by coincidence, the Euler-Lagrange equation is similar in form to Lagrange's equations of

motion since Lagrange applied the same method of calculus of variations and the principle of least action to dynamic systems to his own equations [33:587].

The current form of Lagrange's equations, described here, was formulated by William Rowan Hamilton in 1834 and 1835, when he applied the principle of least action to a Lagrangian function, L = T – V, which will be discussed below [34]. To arrive at Lagrange's equations using Hamilton's method, we start by defining a variation in the configuration space of generalized coordinates to understand the principle of virtual work on a static system. Then we'll use d'Alembert's principle to relate the principle of virtual work to dynamic systems. Finally, we'll use Hamilton's principle, which is simply the integral of d'Alembert's principle, to obtain Lagrange's equations of motion.

2.2.1.1 Variations

The basic problem of calculus of variations seeks to find the path $y(x)$ from (x_1,y_1) to (x_2,y_2) that minimize or maximize the integral $J = \int_{x_1}^{x_2} f(x, y, y')\, dx$ [33:583]. Lagrange proposed small variations to the dynamical path such that an object can travel between the two points in the same time along any path. Consider the example given in Figure 8 in which an object is moving between points $A(q_{iA})$ and $B(q_{iB})$ in the q-dimensional configuration space. The object at point P' on a varied path $F(q, \dot{q}, t)$ is separated from an object at point P on the original dynamical path $f(q, \dot{q}, t)$ by a small variation δf at the exact same time, t. At the endpoints, the variation δf is exactly zero.

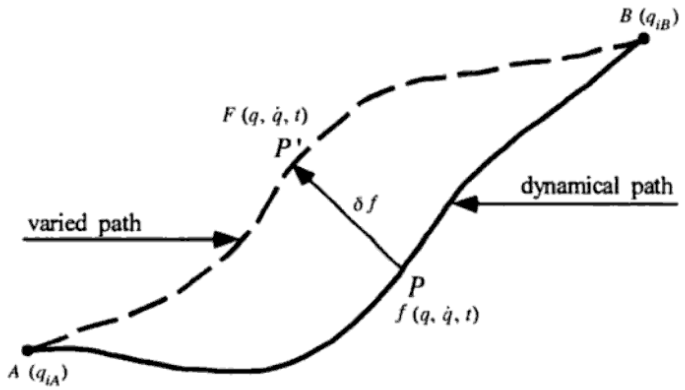

Figure 8. Lagrange's variation in the configuration space.
Credit: Vinti [31:32]

The variation δf is called a *virtual displacement* and it can vary any coordinate at a fixed point in time so long as the variation is consistent with all constraints on the system [30:53]. Virtual displacements are distinct from the differential displacement taking place between the time interval *dt* in which forces and constraints may change [30:53]. Without delving deep into the calculus of variations in our pursuit to develop Lagrange's equations of motion, we need only show that the operator δ is commutable with the *d* designating differentials of displacement. Start by defining the virtual displacement as [31:31]:

$$\delta f = F - f \tag{110}$$

The derivative is then [31:31]:

$$\frac{d}{dt}(\delta f) = \dot{F} - \dot{f} \tag{111}$$

It is also true that [31:31]:

$$\delta \dot{f} = \dot{F} - \dot{f} \tag{112}$$

Equating the variations from (111) and (112) we have [31:31]:

$$\delta \dot{f} = \delta \left(\frac{df}{dt} \right) = \frac{d}{dt} (\delta f) \tag{113}$$

From (113) it is shown that the variation of the derivative is equal to the derivative of the variation where *f* may be a scalar or a derivative. More simply, this commuting property is expressed as [31:31]:

$$\delta d = d\delta \tag{114}$$

2.2.1.2 D'Alembert's Principle

Previously, the concept of virtual displacement was introduced to show the commutability of the δ operator, but virtual displacements can also be used in the same way that a differential displacement is used with a force to describe work on a system. When an applied force acts on a system through an infinitesimal virtual displacement consistent with all system constraints, the work done on the system is zero [30:60]. This is known as the principle of *virtual work* and is a statement of static equilibrium. D'Alembert's Principle extends the principle of virtual work to a dynamic system in which the time derivative of momenta are also present [30:65].

To derive d'Alembert's Principle we start with Newton's second law for a particle of mass, m_k , in inertial space [31:32],

$$m_k \ddot{\vec{r}}_k = \vec{F}_k + \vec{C}_k \tag{115}$$

where $\vec{F}_k$ and $\vec{C}_k$ are applied and constraint forces, respectively. Now if we rearrange the equation and apply the principle of virtual work to the *k*th particle [30:65]:

$$\overline{\delta W} = \left(\vec{\boldsymbol{F}}_k + \vec{\boldsymbol{C}}_k - m_k\ddot{\vec{\boldsymbol{r}}}_k\right) \cdot \delta\vec{\boldsymbol{r}}_k = 0 \tag{116}$$

The work done by the constraint force is zero since the constraint force acts normal to the virtual displacement. So for a system of N particles, d'Alembert's Principle is expressed mathematically as [31:32]:

$$\overline{\delta W} = \sum_{k=1}^{N} \left(\vec{\boldsymbol{F}}_k - m_k\ddot{\vec{\boldsymbol{r}}}_k\right) \cdot \delta\vec{\boldsymbol{r}}_k = 0 \tag{117}$$

The difference between the applied forces and inertial forces, $\vec{\boldsymbol{F}}_k - m_k\ddot{\vec{\boldsymbol{r}}}_k$, is called the effective force. As such, *d'Alembert's Principle* states that the virtual work of effective forces acting on a system through an infinitesimal virtual displacement is zero.

For a monogenic system, d'Alembert's Principle can be altered to show the relationship between generalized forces and generalized potential [31:32],

$$\sum_{k=1}^{N} \vec{\boldsymbol{F}}_k \cdot \delta\vec{\boldsymbol{r}}_k = -\delta V(q,t) \tag{118}$$

where *V* is the potential. The interest of this author is its application to satellites in which it will later be used to represent the satellite's gravitational potential energy.

2.2.1.3 Hamilton's Principle

Hamilton's Principle is merely an integrated form of d'Alembert's Principle, but its real distinction is the ease with which Lagrange's equations of motion can be found. The derivation of Lagrange's equations can be done using either principle, but it can be a chore using d'Alembert's Principle since (117) uses position coordinates that may not all be independent [30:66]. Hamilton's Principle reduces the problem to a scalar definite

integral so that generalized coordinates may be used, and in the case of a holonomic system, the coordinates are independent [30:72].

Start by integrating (117) from 0 to *t* [31:33]:

$$\sum_{k=1}^{N} \int_0^t \vec{\boldsymbol{F}}_k \cdot \delta\vec{\boldsymbol{r}}_k \, dt = \sum_{k=1}^{N} \int_0^t m_k \ddot{\vec{\boldsymbol{r}}}_k \cdot \delta\vec{\boldsymbol{r}}_k \, dt \tag{119}$$

The integral on the right can be rendered as [31:33]:

$$\int_0^t \ddot{\vec{\boldsymbol{r}}}_k \cdot \delta\vec{\boldsymbol{r}}_k \, dt = \int_0^t \delta\vec{\boldsymbol{r}}_k \cdot \frac{d\dot{\vec{\boldsymbol{r}}}_k}{dt} dt = \dot{\vec{\boldsymbol{r}}}_k \cdot \delta\vec{\boldsymbol{r}}_k \Big|_0^t - \int_0^t \dot{\vec{\boldsymbol{r}}}_k \cdot d\delta\vec{\boldsymbol{r}}_k \tag{120}$$

From the discussion of variations in 2.2.1.1, $\delta\vec{\boldsymbol{r}}_k = 0$ at the endpoints of the dynamical path, so the first term on the right goes to zero. Also recalling the commutability property in which $d(\delta\vec{\boldsymbol{r}}_k) = \delta(d\vec{\boldsymbol{r}}_k) = \delta\big(\dot{\vec{\boldsymbol{r}}}_k\big)dt$, (120) can be rewritten in the form [31:33]:

$$\int_0^t \ddot{\vec{\boldsymbol{r}}}_k \cdot \delta\vec{\boldsymbol{r}}_k \, dt = -\int_0^t \dot{\vec{\boldsymbol{r}}}_k \cdot \delta\dot{\vec{\boldsymbol{r}}}_k \, dt = -\frac{1}{2}\int_0^t \delta\dot{\vec{\boldsymbol{r}}}_k^2 \, dt \tag{121}$$

Since the total kinetic energy for a system of particles is given by $T = \frac{1}{2}\sum_{k=1}^{N} m_k \dot{\vec{\boldsymbol{r}}}_k^2$, the right side of (119) is just [31:33]:

$$\sum_{k=1}^{N} \int_0^t m_k \ddot{\vec{\boldsymbol{r}}}_k \cdot \delta\vec{\boldsymbol{r}}_k \, dt = -\int_0^t \delta T \, dt \tag{122}$$

For a monogenic system, (118) can be substituted into the left side of (119) to get:

$$\sum_{k=1}^{N} \int_0^t \vec{\boldsymbol{F}}_k \cdot \delta\vec{\boldsymbol{r}}_k \, dt = -\int_0^t \delta V \, dt \tag{123}$$

Upon substituting (122) and (123) into (119), Hamilton's principle can be expressed as [31:33]:

$$\int_0^t \delta(T - V)\, dt = 0 \tag{124}$$

The *Lagrangian function* is defined as [31:34]:

$$L \equiv T(q, \dot{q}, t) - V(q, t) \tag{125}$$

So Hamilton's Principle, in its most generic form, is simply [31:34]:

$$\int_0^t \delta L\, dt = 0 \tag{126}$$

2.2.1.4 Lagrange's Equations of Motion

With Hamilton's Principle in hand, we can directly deduce Lagrange's equations of motion. Start by forming [31:34]:

$$\delta L = \sum_{k=1}^{N} \left(\frac{\partial L}{\partial q_k} \delta q_k + \frac{\partial L}{\partial \dot{q}_k} \delta \dot{q}_k \right) \tag{127}$$

The partial with respect to *t* is not included since corresponding points along the varied and dynamical paths are reached at the same time. Substituting (127) into (126) for the case of no constraints:

$$\int_0^t \sum_{k=1}^{N} \left(\frac{\partial L}{\partial q_k} \delta q_k + \frac{\partial L}{\partial \dot{q}_k} \delta \dot{q}_k \right) dt = 0 \tag{128}$$

The second component in parenthesis can be resolved as [31:34]:

$$\int_0^t \frac{\partial L}{\partial \dot{q}_k} \delta \dot{q}_k\, dt = \int_0^t \frac{\partial L}{\partial \dot{q}_k} \frac{d}{dt} (\delta q_k)\, dt = \frac{\partial L}{\partial q_k} \delta q_k \Big|_0^t - \int_0^t \frac{d}{dt} \left(\frac{\partial L}{\partial \dot{q}_k} \right) \delta q_k\, dt \tag{129}$$

From the discussion of variations in 2.2.1.1, $\delta q_k = 0$ at the endpoints, so the first term on the right goes to zero. Plugging back into (128):

$$\int_0^t \sum_{k=1}^{N} \left[\frac{d}{dt}\left(\frac{\partial L}{\partial \dot{q}_k}\right) - \frac{\partial L}{\partial q_k}\right] \delta q_k dt = 0 \tag{130}$$

It follows from the fundamental lemma of calculus of variations, the coefficient of δq_k in the integrand vanishes over the range of 0 to *t* [35:34]. It is this coefficient from which we deduce *Lagrange's equations of motion* [31:34]:

$$\frac{d}{dt}\left(\frac{\partial L}{\partial \dot{q}_k}\right) = \frac{\partial L}{\partial q_k} \tag{131}$$

2.2.2 Hamiltonian Dynamics

The equations of motion given by Lagrangian dynamics consists of *n* second-order differential equations; however, it is sometimes more convenient to express the dynamics in terms of 2*n* first-order differential equations called Hamilton's equations. Both Lagrangian and Hamiltonian dynamics require the use of generalized coordinates, but they differ in the choice of auxiliary coordinates. The Hamiltonian form uses generalized momentum, p_k, rather than generalized velocities, $\dot{q}_k$, as was the case in Lagrange's equations. The momenta are simply [31:37]:

$$p_k = \frac{\partial L(q, \dot{q}, t)}{\partial \dot{q}_k} \tag{132}$$

Hamilton's equations of motion are given by the time derivatives of the generalized coordinates and momenta. To derive them as a function of the variable set (q, p, t) rather than $(q, \dot{q}, t)$, a Legendre transformation must be used. Its derivation, shown in [30:93], leads to the Hamiltonian function [31:37]:

$$H(q,p,t) = \sum_{k=1}^{N} p_k \dot{q}_k - L(q,\dot{q},t) \tag{133}$$

The time derivative of q can be found by taking the partial of H with respect to the momenta and recognizing that the $\dot{q}$'s are a function of q's and p's [31:37]:

$$\begin{aligned} \frac{\partial H(q,p,t)}{\partial p_j} &= \dot{q}_j + \sum_{k=1}^{N} p_k \frac{\partial \dot{q}_k}{\partial p_j} - \sum_{k=1}^{N} \frac{\partial L}{\partial \dot{q}_k} \frac{\partial \dot{q}_k}{\partial p_j} \\ &= \dot{q}_j + \sum_{k=1}^{N} \left(p_k - \frac{\partial L}{\partial \dot{q}_k} \right) \frac{\partial \dot{q}_k}{\partial p_j} \\ &= \dot{q}_j \end{aligned} \tag{134}$$

For a system with rectangular coordinates, the summation term in the second line of (134) vanishes since the partial of the Lagrangian given by $L = \sum_{k=1}^{N} \frac{1}{2} m_k (\dot{x}_k^2 + \dot{y}_k^2 + \dot{z}_k^2) - V(x,y,z,t)$ is just the momenta $p_{x_k} = m_k \dot{x}_k$, $p_{y_k} = m_k \dot{y}_k$, and $p_{z_k} = m_k \dot{z}_k$ [31:37]. Thus, Hamilton's first *n* equations of motion are [31:37]:

$$\frac{dq_k}{dt} = \frac{\partial H(q,p,t)}{\partial p_k} \tag{135}$$

The time derivative of p can be found by taking the partial of H with respect to the generalized coordinates [31:38]:

$$\frac{\partial H(q,p,t)}{\partial q_j} = \sum_{k=1}^{N} p_k \frac{\partial \dot{q}_k}{\partial q_j} - \frac{\partial L}{\partial q_j} - \sum_{k=1}^{N} \frac{\partial L}{\partial \dot{q}_k}\frac{\partial \dot{q}_k}{\partial q_j}$$

$$= \sum_{k=1}^{N} \left(p_k - \frac{\partial L}{\partial \dot{q}_k}\right)\frac{\partial \dot{q}_k}{\partial q_j} - \frac{\partial L}{\partial q_j} \tag{136}$$

$$= -\frac{\partial L(q,\dot{q},t)}{\partial q_j}$$

Substituting (131) into (136) and recognizing the definition of momenta from (132) [31:38]:

$$\frac{\partial H(q,p,t)}{\partial q_j} = -\frac{d}{dt}\left(\frac{\partial L}{\partial \dot{q}_k}\right) = -\frac{d}{dt}(p_j) \tag{137}$$

Thus, Hamilton's second *n* equations of motion are [31:38]:

$$\frac{dp_k}{dt} = -\frac{\partial H(q,p,t)}{\partial q_k} \tag{138}$$

2.3 KAM Theory

In his famous 1954 address to the International Congress of Mathematicians, Andrey Kolmogorov first posed the theory that a lightly perturbed, conservative, dynamical system will exhibit lasting quasi-periodic motion on an invariant N-torus [36]. Kolmogorov's student, Vladimir Arnold, and German-American mathematician Jürgen Moser rigorously proved the theory for Hamiltonian systems [37; 38]. This new approach to stability problems in celestial mechanics would become the foundation for more than a half-century of work in a field that now bears their names: Kolmogorov–Arnold–Moser theorem.

In its simplest mathematical representation, KAM theory is not unlike classical perturbation theory with the initial state governed by [39:6]:

$$H_\varepsilon(I,\varphi) = h(I) + \varepsilon f(I,\varphi) \tag{139}$$

where H_ε is a perturbed Hamiltonian which is 2π-periodic, h and f are real-analytic functions representing an unperturbed Hamiltonian and a perturbing function, respectively, ε is a small ($\ll 1$) real valued perturbing parameter, and (I,φ) are symplectic action-angle variables on the torus. One distinct difference between the two theories and proof of KAM theorem's value is the speed at which the solution is converged upon. Using a sequence of canonical transformations, the solution from classical theory is converged upon linearly, if at all. For example, in the first step, the initial Hamiltonian $H_1 = h_1 + \varepsilon f_1$ can be transformed to $H_2 = h_2 + \varepsilon^2 f_2$ in which the *order* of the perturbation grows linearly to ε^2. On the jth iteration, the Hamiltonian is of the form $H_j = h_j + \varepsilon^j f_j$ and the perturbation has grown to ε^j [40:43]. With every iteration, the denominator of the generating function can grow arbitrarily small, causing a divergence from the solution with higher orders of ε [40:39]. This is the well-known small divisor problem that plagued mathematicians such as Henri Poincaré [41]. Kolmogorov's theorem overcame the small divisor problem by converging upon the solution quadratically such that after the jth iteration the Hamiltonian is of the form $H_j = h_j + \varepsilon^{2^{j-1}} f_j$. This approach controls the small divisor in the sequence of canonical transformations so that infinitely many iterations may be used [40:43].

This super-convergent analytical technique was used to prove KAM theory and show that solutions to a non-degenerate Hamiltonian will persist on an invariant torus as long

as the perturbations remain small—an entirely new approach to perturbation theory. Classical perturbation theory seeks to approximate the solutions and then explore its evolution/stability from a fixed initial condition, whereas KAM theory doesn't concern itself with the motion incurred from preassigned initial conditions, but instead explores the dynamic stability in phase space using a set of fixed frequencies that govern quasi-periodic motion [40:40]. In the integrable case when $\varepsilon = 0$, the phase space solution will lie on an invariant torus with a set of N fundamental frequencies. When ε is sufficiently small and the frequencies are sufficiently incommensurate (satisfying the diophantine inequality), a solution is quickly converged upon that remains on the invariant torus (a condition of stability). As ε grows, the torus is deformed or displaced until it ceases to exist [40:42].

2.3.1 Torus Visualization

To fully understand the nature of the torus, its dimensionality must be explored. For the typical Hamiltonian system encountered in an earth satellite orbit, the simplified point-mass experiences three-degrees of freedom in three-dimensional "native" space characterized by the generalized coordinates $\vec{\boldsymbol{q}} = (q_1, q_2, q_3)$ and their conjugate momenta $\vec{\boldsymbol{p}} = (p_1, p_2, p_3)$. Later, we will develop the exact Hamiltonian, $H(q, p)$, represented by these variables. In the meantime, it is enough to say that KAM theory seeks to map this lightly perturbed Hamiltonian to one represented by new coordinates, $\vec{\boldsymbol{Q}} = (Q_1, Q_2, Q_3)$, and momenta, $\vec{\boldsymbol{P}} = (P_1, P_2, P_3)$, in which only the momenta appear in the new Hamiltonian, $\mathcal{K}(P)$. (See Wiesel [19:7] for further discussion of the new Hamiltonian and generating function as approximated with the Delaunay variables.) The

absence of the new coordinates merely implies from Hamilton-Jacobi theory that the coordinates have constant frequencies. The three present momenta combined with the three missing coordinates produce 6-dimensions defining the phase space of the torus. This is equivalent to three sets of action-angle pairs, each pair defining a circuit on the torus. The new coordinates are the angles which, like their native counterparts, enable three-degrees of freedom. The three new momenta are integrals of motion which mandate that the solutions lie on a three-dimensional manifold which is topologically equivalent to a three-torus [42].

Any torus larger than a two-torus is impossible to intuitively comprehend since an *n*-torus must exist in at least $n + 1$ dimensions. The three-torus of interest to this work is impossible to visualize since it is given by six dimensions, but no loss is incurred since it can still be communicated perfectly in mathematical form. It is possible to consider partial visualization techniques with lower order tori. For example, a one-torus (given by one action-angle pair) with one degree of freedom exhibits bounded motion that looks like a circle (two-dimensional). A two-torus (given by two action-angle pairs) with two degrees of freedom exhibits bounded motion with respect to two closed circuits that resemble a doughnut (three-dimensional). For higher order tori, an approach similar to Poincaré mapping can be used to visualize the orbit in a lower dimensional subspace [27:25]. In this case, a two-torus can be generated by taking the "cross-section" of the three-torus which effectively divorces one of the coordinates and its conjugate momenta from the others. Figure 9 depicts a standard two-torus.

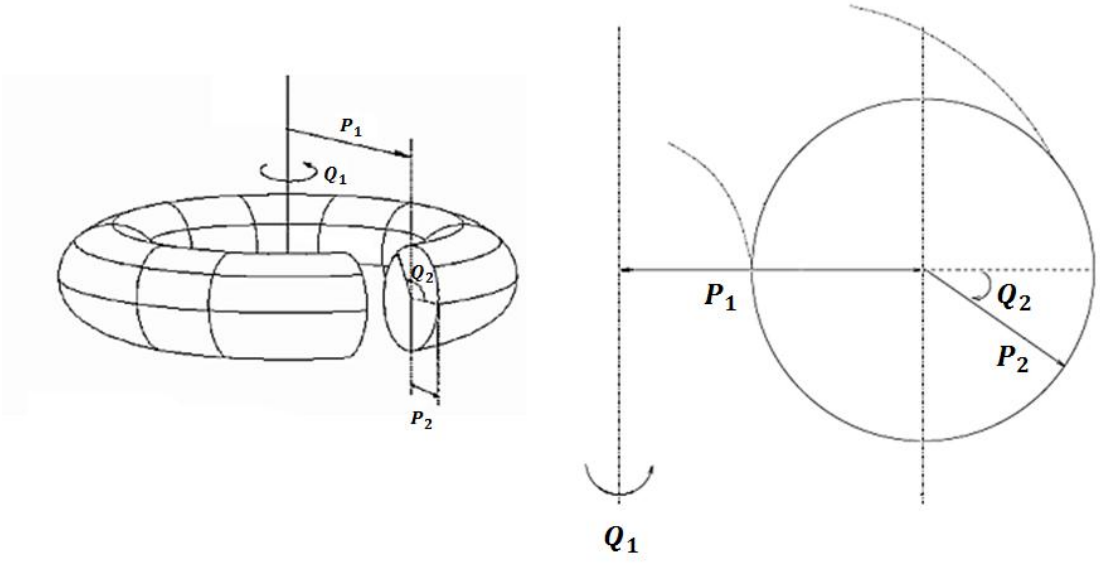

Figure 9. Cross-sectional view of an invariant two-torus defined with the typical action angle variables. In this case the new momenta resemble the actions which define the shape of the torus onto which the motion may be projected and the angles give the position.

III. Methodology

Orbital data from the ISS will be fit to a phase space trajectory that exhibits drifting toroidal motion over a dense continuum of adjacent tori due to stochastic and deterministic forces. This is distinct from multiply periodic motion on a single torus that accounts for purely deterministic forces. The fitting process begins with the construction of an initial reference torus from a numerically integrated orbit that includes the full geopotential up to order and degree $m,n = 20$. Wiesel has shown that deterministic tori, such as the reference torus, exhibit exquisite accuracy to within a few meters over a decade when compared to the integrated orbit (considered as the truth source). The next step is to account for stochastic effects in the orbital data that are not modeled by the reference torus. Intuitively, the stochastic forces impart an offset to the reference state vector. This appears as a displacement in the reference torus' initial momenta and coordinates, the impact of which is motion on an adjacent torus. Bayesian estimation is used to find a vector offset that minimizes the residual between the actual orbit and the reference torus. Sequential outputs from the Bayes filter provide updates to the reference torus that should produce a very good estimate of the ISS orbit over an extended period of time. The entire process of constructing the reference torus and fitting ISS data to the reference torus is explored and developed here.

3.1 Reference KAM Torus

Unfortunately, there doesn't exist an easy homeomorphism from the three-dimensional space (given by generalized coordinates, q_i, and their momenta, p_i) to the six-dimensional phase space of a torus (given by actions, I_i, and angles, φ_i).

Nevertheless, the common periodic nature of the physical coordinates and the torus angle variables makes an N-tuple Fourier series a possible solution for mapping between both spaces. There are generally two approaches used for constructing the torus Fourier series: 1) trajectory-following techniques that perform a Fourier decomposition of data from long numerically integrated orbits, and 2) iterative techniques that find successively better approximations of the series using Hamilton's equations [43:147]. Binney and Spergel pioneered the first approach for non-integrable galactic dynamics in 1982 and it has since become the most straightforward and robust approach for orbits [43:149]. Wiesel has recently shown two variants of this type for earth orbits [17; 18]. The first is a one-pass approach that uses least squares to fit a Fourier series to the integrated orbit and the second is a two-pass approach that identifies the fundamental frequencies on the first pass and then seeks the series coefficients on the second pass. The latter will be employed later in this section.

The aim of both methods is to construct the following finite Fourier series truncated to order $M = \left(j_{1_{limit}},\ j_{2_{limit}},\ j_{3_{limit}}\right)$,

$$\vec{\boldsymbol{q}}\left(\vec{\boldsymbol{I}}, \vec{\boldsymbol{\varphi}}\right) = \sum_{j=-M}^{M} \vec{\boldsymbol{D}}_{\vec{\boldsymbol{j}}}\left(\vec{\boldsymbol{I}}\right) exp(i\vec{\boldsymbol{j}} \cdot \vec{\boldsymbol{\varphi}}) \tag{140}$$

where $\vec{\boldsymbol{D}}_{\vec{\boldsymbol{j}}}$ are the complex series coefficients, $\vec{\boldsymbol{j}}$ is the index summation vector, and $\vec{\boldsymbol{j}} \cdot \vec{\boldsymbol{\varphi}}$ are the associated frequency combinations. The more conventional real form gives the Fourier series as:

$$\vec{\boldsymbol{q}}(t) = C_{(0,0,\ldots,0)^N} + \sum_{j=-M}^{M} \left\{\vec{\boldsymbol{C}}_{\boldsymbol{j}} \cos\left(\vec{\boldsymbol{j}} \cdot \vec{\mathbf{Q}}\right) + \vec{\boldsymbol{S}}_{\boldsymbol{j}} \sin\left(\vec{\boldsymbol{j}} \cdot \vec{\mathbf{Q}}\right)\right\} \tag{141}$$

$$\vec{\mathbf{Q}}(t) = \vec{\boldsymbol{\Omega}}(t - t_0) + \vec{\mathbf{Q}}(t_0) \tag{142}$$

Here $\vec{\boldsymbol{q}}(t)$ are the physical trajectory coordinates in the time domain, $\vec{\mathbf{Q}}(t)$ are the torus angle variables incremented linearly in time, $\vec{\boldsymbol{\Omega}}$ is a set of N fundamental or basis frequencies, $\vec{\boldsymbol{C}}_{\boldsymbol{j}}$ and $\vec{\boldsymbol{S}}_{\boldsymbol{j}}$ are the Fourier coefficients for each coordinate, and $\vec{\boldsymbol{j}}$ is the index summation vector. The basis frequencies describe the satellite's underlying periodic behavior and are easily extracted from a power spectral density (PSD) plot of the phase-space trajectory. The Fourier coefficients are just the amplitudes of the Fourier transform at each integer combination of the basis frequencies. The index summation is an incrementing scheme that allows for integer combinations of the basis frequencies. It also ensures that the first non-zero term in $\vec{\boldsymbol{j}}$ isn't negative so as to avoid repeated angle combinations in the numerical routine, the effects of which are not lost to symmetrical trigonometric properties, specifically $\sin(\theta) = -\sin(\theta)$ and $\cos(\theta) = \cos(-\theta)$.

A variation of Jacques Laskar's Numerical Algorithm of the Fundamental Frequency (NAFF) will be the machinery of choice for finding frequencies and coefficients to construct the torus Fourier series. The NAFF is a technique that approximates the truncated, continuous Fourier transform (TCFT) so that prominent spectral lines can be identified without the destructive effects of aliasing and leakage which will be attended to momentarily [44; 45]. The frequency approximations at these peaks can then be used in a least squares approach to identify the basis set. With the basis set, Laskar's NAFF would typically be used to extract the coefficients from individual spectral peaks; however, the spectral decomposition method used here is a variation of the NAFF that extracts

coefficients from clusters of peaks using the analytical form of the truncated, continuous, Fourier transform (ATCFT) in the fitting process [46].

One is left to ponder the exact relationship between the Fourier series parameters and the action-angle variables that describe the satellite position on the torus. From classical mechanics, the constant actions define the shape of invariant tori, while the angles are the coordinates on the tori. Mathematically, the canonical angle coordinates are those given in (142), but their conjugate action momenta are nowhere to be found (explicitly) in the Fourier series. The momenta represent the dimensions in phase space that are directed away from the torus surface and are only implicitly present through the series coefficients. Nevertheless, they can still be calculated explicitly from the Poincaré integral invariants [17; 18; 19]:

$$P_i = \frac{1}{2\pi}\oint_{\Gamma_i} \vec{\boldsymbol{p}} \cdot \mathrm{d}\vec{\boldsymbol{q}} = \frac{1}{2\pi}\int_0^{2\pi} \vec{\boldsymbol{p}} \cdot \frac{\partial \vec{\boldsymbol{q}}}{\partial Q_i}\,\mathrm{d}Q_i \tag{143}$$

where Q_i are the angle coordinates, p_i and q_i are the native coordinates and momenta, and Γ_i is a fundamental contour about the torus. As the system oscillates around the torus, the time derivative of the coordinates is equivalent to the basis frequencies. Since the action momenta are constant on a torus, their time derivative is simply zero, which infers the system's Hamiltonian function is only a function of action momenta. This makes sense because the Hamiltonian is conserved. As such, the Hamiltonian equations of motion are resolved as:

$$\frac{dQ_i}{dt} = \frac{\partial \mathcal{K}(P)}{\partial P_i} = \Omega_i(P) \tag{144}$$

$$\frac{dP_i}{dt} = -\frac{\partial \mathcal{K}(P)}{\partial Q_i} = 0 \tag{145}$$

From (144) it is apparent that the frequencies in the orbital motion are a function of the action momenta. Thus, the influence of the action momenta on the Fourier series is apparent in the Fourier coefficients as amplitudes of the frequencies and their combinations in time.

The subsections that follow will document the exact procedures for generating the reference torus, but a preliminary roadmap is given here:

- Define the satellite's dynamics with a Hamiltonian.
- Numerically integrate the Hamiltonian using the satellite's reference position and velocity as the initial condition.
- Convert the integrated trajectory from the time domain to the frequency domain using a finite Fourier transform.
- Extract the basis frequencies and Fourier coefficients using Laskar's method.
- Construct a Fourier series representation of the KAM torus.

3.1.1 Earth Satellite Dynamics

A fixed torus about the Earth can only be constructed from a lightly perturbed autonomous Hamiltonian system. The reference satellite orbit includes perturbations from the geopotential and ignores all nonconservative forces, so the only temporal variations are induced from the rotating Earth. To freeze the geopotential and obtain an autonomous dynamical system, the ECEF frame is imposed on the system. The Hamiltonian dynamics can then be formulated as done by Wiesel [17:1-2].

Start by defining the generalized coordinates in the ECEF frame and their inertial velocities resolved in the ECEF frame:

$$\vec{\boldsymbol{q}} = \begin{bmatrix} x \\ y \\ z \end{bmatrix} \qquad \dot{\vec{\boldsymbol{q}}} = \begin{bmatrix} \dot{x} - \omega_{\oplus} y \\ \dot{y} + \omega_{\oplus} x \\ \dot{z} \end{bmatrix} \tag{146}$$

The Lagrangian function given by (125) is no longer a function of time since the dynamics are autonomous in the non-rotating frame,

$$\begin{aligned} L &= T(q, \dot{q}) - V(q) \\ &= \frac{1}{2}((\dot{x} - \omega_{\oplus} y)^2 + (\dot{y} + \omega_{\oplus} x)^2 + \dot{z}^2) - V(q) \end{aligned} \tag{147}$$

where $V(q)$ is the expanded geopotential from (95). The canonical momenta are calculated from (132) and are identically equal to the inertial velocity components,

$$\vec{\boldsymbol{p}} = \begin{bmatrix} \dot{x} - \omega_{\oplus} y \\ \dot{y} + \omega_{\oplus} x \\ \dot{z} \end{bmatrix} \tag{148}$$

where $\omega_{\oplus}$ is the Earth's rotation rate in canonical units of 0.0588335998 rad/TU where 1 time unit (TU) is 13.446852 minutes. Substituting the appropriate terms into the Hamiltonian function given by (133) yields:

$$\begin{aligned} H(q, p, t) = \frac{1}{2}\left(p_x^2 + p_y^2 + p_z^2\right) + \omega_{\oplus}\left(y p_x - x p_y\right) \\ - \frac{\mu}{r} \sum_{n=0}^{\infty} \sum_{m=0}^{n} \left(\frac{r}{R_{\oplus}}\right)^{-n} P_n^m(\cos\delta) \\ \times \left[C_{nm} \cos(m\lambda) + S_{nm} \sin(m\lambda)\right] \end{aligned} \tag{149}$$

$R_{\oplus}$ is the equatorial radius of the Earth equal to 6378.137 km or, in canonical units, 1 distance unit (DU); μ is the Earth's gravitational constant equal to 398600.4418 km^3/s^2 or, in canonical units, 1 DU^3/TU^2; and as before, *n* and *m* are the degree and order of the geopotential expansion, P_n^m are the Legendre polynomials, and C_{nm} and S_{nm} are

dimensionless coefficients from the gravity model. Finally, the radius, *r*, the geocentric latitude, δ, and the east longitude, λ, are found from:

$$r = \sqrt{x^2 + y^2 + z^2} \tag{150}$$

$$\sin\delta = \frac{z}{\sqrt{x^2 + y^2}} \tag{151}$$

$$\tan\lambda = \frac{y}{x} \tag{152}$$

The Hamiltonian equations of motion are determined by taking the partials of the Hamiltonian function as specified in (135) and (138) such that,

$$\begin{bmatrix} \dot{\vec{q}} \\ \dot{\vec{p}} \end{bmatrix} = \begin{bmatrix} p_x + \omega_\oplus q_y \\ p_y - \omega_\oplus q_x \\ p_z \\ \omega_\oplus p_y - \dfrac{\partial V(q)}{\partial q_x} \\ \omega_\oplus p_x - \dfrac{\partial V(q)}{\partial q_y} \\ -\dfrac{\partial V}{\partial q_z} \end{bmatrix} \tag{153}$$

where the partials of $V(q)$ are the geopotential force upon the satellite and are only dependent on the satellite's position. Given the autonomous nature of the Hamiltonian function, the equations of motion are independent of time and the Hamiltonian is a constant of motion.

3.1.2 Numerical Integration

A Hamming fourth-order predictor-corrector algorithm is used to integrate the satellite's Hamiltonian equations of motion across a one-year timespan from time -*T* to time *T* to produce coordinate data, $f(t)$. This amounts to a 6-months forward and 6-

months backward integration with initial conditions given at time 0. The deliberately symmetric forward and backward integration is convenient for a finite Fourier transform, but more importantly, it limits the accumulation of total error compared to a 1-year forward integration to time *2T* or a one year backward integration to time *-2T*. Since the associated local error induced by the algorithm is of order h^5 where *h* is the time-step, the steps are limited to 40.340556 seconds for a total of 400,000 steps in each direction.

The total error growth can be conveniently checked at each time-step by calculating the absolute change in the Hamiltonian function:

$$\Delta H = |H(t) - H(t_0)| \tag{154}$$

The Hamiltonian should be a constant of motion, yet $\Delta H \neq 0$ because the integrator is not symplectic. In other words, the time evolution of the equations of motion do not possess a conserved Hamiltonian. This is a common result for most numerical integration schemes since the integration does not conserve the symplectic two-form, $dp \wedge dq$.

The numerical integration of the ISS trajectory is initialized at,

$$\left[\frac{\vec{q}}{\vec{p}}\right] = \left[\begin{pmatrix} -0.682606200715413 \\ -0.082702006542665 \\ 0.797396182426368 \end{pmatrix}, \begin{pmatrix} 0.339437086117151 \\ -0.892456547165198 \\ 0.197152638998895 \end{pmatrix}\right]^T \tag{155}$$

where the position vector is given in DU and the momenta vector is given in DU/TU. All geopotential terms up to order and degree *m*,*n* = 20 are included in the integration. Figure 10 depicts the first 30 days of the orbit propagation in the TDR frame. By comparison, a full one-year representation of the orbit would cover virtually the entire globe between 52 degrees north and 52 degrees south of the equator.

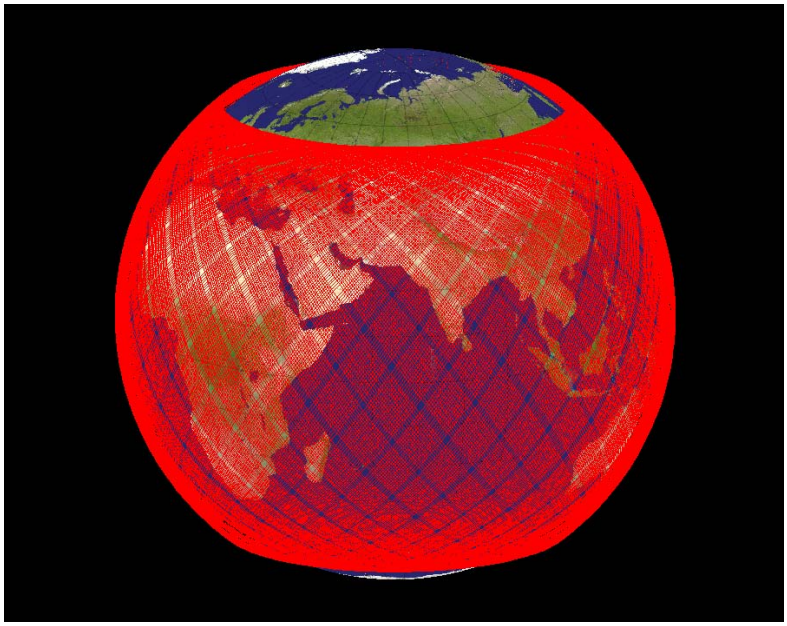

Figure 10. 30-day representation of ISS orbit propagation

As seen from Figure 11, the maximum amplitude error is roughly 10^{-12} which is only four orders of magnitude from double precision accuracy. Given that the Hamiltonian and state vector are scaled to order unity, this miniscule error assures that the propagated Hamiltonian is only faintly perturbed from the original one and KAM theorem will still apply.

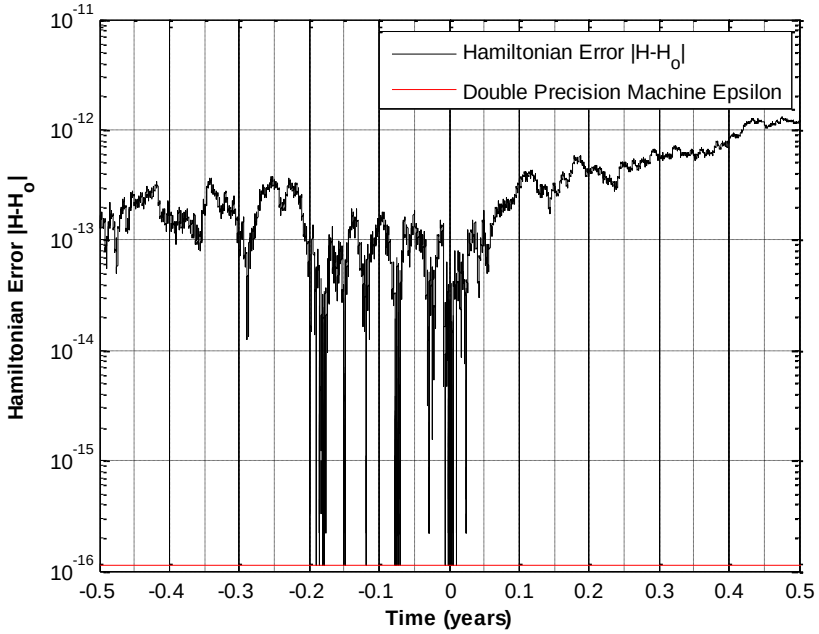

Figure 11. Hamiltonian error from Hamming fourth-order integrator.

3.1.3 Fourier Transform and Spectral Analysis

The transformation of the numerically integrated coordinate data, $f(t)$, from the time domain to the frequency domain is done using a finite Fourier transform over the symmetric time interval [-*T*, *T*]. The typical Fourier transform of a function over an infinite time span is done by,

$$\mathcal{F}(\nu) = \int_{-\infty}^{\infty} f(t) e^{-2\pi\nu i t} \mathrm{d}t \tag{156}$$

where *ν* is the cycle frequency. The Fourier transform assumes infinite periodicity in the signal, but over an arbitrary, finite time interval it is doubtful that the signal endpoints are of the same value. The consequence of this discontinuity is a phenomenon known as spectral leakage in the Fourier transform [47]. To inhibit this, the signal is multiplied by

a window function that forces the signal to start and end at zero amplitude. Laskar's NAFF uses a Hanning window of the form [44, 45],

$$\chi_p\left(\frac{t}{T}\right) = \frac{2^p (p!)^2}{(2p)!}\left(1 + \cos\left(\pi\frac{t}{T}\right)\right)^p \tag{157}$$

where p is the order of the cosine function and T is the frequency interval.

The window function is shown graphically for various values of p in Figure 12 for timespan [-T, T]. With the window function, the finite Fourier transform over the timespan [-T, T] becomes:

$$\begin{aligned}\mathcal{F}(v) &= \frac{1}{2T}\int_{-T}^{T} f(t)e^{-2\pi vit}\chi_p\left(\frac{t}{T}\right)\mathrm{d}t \\ &= \frac{1}{2T}\int_{0}^{T} f(t)e^{-2\pi vit}\chi_p\left(\frac{t}{T}\right)\mathrm{d}t - \frac{1}{2T}\int_{0}^{-T} f(t)e^{-2\pi vit}\chi_p\left(\frac{t}{T}\right)\mathrm{d}t\end{aligned} \tag{158}$$

The domain of the Fourier transform can be expressed as cycle frequency, v, or angular frequency, $\omega = 2\pi v$, but the latter will typically be used for the torus.

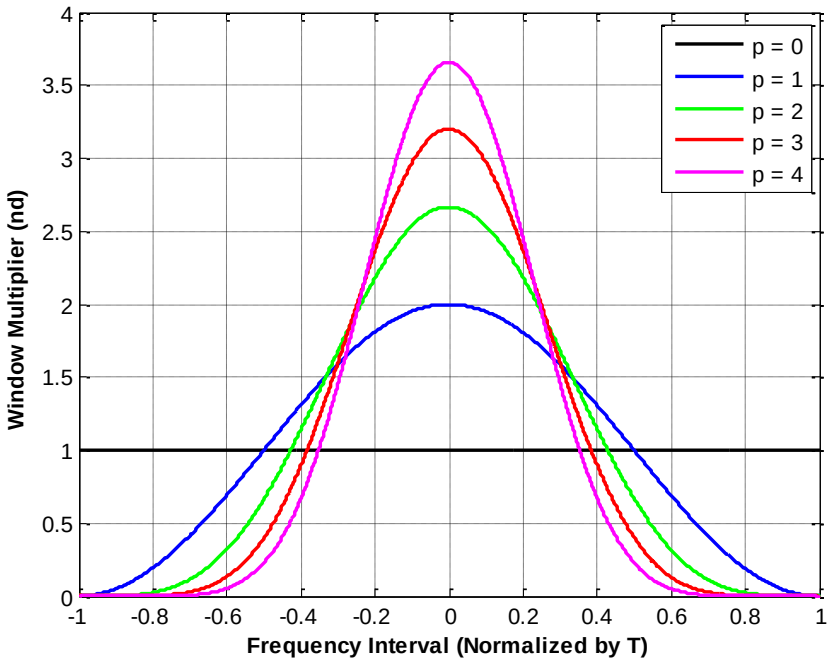

Figure 12. Hanning window of order p.

Choosing an appropriate window power is essential to dissecting spectral content from the transformed data. The effect of increasing the window power is shown in Figure 13 by applying a Fourier transform on a single spectral line of unit amplitude over the timespan [-1, 1] as demonstrated by Laskar [44:10] and Wiesel [18:4]:

$$\mathcal{F}(\omega) = \frac{1}{2}\int_{-1}^{1} e^{\omega i t}\chi_p(t)\mathrm{d}t = \frac{(-1)^p \pi^{2p}(p!)^2 \sin\omega}{\omega(\omega^2-\pi^2)\cdots(\omega^2-p^2\pi^2)} \tag{159}$$

In this example, the signal is a gate function and has a single spectral line at $\omega_0 = 0$, but Figure 13 shows sidelobe oscillations of $\omega_T = \pi/T$ which appear from the cosine term in (157). As p increases, the main lobe of the ω_0 spectral line is broadened and the sidelobes around it fall off more rapidly. The amplitude of the spectral line remains the same with increasing p, so the advantage of higher order window functions is an accelerated convergence upon the basis frequency. One disadvantage is found in signals containing

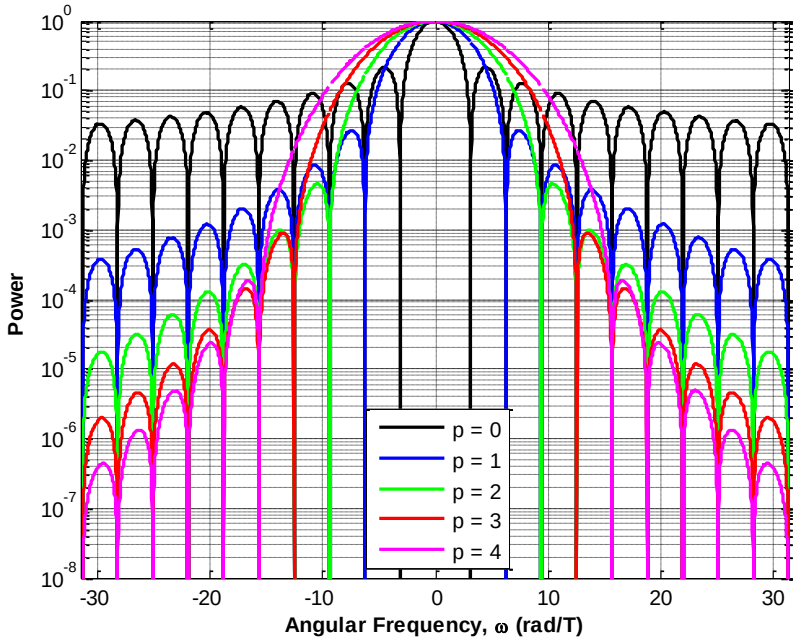

Figure 13. Graph of sidelobe effects from $\boldsymbol{\mathcal{F}_0(\omega)}$ to $\boldsymbol{\mathcal{F}_4(\omega)}$.

integer combinations of frequency sets in which one frequency is significantly smaller than the other:

$$\exists\ (\Omega_m, \Omega_n)\ \in\ \vec{\boldsymbol{\Omega}}\ \big|\ \Omega_m \ll \Omega_n, m \neq n \tag{160}$$

where mathematical jargon compresses the conditional statement to read: if there exists ($\exists$) a pair of frequencies (Ω_m, Ω_n) as an element of ($\in$) the basis set $\vec{\boldsymbol{\Omega}}$, such that (|) Ω_m is significantly smaller than Ω_n where *m* and *n* are not equal. When this occurs, such as the case of cascading harmonics from the small apsidal regression frequency, the higher order window functions can "swallow" nearby spectral content. This is known as *spectral shadowing*.

Ultimately, the choice of the Hanning window power is contingent upon the signal characteristics, but Laskar shows for KAM solutions that the accuracy of the frequency

analysis (order $1/T^{2p+2}$) generally improves by increasing p. He suggests using the highest possible value of p until precision begins to decrease. Wiesel has typically used a Hanning window of order p=2 to avoid spectral shadowing. This was found to be sufficient for the integrated ISS data.

Once the data is represented in the frequency domain with an appropriate window function, the spectrum must be decomposed into a set of precise basis frequencies and Fourier coefficients. Wiesel does this by specifying an approximate set of basis frequencies (described in §3.1.3.1) followed by a Newton-Rhapson algorithm that seeks the maximum spectral power, $\mathcal{P} = |\phi|^2$, in the vicinity of integer combinations of the approximate basis frequencies [17:5]. As the peaks are identified, the basis set can be determined from a least squares solution of the frequency approximations. With the newly estimated basis set, the coefficients of the Fourier transform are determined according to the following:

$$C_{(0,0,\ldots,0)^N} = \Re\Phi(0) \tag{161}$$

$$C_j = 2\Re\Phi\left(\omega_{\vec{j}}\right) \tag{162}$$

$$S_j = -2\Im\Phi\left(\omega_{\vec{j}}\right) \tag{163}$$

$\Phi\left(\omega_{\vec{j}}\right)$ is the complex Fourier transform at the composite frequency $\omega_{\vec{j}} = \vec{\boldsymbol{j}} \cdot \vec{\boldsymbol{\Omega}}$, or in the case of the constant term, $C_{(0,0,\ldots,0)^N}$, at $\omega = 0$.

3.1.3.1 Basis Frequency Approximations

The starting guess for the three basis frequencies in the TDR frame are determined from motion in the two-body orbit with the addition of secular rates from the J_2

disturbing function (see the Lagrange Planetary Equations from §2.1.6.1). The largest frequency is the *anomalistic frequency* found in the orbit plane. In terms of the classical orbital elements, it is approximately the Keplarian frequency with the mean anomaly correction:

$$\Omega_1 \approx \sqrt{\frac{\mu}{a^3}} - \frac{3\sqrt{\mu}J_2R_\oplus^2}{2a^{7/2}(1-e^2)^{3/2}}\left(\frac{3}{2}\sin^2(i)-1\right) \tag{164}$$

The second largest frequency appears in the true of date equator. It is approximately the Earth's rotation rate (which must be negative since the node appears to move clockwise about the TDR z-axis) with the nodal regression correction:

$$\Omega_2 \approx \omega_\oplus - \frac{3\sqrt{\mu}J_2R_\oplus^2}{2a^{7/2}(1-e^2)^2}\cos i \tag{165}$$

The smallest frequency is approximately the *apsidal regression rate* that characterizes the rotation of the line of apsides due to the Earth's oblateness:

$$\Omega_3 \approx -\frac{3\sqrt{\mu}J_2R_\oplus^2}{2a^{7/2}(1-e^2)^2}\left(\frac{5}{2}\sin^2(i)-2\right) \tag{166}$$

3.2 Motion Near an Earth Satellite KAM Torus

The motion of an Earth orbiting satellite is dependent on more than just conservative gravitational forces, so the reference torus alone will not suffice for most satellites (especially those in low Earth orbit). Wiesel claims that the satellite's physical state vector can be modeled with a contribution to the reference torus from non-deterministic forces such that,

$$\vec{\mathbf{X}}(t) = \left[x, y, z, v_x, v_y, v_z\right]^T = \vec{\mathbf{X}}_{ref}(t) + \delta\vec{\mathbf{X}}_{stoc}(t) \tag{167}$$

where $\delta\vec{\mathbf{X}}_{stoc}(t)$ is the non-deterministic or stochastic displacement. The stochastic displacement can occur parallel to the torus surface and perpendicular to it. The parallel portion results in a displacement to the torus coordinates, $\vec{\mathbf{Q}}$, which can be accounted for on the surface of the reference torus. The perpendicular portion *cannot* be accounted for on the surface of the reference torus since any displacement to the torus momenta, $\vec{\mathbf{P}}$, steps off the torus surface. Thus the stochastic displacement must be broken into two parts: that within the reference torus and that beyond the reference torus. Reflecting both parts, the displacement can easily be resolved in terms of the torus coordinates and momenta using the chain rule [48:2],

$$\begin{aligned}\vec{\mathbf{X}}(t) &= \vec{\mathbf{X}}_{ref}(t) + \frac{\partial\vec{\mathbf{X}}(t)}{\partial\vec{\mathbf{Y}}(t)}\frac{\partial\vec{\mathbf{Y}}(t)}{\partial\vec{\mathbf{Y}}(t_0)}\delta\vec{\mathbf{Y}}(t_0) \\ &= \vec{\mathbf{X}}_{ref}(t) + \underbrace{\frac{\partial\vec{\mathbf{X}}(t)}{\partial\vec{\mathbf{Q}}(t)}\frac{\partial\vec{\mathbf{Q}}(t)}{\partial\vec{\mathbf{Y}}(t_0)}\delta\vec{\mathbf{Y}}(t_0)}_{\text{Parallel}} + \underbrace{\frac{\partial\vec{\mathbf{X}}(t)}{\partial\vec{\mathbf{P}}(t)}\frac{\partial\vec{\mathbf{P}}(t)}{\partial\vec{\mathbf{Y}}(t_0)}\delta\vec{\mathbf{Y}}(t_0)}_{\text{Perpendicular}}\end{aligned} \tag{168}$$

where the local displacement with respect to the reference torus is given by:

$$\delta\vec{\mathbf{Y}}(t) = \begin{bmatrix}\delta\vec{\boldsymbol{Q}}(t) \\ \delta\vec{\boldsymbol{P}}(t)\end{bmatrix} \tag{169}$$

The process for determining the local displacements is left for the next section, but first, let us direct our attention to how they are used for both parallel and perpendicular motion. There are two ways to account for the parallel motion labeled in (168). Not surprisingly, the most direct method simply adds the parallel $\delta\vec{\mathbf{X}}$ component to the torus generated $\vec{\mathbf{X}}_{ref}$, exactly as indicated. The preferred, indirect method adds $\delta\vec{\mathbf{Q}}$ to the torus coordinates which makes it unnecessary to add the parallel $\delta\vec{\mathbf{X}}$ component to $\vec{\mathbf{X}}_{ref}$. Either

way, the contributions of $\delta\vec{\mathbf{Q}}$ must be accumulated over time and stored in $\vec{\mathbf{Q}}(t_0)$ to minimize error growth in the reference torus and avoid a breakdown of the linearization model. Unlike parallel motion, there is only one way to account for the perpendicular $\delta\vec{\mathbf{X}}$ component; it must be added directly to $\vec{\mathbf{X}}_{ref}$ since $\vec{\mathbf{P}}$ remains unchanged on the reference torus.

Even though the momenta do not change on the reference torus, the actual orbit is characterized by new momenta formed by the displacement, $\vec{\boldsymbol{P}} + \delta\vec{\boldsymbol{P}}$, which is still constant, but describing an adjacent torus with different frequencies. This frequency shift must be accounted for in the reference torus coordinates if it is to accurately approximate motion nearby. Recall that the state vector for the torus coordinates and momenta is given by:

$$\vec{\mathbf{Y}}(t) = \begin{bmatrix} \vec{\boldsymbol{Q}}(t) \\ \vec{\boldsymbol{P}}(t) \end{bmatrix} = \begin{bmatrix} \vec{\boldsymbol{\Omega}} \cdot (t - t_0) + \vec{\mathbf{Q}}(t_0) \\ constant \end{bmatrix} \tag{170}$$

It was previously shown in (144) that the constant frequencies, $\vec{\boldsymbol{\Omega}}$, are a function of the momenta, so if the momenta change by an incremental amount, so too do the frequencies [48:7]:

$$\delta\dot{\vec{\mathbf{Q}}} = \delta\vec{\boldsymbol{\Omega}} = \frac{\partial\vec{\boldsymbol{\Omega}}}{\partial\vec{\boldsymbol{P}}}\delta\vec{\mathbf{P}} \tag{171}$$

Since the torus coordinates, $\vec{\boldsymbol{Q}}$, increment linearly with time as seen in (170), a slightly different frequency manifests as a linear drift in the corresponding torus coordinate. We directly observe the drift magnitude by integrating (171) to get:

$$\delta\vec{\mathbf{Q}} = \delta\vec{\mathbf{Q}}_0 + \frac{\partial\vec{\boldsymbol{\Omega}}}{\partial\vec{\boldsymbol{P}}}\delta\vec{\mathbf{P}} \cdot (t - t_0) \tag{172}$$

When the offset, $\delta\vec{\mathbf{Q}}$, is added to the reference torus coordinates, it should minimize the error between the actual orbit (potentially on an adjacent torus) and the reference torus (likely nearby). That is to say, the $\delta\vec{\mathbf{Q}}$ update to the reference torus should maintain a close proximity to the actual orbit by accounting for parallel local motion near the reference torus. With the update, the reference torus coordinates are simply:

$$\vec{\boldsymbol{Q}}(t) = \vec{\boldsymbol{\Omega}} \cdot (t - t_0) + \vec{\mathbf{Q}}(t_0) + \delta\vec{\mathbf{Q}} \tag{173}$$

Wiesel indicates that the reference torus initial coordinates must be routinely updated with the offset, $\delta\vec{\mathbf{Q}}$, to remain within the region for which the linear observation model is a valid approximation of the satellite's motion.

Next, let us direct our attention to the partial derivative matrices from (168) which will be needed for sequential-batch estimation. $\partial\vec{\mathbf{Q}}(t)/\partial\vec{\mathbf{Y}}(t_0)$ is shown to be the following 3x6 matrix:

$$\partial\vec{\mathbf{Q}}(t)/\partial\vec{\mathbf{Y}}(t_0) = \begin{bmatrix} \frac{\partial\vec{\mathbf{Q}}}{\partial\vec{\mathbf{Q}}_0} & \frac{\partial\vec{\mathbf{Q}}}{\partial\vec{\mathbf{P}}_0} \end{bmatrix} \tag{174}$$

Taking the partials of (173) with respect to $\vec{\mathbf{Q}}_0$, it is clear that the left Jacobian is a 3x3 identity matrix. The right Jacobian is much more complicated. If (144) is expanded with the chain rule to include a small change in the fundamental frequencies [49],

$$\frac{d\vec{\mathbf{Q}}}{dt} = \vec{\boldsymbol{\Omega}} + \frac{\partial\vec{\boldsymbol{\Omega}}}{\partial\vec{\mathbf{P}}}\delta\vec{\mathbf{P}} = \vec{\boldsymbol{\Omega}} + \frac{\partial^2\mathcal{K}}{\partial\vec{\mathbf{P}}^2}\delta\vec{\mathbf{P}} \tag{175}$$

$\partial\vec{\mathbf{Q}}/\partial\vec{\mathbf{P}}_0$ can then be approximated from the second partial derivative of the Hamiltonian function, $\mathcal{K}$[19:8]:

$$\mathcal{K} = -\frac{\mu^2}{2P_1^2} - P_2\omega_\oplus + \frac{\mu^4 J_2 R_\oplus^2 (P_3^2 - 3P_2^2)}{4P_1^3 P_3^5} \tag{176}$$

where the first term is from two-body motion, the second is a vestige of the partial derivative of the generating function with respect to time (an artifact of using the TDR frame for the torus coordinates), and the last term is the J2 potential in terms of the Delaunay momenta. The first partial of $\mathcal{K}$ is the frequency given by (144), or written as a scalar [48:7]:

$$\frac{\partial \mathcal{K}}{\partial P_i} \approx \Omega_i \tag{177}$$

The second partial derivative of $\mathcal{K}$ is then the typical Jacobian [48:7]:

$$\frac{\partial^2 \mathcal{K}}{\partial \vec{\mathbf{P}}^2} \approx \frac{\partial \vec{\mathbf{\Omega}}}{\partial \vec{\mathbf{P}}} \tag{178}$$

Applying the finishing touch to (174), the full matrix is,

$$\partial\vec{\mathbf{Q}}(t)/\partial\vec{\mathbf{Y}}(t_0) = \begin{bmatrix} 1 & 0 & 0 & \frac{\partial \Omega_1}{\partial P_1}\Delta t & \frac{\partial \Omega_1}{\partial P_2}\Delta t & \frac{\partial \Omega_1}{\partial P_3}\Delta t \\ 0 & 1 & 0 & \frac{\partial \Omega_2}{\partial P_1}\Delta t & \frac{\partial \Omega_2}{\partial P_2}\Delta t & \frac{\partial \Omega_2}{\partial P_3}\Delta t \\ 0 & 0 & 1 & \frac{\partial \Omega_3}{\partial P_1}\Delta t & \frac{\partial \Omega_3}{\partial P_2}\Delta t & \frac{\partial \Omega_3}{\partial P_3}\Delta t \end{bmatrix} \tag{179}$$

where the matrix components are [48:7]:

$$\frac{\partial \Omega_1}{\partial P_1} = -\frac{3\mu^2}{P_1^4} + \frac{3\mu^4 J_2 R_\oplus^2 (P_3^2 - P_2^2)}{P_1^5 P_3^5} \tag{180}$$

$$\frac{\partial \Omega_1}{\partial P_2} = \frac{\partial \Omega_2}{\partial P_1} = \frac{9\mu^4 J_2 R_\oplus^2 P_2}{2P_1^4 P_3^5} \tag{181}$$

$$\frac{\partial \Omega_1}{\partial P_3} = \frac{\partial \Omega_3}{\partial P_1} = \frac{9\mu^4 J_2 R_\oplus^2 (P_3^2 - 5P_2^2)}{P_1^4 P_3^6} \tag{182}$$

$$\frac{\partial \Omega_2}{\partial P_2} = -\frac{3\mu^4 J_2 R_\oplus^2}{2P_1^3 P_3^5} \tag{183}$$

$$\frac{\partial \Omega_2}{\partial P_3} = \frac{\partial \Omega_3}{\partial P_2} = \frac{15\mu^4 J_2 R_\oplus^2 P_2}{2P_1^3 P_3^6} \tag{184}$$

$$\frac{\partial \Omega_3}{\partial P_3} = \frac{3\mu^4 J_2 R_\oplus^2 (2P_3^2 - 15P_2^2)}{2P_1^3 P_3^7} \tag{185}$$

In a similar manner, $\partial\vec{\mathbf{P}}(t)/\partial\vec{\mathbf{Y}}(t_0)$ is easily shown to be:

$$\partial\vec{\mathbf{P}}(t)/\partial\vec{\mathbf{Y}}(t_0) = \begin{bmatrix} \dfrac{\partial\vec{\mathbf{P}}}{\partial\vec{\mathbf{Q}}_0} & \dfrac{\partial\vec{\mathbf{P}}}{\partial\vec{\mathbf{P}}_0} \end{bmatrix} \tag{186}$$

From (144), the momenta are constant, so the left Jacobians is a 3x3 zero matrix and the right Jacobian is a 3x3 identity matrix.

$$\partial\vec{\mathbf{P}}(t)/\partial\vec{\mathbf{Y}}(t_0) = \begin{bmatrix} 0 & 0 & 0 & 1 & 0 & 0 \\ 0 & 0 & 0 & 0 & 1 & 0 \\ 0 & 0 & 0 & 0 & 0 & 1 \end{bmatrix} \tag{187}$$

The first three rows of the 6x3 Jacobian matrix, $\partial\vec{\mathbf{X}}(t)/\partial\vec{\mathbf{Q}}(t)$, are all that is required to produce displacements to the native coordinates and can be determined directly from the partial derivatives of the torus Fourier series previously specified by (141) such that,

$$\partial\vec{\mathbf{q}}(t)/\partial \mathrm{Q}_i(t) = \sum_{j=-M}^{M} j_i\{-\vec{\boldsymbol{C}}_{\boldsymbol{j}} \sin(\vec{\boldsymbol{j}} \cdot \vec{\mathbf{Q}}) + \vec{\boldsymbol{S}}_{\boldsymbol{j}} \cos(\vec{\boldsymbol{j}} \cdot \vec{\mathbf{Q}})\} \tag{188}$$

A less accurate alternative is to approximate the full Jacobian matrix from the derivatives of the linearized two-body problem. This is the same method required for determining $\partial\vec{\mathbf{X}}(t)/\partial\vec{\mathbf{P}}(t)$.

It follows that the 6x6 observation partial derivative matrix, $\partial\vec{\mathbf{X}}(t)/\partial\vec{\mathbf{Y}}(t)$, is just the concatenation of $\partial\vec{\mathbf{X}}(t)/\partial\vec{\mathbf{Q}}(t)$ and $\partial\vec{\mathbf{X}}(t)/\partial\vec{\mathbf{P}}(t)$. The first three columns of

$\partial\vec{\mathbf{X}}(t)/\partial\vec{\mathbf{Y}}(t)$ are $\partial\vec{\mathbf{X}}(t)/\partial\vec{\mathbf{Q}}(t)$ and the last three columns are $\partial\vec{\mathbf{X}}(t)/\partial\vec{\mathbf{P}}(t)$. The matrix, $\partial\vec{\mathbf{X}}(t)/\partial\vec{\mathbf{Y}}(t)$, cannot be determined directly, but it can be formulated from a mapping between two separate Jacobians, namely $\partial\vec{\mathbf{Y}}/\partial\vec{\mathbf{Z}}$ and $\partial\vec{\mathbf{Z}}/\partial\vec{\mathbf{X}}$, where $\vec{\mathbf{Z}}$ is the vector formulation of the classical orbital elements:

$$\vec{\mathbf{Z}}(t) = [M, \Omega, \omega, a, e, i]^T \tag{189}$$

This mapping is possible since the canonical torus coordinates are very nearly equivalent to the first three classical orbital elements. As a consequence, we can write $\vec{\mathbf{Z}}$ as [48:2]:

$$\vec{\mathbf{Z}}(t) = [Q_1, Q_2, Q_3, a, e, i]^T \tag{190}$$

The first partial derivative, $\partial\vec{\mathbf{Y}}/\partial\vec{\mathbf{Z}}$, is the *Delaunay elements Jacobian*. Wiesel has shown that upon ignoring Earth's rotation rate and limiting the gravity field to a single point mass term, as in the two-body problem, the torus coordinates and momenta revert to the Delaunay elements given in (84) - (89) [19:7]. Thus, the state vector Y can be written in terms of the Delaunay elements as a reasonable approximation [48:6]:

$$\vec{\mathbf{Y}}(t) = \begin{bmatrix} Q_1 = M \\ Q_2 = \Omega \\ Q_3 = \omega \\ P_1 = \sqrt{\mu a} \\ P_2 = \sqrt{\mu a}\sqrt{1-e^2}\cos i \\ P_3 = \sqrt{\mu a}\sqrt{1-e^2} \end{bmatrix} \tag{191}$$

The Delaunay elements Jacobian is discerned in the usual fashion:

$$\partial\vec{\mathbf{Y}}/\partial\vec{\mathbf{Z}} = \begin{bmatrix} 1 & 0 & 0 & 0 & 0 & 0 \\ 0 & 1 & 0 & 0 & 0 & 0 \\ 0 & 0 & 1 & 0 & 0 & 0 \\ 0 & 0 & 0 & \frac{\partial \mathrm{P}_1}{\partial a} & \frac{\partial \mathrm{P}_1}{\partial e} & \frac{\partial \mathrm{P}_1}{\partial i} \\ 0 & 0 & 0 & \frac{\partial \mathrm{P}_2}{\partial a} & \frac{\partial \mathrm{P}_2}{\partial e} & \frac{\partial \mathrm{P}_2}{\partial i} \\ 0 & 0 & 0 & \frac{\partial \mathrm{P}_3}{\partial a} & \frac{\partial \mathrm{P}_3}{\partial e} & \frac{\partial \mathrm{P}_3}{\partial i} \end{bmatrix} \tag{192}$$

where the matrix components are [48:6]:

$$\frac{\partial \mathrm{P}_1}{\partial a} = \frac{1}{2}\sqrt{\frac{\mu}{a}} \tag{193}$$

$$\frac{\partial \mathrm{P}_1}{\partial e} = 0 \tag{194}$$

$$\frac{\partial \mathrm{P}_1}{\partial i} = 0 \tag{195}$$

$$\frac{\partial \mathrm{P}_2}{\partial a} = \frac{1}{2}\sqrt{\frac{\mu}{a}}\sqrt{1-e^2}\cos i \tag{196}$$

$$\frac{\partial \mathrm{P}_2}{\partial e} = -e\sqrt{\frac{\mu a}{1-e^2}}\cos i \tag{197}$$

$$\frac{\partial \mathrm{P}_2}{\partial i} = -\sqrt{\mu a}\sqrt{1-e^2}\sin i \tag{198}$$

$$\frac{\partial \mathrm{P}_3}{\partial a} = \frac{1}{2}\sqrt{\frac{\mu}{a}}\sqrt{1-e^2} \tag{199}$$

$$\frac{\partial \mathrm{P}_3}{\partial e} = -e\sqrt{\frac{\mu a}{1-e^2}} \tag{200}$$

$$\frac{\partial \mathrm{P}_3}{\partial i} = 0 \tag{201}$$

The second partial derivative, $\partial\vec{\mathbf{Z}}/\partial\vec{\mathbf{X}}$, is the *two-body elements Jacobian* in which the classical orbital elements are linearized in the TDR frame. Start by characterizing the Jacobian matrix as:

$$\partial\vec{\mathbf{Z}}/\partial\vec{\mathbf{X}} = \begin{bmatrix} \frac{\partial M}{\partial x} & \frac{\partial M}{\partial y} & \frac{\partial M}{\partial z} & \frac{\partial M}{\partial v_x} & \frac{\partial M}{\partial v_y} & \frac{\partial M}{\partial v_z} \\ \frac{\partial \Omega}{\partial x} & \frac{\partial \Omega}{\partial y} & \frac{\partial \Omega}{\partial z} & \frac{\partial \Omega}{\partial v_x} & \frac{\partial \Omega}{\partial v_y} & \frac{\partial \Omega}{\partial v_z} \\ \frac{\partial \omega}{\partial x} & \frac{\partial \omega}{\partial y} & \frac{\partial \omega}{\partial z} & \frac{\partial \omega}{\partial v_x} & \frac{\partial \omega}{\partial v_y} & \frac{\partial \omega}{\partial v_z} \\ \frac{\partial a}{\partial x} & \frac{\partial a}{\partial y} & \frac{\partial a}{\partial z} & \frac{\partial a}{\partial v_x} & \frac{\partial a}{\partial v_y} & \frac{\partial a}{\partial v_z} \\ \frac{\partial e}{\partial x} & \frac{\partial e}{\partial y} & \frac{\partial e}{\partial z} & \frac{\partial e}{\partial v_x} & \frac{\partial e}{\partial v_y} & \frac{\partial e}{\partial v_z} \\ \frac{\partial i}{\partial x} & \frac{\partial i}{\partial y} & \frac{\partial i}{\partial z} & \frac{\partial i}{\partial v_x} & \frac{\partial i}{\partial v_y} & \frac{\partial i}{\partial v_z} \end{bmatrix} \tag{202}$$

Given the definition of the semimajor axis in (41), the partial derivative components in the fourth row of (202) are:

$$\frac{\partial a}{\partial x} = \frac{\mu^4 x}{8a^2 r^3} \tag{203}$$

$$\frac{\partial a}{\partial y} = \frac{\mu^4 y}{8a^2 r^3} \tag{204}$$

$$\frac{\partial a}{\partial z} = \frac{\mu^4 z}{8a^2 r^3} \tag{205}$$

$$\frac{\partial a}{\partial v_x} = \frac{\mu^3 v_x}{8a^2} \tag{206}$$

$$\frac{\partial a}{\partial v_y} = \frac{\mu^3 v_y}{8a^2} \tag{207}$$

$$\frac{\partial a}{\partial v_z} = \frac{\mu^3 v_z}{8a^2} \tag{208}$$

Given the definition of the magnitude of the eccentricity vector in (69), the partial derivative components in the fifth row of (202) are [48:3]:

$$\frac{\partial e}{\partial x} = \frac{1}{\|\vec{e}\|}\left(e_x \frac{\partial e_x}{\partial x} + e_y \frac{\partial e_y}{\partial x} + e_z \frac{\partial e_z}{\partial x}\right) \tag{209}$$

$$\frac{\partial e}{\partial y} = \frac{1}{\|\vec{e}\|}\left(e_x \frac{\partial e_x}{\partial y} + e_y \frac{\partial e_y}{\partial y} + e_z \frac{\partial e_z}{\partial y}\right) \tag{210}$$

$$\frac{\partial e}{\partial z} = \frac{1}{\|\vec{e}\|}\left(e_x \frac{\partial e_x}{\partial z} + e_y \frac{\partial e_y}{\partial z} + e_z \frac{\partial e_z}{\partial z}\right) \tag{211}$$

$$\frac{\partial e}{\partial v_x} = \frac{1}{\|\vec{e}\|}\left(e_x \frac{\partial e_x}{\partial v_x} + e_y \frac{\partial e_y}{\partial v_x} + e_z \frac{\partial e_z}{\partial v_x}\right) \tag{212}$$

$$\frac{\partial e}{\partial v_y} = \frac{1}{\|\vec{e}\|}\left(e_x \frac{\partial e_x}{\partial v_y} + e_y \frac{\partial e_y}{\partial v_y} + e_z \frac{\partial e_z}{\partial v_y}\right) \tag{213}$$

$$\frac{\partial e}{\partial v_z} = \frac{1}{\|\vec{e}\|}\left(e_x \frac{\partial e_x}{\partial v_z} + e_y \frac{\partial e_y}{\partial v_z} + e_z \frac{\partial e_z}{\partial v_z}\right) \tag{214}$$

The partial derivatives of the eccentricity vector required in (209) - (214) are determined from (68) [48:3]:

$$\frac{\partial e_x}{\partial x} = \frac{1}{\mu}\left(v^2 - \frac{\mu}{r} + \frac{\mu x^2}{r^3} - v_x^2\right) \tag{215}$$

$$\frac{\partial e_x}{\partial y} = \frac{\partial e_y}{\partial x} = \frac{1}{\mu}\left(\frac{\mu xy}{r^3} - v_x v_y\right) \tag{216}$$

$$\frac{\partial e_x}{\partial z} = \frac{\partial e_z}{\partial x} = \frac{1}{\mu}\left(\frac{\mu xz}{r^3} - v_x v_z\right) \tag{217}$$

$$\frac{\partial e_y}{\partial y} = \frac{1}{\mu}\left(v^2 - \frac{\mu}{r} + \frac{\mu y^2}{r^3} - v_y^2\right) \tag{218}$$

$$\frac{\partial e_y}{\partial z} = \frac{\partial e_z}{\partial y} = \frac{1}{\mu}\left(\frac{\mu yz}{r^3} - v_y v_z\right) \tag{219}$$

$$\frac{\partial e_z}{\partial z} = \frac{1}{\mu}\left(v^2 - \frac{\mu}{r} + \frac{\mu z^2}{r^3} - v_z^2\right) \tag{220}$$

$$\frac{\partial e_x}{\partial v_x} = \frac{1}{\mu}\left(-yv_y - zv_z\right) \tag{221}$$

$$\frac{\partial e_x}{\partial v_y} = \frac{1}{\mu}\left(2xv_y - yv_x\right) \tag{222}$$

$$\frac{\partial e_x}{\partial v_z} = \frac{1}{\mu}\left(2xv_z - zv_x\right) \tag{223}$$

$$\frac{\partial e_y}{\partial v_x} = \frac{1}{\mu}\left(2yv_x - xv_y\right) \tag{224}$$

$$\frac{\partial e_y}{\partial v_y} = \frac{1}{\mu}\left(-xv_x - zv_z\right) \tag{225}$$

$$\frac{\partial e_y}{\partial v_z} = \frac{1}{\mu}\left(2yv_z - zv_y\right) \tag{226}$$

$$\frac{\partial e_z}{\partial v_x} = \frac{1}{\mu}\left(2zv_x - xv_z\right) \tag{227}$$

$$\frac{\partial e_z}{\partial v_y} = \frac{1}{\mu}\left(2zv_y - yv_z\right) \tag{228}$$

$$\frac{\partial e_z}{\partial v_z} = \frac{1}{\mu}\left(-xv_x - yv_y\right) \tag{229}$$

Given the quadrant conclusive definition of inclination in (71), the partial derivative components in the sixth row of (202) are [48:4],

$$\frac{\partial i}{\partial x} = \frac{-1}{\sqrt{1 - \left(\frac{h_z}{h^2}\right)^2}}\left(\frac{1}{h}\frac{\partial h_z}{\partial x} - \frac{h_z}{h^3}\left[h_x\frac{\partial h_x}{\partial x} + h_y\frac{\partial h_y}{\partial x} + h_z\frac{\partial h_z}{\partial x}\right]\right) \tag{230}$$

$$\frac{\partial i}{\partial y}=\frac{-1}{\sqrt{1-\left(\frac{h_z}{h^2}\right)^2}}\left(\frac{1}{h}\frac{\partial h_z}{\partial y}-\frac{h_z}{h^3}\left[h_x\frac{\partial h_x}{\partial y}+h_y\frac{\partial h_y}{\partial y}+h_z\frac{\partial h_z}{\partial y}\right]\right) \tag{231}$$

$$\frac{\partial i}{\partial z}=\frac{-1}{\sqrt{1-\left(\frac{h_z}{h^2}\right)^2}}\left(\frac{1}{h}\frac{\partial h_z}{\partial z}-\frac{h_z}{h^3}\left[h_x\frac{\partial h_x}{\partial z}+h_y\frac{\partial h_y}{\partial z}+h_z\frac{\partial h_z}{\partial z}\right]\right) \tag{232}$$

$$\frac{\partial i}{\partial v_x}=\frac{-1}{\sqrt{1-\left(\frac{h_z}{h^2}\right)^2}}\left(\frac{1}{h}\frac{\partial h_z}{\partial v_x}-\frac{h_z}{h^3}\left[h_x\frac{\partial h_x}{\partial v_x}+h_y\frac{\partial h_y}{\partial v_x}+h_z\frac{\partial h_z}{\partial v_x}\right]\right) \tag{233}$$

$$\frac{\partial i}{\partial v_y}=\frac{-1}{\sqrt{1-\left(\frac{h_z}{h^2}\right)^2}}\left(\frac{1}{h}\frac{\partial h_z}{\partial v_y}-\frac{h_z}{h^3}\left[h_x\frac{\partial h_x}{\partial v_y}+h_y\frac{\partial h_y}{\partial v_y}+h_z\frac{\partial h_z}{\partial v_y}\right]\right) \tag{234}$$

$$\frac{\partial i}{\partial v_z}=\frac{-1}{\sqrt{1-\left(\frac{h_z}{h^2}\right)^2}}\left(\frac{1}{h}\frac{\partial h_z}{\partial v_z}-\frac{h_z}{h^3}\left[h_x\frac{\partial h_x}{\partial v_z}+h_y\frac{\partial h_y}{\partial v_z}+h_z\frac{\partial h_z}{\partial v_z}\right]\right) \tag{235}$$

where the specific angular momentum vector, $\vec{\boldsymbol{h}}$, is given in (13) and its partial derivatives are [48:4]:

$$\begin{aligned}\partial\vec{\mathbf{h}}/\partial\vec{\mathbf{X}} &= \begin{bmatrix}\frac{\partial h_x}{\partial x} & \frac{\partial h_x}{\partial y} & \frac{\partial h_x}{\partial z} & \frac{\partial h_x}{\partial v_x} & \frac{\partial h_x}{\partial v_y} & \frac{\partial h_x}{\partial v_z}\\ \frac{\partial h_y}{\partial x} & \frac{\partial h_y}{\partial y} & \frac{\partial h_y}{\partial z} & \frac{\partial h_y}{\partial v_x} & \frac{\partial h_y}{\partial v_y} & \frac{\partial h_y}{\partial v_z}\\ \frac{\partial h_z}{\partial x} & \frac{\partial h_z}{\partial y} & \frac{\partial h_z}{\partial z} & \frac{\partial h_z}{\partial v_x} & \frac{\partial h_z}{\partial v_y} & \frac{\partial h_z}{\partial v_z}\end{bmatrix}\\ &= \begin{bmatrix}0 & v_z & -v_y & 0 & -z & y\\ -v_z & 0 & v_x & z & 0 & -x\\ v_y & -v_x & 0 & -y & x & 0\end{bmatrix}\end{aligned} \tag{236}$$

Given the quadrant conclusive definition of RAAN in (75), the partial derivative components in the second row of (202) are [48:4]:

$$\frac{\partial \Omega}{\partial x} = \frac{1}{h_x^2 + h_y^2}\left(h_x \frac{\partial h_y}{\partial x} - h_y \frac{\partial h_x}{\partial x}\right) \tag{237}$$

$$\frac{\partial \Omega}{\partial y} = \frac{1}{h_x^2 + h_y^2}\left(h_x \frac{\partial h_y}{\partial y} - h_y \frac{\partial h_x}{\partial y}\right) \tag{238}$$

$$\frac{\partial \Omega}{\partial z} = \frac{1}{h_x^2 + h_y^2}\left(h_x \frac{\partial h_y}{\partial z} - h_y \frac{\partial h_x}{\partial z}\right) \tag{239}$$

$$\frac{\partial \Omega}{\partial v_x} = \frac{1}{h_x^2 + h_y^2}\left(h_x \frac{\partial h_y}{\partial v_x} - h_y \frac{\partial h_x}{\partial v_x}\right) \tag{240}$$

$$\frac{\partial \Omega}{\partial v_y} = \frac{1}{h_x^2 + h_y^2}\left(h_x \frac{\partial h_y}{\partial v_y} - h_y \frac{\partial h_x}{\partial v_y}\right) \tag{241}$$

$$\frac{\partial \Omega}{\partial v_z} = \frac{1}{h_x^2 + h_y^2}\left(h_x \frac{\partial h_y}{\partial v_z} - h_y \frac{\partial h_x}{\partial v_z}\right) \tag{242}$$

Given the definition of argument of perigee in (76), the partial derivative components in the third row of (202) are [48:5]:

$$\begin{aligned}\frac{\partial \omega}{\partial x} = \frac{-1}{\sqrt{1 - \left(\frac{h_x e_y - h_y e_x}{e\sqrt{h_x^2 + h_y^2}}\right)^2}}\Bigg\{\frac{1}{e\sqrt{h_x^2 + h_y^2}}\Bigg(e_y \frac{\partial h_x}{\partial x} + h_x \frac{\partial e_y}{\partial x} - e_x \frac{\partial h_y}{\partial x} \\ - h_y \frac{\partial e_x}{\partial x}\Bigg) - \left(h_x e_y - h_y e_x\right)\Bigg[\frac{e^{-3}}{\sqrt{h_x^2 + h_y^2}}\Bigg(e_x \frac{\partial e_x}{\partial x} + e_y \frac{\partial e_y}{\partial x} + e_z \frac{\partial e_z}{\partial x}\Bigg) \\ + \frac{1}{e\left(h_x^2 + h_y^2\right)^{3/2}}\Bigg(h_x \frac{\partial h_x}{\partial x} + h_y \frac{\partial h_y}{\partial x}\Bigg)\Bigg]\Bigg\}\end{aligned} \tag{243}$$

$$\frac{\partial \omega}{\partial y} = \frac{-1}{\sqrt{1-\left(\frac{h_x e_y - h_y e_x}{e\sqrt{h_x^2+h_y^2}}\right)^2}}\left\{\frac{1}{e\sqrt{h_x^2+h_y^2}}\left(e_y\frac{\partial h_x}{\partial y} + h_x\frac{\partial e_y}{\partial y} - e_x\frac{\partial h_y}{\partial y}\right.\right.$$

$$\left. - h_y\frac{\partial e_x}{\partial y}\right) - \left(h_x e_y - h_y e_x\right)\left[\frac{e^{-3}}{\sqrt{h_x^2+h_y^2}}\left(e_x\frac{\partial e_x}{\partial y} + e_y\frac{\partial e_y}{\partial y} + e_z\frac{\partial e_z}{\partial y}\right)\right. \quad (244)$$

$$\left.\left. + \frac{1}{e\left(h_x^2+h_y^2\right)^{3/2}}\left(h_x\frac{\partial h_x}{\partial y} + h_y\frac{\partial h_y}{\partial y}\right)\right]\right\}$$

$$\frac{\partial \omega}{\partial z} = \frac{-1}{\sqrt{1-\left(\frac{h_x e_y - h_y e_x}{e\sqrt{h_x^2+h_y^2}}\right)^2}}\left\{\frac{1}{e\sqrt{h_x^2+h_y^2}}\left(e_y\frac{\partial h_x}{\partial z} + h_x\frac{\partial e_y}{\partial z} - e_x\frac{\partial h_y}{\partial z}\right.\right.$$

$$\left. - h_y\frac{\partial e_x}{\partial z}\right) - \left(h_x e_y - h_y e_x\right)\left[\frac{e^{-3}}{\sqrt{h_x^2+h_y^2}}\left(e_x\frac{\partial e_x}{\partial z} + e_y\frac{\partial e_y}{\partial z} + e_z\frac{\partial e_z}{\partial z}\right)\right. \quad (245)$$

$$\left.\left. + \frac{1}{e\left(h_x^2+h_y^2\right)^{3/2}}\left(h_x\frac{\partial h_x}{\partial z} + h_y\frac{\partial h_y}{\partial z}\right)\right]\right\}$$

$$\frac{\partial \omega}{\partial v_x} = \frac{-1}{\sqrt{1-\left(\frac{h_x e_y - h_y e_x}{e\sqrt{h_x^2+h_y^2}}\right)^2}}\left\{\frac{1}{e\sqrt{h_x^2+h_y^2}}\left(e_y\frac{\partial h_x}{\partial v_x} + h_x\frac{\partial e_y}{\partial v_x} - e_x\frac{\partial h_y}{\partial v_x}\right.\right.$$

$$\left. - h_y\frac{\partial e_x}{\partial v_x}\right) - \left(h_x e_y - h_y e_x\right)\left[\frac{e^{-3}}{\sqrt{h_x^2+h_y^2}}\left(e_x\frac{\partial e_x}{\partial v_x} + e_y\frac{\partial e_y}{\partial v_x} + e_z\frac{\partial e_z}{\partial v_x}\right)\right. \quad (246)$$

$$\left.\left. + \frac{1}{e\left(h_x^2+h_y^2\right)^{3/2}}\left(h_x\frac{\partial h_x}{\partial v_x} + h_y\frac{\partial h_y}{\partial v_x}\right)\right]\right\}$$

$$\frac{\partial \omega}{\partial v_y} = \frac{-1}{\sqrt{1-\left(\frac{h_x e_y - h_y e_x}{e\sqrt{h_x^2+h_y^2}}\right)^2}}\left\{\frac{1}{e\sqrt{h_x^2+h_y^2}}\left(e_y\frac{\partial h_x}{\partial v_y} + h_x\frac{\partial e_y}{\partial v_y} - e_x\frac{\partial h_y}{\partial v_y}\right.\right.$$

$$\left. - h_y\frac{\partial e_x}{\partial v_y}\right) - \left(h_x e_y - h_y e_x\right)\left[\frac{e^{-3}}{\sqrt{h_x^2+h_y^2}}\left(e_x\frac{\partial e_x}{\partial v_y} + e_y\frac{\partial e_y}{\partial v_y} + e_z\frac{\partial e_z}{\partial v_y}\right)\right. \quad (247)$$

$$\left.\left. + \frac{1}{e\left(h_x^2+h_y^2\right)^{3/2}}\left(h_x\frac{\partial h_x}{\partial v_y} + h_y\frac{\partial h_y}{\partial v_y}\right)\right]\right\}$$

$$\frac{\partial \omega}{\partial v_z} = \frac{-1}{\sqrt{1-\left(\frac{h_x e_y - h_y e_x}{e\sqrt{h_x^2+h_y^2}}\right)^2}}\left\{\frac{1}{e\sqrt{h_x^2+h_y^2}}\left(e_y\frac{\partial h_x}{\partial v_z} + h_x\frac{\partial e_y}{\partial v_z} - e_x\frac{\partial h_y}{\partial v_z}\right.\right.$$

$$\left. - h_y\frac{\partial e_x}{\partial v_z}\right) - \left(h_x e_y - h_y e_x\right)\left[\frac{e^{-3}}{\sqrt{h_x^2+h_y^2}}\left(e_x\frac{\partial e_x}{\partial v_z} + e_y\frac{\partial e_y}{\partial v_z} + e_z\frac{\partial e_z}{\partial v_z}\right)\right. \quad (248)$$

$$\left.\left. + \frac{1}{e\left(h_x^2+h_y^2\right)^{3/2}}\left(h_x\frac{\partial h_x}{\partial v_z} + h_y\frac{\partial h_y}{\partial v_z}\right)\right]\right\}$$

where the components of the angular momentum vector, eccentricity vector, and their partials are as before. Since the argument of perigee requires a quadrant check, the partials must be multiplied by -1 if the "z" component of the eccentricity vector is less than zero, $e_z < 0$.

The final set of partial derivatives in the first row of (202) is the most complicated. Starting with the definition of the mean anomaly at epoch (53) [48:6],

$$\frac{\partial \mathrm{M}}{\partial x} = (1 - e\cos E)\frac{\partial E}{\partial x} - \frac{\partial e}{\partial x}\sin E \quad (249)$$

$$\frac{\partial \mathrm{M}}{\partial y} = (1 - e\cos E)\frac{\partial E}{\partial y} - \frac{\partial e}{\partial y}\sin E \quad (250)$$

$$\frac{\partial \mathrm{M}}{\partial z} = (1 - e\cos E)\frac{\partial E}{\partial z} - \frac{\partial e}{\partial z}\sin E \tag{251}$$

$$\frac{\partial \mathrm{M}}{\partial v_x} = (1 - e\cos E)\frac{\partial E}{\partial v_x} - \frac{\partial e}{\partial v_x}\sin E \tag{252}$$

$$\frac{\partial \mathrm{M}}{\partial v_y} = (1 - e\cos E)\frac{\partial E}{\partial v_y} - \frac{\partial e}{\partial v_y}\sin E \tag{253}$$

$$\frac{\partial \mathrm{M}}{\partial v_z} = (1 - e\cos E)\frac{\partial E}{\partial v_z} - \frac{\partial e}{\partial v_z}\sin E \tag{254}$$

Recall that the partial derivatives of the eccentricity are given by (209) - (214); however, the partial derivatives of the eccentric anomaly come from (66) such that [48:5]:

$$\frac{\partial \mathrm{E}}{\partial x} = \frac{2}{1 + \frac{1-e}{1+e}\tan^2\left(\frac{v}{2}\right)}\left[\frac{1}{2}\sqrt{\frac{1-e}{1+e}}\sec^2\left(\frac{v}{2}\right)\frac{\partial v}{\partial x} - \frac{1}{2}\tan\left(\frac{v}{2}\right)\sqrt{\frac{1+e}{1-e}}\left(\frac{1}{1+e} + \frac{1-e}{(1+e)^2}\right)\frac{\partial e}{\partial x}\right] \tag{255}$$

$$\frac{\partial \mathrm{E}}{\partial y} = \frac{2}{1 + \frac{1-e}{1+e}\tan^2\left(\frac{v}{2}\right)}\left[\frac{1}{2}\sqrt{\frac{1-e}{1+e}}\sec^2\left(\frac{v}{2}\right)\frac{\partial v}{\partial y} - \frac{1}{2}\tan\left(\frac{v}{2}\right)\sqrt{\frac{1+e}{1-e}}\left(\frac{1}{1+e} + \frac{1-e}{(1+e)^2}\right)\frac{\partial e}{\partial y}\right] \tag{256}$$

$$\frac{\partial \mathrm{E}}{\partial z} = \frac{2}{1 + \frac{1-e}{1+e}\tan^2\left(\frac{v}{2}\right)}\left[\frac{1}{2}\sqrt{\frac{1-e}{1+e}}\sec^2\left(\frac{v}{2}\right)\frac{\partial v}{\partial z} - \frac{1}{2}\tan\left(\frac{v}{2}\right)\sqrt{\frac{1+e}{1-e}}\left(\frac{1}{1+e} + \frac{1-e}{(1+e)^2}\right)\frac{\partial e}{\partial z}\right] \tag{257}$$

$$\frac{\partial \mathrm{E}}{\partial v_x} = \frac{2}{1+\frac{1-e}{1+e}\tan^2\left(\frac{v}{2}\right)}\left[\frac{1}{2}\sqrt{\frac{1-e}{1+e}}\sec^2\left(\frac{v}{2}\right)\frac{\partial v}{\partial v_x} - \frac{1}{2}\tan\left(\frac{v}{2}\right)\sqrt{\frac{1+e}{1-e}}\left(\frac{1}{1+e}+\frac{1-e}{(1+e)^2}\right)\frac{\partial e}{\partial v_x}\right] \tag{258}$$

$$\frac{\partial \mathrm{E}}{\partial v_y} = \frac{2}{1+\frac{1-e}{1+e}\tan^2\left(\frac{v}{2}\right)}\left[\frac{1}{2}\sqrt{\frac{1-e}{1+e}}\sec^2\left(\frac{v}{2}\right)\frac{\partial v}{\partial v_y} - \frac{1}{2}\tan\left(\frac{v}{2}\right)\sqrt{\frac{1+e}{1-e}}\left(\frac{1}{1+e}+\frac{1-e}{(1+e)^2}\right)\frac{\partial e}{\partial v_y}\right] \tag{259}$$

$$\frac{\partial \mathrm{E}}{\partial v_z} = \frac{2}{1+\frac{1-e}{1+e}\tan^2\left(\frac{v}{2}\right)}\left[\frac{1}{2}\sqrt{\frac{1-e}{1+e}}\sec^2\left(\frac{v}{2}\right)\frac{\partial v}{\partial v_z} - \frac{1}{2}\tan\left(\frac{v}{2}\right)\sqrt{\frac{1+e}{1-e}}\left(\frac{1}{1+e}+\frac{1-e}{(1+e)^2}\right)\frac{\partial e}{\partial v_z}\right] \tag{260}$$

The partial derivatives of the eccentric anomaly introduce the need for the partial derivatives of the true anomaly, v. From (81) we know that for the non-degenerate case,

$$v = \omega - u \tag{261}$$

$$\frac{\partial v}{\partial \vec{\mathbf{X}}} = \frac{\partial \omega}{\partial \vec{\mathbf{X}}} - \frac{\partial u}{\partial \vec{\mathbf{X}}} \tag{262}$$

Since the partial derivatives of argument of perigee have already been determined, all that is required are the partial derivatives of the argument of latitude, u, given by (80) [48:5]:

$$\frac{\partial u}{\partial x}=\frac{-1}{\sqrt{1-\left(\frac{h_x y-h_y x}{r\sqrt{h_x^2+h_y^2}}\right)^2}}\left\{\frac{1}{r\sqrt{h_x^2+h_y^2}}\left(y\frac{\partial h_x}{\partial x}-x\frac{\partial h_y}{\partial x}-h_y\right)\right.$$
$$\left.-\left(h_x y-h_y x\right)\left[\frac{x}{r^3\sqrt{h_x^2+h_y^2}}+\frac{1}{r\left(h_x^2+h_y^2\right)^{3/2}}\left(h_x\frac{\partial h_x}{\partial x}+h_y\frac{\partial h_y}{\partial x}\right)\right]\right\} \quad (263)$$

$$\frac{\partial u}{\partial y}=\frac{-1}{\sqrt{1-\left(\frac{h_x y-h_y x}{r\sqrt{h_x^2+h_y^2}}\right)^2}}\left\{\frac{1}{r\sqrt{h_x^2+h_y^2}}\left(y\frac{\partial h_x}{\partial y}-x\frac{\partial h_y}{\partial y}+h_x\right)\right.$$
$$\left.-\left(h_x y-h_y x\right)\left[\frac{y}{r^3\sqrt{h_x^2+h_y^2}}+\frac{1}{r\left(h_x^2+h_y^2\right)^{3/2}}\left(h_x\frac{\partial h_x}{\partial y}+h_y\frac{\partial h_y}{\partial y}\right)\right]\right\} \quad (264)$$

$$\frac{\partial u}{\partial z}=\frac{-1}{\sqrt{1-\left(\frac{h_x y-h_y x}{r\sqrt{h_x^2+h_y^2}}\right)^2}}\left\{\frac{1}{r\sqrt{h_x^2+h_y^2}}\left(y\frac{\partial h_x}{\partial z}-x\frac{\partial h_y}{\partial z}\right)\right.$$
$$\left.-\left(h_x y-h_y x\right)\left[\frac{z}{r^3\sqrt{h_x^2+h_y^2}}+\frac{1}{r\left(h_x^2+h_y^2\right)^{3/2}}\left(h_x\frac{\partial h_x}{\partial z}+h_y\frac{\partial h_y}{\partial z}\right)\right]\right\} \quad (265)$$

$$\frac{\partial u}{\partial v_x}=\frac{-1}{\sqrt{1-\left(\frac{h_x y-h_y x}{r\sqrt{h_x^2+h_y^2}}\right)^2}}\left\{\frac{1}{r\sqrt{h_x^2+h_y^2}}\left(y\frac{\partial h_x}{\partial v_x}-x\frac{\partial h_y}{\partial v_x}\right)\right.$$
$$\left.-\left(h_x y-h_y x\right)\left[\frac{1}{r\left(h_x^2+h_y^2\right)^{3/2}}\left(h_x\frac{\partial h_x}{\partial v_x}+h_y\frac{\partial h_y}{\partial v_x}\right)\right]\right\} \quad (266)$$

$$\frac{\partial u}{\partial v_y} = \frac{-1}{\sqrt{1-\left(\frac{h_x y - h_y x}{r\sqrt{h_x^2+h_y^2}}\right)^2}}\left\{\frac{1}{r\sqrt{h_x^2+h_y^2}}\left(y\frac{\partial h_x}{\partial v_y} - x\frac{\partial h_y}{\partial v_y}\right)\right.$$
$$\left. - \left(h_x y - h_y x\right)\left[\frac{1}{r\left(h_x^2+h_y^2\right)^{3/2}}\left(h_x\frac{\partial h_x}{\partial v_y} + h_y\frac{\partial h_y}{\partial v_y}\right)\right]\right\} \tag{267}$$

$$\frac{\partial u}{\partial v_z} = \frac{-1}{\sqrt{1-\left(\frac{h_x y - h_y x}{r\sqrt{h_x^2+h_y^2}}\right)^2}}\left\{\frac{1}{r\sqrt{h_x^2+h_y^2}}\left(y\frac{\partial h_x}{\partial v_z} - x\frac{\partial h_y}{\partial v_z}\right)\right.$$
$$\left. - \left(h_x y - h_y x\right)\left[\frac{1}{r\left(h_x^2+h_y^2\right)^{3/2}}\left(h_x\frac{\partial h_x}{\partial v_z} + h_y\frac{\partial h_y}{\partial v_z}\right)\right]\right\} \tag{268}$$

Since the argument of latitude requires a quadrant check, the partials must be multiplied by -1 if z < 0.

With the completion of (202), the observation partial derivative matrix, $\partial\vec{\mathbf{X}}/\partial\vec{\mathbf{Y}}$, can be formed by inverting the product of the Delaunay elements Jacobian and the two-body elements Jacobian [48:6]:

$$\frac{\partial\vec{\mathbf{X}}}{\partial\vec{\mathbf{Y}}} = \left(\frac{\partial\vec{\mathbf{Y}}}{\partial\vec{\mathbf{Z}}}\frac{\partial\vec{\mathbf{Z}}}{\partial\vec{\mathbf{X}}}\right)^{-1} \tag{269}$$

One method to verify the two-body analytical formation of $\partial\vec{\mathbf{X}}/\partial\vec{\mathbf{Y}}$ is to numerically differentiate a collocation formula. Here I've chosen Stirling's formula to get [50:112],

$$\frac{\partial X_m}{\partial Y_n}\left(\delta Y_{n_0}\right) = \frac{1}{12h}\left(x_{m_{-2}} - 8x_{m_{-1}} + 8x_{m_1} - x_{m_2}\right) \tag{270}$$

where x_m are native coordinates and momenta determined from the torus Fourier series at one observation time. For each observation, (270) must be evaluated with five data

points, $\left(x_{m_{-2}}, x_{m_{-1}}, x_{m_0}, x_{m_1}, x_{m_2}\right)_{m=1\ldots6}$. Each is formed from a slight variation to the core δY_{n_0} such that $\left(\delta Y_{n_{-2}}, \delta Y_{n_{-1}}, \delta Y_{n_0}, \delta Y_{n_1}, \delta Y_{n_2}\right)_{n=1\ldots6}$ are all separated by a small step size, h. In other words, $\left(\delta Y_{n_0} - 2h, \delta Y_{n_0} - h, \delta Y_{n_0}, \delta Y_{n_0} + h, \delta Y_{n_0} + 2h\right)_{n=1\ldots6}$. During the least squares fitting process, which will be discussed in the next section, h can be set to any small step size on the first iteration since $\delta Y_{n_0} = 0$. On subsequent iterations and for Bayesian filtration, it is preferred that the step size be scaled relative to the magnitude of δY_{n_0}. The overall 6x6 partial derivative matrix is then formed according to the typical Jacobian,

$$\partial\vec{\mathbf{X}}/\partial\vec{\mathbf{Y}}_i = \begin{bmatrix} \frac{\partial x}{\partial Q_1} & \frac{\partial x}{\partial Q_2} & \frac{\partial x}{\partial Q_3} & \frac{\partial x}{\partial P_1} & \frac{\partial x}{\partial P_2} & \frac{\partial x}{\partial P_3} \\ \frac{\partial \mathrm{y}}{\partial Q_1} & \frac{\partial \mathrm{y}}{\partial Q_2} & \frac{\partial \mathrm{y}}{\partial Q_3} & \frac{\partial \mathrm{y}}{\partial P_1} & \frac{\partial \mathrm{y}}{\partial P_2} & \frac{\partial \mathrm{y}}{\partial P_3} \\ \frac{\partial z}{\partial Q_1} & \frac{\partial z}{\partial Q_2} & \frac{\partial z}{\partial Q_3} & \frac{\partial z}{\partial P_1} & \frac{\partial z}{\partial P_2} & \frac{\partial z}{\partial P_3} \\ \frac{\partial v_x}{\partial Q_1} & \frac{\partial v_x}{\partial Q_2} & \frac{\partial v_x}{\partial Q_3} & \frac{\partial v_x}{\partial P_1} & \frac{\partial v_x}{\partial P_2} & \frac{\partial v_x}{\partial P_3} \\ \frac{\partial v_y}{\partial Q_1} & \frac{\partial v_y}{\partial Q_2} & \frac{\partial v_y}{\partial Q_3} & \frac{\partial v_y}{\partial P_1} & \frac{\partial v_y}{\partial P_2} & \frac{\partial v_y}{\partial P_3} \\ \frac{\partial v_z}{\partial Q_1} & \frac{\partial v_z}{\partial Q_2} & \frac{\partial v_z}{\partial Q_3} & \frac{\partial v_z}{\partial P_1} & \frac{\partial v_z}{\partial P_2} & \frac{\partial v_z}{\partial P_3} \end{bmatrix} \tag{271}$$

3.3 Toroidal Sequential-Batch Estimation

The process of estimating an actual orbit with a reference torus is a new one. With both slow and fast variational forces acting on a satellite, uncertainties in the dynamics, and errors in observational data, a stochastic approach must be applied to determine a best estimate of the state. The primary question arising from this concerns when and how state updates, $\delta\vec{\mathbf{Y}}_{\mathbf{0}}$, should be incorporated into the reference torus. Should it be done at

each successive observation time (as done with Kalman filters) or should it be done at the beginning of a batch of observations over an extended period of time (as done with nonlinear least squares)? If the answer is the latter, how should the state and covariance be brought forward in time for every new batch of data? Without a previously published or accepted technique for filtering the data and estimating the orbit with a KAM torus, this author considered all possibilities from the traditional carte du jour for nonlinear systems.

In the Kalman filter class of differential correction techniques, two were considered: linearized and extended Kalman filters. Given the complexities of generating a reference torus at this time, the so-called *extended Kalman filter* was immediately discounted since it requires re-integrating the orbit (thus generating a new torus) at each observation time [24:736]. The *linearized Kalman filter* which avoids having to re-integrate the reference trajectory also will not work since it does not utilize state updates in subsequent predictions [24:735]. It is crucially important that routine updates be provided to the reference torus to prevent the actual orbit from drifting beyond a region correctable by linearized models. The usual sequential-batch least squares method, sometimes called a Bayes Filter, was also dismissed for its inability to propagate the state and covariance through time [24:716]. Nevertheless, a *variation* of the Bayes filter that *does* provide updates to the reference torus was deemed appropriate.

Our version of the Bayes filter produces an update to the initial phase angles, $\vec{\boldsymbol{Q}}_0$, of the torus after every batch of observational data is processed. Subsequent torus predictions are produced from the updated epoch coordinates. In addition to phase angle

updates, Bayesian estimation demands a priori data passed from batch to batch. On the first batch, the nonlinear least squares algorithm is used to generate the first phase angle update and covariance matrix. But before either the nonlinear least squares algorithm or the Bayes filter, the data must be "pre-filtered" to eliminate rogue data. Thus we begin with the development of the so-called pre-filter.

3.3.1 Pre-filtration

A pre-filtration routine was developed by this author to eliminate fallacious observational data, $\vec{\boldsymbol{Z}}$, that appears as improbable spikes in the residual vector given by:

$$\vec{\boldsymbol{r}}_i = \begin{bmatrix} x_i - \hat{x}_i \\ y_i - \hat{y}_i \\ z_i - \hat{z}_i \end{bmatrix} \tag{272}$$

where the predicted coordinates from the state vector, $\vec{\boldsymbol{X}}$, are notated by the "hat." The residual from GPS data is generally smooth except in the case of a maneuver, but even post-maneuver the residual is still quite smooth, just with a different magnitude. As such, outlier data is easy to identify. The entirety of the data is not pre-filtered all at once; rather, it is pre-filtered in batches in sequence with the nonlinear least squares and bayes filter. This ensures the residuals between the observation data and the reference torus remain small compared to outlier data.

The pre-filter evaluates the data on three passes using three different techniques to identify rogue data. The first pass merely eliminates data outside of four standard deviations. The second pass generates a moving average and moving standard deviation from eleven data points – five before and five after the current observation, except at the beginning and end of the data file which uses the first and last eleven data points,

respectively. Data outside of 3 moving standard deviations from the moving average are eliminated. The third pass evaluates the absolute value of the slope between the current and previous data point and if the slope exceeds 10 km/TU, the current data is rejected. The first data point must be good for the third pass to work. The author monitored which data were rejected and the total effect of the three passes was flawless for an entire week of ISS data sampled at one minute intervals.

3.3.2 Nonlinear Least Squares (NLS)

Once the data is pre-filtered, the iterative non-linear least squares algorithm is initiated. At zero epoch, the residual between the observation data and the reference torus should be small. If it is not, the reference torus is probably not sufficient for an accurate estimate and must be refined. When the residual is small enough (less than 1 m is ideal), the state vector can be predicted at each observation time using a null displacement on the first iteration:

$$\overrightarrow{\boldsymbol{\delta Y}}_0 = [0 \quad 0 \quad 0 \quad 0 \quad 0 \quad 0]^T \tag{273}$$

Next, determine the residuals from observation data, $\vec{\boldsymbol{Z}}$, and estimated data, $\vec{\boldsymbol{X}}$, using (272). The observation data of the ISS is from the Global Positioning System (GPS) which shows very little noise. We approximate the total instrumental covariance matrix:

$$\boldsymbol{Q} = \begin{bmatrix} 10^2 & 0 & 0 \\ 0 & 10^2 & 0 \\ 0 & 0 & 10^2 \end{bmatrix} m^2 = \left(\frac{10}{1000(6378.135)}\right)^2 \begin{bmatrix} 1 & 0 & 0 \\ 0 & 1 & 0 \\ 0 & 0 & 1 \end{bmatrix} DU^2 \tag{274}$$

If both position and velocity were of interest to this study, the observer would be defined as a 6x6 identity matrix; however, since only the native position coordinates are of interest, define the observer as:

$$\boldsymbol{H} = \begin{bmatrix} 1 & 0 & 0 & 0 & 0 & 0 \\ 0 & 1 & 0 & 0 & 0 & 0 \\ 0 & 0 & 1 & 0 & 0 & 0 \end{bmatrix} \tag{275}$$

From the local dynamics given in (168), form the 6x6 state transition matrix as:

$$\begin{aligned} \boldsymbol{\Phi}(t_i, t_0) &= \frac{\partial \vec{\mathbf{X}}(t)}{\partial \vec{\mathbf{Y}}(t)} \frac{\partial \vec{\mathbf{Y}}(t)}{\partial \vec{\mathbf{Y}}(t_0)} \\ &= \frac{\partial \vec{\mathbf{X}}(t)}{\partial \vec{\mathbf{Q}}(t)} \frac{\partial \vec{\mathbf{Q}}(t)}{\partial \vec{\mathbf{Y}}(t_0)} + \frac{\partial \vec{\mathbf{X}}(t)}{\partial \vec{\mathbf{P}}(t)} \frac{\partial \vec{\mathbf{P}}(t)}{\partial \vec{\mathbf{Y}}(t_0)} \end{aligned} \tag{276}$$

where the partial derivatives are the same as those developed previously. For each observation, form the 3x6 version of the observation partial derivatives matrix according to:

$$\boldsymbol{T}_i = \boldsymbol{H}\,[\boldsymbol{\Phi}(t_i, t_0)] \tag{277}$$

Since the observational data is pre-filtered to eliminate fallacious points, rejection processing during the nonlinear least squares algorithm is turned off; nevertheless, if the reference torus predictions are accurate enough, each observation can be processed to reject data in which the residual is beyond 3 standard deviations of the instrumental noise:

$$\left|r_{x,y,z}\right| > 3\sqrt{Q_{x,y,z}} \implies rejected \tag{278}$$

If the data is not rejected, add to the running sums of the inverted covariance matrix, $\boldsymbol{P}^{-1}$, and the vector, $\vec{\boldsymbol{\rho}}$:

$$\boldsymbol{P}^{-1} = \sum_i \boldsymbol{T}_i^T\, \boldsymbol{Q}_i^{-1} \boldsymbol{T}_i \tag{279}$$

$$\vec{\boldsymbol{\rho}} = \sum_i \boldsymbol{T}_i^T\, \boldsymbol{Q}_i^{-1} \vec{\boldsymbol{r}}_i \tag{280}$$

For each position coordinate, add the square of the residual to a running sum. Once all observations have been processed, calculate the RMS of residuals according to:

$$RMS_{x,y,z} = \sqrt{\frac{\sum_i r_{x,y,z}^2}{N}} \tag{281}$$

Check for convergence. If the RMS of residuals for each coordinate is less than the standard deviation of the instrument noise, the solution is at hand.

$$RMS_{x,y,z} < \sqrt{Q_{x,y,z}} \implies converged \tag{282}$$

If the solution has not converged, improve the estimate of $\overrightarrow{\boldsymbol{\delta Y}}_0$ at epoch by adding the product of the covariance matrix and the vector, $\vec{\boldsymbol{\rho}}$:

$$\overrightarrow{\boldsymbol{\delta Y}}_0(+) = \overrightarrow{\boldsymbol{\delta Y}}_0(-) + \boldsymbol{P}\vec{\boldsymbol{\rho}} \tag{283}$$

Then repeat the process from the beginning using the new estimate of $\overrightarrow{\boldsymbol{\delta Y}}_0$. Note that we are not calculating $\overrightarrow{\boldsymbol{\delta Y}}_0$ at every observation; we are doing so for the whole batch of data. Also, this update will be discarded if the convergence criteria are met in the current iteration.

Once converged or when the maximum number of iterations has been reached, log $\overrightarrow{\boldsymbol{\delta Y}}_0$ and the observation covariance matrix to pass forward to the Bayes filter for the second batch of data.

3.3.3 Bayesian Filtration

Begin by pre-filtering the data as before, but predictions from the reference torus are determined using $\overrightarrow{\boldsymbol{\delta Y}}_0$ from the least squares routine (only if on the second batch) or from the previous Bayes filtration. To avoid confusion with the new displacement that will be

determined, we will call this $\overrightarrow{\boldsymbol{\delta Y}}_{0_{old}}$**.** Next, bring the initial phase angles and covariance matrix forward to the current epoch using $\overrightarrow{\boldsymbol{\delta Y}}_{0_{old}}$. The update to $\vec{\boldsymbol{Q}}_0$ is determined from (172) such that:

$$\vec{\boldsymbol{Q}}_{0_{new}} = \vec{\boldsymbol{Q}}_{0_{old}} + \overrightarrow{\boldsymbol{\delta Q}}\left(t_{0_{new}}, t_{0_{old}}\right) \tag{284}$$

where the value of $\overrightarrow{\boldsymbol{\delta Q}}$ is accumulated from the old epoch to the new epoch**.** The covariance matrix is propagated using the state transition matrix, $\boldsymbol{\Phi}\left(t_{0_{new}}, t_{0_{old}}\right)$, from (276) and using the covariance matrix, $\boldsymbol{P}_{old}$, from the previous epoch:

$$\boldsymbol{P}_{new}(-) = \boldsymbol{\Phi}\boldsymbol{P}_{old}\boldsymbol{\Phi}^{\boldsymbol{T}} \tag{285}$$

With the phase angle update and a priori data now available at the new epoch, begin the first iteration using the previous correction to the torus state vector:

$$\overrightarrow{\boldsymbol{\delta Y}}_{0_{new}}(-) = \overrightarrow{\boldsymbol{\delta Y}}_{0_{old}} \tag{286}$$

As before, calculate the residuals and observation partial derivative matrix (277) for each observation, and accumulate the summation matrices (279) and (280). After all observations have been processed, the inverse covariance matrix is given by:

$$\boldsymbol{P}_{new}^{-1}(+) = \boldsymbol{P}_{new}^{-1}(-) + \sum_i \boldsymbol{T}_i^T\, \boldsymbol{Q}_i^{-1}\boldsymbol{T}_i \tag{287}$$

Next, check for convergence using the RMS for each coordinate as presented previously in (281) and (282). If the solution has not converged, improve the estimate of $\overrightarrow{\boldsymbol{\delta Y}}_{\boldsymbol{0}}$ at epoch according to:

$$\overrightarrow{\boldsymbol{\delta Y}}_{0_{new}}(+) = \boldsymbol{P}_{new}(+)\left(\boldsymbol{P}_{new}^{-1}(-)\left(\vec{\boldsymbol{Y}}_{0_{new}}(-) - \vec{\boldsymbol{Y}}_{0_{new}}\right) + \vec{\boldsymbol{\rho}}\right) \tag{288}$$

Since $\vec{\boldsymbol{\Omega}}$ is constant and $\vec{\mathbf{Q}}_0$ is constant for a single batch, $\delta\vec{\mathbf{Q}}$ and $\delta\vec{\mathbf{P}}$ are all that change, so:

$$\vec{\boldsymbol{Y}}_{0_{new}}(-) - \vec{\boldsymbol{Y}}_{0_{new}} = \overrightarrow{\boldsymbol{\delta Y}}_{0_{new}}(-) - \overrightarrow{\boldsymbol{\delta Y}}_{0_{new}} \tag{289}$$

As with the nonlinear least squares, repeat the process with every new estimate of $\overrightarrow{\boldsymbol{\delta Y}}_0$ until the solution converges or until the maximum number of iterations has been reached. Then log $\overrightarrow{\boldsymbol{\delta Y}}_0$ and the observation covariance matrix to pass forward to the next batch of data.

3.4 Stochastic Orbit Modeling

Modeling stochastic orbits requires discrete knowledge of both gravitational and non-gravitational perturbations. The reference torus allows us to distinguish between them since it already contains the earth's geopotential effects. The added dynamics near the reference torus, as estimated by the least squares fitting process in the previous section, is a result of non-gravitational perturbations and can be parameterized for apparent stochastic behavior. Stochastic, by definition, infers a random nature, but because it is believed motion near the torus exhibits an ostensible orderliness that can be modeled for a period of time under similar environmental conditions, this author shall refer to torus perturbations as pseudo-stochastic.

To produce stochastic predictions via the reference torus, the initial phase angles, $\vec{\boldsymbol{Q}}_0$, must be varied with time (think of this as *parallel motion* on the surface of the torus) as do the momenta offsets, $\overrightarrow{\boldsymbol{\delta P}}$, which allow the satellite to move off the surface of the reference torus (think of this as *perpendicular motion*). The behavior of the initial phase

angles and momenta offsets are first determined through Bayesian estimation which may be sensitive to the number of observations included in each batch. During the estimation process, the torus' initial phase angles are updated after every batch which encapsulates the influence of non-gravitational perturbations and the momenta offsets are stored for later use. Assuming these empirical parameters are well-behaved and can be modeled with a time-varying curve, their propagation can provide autonomous updates to the reference torus for non-gravitational perturbations. For now on this author will refer to these as the pseudo-stochastic parameters. Given a reference torus and the pseudo-stochastic parameters, one should be able to predict the non-chaotic orbit of any satellite.

3.5 Observational Data

The procedures outlined in this chapter may be applied to any satellite in a non-chaotic earth orbit. As such, virtually any satellite could be used to verify and validate the procedures since it is not the practice of the launch community to place satellites in chaotic orbits. The ISS was chosen as the test case in this study for two reasons. First, it is crucial that the observational data be extensive and well documented to eliminate or isolate external variables in the study. Since human spaceflight missions have the highest priority for tracking and predictions, the ISS offers extensive data options as well as highly specialized trajectory personnel that monitor the orbit fulltime. The ISS is also an ideal vessel for studying stochastic predictions since it is the largest manmade object orbiting the earth. In its LEO orbit, air drag imparts a significant perturbing force on the vast surface areas spanning the ISS. The current configuration of the ISS measures 357

feet, end-to-end [51]. Figure 14 shows an excellent juxtaposition of the ISS with the famous Lambeau Field which measures 360 feet including the end zones.

Figure 14. The International Space Station measures 357 ft, end-to-end, whereas an NFL football field measures 360 ft. *Credit: T. Brian Jones*

Observational data was provided by the ISS Trajectory Operations and Planning Branch (DM33), Mission Operations Directorate, Johnson Space Center in Houston, Texas. The data was transmitted from the ISS's primary onboard GPS receiver/processor. The parameters used include:

Table 1. Onboard Primary GPS Parameters.

LADP06MDQ000H	x position, TDR coordinate system (m)
LADP06MDQ001H	y position, TDR coordinate system (m)
LADP06MDQ002H	z position, TDR coordinate system (m)
LADP06MDQ003R	x velocity, TDR coordinate system (m/s)
LADP06MDQ004R	y velocity, TDR coordinate system (m/s)
LADP06MDQ005R	z velocity, TDR coordinate system (m/s)
LADP06MDQ006W	Nav time (milliseconds since the beginning of the week which starts on Sunday at midnight)
LADP06MDQ452W	GPS time (seconds since Jan 6, 1980 at 00:00 UTC)
LADP06MD2946W	State quality (1=good or 0=poor)

The data was sampled at 1-minute intervals from 00:01:00.000 UTC on 25 March 2010 to 12:18:01.000 UTC on 23 April 2010. This corresponds to 42,000 observations. To give a sense of the orbit's coverage, the pre-filtered data appears in Figure 15.

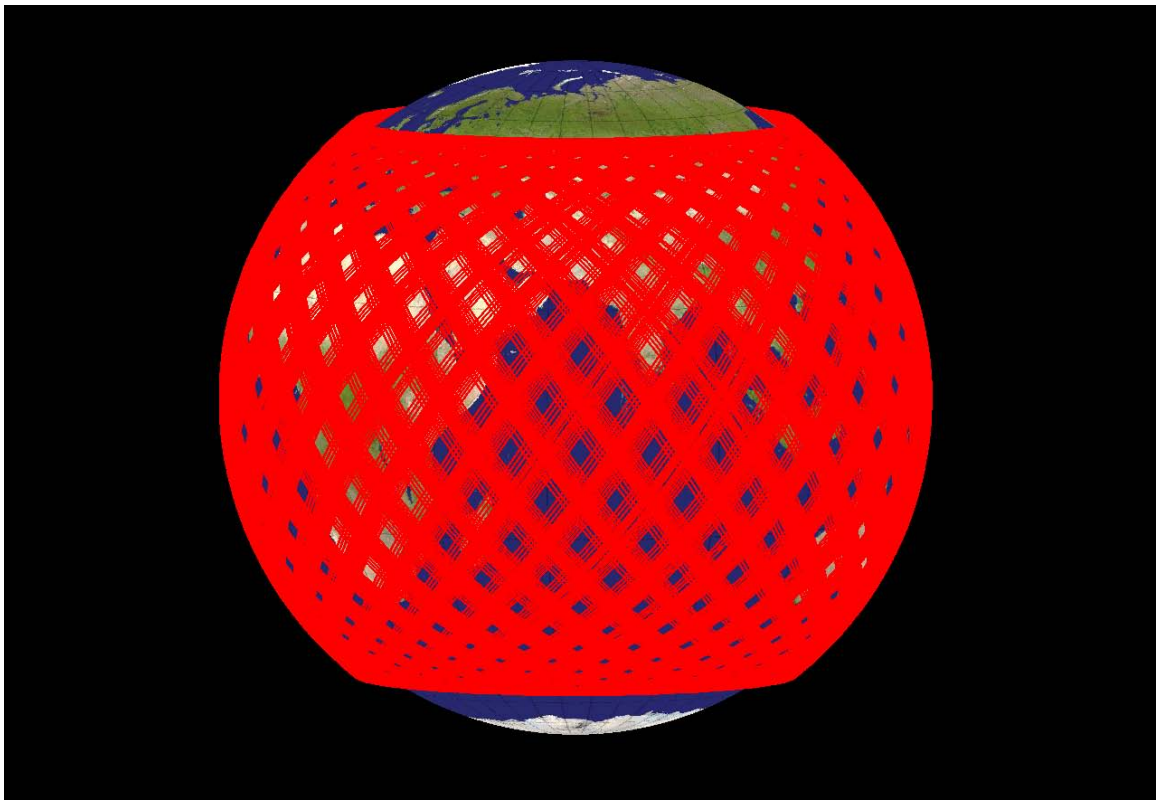

Figure 15. Pre-filtered ISS data from 25 March – 23 April 2010.

IV. Results

Recalling back to §1.6, three primary topics were to be explored by this thesis. The first two were addressed in the previous chapter with a derivation of the linearized equations of motion near tori followed by their application to an estimation routine for fitting observational data to a continuum of tori. This chapter will answer the final and most important question of whether or not stochastic predictions can be generated from a reference torus and, if so, for how long. The chapter begins with results from the reference torus construction machinery followed by a simple verification of the Bayesian filtration algorithms. The chapter concludes with the estimation and prediction results.

4.1 Reference Torus Construction

A relatively good fit was obtained between the reference torus and the integrated orbit, the results of which will be discussed shorty, but first, we begin with the difficulties surrounding its development. The basis frequencies proved to be the biggest challenge. For the ISS, the approximate basis set from Keplarian and perturbation theory, equations (164) - (166), were found to be:

Table 2. J_2 basis frequencies for spectral analysis.

Coordinate	Frequency (rad/TU)
$\boldsymbol{\Omega_1}$	9.24464666422975e-001
$\boldsymbol{\Omega_2}$	-5.96726955036933e-002
$\boldsymbol{\Omega_3}$	6.26401586397507e-004

The Newton-Rhapson algorithm is very sensitive to the precision of the basis frequency frequency approximations since it can easily settle on an adjacent peak. This was the case for the ISS data. The most prominent peaks could not be identified by the J_2 frequencies

alone. The author directly examined the spectral lines to improve the accuracy of the approximate basis set with a manual override. Figure 16 - Figure 18 show segments of the power spectral density plots used to identify the frequencies.

Appendix A contains a full accounting of the power spectral frequency combinations from 0 to 3 rad/TU.

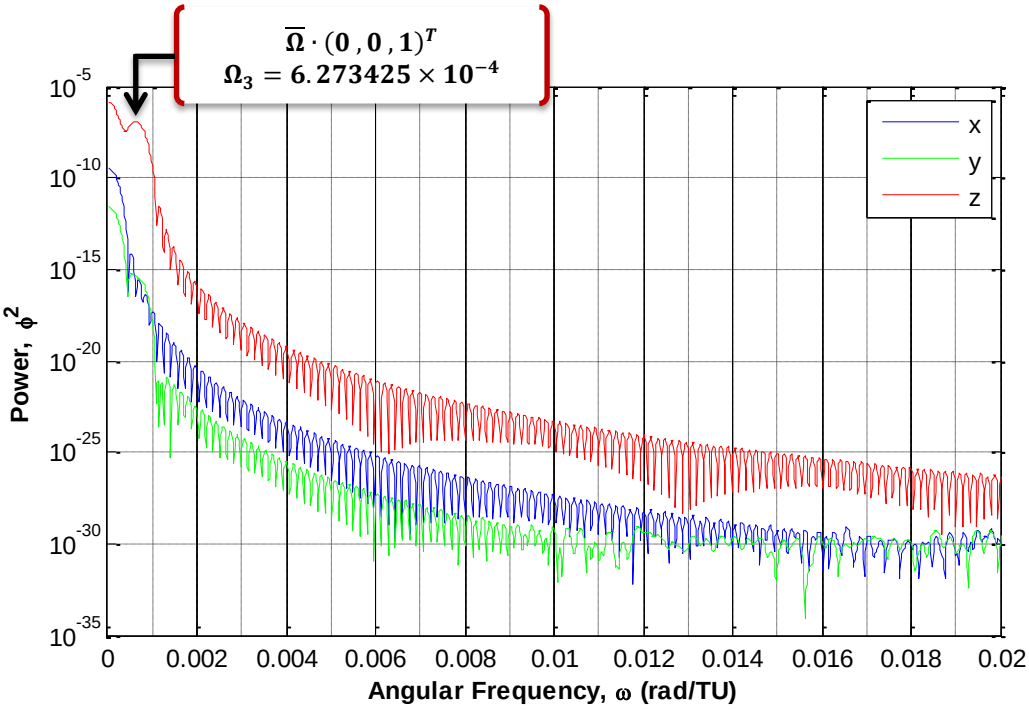

Figure 16. PSD plot identifying the apsidal frequency in the z coordinate.

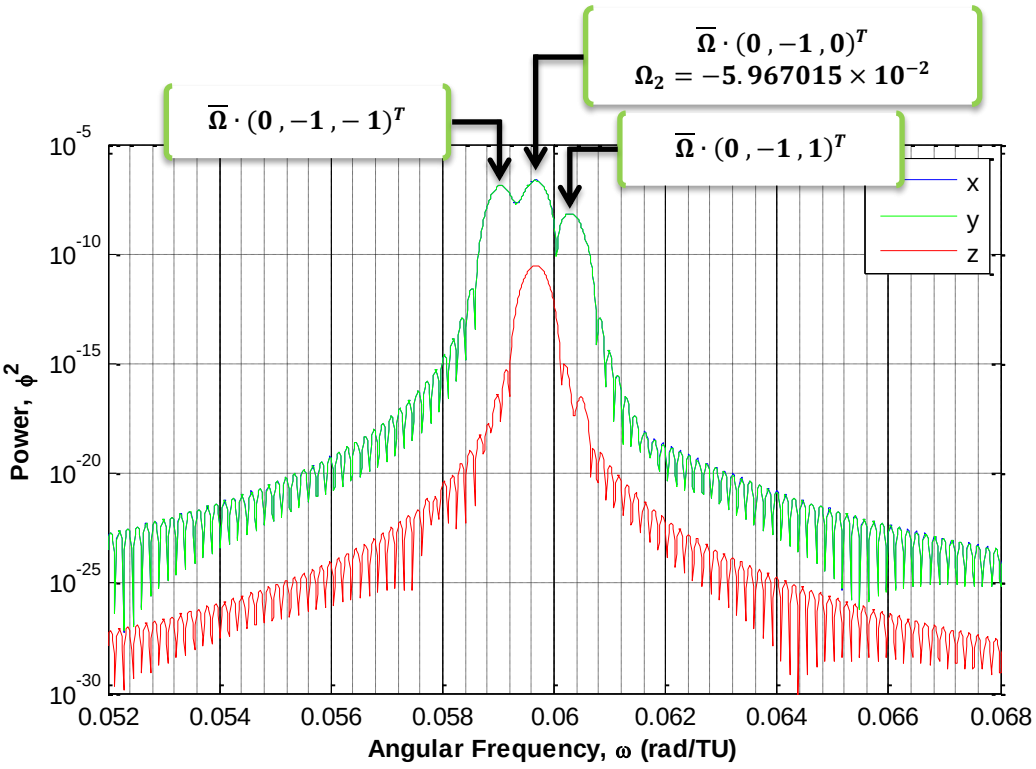

Figure 17. PSD plot identifying the nodal frequency in the x and y coordinates.

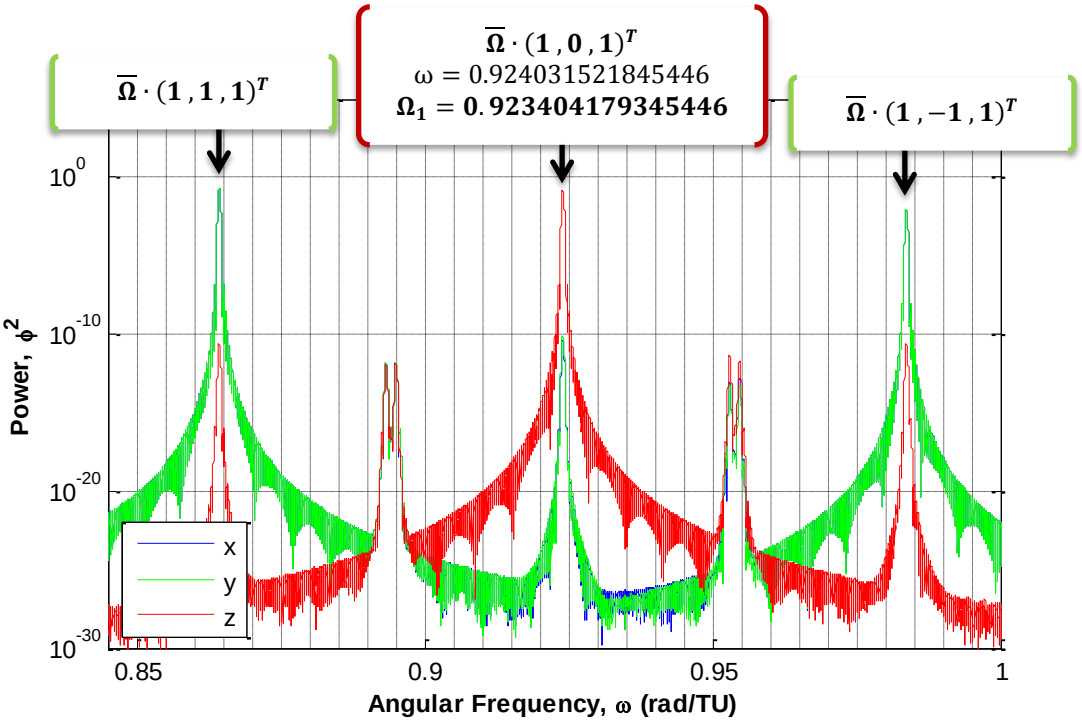

Figure 18. PSD plot identifying the anomalistic frequency in the x, y, and z coordinates.

$\boldsymbol{\Omega_2}$ and $\boldsymbol{\Omega_3}$ were identified by producing PSD plots near the expected peaks with up to seven significant digits. $\boldsymbol{\Omega_1}$ was identified to a higher precision from the Newton-Rhapson algorithm which successfully identified the $\vec{\boldsymbol{j}} = (\mathbf{1}, \mathbf{0}, \mathbf{1})^{\boldsymbol{T}}$ peak in previous software outputs. Deducting $\boldsymbol{\Omega_3}$ from this frequency provided a good approximation of $\boldsymbol{\Omega_1}$. Thus, the basis frequencies that were used to initialize the spectral analysis are given in Table 3.

Table 3. Manual basis frequencies for spectral analysis.

Coordinate	Frequency (rad/TU)
$\boldsymbol{\Omega_1}$	9.23404179345446e-001
$\boldsymbol{\Omega_2}$	-5.967015e-002
$\boldsymbol{\Omega_3}$	6.273425e-004

It is important to note that the manual basis set is not the final solution; it is merely an approximation used to identify prominent spectral lines. The frequencies from those lines are used to generate a least squares estimate of the basis set. A quick review of the spectral lines employed, listed in Table 4, shows that the line peak powers are reasonable and their frequencies are extremely close to the expected frequencies from the manual set. The estimated basis set from the least squares solution is shown in Table 5.

Table 4. Line peak analysis from NAFF and Newton-Rhapson results.

Native Coordinate	Spectral Line ($\vec{j}^T$)	Residual Freq. (rad/TU) Actual - Expected	Power Spectral Density, $\|\boldsymbol{\phi}\|^2$
x	$(1, 1, 1)$	2.04460104402671e-009	1.82588844891577e-001
	$(1, -1, 1)$	-2.04559291727691e-009	9.99713308702777e-003
	$(2, 1, 1)$	1.84465311980908e-006	1.38656419943255e-008
	$(2, -1, 1)$	1.82975753992842e-006	7.67087643648475e-010
y	$(1, 1, 1)$	2.04458305841371e-009	1.82585311258691e-001
	$(1, -1, 1)$	-2.04558192606896e-009	9.99362401708964e-003
	$(2, 1, 1)$	1.84063454988781e-006	1.38656758742673e-008
	$(2, -1, 1)$	1.86371049992751e-006	7.66612586491125e-010
z	$(1, 0, 1)$	0	1.70839929172321e-001
	$(2, 0, 1)$	1.84468687014494e-006	1.30338647593972e-008

Table 5. Estimated basis frequencies.

Coordinate	Frequency (rad/TU)
$\boldsymbol{\Omega_1}$	9.23406024034362e-001
$\boldsymbol{\Omega_2}$	-5.96701449186667e-002
$\boldsymbol{\Omega_3}$	6.25497810686326e-004

As one final check, the estimated basis set was used to generate new expected frequencies for the ten most prominent spectral lines to ensure that the residuals are small after differencing the actual and expected frequencies. Table 6 depicts these values and, again, they are quite convincing.

Table 6. Residuals from actual and estimated basis frequencies.

Native Coordinate	Spectral Line ($\vec{j}^T$)	Residual Freq. (rad/TU) Actual - Expected
x	$(1\,,1\,,1)$	2.0449984e-009
	$(1\,,-1\,,1)$	2.0449805e-009
	$(2\,,1\,,1)$	-2.0451945e-009
	$(2\,,-1\,,1)$	-2.0451836e-009
y	$(1\,,1\,,1)$	3.9779291e-013
	$(1\,,-1\,,1)$	-3.5392383e-011
	$(2\,,1\,,1)$	-4.0539610e-009
	$(2\,,-1\,,1)$	-1.4930977e-008
z	$(1\,,0\,,1)$	1.9021981e-008
	$(2\,,0\,,1)$	-1.6506796e-012

Given a seemingly good fit to the spectral data, the estimated frequencies were used to extract the Fourier coefficients. The resulting Fourier series, truncated to order $M = (6,\ 17,\ 6)$, was used to generate native coordinates to compare to the integrated orbit. The limit on the index summation vector was decided after numerous trials with lower and higher order truncations. The Fourier series from lower order truncations could be generated and evaluated faster, but also introduced greater error. Craft shows the

relationship between improvements in accuracy and increases in the number of terms [52:40]. At a certain point, the improvements become computationally burdensome with little gain in accuracy, if at all. He also showed that lower altitude orbits require more terms to compensate for stronger geopotential perturbations. At an altitude of 320 km (which is close enough to the ISS altitude near 350 km), he suggests that there is little relative accuracy gain after 750 frequency combinations. A truncation of order $M = (6,\ 17,\ 6)$ corresponds to 2,958 frequency combinations, far exceeding his accuracy threshold where errors are sub-meter. Since the time and effort had already been invested in generating this torus of higher order truncation, it made little sense to downgrade to a torus produced with lower order terms. Doing so would have sacrificed higher precision for nearly unnoticeable timing improvements in the MATLAB code that sums the Fourier series.

With the chosen truncation, Figure 19 shows the RMS residuals for coordinates x, y and z are 121.9, 121.7, and 75.7 meters, respectively. Since the truncation is not a significant cause of the error and since a periodic nature appears in the residuals, it must be due to incorrect basis frequencies.

Since the author is confident that the Newton-Rhapson algorithm nailed the peak at $\omega_{1,0,1} = \vec{\boldsymbol{\Omega}} \cdot (\mathbf{1}\ ,\mathbf{0}\ ,\mathbf{1})^{\boldsymbol{T}}$, Ω_2 and Ω_3 are the only frequencies in question since Ω_1 is just a function of Ω_3, specifically $\Omega_1 = \omega_{1,0,1} - \Omega_3$. To improve the frequencies without repeating the spectral analysis, a honing function was written that adjusted the frequencies until the RMS residuals were minimized. This is a two-step process that first tweaks Ω_3 while holding Ω_2 constant and allowing Ω_1 to vary with Ω_3. In the second

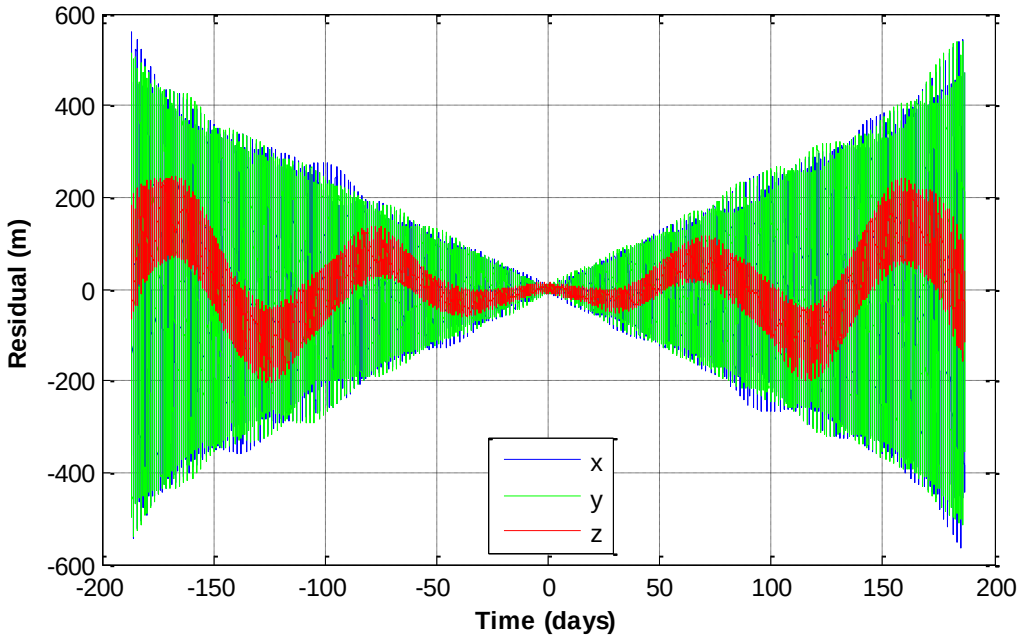

Figure 19. Residuals from differencing the integrated orbit and reference torus native coordinates (uses Fourier series truncation of order $\boldsymbol{M = (6,\ 17,\ 6)}$ and NAFF estimated frequencies).

step, Ω_1 and Ω_3 are held constant while Ω_2 is tweaked. Ω_2 was initialized at the NAFF estimate and Ω_3 was initialized at the value previously determined by detailed PSD plots near the expected peak. It really doesn't matter where they are initialized, but a smart choice does speed up the process. The honed basis set and the residuals from the previous estimates are given in Table 7.

Table 7. Honed basis frequencies and residuals from NAFF estimate.

Coordinate	Honed Basis Set (rad/TU)	Residuals (rad/TU) Honed - Estimated
$\boldsymbol{\Omega_1}$	9.23407979345446 e-001	1.95531108304614e-006
$\boldsymbol{\Omega_2}$	-5.96701428186668 e-002	2.10000019457146e-009
$\boldsymbol{\Omega_3}$	6.235425 e-004	-1.95531068455002e-006

The newly honed basis set was used to test the deterministic torus accuracy again. Figure 20 shows the RMS residuals for coordinates x, y and z are 18.7, 17.6, and 19.8 meters, respectively. Although the result is a significant improvement over the previously estimated frequencies, it must be noted that the coefficients still contain errors from picking off peaks using the NAFF estimated frequencies. A better fit between the torus and the integrated orbit cannot be obtained until the NAFF method is improved to identify a more accurate basis set.

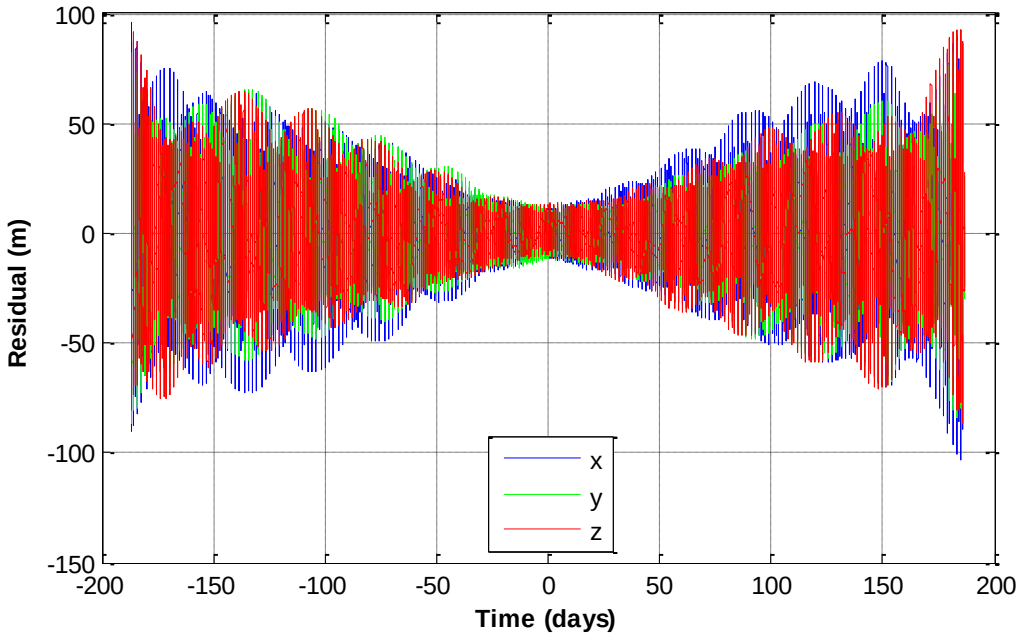

Figure 20. Residuals from differencing the integrated orbit and reference torus native coordinates (uses Fourier series truncation of order $\boldsymbol{M = (6,\ 17,\ 6)}$ and honed frequencies).

As a final comment, one interesting observation from a review of the spectra in the frequency domain (see

Appendix A) is that the peaks used for the least squares solution given in Table 4 are not the most prominent peaks. The most prominent peaks are centered about $\omega_{n,0,n} = \vec{\boldsymbol{\Omega}} \cdot (\boldsymbol{n}, \boldsymbol{0}, \boldsymbol{n})^{\boldsymbol{T}}$ in the z coordinate. For example, the peak thought to be the maximum at $\omega_{2,0,1} = \vec{\boldsymbol{\Omega}} \cdot (\boldsymbol{2}, \boldsymbol{0}, \boldsymbol{1})^{\boldsymbol{T}}$ is actually overshadowed by $\omega_{2,0,2} = \vec{\boldsymbol{\Omega}} \cdot (\boldsymbol{2}, \boldsymbol{0}, \boldsymbol{2})^{\boldsymbol{T}}$. Similarly, the x and y coordinates show the same behavior. The peak thought to be the maximum at $\omega_{2,1,1} = \vec{\boldsymbol{\Omega}} \cdot (\boldsymbol{2}, \boldsymbol{1}, \boldsymbol{1})^{\boldsymbol{T}}$ is actually overshadowed by $\omega_{2,1,2} = \vec{\boldsymbol{\Omega}} \cdot (\boldsymbol{2}, \boldsymbol{1}, \boldsymbol{2})^{\boldsymbol{T}}$. This may be the reason the least squares solution gives the wrong frequencies.

4.2 Filter Verification

A verification of the NLS and Bayes filters was completed using observation data that was manufactured directly from the reference torus using a constant $\overrightarrow{\boldsymbol{\delta Y_0}}$ offset. This was necessary to show that the filters converge on the correct $\overrightarrow{\boldsymbol{\delta Y_0}}$ and can be trusted with real data when $\overrightarrow{\boldsymbol{\delta Y_0}}$ is unknown. The data, shown in Figure 21, was generated from the following offset to the reference torus:

$$\overrightarrow{\boldsymbol{\delta Y}}_0 = \begin{bmatrix} 0.003051846308510 \\ 3.364795882078831 \times 10^{-6} \\ -0.003041378665051 \\ 2.530687412213637 \times 10^{-6} \\ -2.032460083183908 \times 10^{-5} \\ 2.521736621432707 \times 10^{-6} \end{bmatrix} \tag{290}$$

The known offsets were recovered by the filters to within machine double precision. As confirmation that the filter indeed found the correct offsets to the reference torus, Figure 22 shows the native coordinate residuals from the manufactured observation data and the updated reference torus (updated with the discovered $\overrightarrow{\boldsymbol{\delta Y_0}}$).

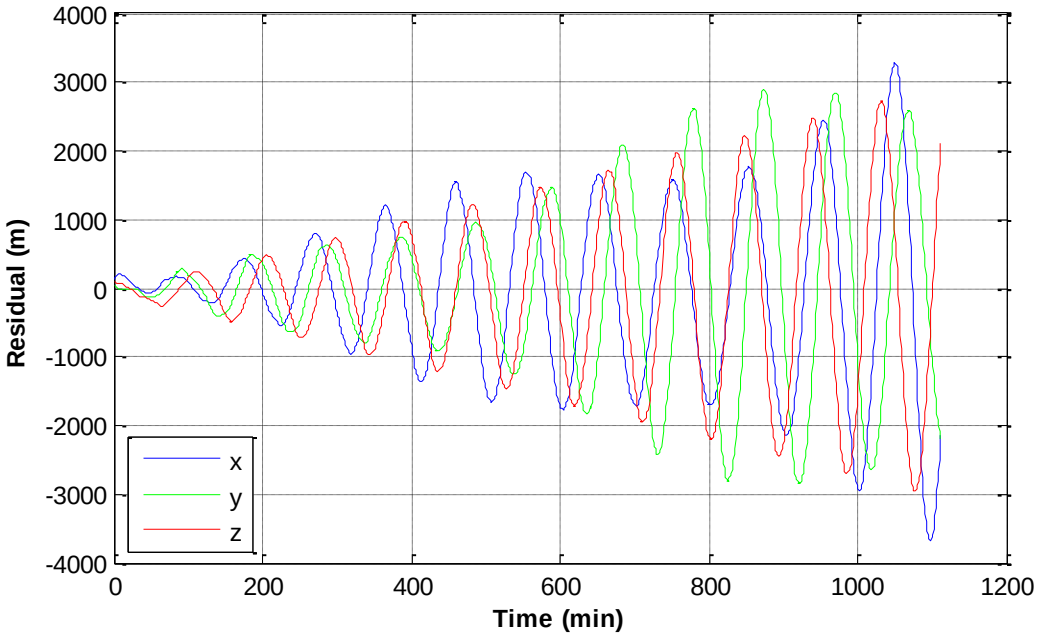

Figure 21. Residuals from manufactured observation data generated by offsets to the reference torus.

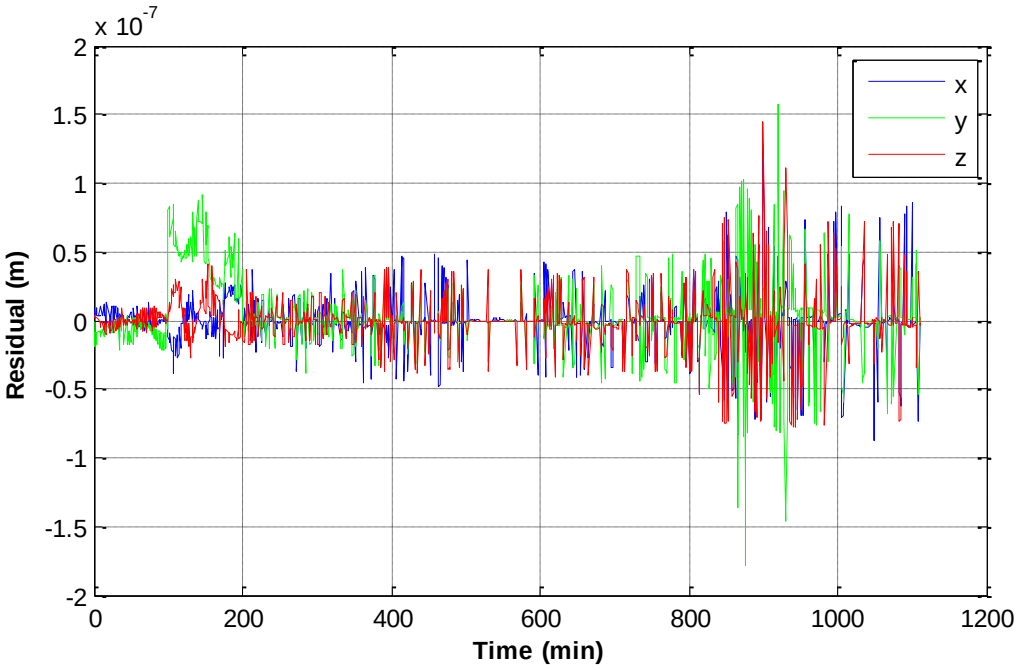

Figure 22. Coordinate residuals show reference torus was corrected to match the manufactured data.

Of further interest is the effect the simulated offsets had on the reference torus. The filter results show a linear drift in the initial phase angles from the $\overrightarrow{\delta Q}$ updates at each new epoch as indicated in Figure 23 - Figure 25. This is expected from (172).

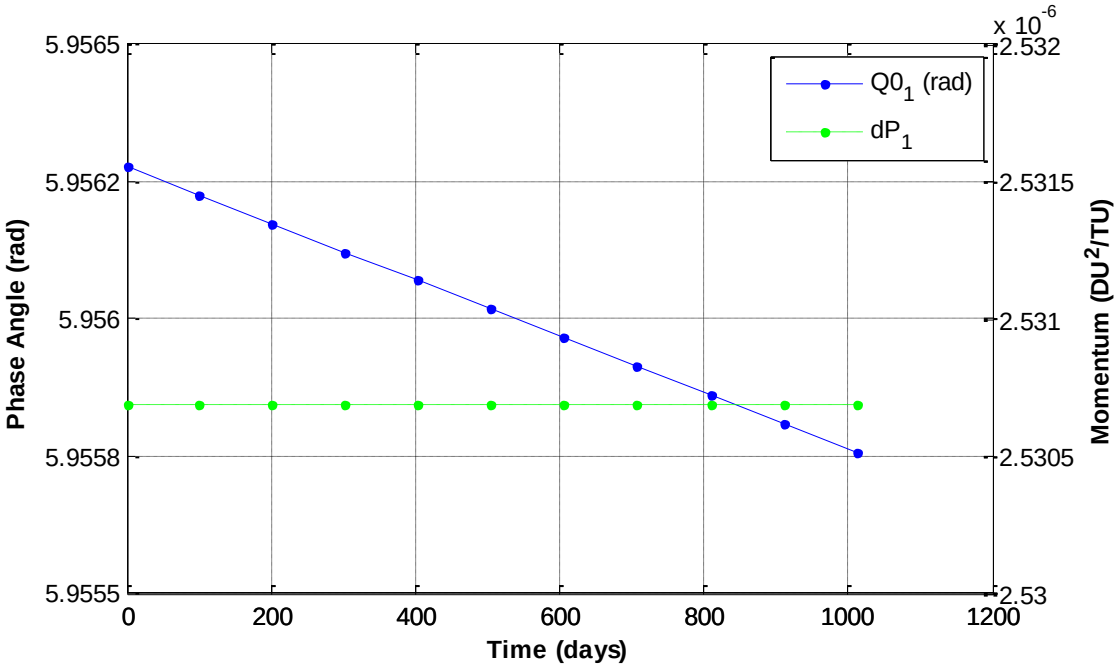

Figure 23. Linear drift in $Q0_1$ due to constant dP_1.

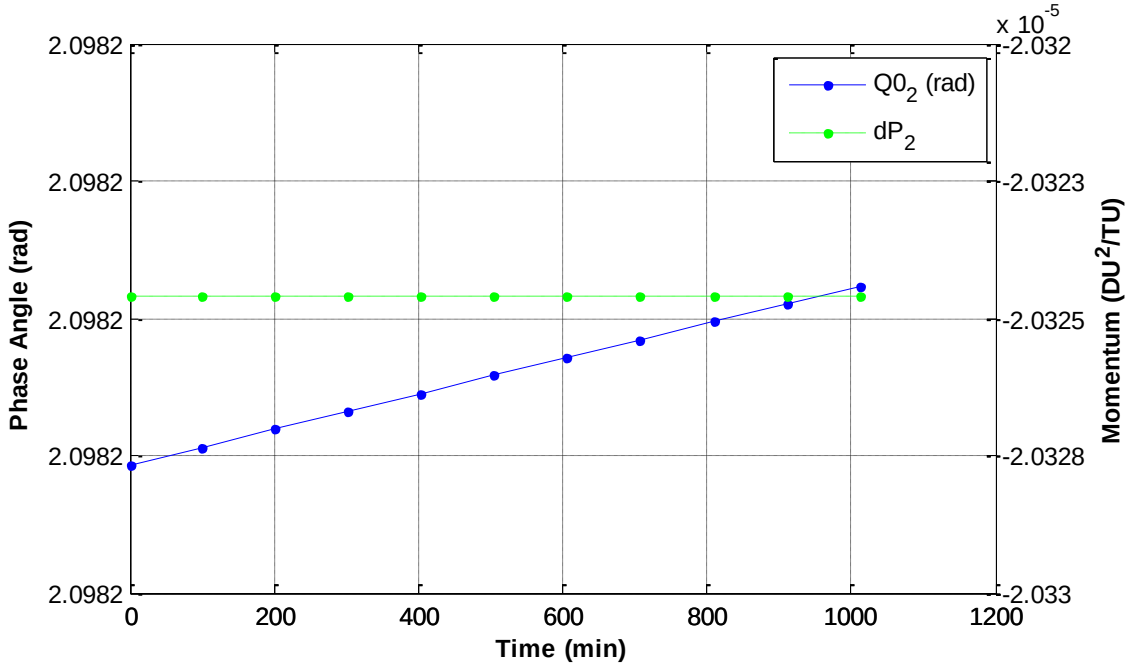

Figure 24. Linear drift in $Q0_2$ due to constant dP_2.

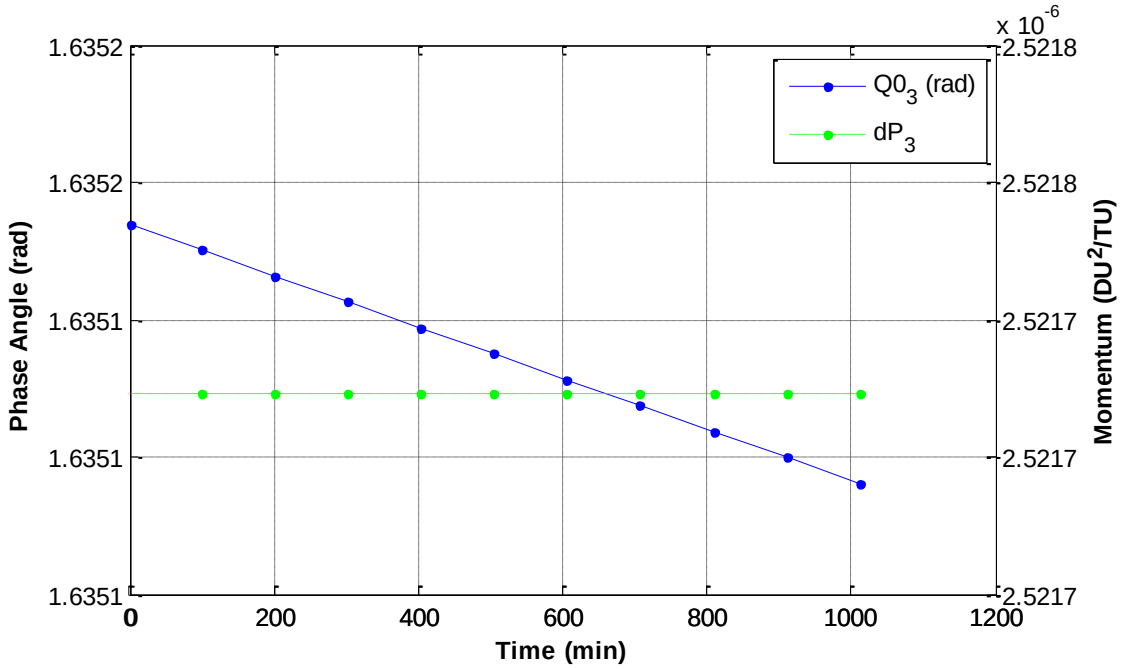

Figure 25. Linear drift in $Q0_3$ due to constant dP_3.

4.3 Orbit Fitting

The KAM torus was used to generate deterministic and stochastic predictions to compare to the ISS data. The predictions from the purely deterministic model gives a real sense of how quickly the ISS navigates off of the reference torus without perturbation updates. The stochastic predictions were formed with updates to the reference torus using a pseudo-stochastic parameterization of the initial phase angles and momenta offsets.

4.3.1 Deterministic Predictions

In its unmodified state at epoch, the reference torus can be used to generate deterministic predictions of the ISS native coordinates when time is the only parameter that is varied. This allows for a direct comparison to the actual ISS data to discern how well the gravitationally perturbed torus represents reality. Doing so reveals a quadratic growth in the residuals exceeding 500 km in just 8 days. Figure 26 shows the residuals from the raw data, whereas Figure 27 shows the residuals after fallacious data is rejected by the pre-filter. Notice that the pre-filter removed a lot of trashy data near the 11^{th} day. This is an important clue for later analysis of the stochastic predictions.

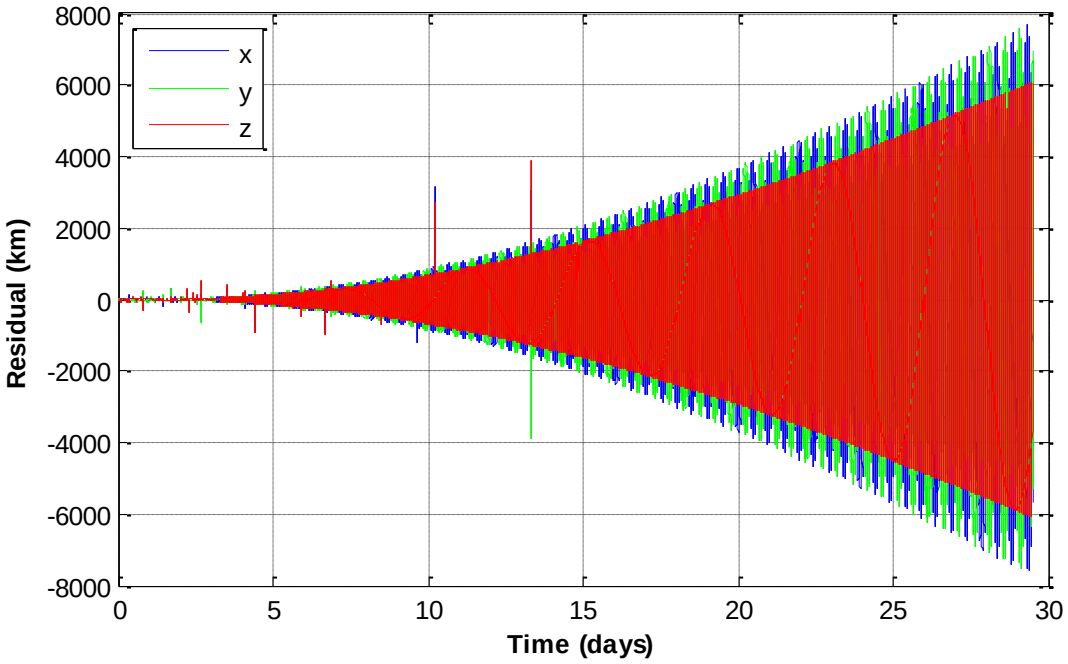

Figure 26. Residuals from direct comparison of deterministic reference torus to observation data.

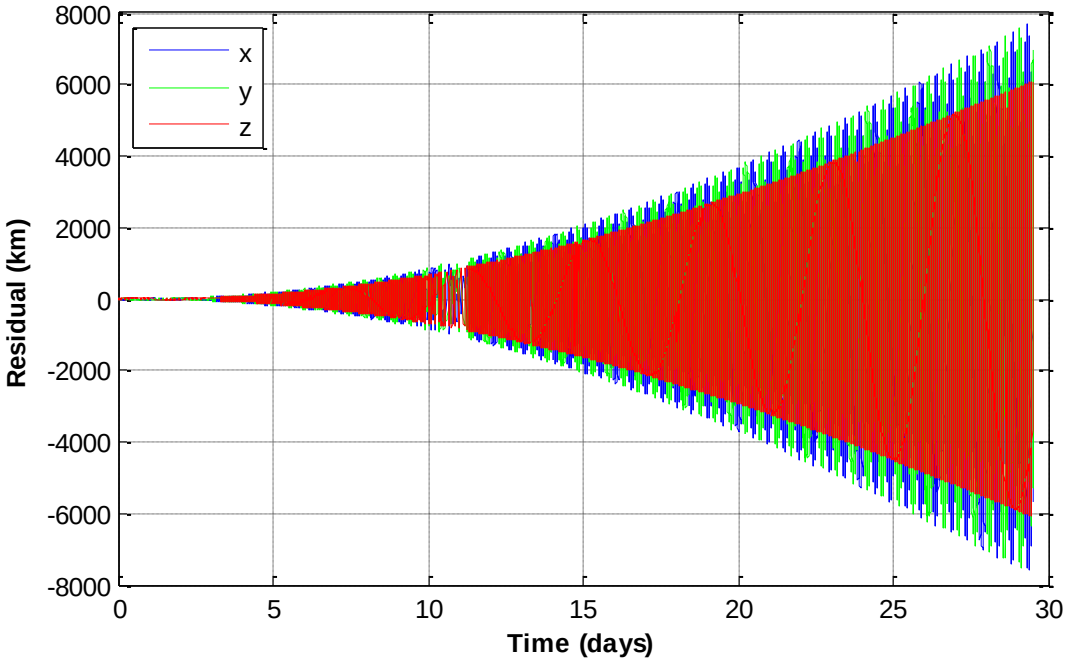

Figure 27. Pre-filtered residuals from direct comparison of deterministic reference torus to observation data.

4.3.2 Stochastic Predictions

The time varying polynomials characterizing the initial phase angles and momenta offsets were used to generate stochastic predictions from the reference torus. Since their behavior may be sensitive to the batch size during the estimation process, batches of 100, 300 and 1000 observations were used at roughly 1 minute intervals. Only the first half of the ISS data were used in the fitting process, whereas the remaining half were used as fresh, new observations to simulate a "real time" evaluation of the predictions.

4.3.2.1 Estimations and Predictions: Batches of 1000 Observations

As an assurance that the data were processed correctly by the pre-filter, NLS and Bayes filter, results from the first two batches will be presented in addition to the full string of 21 batches required to process the nearly 2-weeks of ISS data at 1,000 observations per batch.

The first batch of data was processed by the NLS since a priori data was not available. Prior to the first iteration of NLS, the residuals from the raw data are plotted in Figure 28 for monitoring the accuracy of the pre-filter. Figure 29 shows the residuals after pre-filtration and Figure 30 shows the residuals after 10 iterations of NLS. The final RMS residuals for coordinates x, y and z are 357.17, 334.23, and 338.26 meters, respectively.

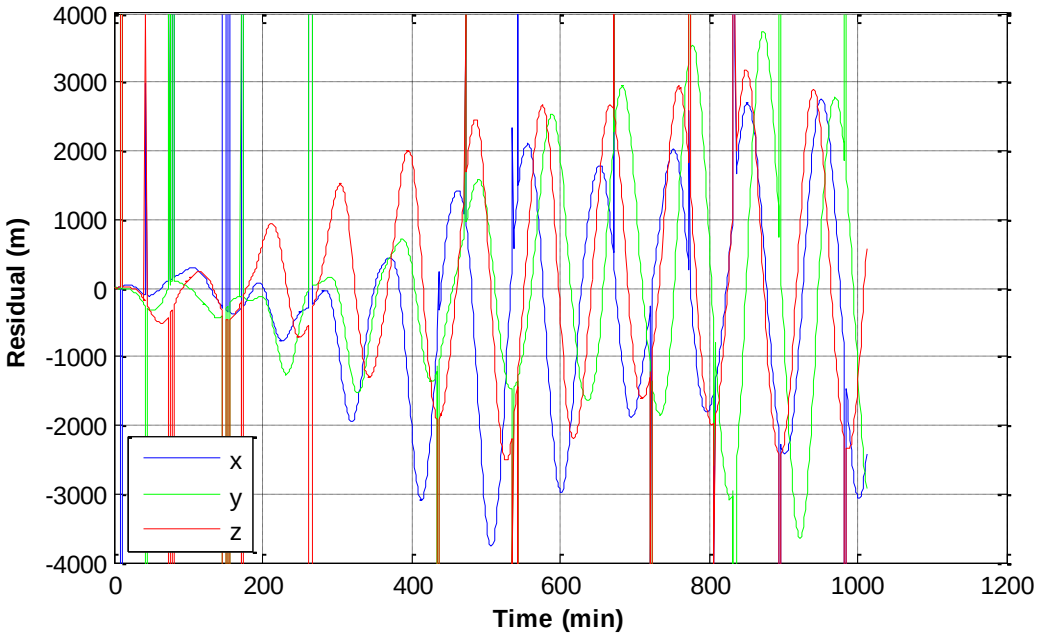

Figure 28. Residuals from first set of 1000 observations prior to pre-filter and NLS.

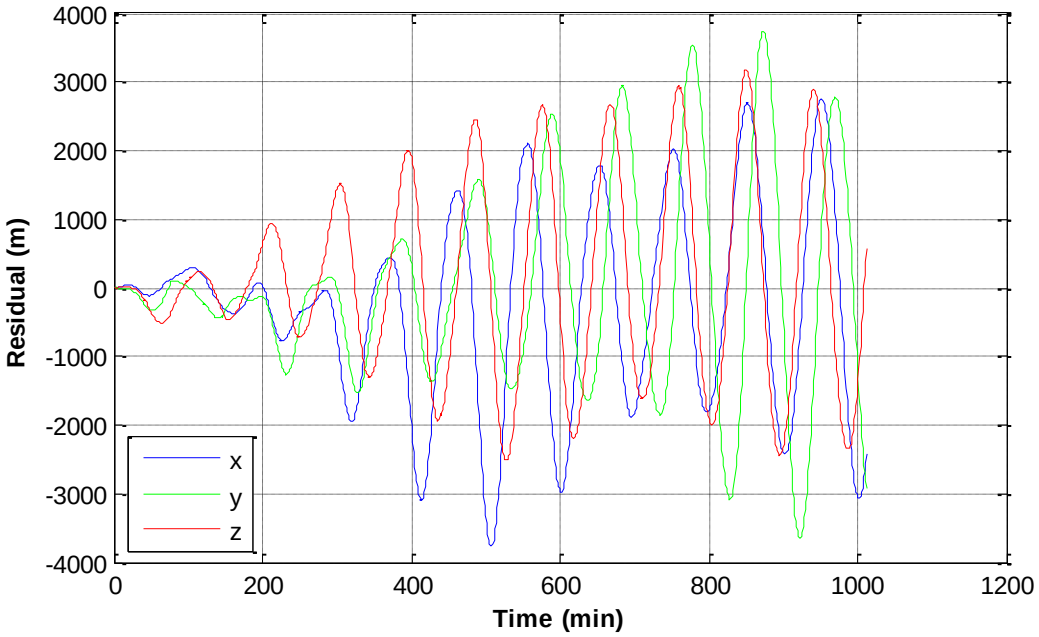

Figure 29. Pre-filtered residuals from first set of 1000 observations prior to NLS.

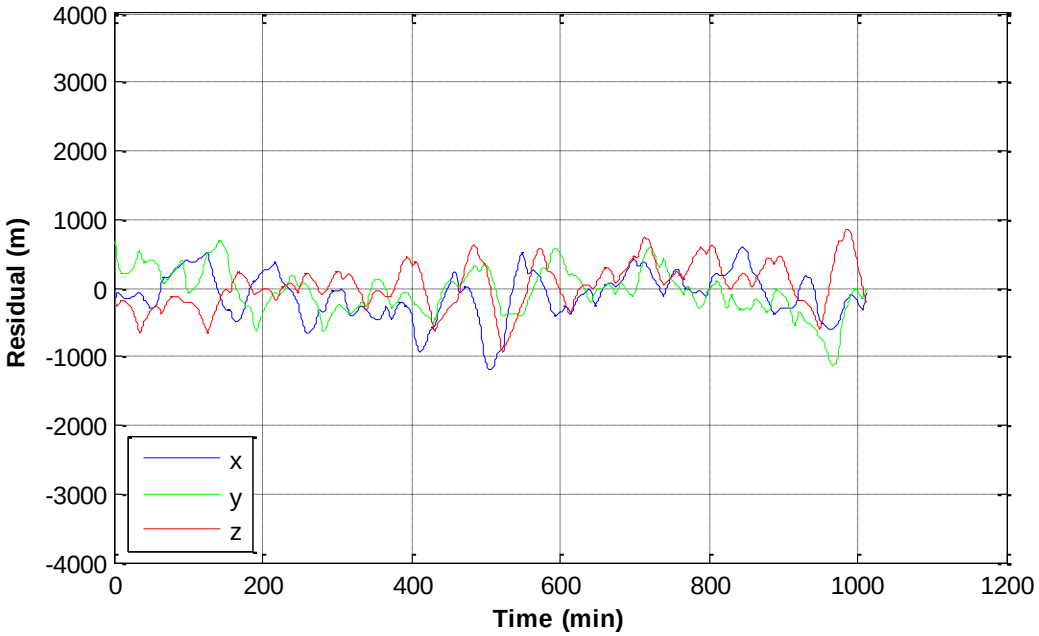

Figure 30. NLS filtered residuals from first set of 1000 observations.

Subsequent batches (after the NLS batch) are processed by the Bayes filter. The residuals from the second batch of raw data are plotted in Figure 31 for monitoring the accuracy of the pre-filter prior to the first iteration of the Bayes filter. Figure 32 shows the residuals after pre-filtration and Figure 33 shows the residuals after 10 iterations of Bayes. The final RMS residuals for coordinates x, y and z are 471.53, 326.24, and 263.47 meters, respectively.

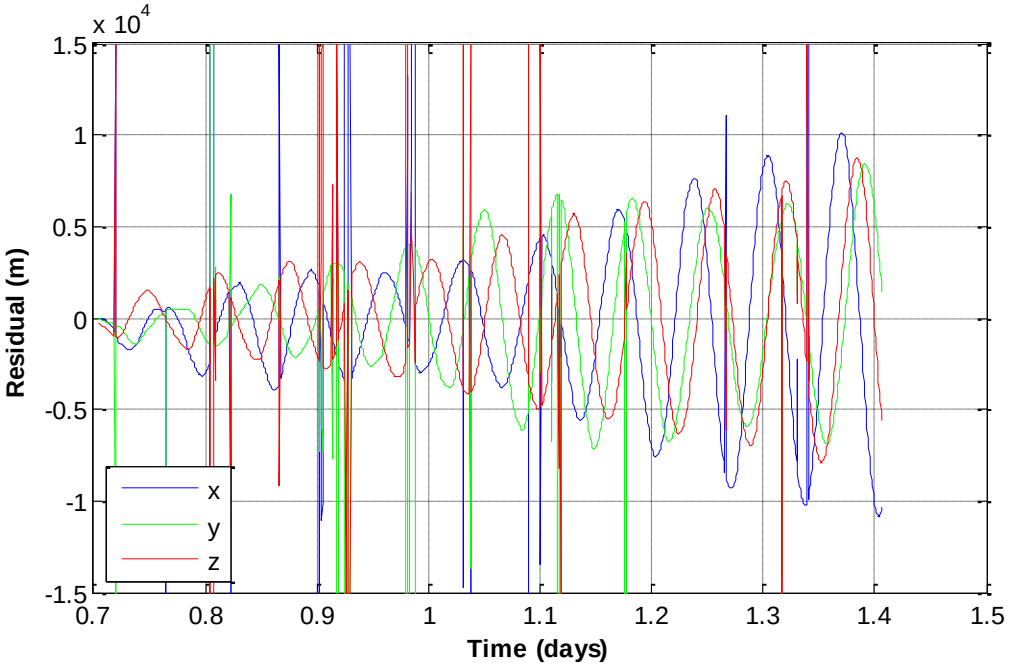

Figure 31. Residuals from second set of 1000 observations prior to pre-filter and Bayes.

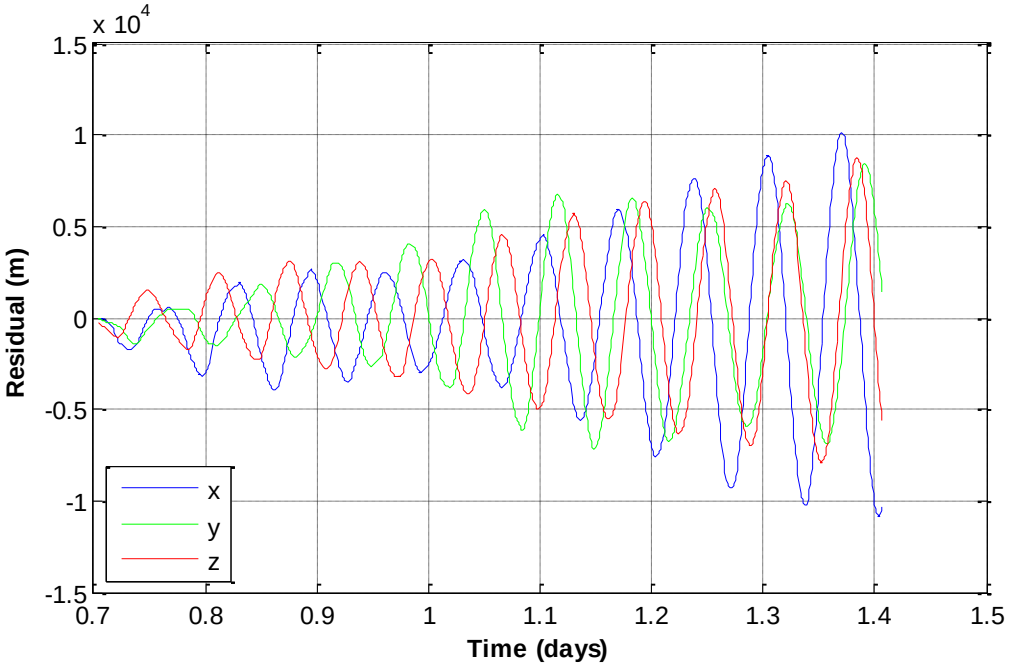

Figure 32. Pre-filtered residuals from second set of 1000 observations prior to Bayes.

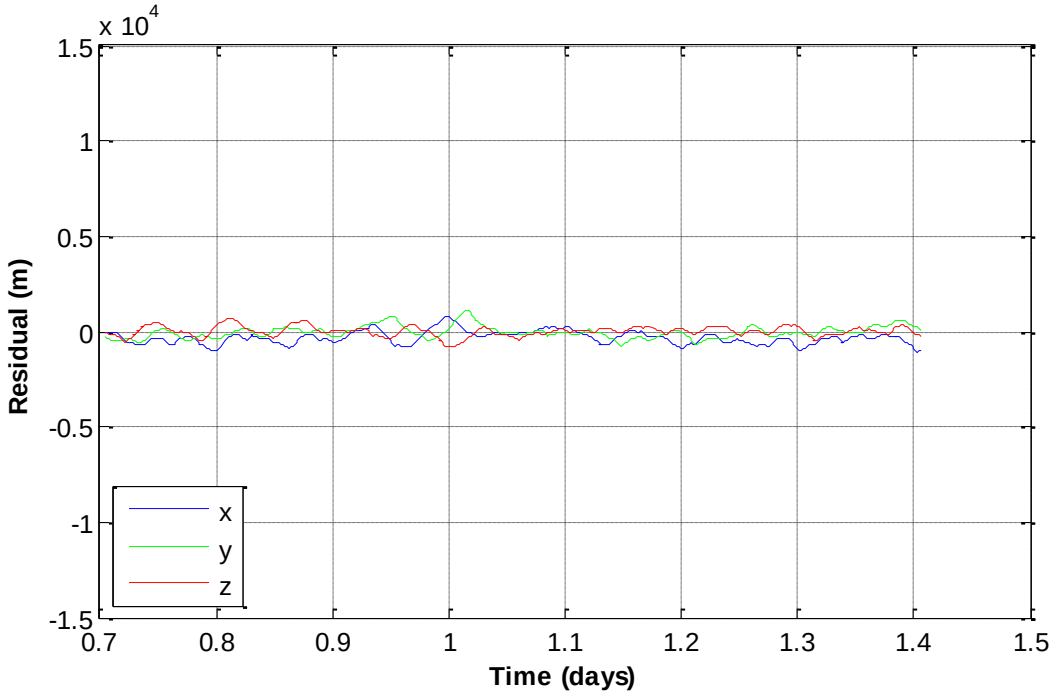

Figure 33. Bayes filtered residuals from second set of 1000 observations.

A concatenation of the final residuals after 10 iterations from all 21 batches is shown in Figure 34. The RMS residuals for coordinates x, y and z are 495.5, 440.9, and 370.1 meters, respectively. The same is done for the reference torus corrections in Figure 35 - Figure 37 to show the change in the initial phase angles and momenta that best fit the data. The plots reveal a linear trend in the momenta and a periodicity in the phase angles. The linearity in the momenta is a pleasant finding since a line can easily be fit to the data – precisely what is needed to utilize the reference torus for stochastic predictions. The periodicity in the phase angle corrections is not cause for alarm since they oscillate about zero with small amplitudes which will have a marginal effect when pooled with the initial phase angles, but a peculiar pattern arises in which dQ_1 and dQ_3 exactly oppose one

another. As dQ_1 increases, dQ_3 decreases, and vice versa. This is the classic *mean anomaly vs. argument of perigee* problem for low eccentricity orbits.

Recall that the time derivative of Q_1 is analogous to mean motion and the time derivative of Q_3 is analogous to the apsidal regression rate, so both coordinates have the physical effect of displacements on the orbital plane. Since the ISS orbit has a very low eccentricity (~0.0007 – 0.002) the apsidal regression rate is very small (~7.7e-7 s^{-1}) and is easily overlooked by the mean motion (~0.00114 s^{-1}) in the same plane. This makes it susceptible to modeling errors as the two coordinates fight to converge upon a solution. More will be said on this later.

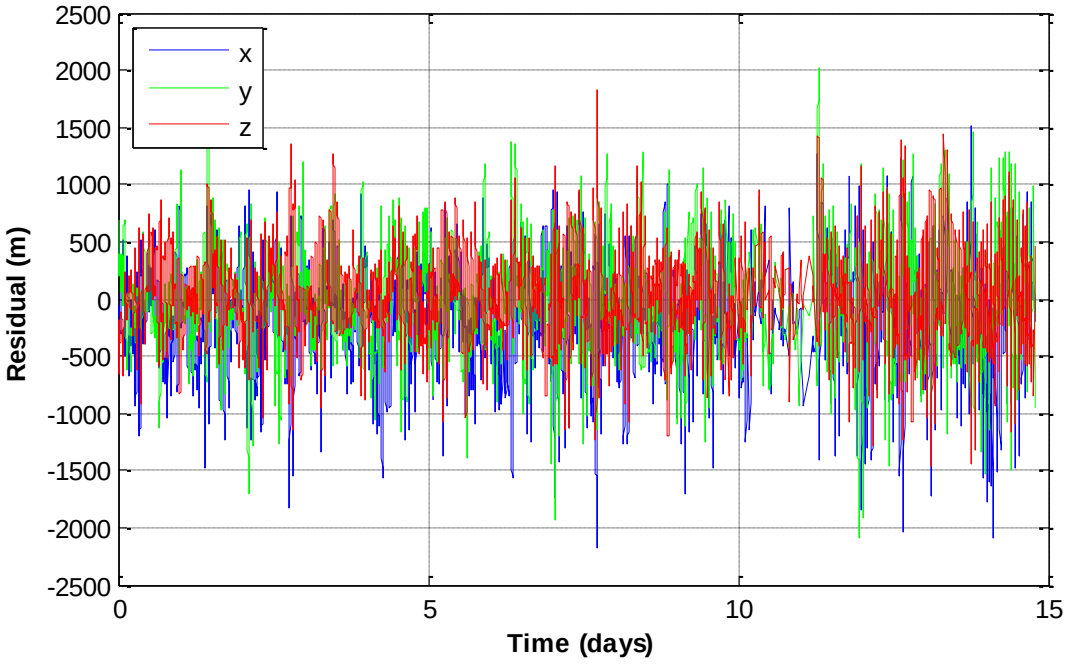

Figure 34. Bayes filtered residuals from batches of 1000 observations.

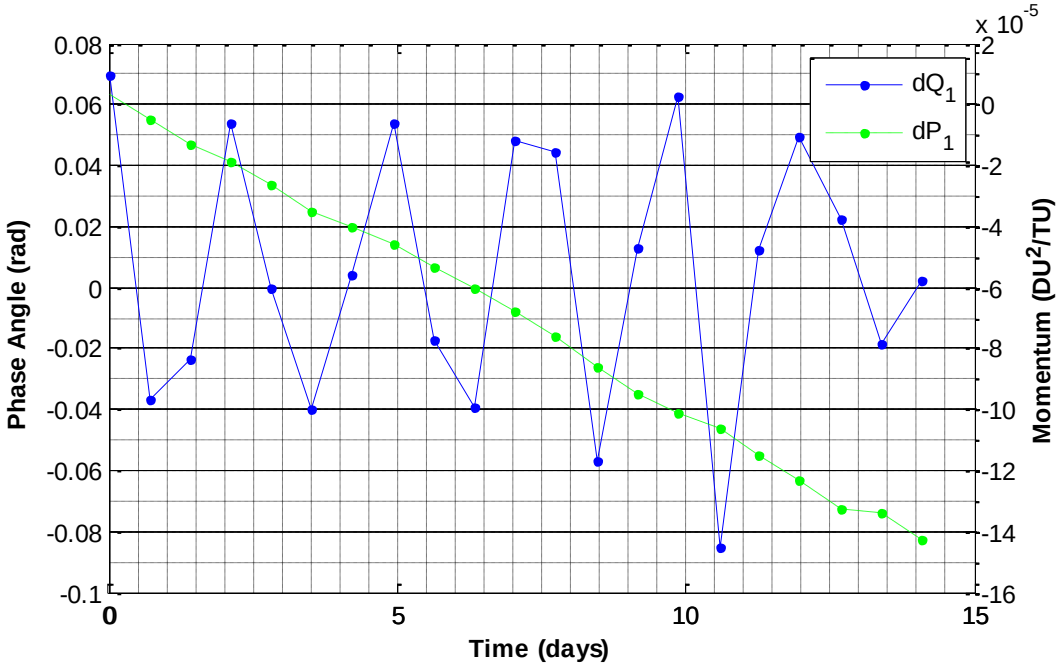

Figure 35. dQ_1 and dP_1 torus corrections from Bayes filtered batches of 1000 observations.

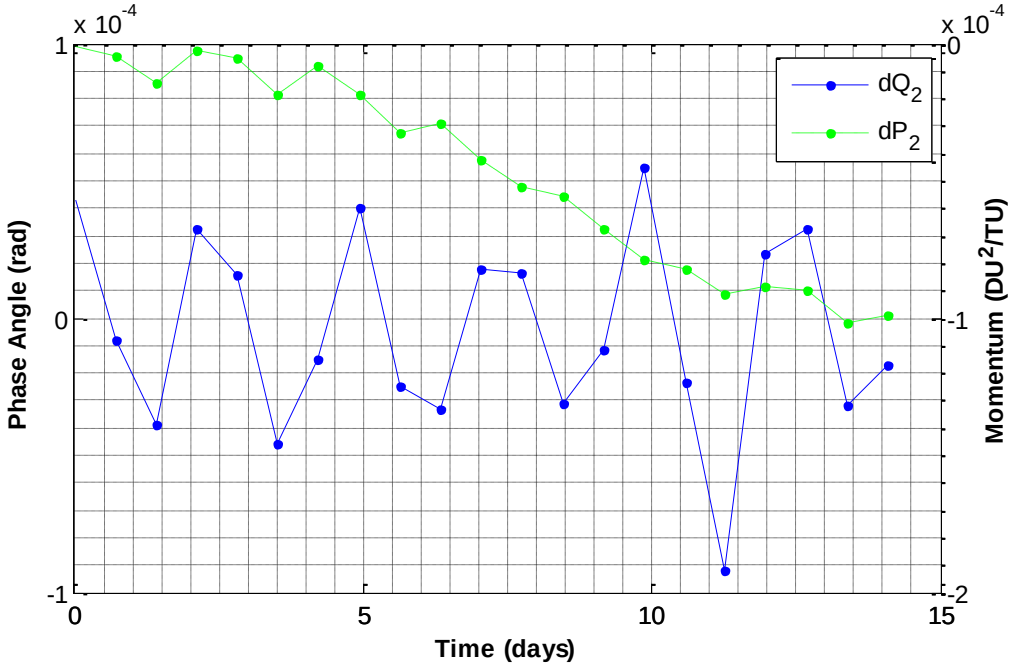

Figure 36. dQ_2 and dP_2 torus corrections from Bayes filtered batches of 1000 observations.

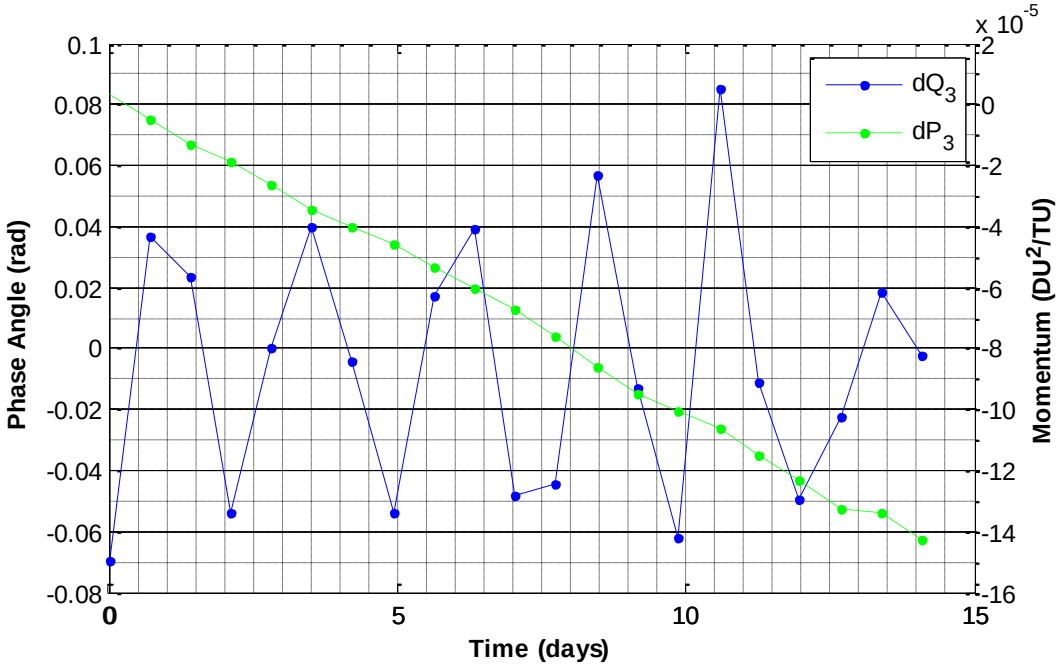

Figure 37. dQ_3 and dP_3 torus corrections from Bayes filtered batches of 1000 observations.

After accumulating the updates to $\vec{\boldsymbol{Q}}_{\boldsymbol{0}}$ from (172), a polynomial of degree two was fit to the data. Similarly, a polynomial of degree one was fit to $\overrightarrow{\boldsymbol{\delta P}}$ as shown in Figure 38 - Figure 40.

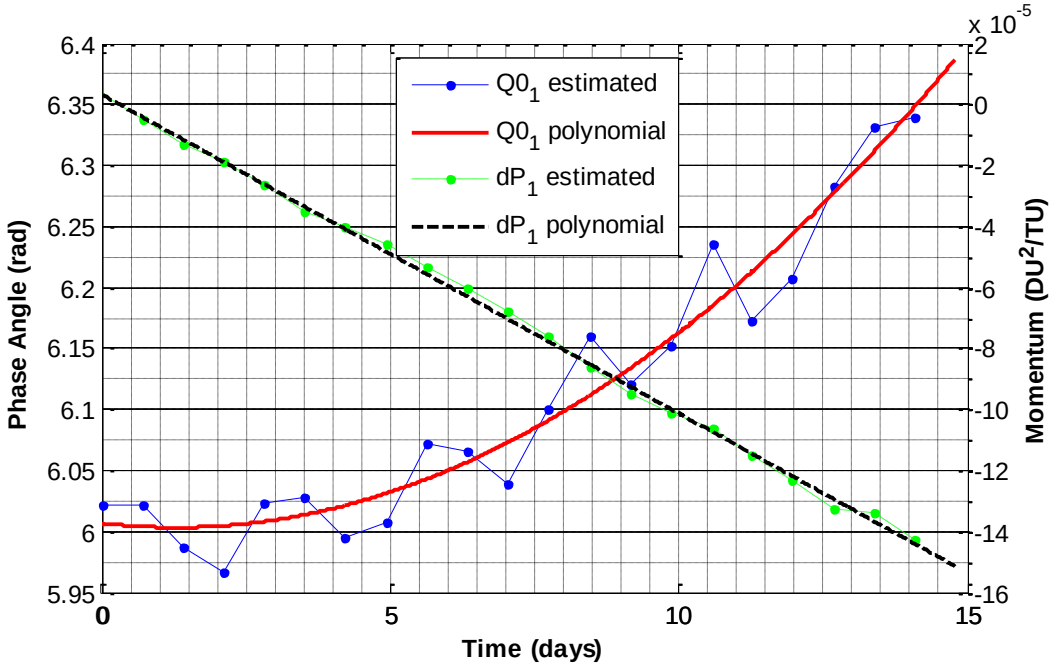

Figure 38. Polynomial approximations of $Q0_1$ and dP_1 from Bayes filtered batches of 1000 observations.

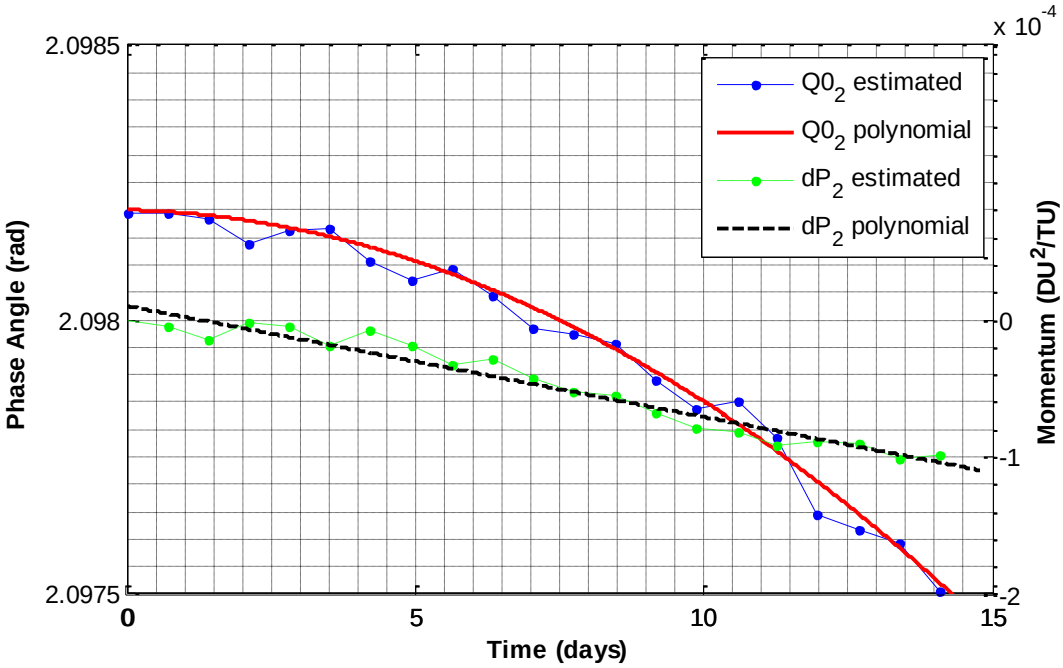

Figure 39. Polynomial approximations of $Q0_2$ and dP_2 from Bayes filtered batches of 1000 observations.

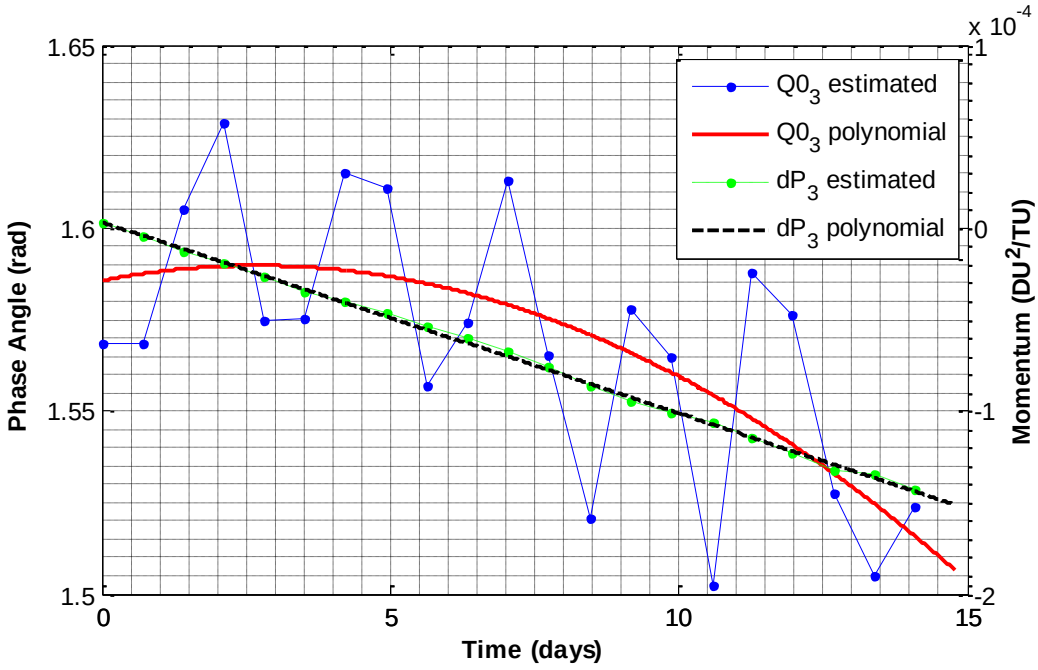

Figure 40. Polynomial approximations of $Q0_3$ and dP_3 from Bayes filtered batches of 1000 observations.

The polynomial functions representing the pseudo-stochastic parameters were used with the reference torus to generate stochastic predictions. All 42,000 observations, including the first 21,000 that were used during the estimation process, were compared to the stochastic prediction from the torus. The last 21,000 observations are used to simulate the torus' ability to predict in "real time" since these data were not processed previously by the Bayes filter. Figure 41 shows the residuals for the full 42,000 observations. Prior to the degradation in the prediction at 18.5 days, the RMS residuals for coordinates x, y and z are 2.586, 2.602, and 2.455 kilometers, respectively.

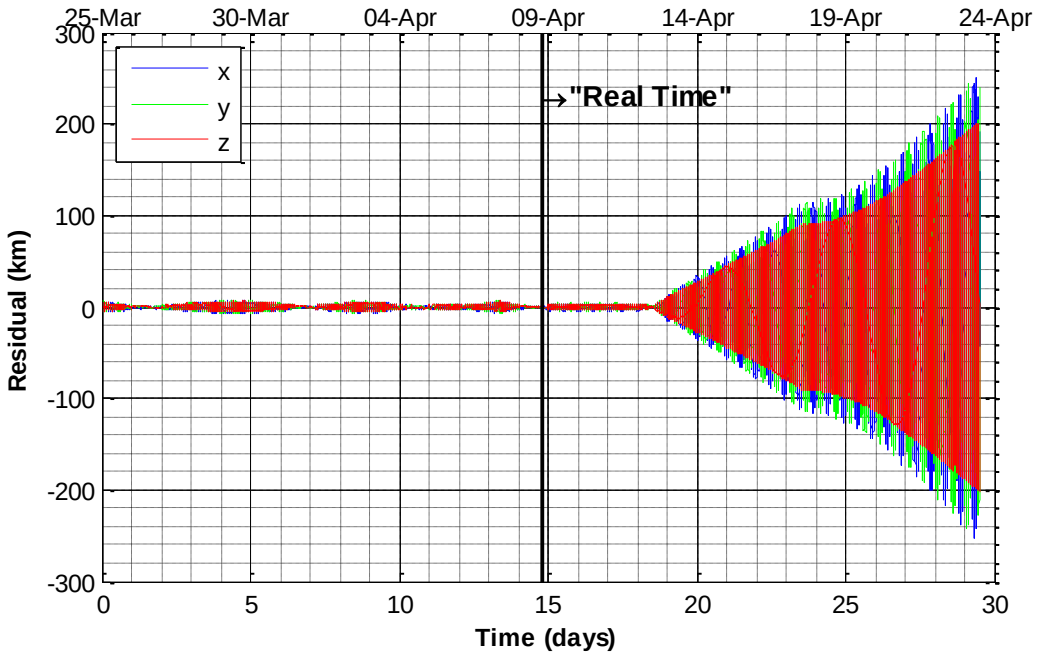

Figure 41. Residuals generated using pseudo-stochastic parameters estimated from batches of 1000 observations.

After observing the results, the obvious question is: why did the predictions hold so consistently for 18.5 days (almost 4 days into the real time segment) and then suddenly breakdown midway through April 12? A review of the dynamic events during the prediction times, listed in Table 8, show no activity on that day. However, a correlation of these events with the results gives an important clue. Consider again the residuals depicted with these overlapping events in Figure 42.

Table 8. ISS Dynamic Events.

Time (GMT)	Event
4 Apr 03:10 – 06:50	Soyuz (TMA-18) docking
7 Apr 04:13 – 07:44	Discovery (STS-131) docking
17 Apr 10:20 – 15:06	Discovery (STS-131) undocking
17 Apr 19:55 – 18 Apr 02:15	Progress 35 Prop Purge
22 Apr 13:15 – 18:04	Progress 35 undocking

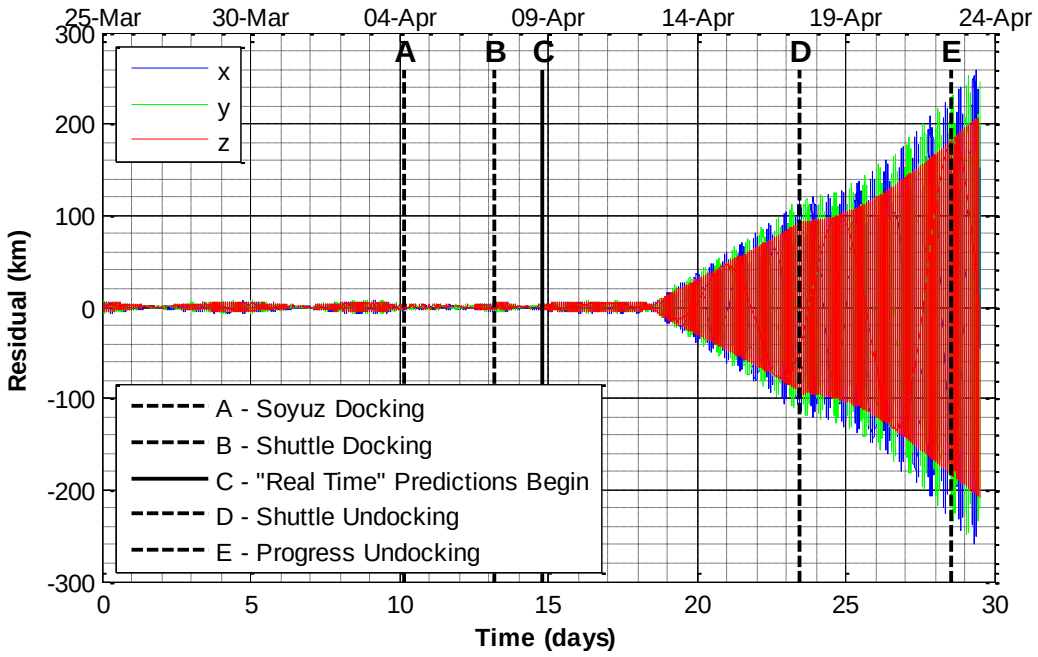

Figure 42. Residuals from stochastic predictions correlated with dynamic events.

Notice that the slope of the residuals changes at the time of the Shuttle's undocking. This is due to a large decrease in drag that causes a divergence from the pseudo-stochastic torus parameters. In its current configuration, the ISS is flown with its x-axis in the velocity vector (XVV attitude) and the z-axis pointing nadir [53]. This means the velocity vector is nearly normal to the underside of the shuttle. Figure 43 gives a sense of how much additional drag is

Figure 43. Artist rendering of the Space Shuttle docked with the ISS. *Credit: NASA*

incurred when the shuttle is docked.

It stands to reason that any significant change in drag or increase in thrust will cause a divergence from the predictions. The arrival of the Soyuz and Shuttle did not induce the same divergence because the pseudo-stochastic parameters were estimated during those docking events and therefore the curves were bent to compensate for the change in drag. But this does not excuse the Russian Progress cargo ship's departure from the ISS on April 22. Figure 44 shows a graphic of the ISS with the solar arrays and Active Thermal Control System (ATCS) radiators removed for viewing of the Russian segment, particularly a Russian Progress resupply vehicle docked at the Poisk Mini Research Module 2 (MRM2). This zenith port was the same one used for Progress 35 so it gives a sense of the drag contribution. Because its projected surface area is so much smaller than the Shuttle, its effect is more difficult to observe in the residual growth that is already increasing rapidly due to the Shuttle's departure.

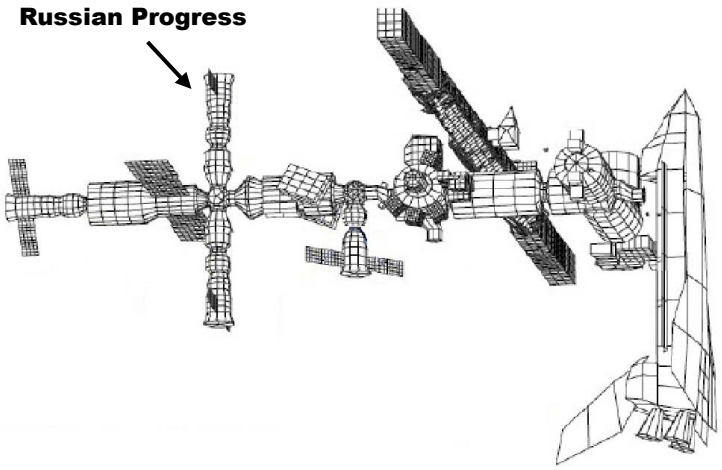

Figure 44. Scaled comparison of Progress resupply vehicle and Space Shuttle docked to the ISS. *Credit: NASA*

The Shuttle's departure is proof that a significant change in drag will cause degradation in the torus prediction, but if there were no changes to the total surface area of the ISS on April 12, the only other possibility for a change in drag is a change in

particle density. Space weather reports from the National Oceanic and Atmospheric Administration (NOAA) were used to assess geomagnetic activity that may have contributed to changes in drag that day [54].

The NOAA uses the K-index from the Boulder Magnetometer to approximate the planetary Kp-index for real-time alerts and warnings. According to the NOAA Space Weather Scale for Geomagnetic Storms [55], minor storms (G1 class) are characterized by Kp values less than or equal to 5. These typically have negligible impacts on spacecraft operations. Moderate storms (G2 class) are characterized by Kp values equal to 6. Under these conditions the NOAA states, "corrective actions to orientation may be required by ground control; possible changes in drag affect orbit predictions" [55]. Strong storms (G3 class), severe storms (G4 class) and extreme storms (G5 class) are characterized by Kp values equal to 7, 8 (including a 9-) and 9, respectively. The NOAA warns that the effects of these higher class storms usually include surface charging, orientation, tracking and prediction problems commensurate with the severity of the storm. G3 class storms are powerful enough that the NOAA specifically warns LEO satellites can experience increased drag. For the time period of ISS observations, all NOAA alerts for G2 through G5 class storms were logged in Table 9 [56-60].

Table 9. Moderate to Extreme Space Weather Events.

Time (GMT)	Event
05 Apr 0920	ALERT: Geomagnetic K = 6
05 Apr 0955	ALERT: Geomagnetic K = 7
06 Apr 0422	ALERT: Geomagnetic K = 6
12 Apr 0225	ALERT: Geomagnetic K = 6
12 Apr 0240	ALERT: Geomagnetic K = 7

From 25 March through 4 April 2010, the NOAA reported mostly quiet to minor storm levels in the geomagnetic field with only brief active periods where the Kp index peaked at 4. A halo coronal mass ejection (CME) observed on 3 April caused an increase in geomagnetic activity starting on 5 April that peaked with G3 class storms. The effects of the CME waned on 7 April. Any change in particle density incurred from this CME would have been absorbed by the pseudo-stochastic parameters during the estimation process and won't appear in the predictions. Conditions were then mostly quiet with some isolated minor storm ensuing through 11 April. A full halo CME aimed almost directly at earth was observed on 8 April at 0325 UTC causing major to sever storms on 12 April. It is shown in Figure 45. By 13 April the active storms dwindled to quiet levels at which conditions predominantly remained with only minor storms through 24 April.

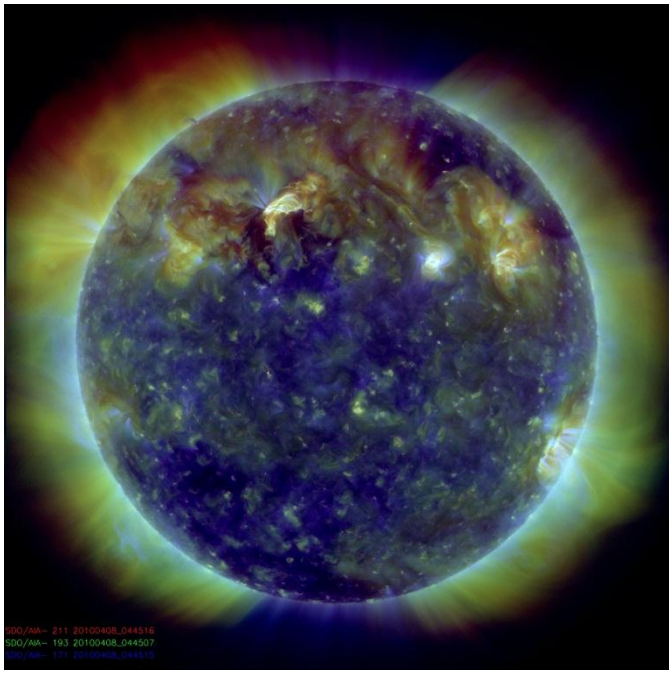

Figure 45. Solar flare in upper left quadrant on 8 April 2010 produced an earth-directed CME. *Credit: NASA Solar Dynamics Observatory*

The presence of major geomagnetic storms on 12 April certainly leaves a possible explanation for the degradation in the predictions, but to be sure, further investigations will be required. The first step is to run the last set of 21,000 observations through the

Bayes filter to estimate what the pseudo-stochastic parameters should have been and compare those to the curves generated from the first set of 21,000 observations.

Figure 46 - Figure 48 show that the polynomials fit the estimates fairly well until April 12 when the predictions degenerated. A clear jump is observed in the momenta offsets at the times of interest, further supporting the hypothesis that drag changes shifted the ISS onto an adjacent torus trajectory that was not modeled.

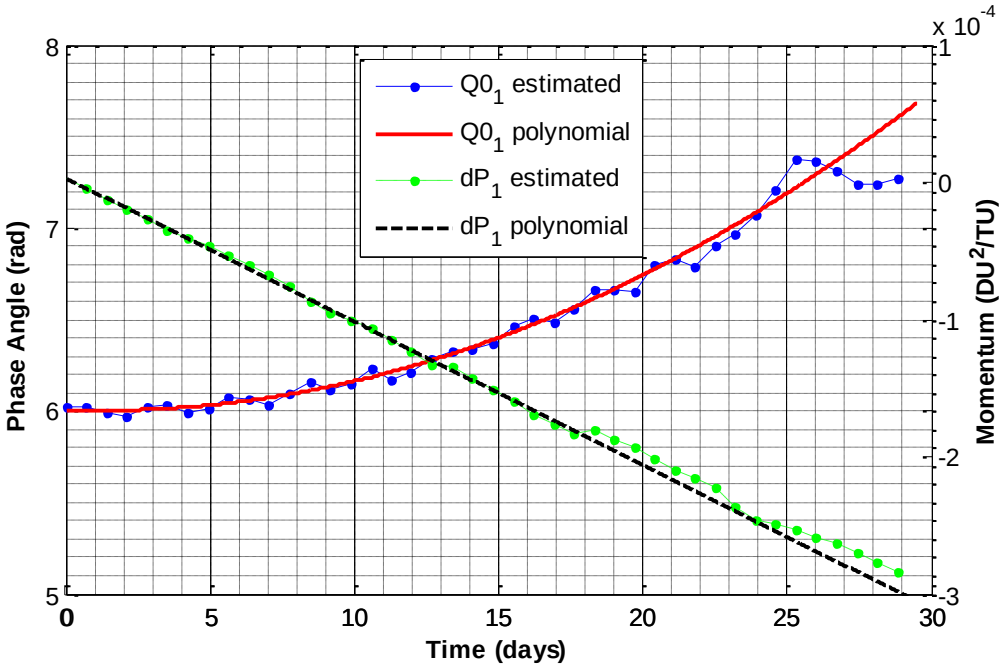

Figure 46. Estimates of dP_1 from Bayes filtered batches of 1000 observations show a slight offset from the polynomial approximations at times of interest.

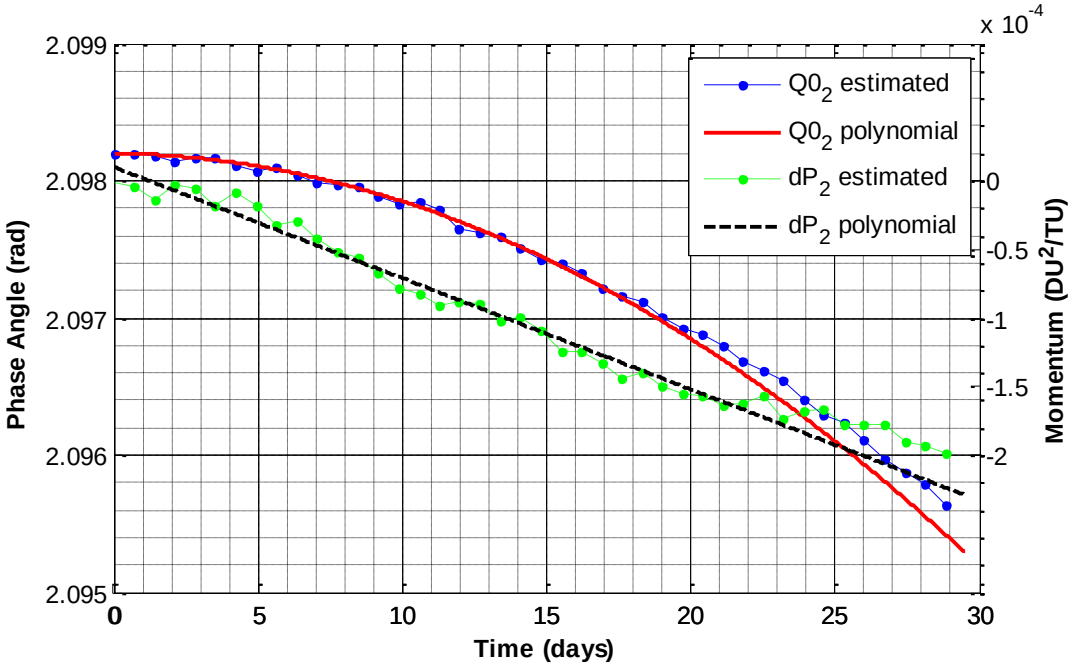

Figure 47. Estimates of dP_2 from Bayes filtered batches of 1000 observations show a slight offset from the polynomial approximations at times of interest.

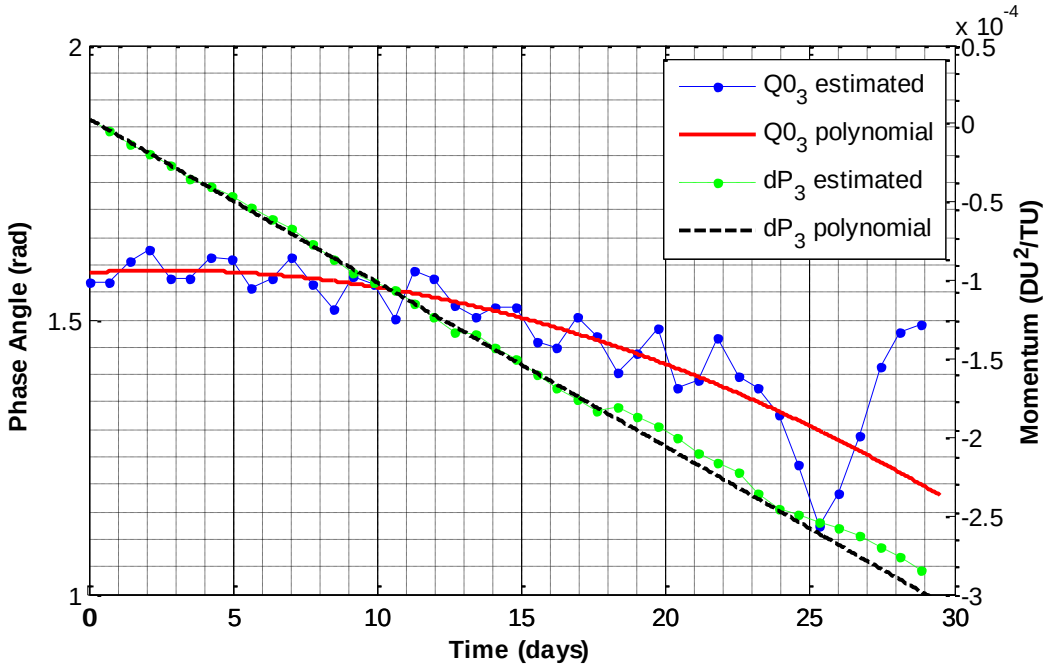

Figure 48. Estimates of dP_3 from Bayes filtered batches of 1000 observations show a slight offset from the polynomial approximations at times of interest.

The indisputable proof is found by calling upon the unforsaken osculating orbital elements. The semimajor axis is known to transfigure with variations in atmospheric drag. Figure 49 shows that this is precisely what happened. Because the change is so subtle, the event markups have been removed in Figure 50 to more clearly reveal the changes.

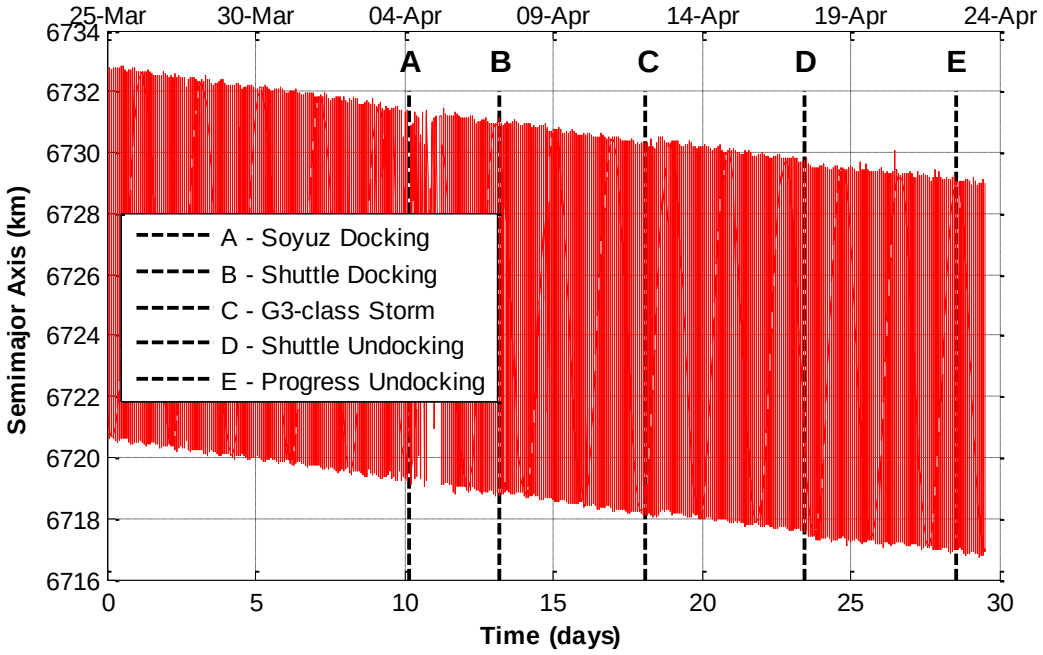

Figure 49. The pre-filtered, osculating semimajor axis reveals subtle mutations near the events of interest.

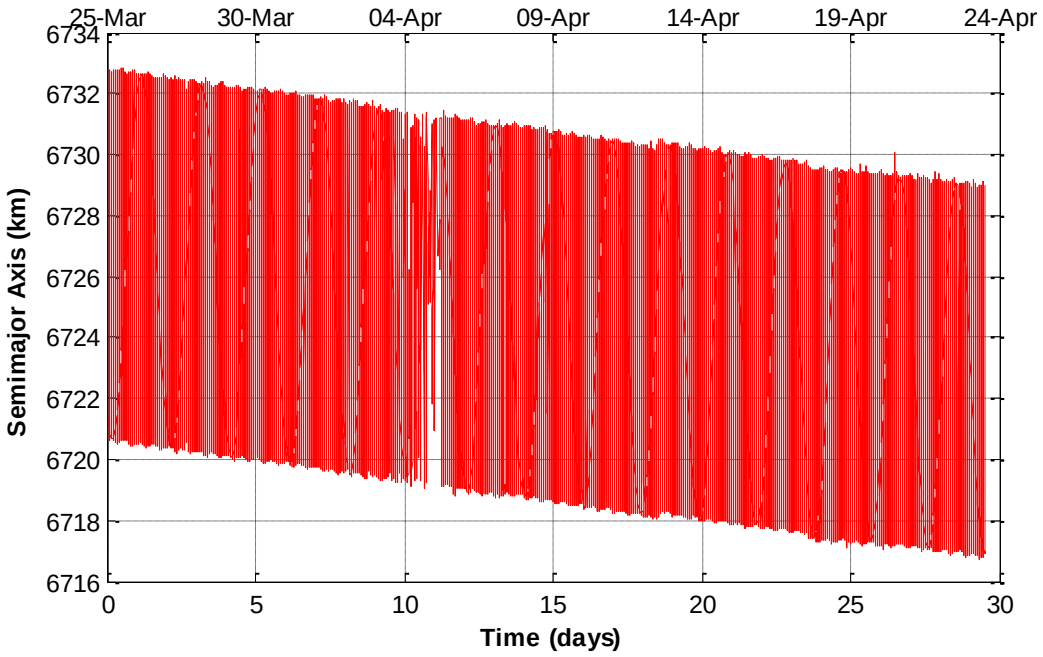

Figure 50. The pre-filtered, osculating semimajor axis reveals subtle mutations near the events of interest. The event markups have been removed for unaided viewing.

The next set of results will reveal, prior to the time at which the predictions break down due to the G3-class storm, whether or not the predictions can be improved using pseudo-stochastic parameters estimated with different sized batches.

4.3.2.2 Estimations and Predictions: Batches of 300 Observations

The ensuing results are produced from batches of 300 observations which translate to a little more than 3 full orbital revolutions. As an assurance that the data was processed correctly by the pre-filter, NLS and Bayes filter, results from the first two batches will be presented in addition to the full string of 70 batches required to process the nearly 2-weeks of ISS data at 300 observations per batch.

The first batch of data was processed by the NLS since a priori data was not available. Prior to the first iteration of NLS, the residuals from the raw data are plotted in Figure 51 for monitoring the accuracy of the pre-filter. Figure 52 shows the residuals after pre-filtration and Figure 53 shows the residuals after 10 iterations of NLS. The final RMS residuals for coordinates x, y and z are 225.49, 202.20, and 195.93 meters, respectively.

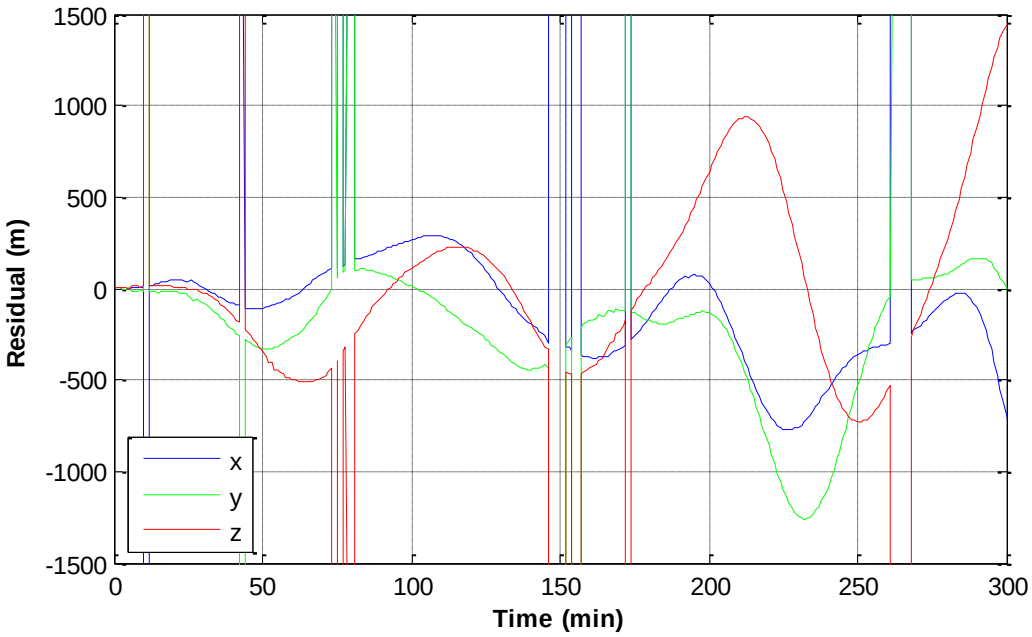

Figure 51. Residuals from first set of 300 observations prior to pre-filter and NLS.

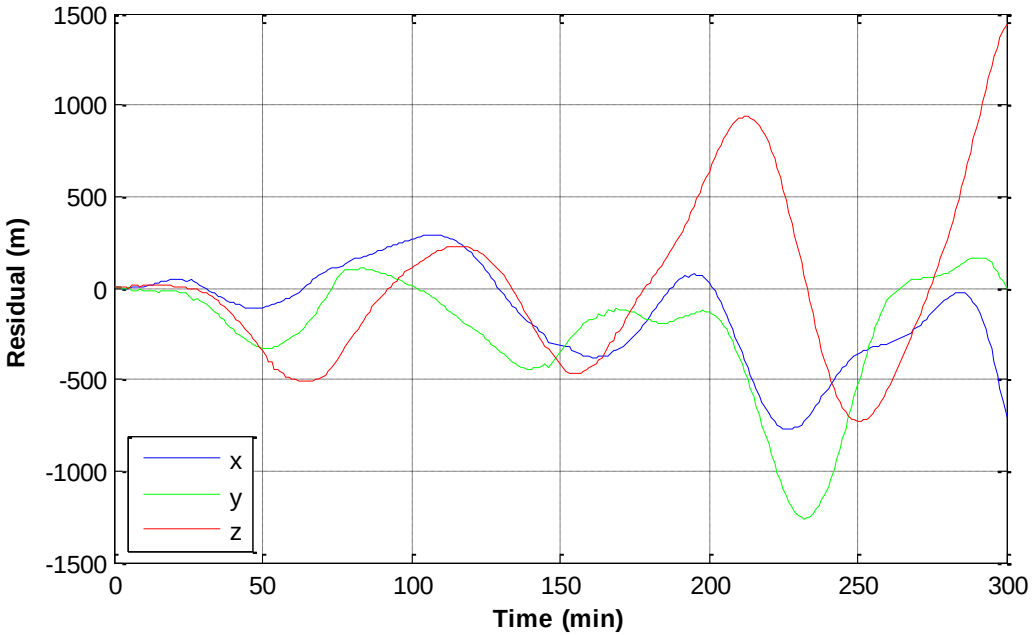

Figure 52. Pre-filtered residuals from first set of 300 observations prior to NLS.

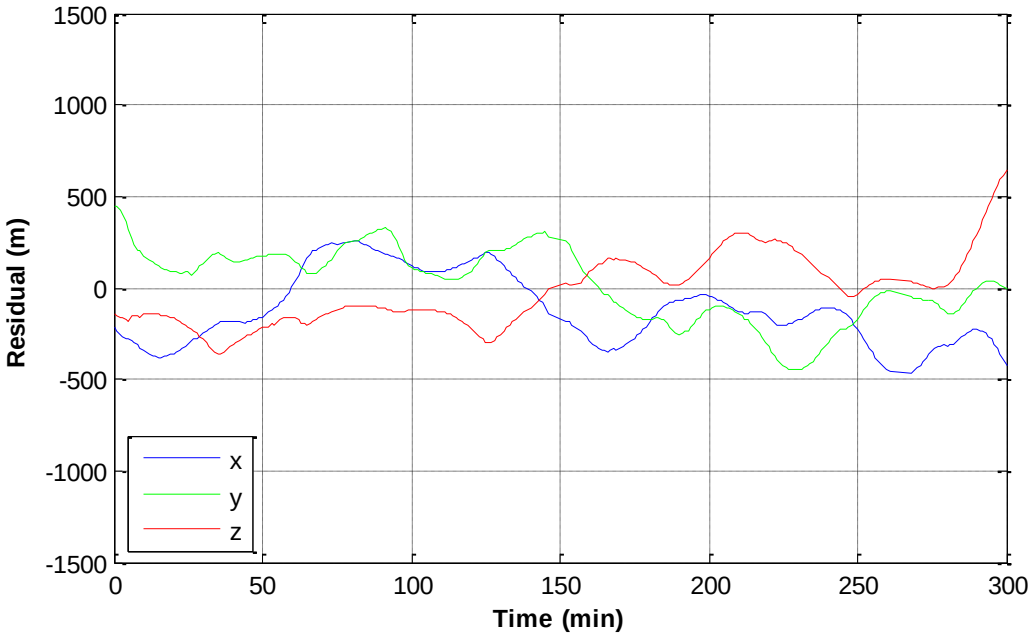

Figure 53. NLS filtered residuals from first set of 300 observations.

Subsequent batches (after the NLS batch) are processed by the Bayes filter. The residuals from the second batch of raw data are plotted in Figure 54 for monitoring the accuracy of the pre-filter prior to the first iteration of the Bayes filter. Figure 55 shows the residuals after pre-filtration and Figure 56 shows the residuals after 10 iterations of NLS. The final RMS residuals for coordinates x, y and z are 218.91, 118.23, and 121.68 meters, respectively.

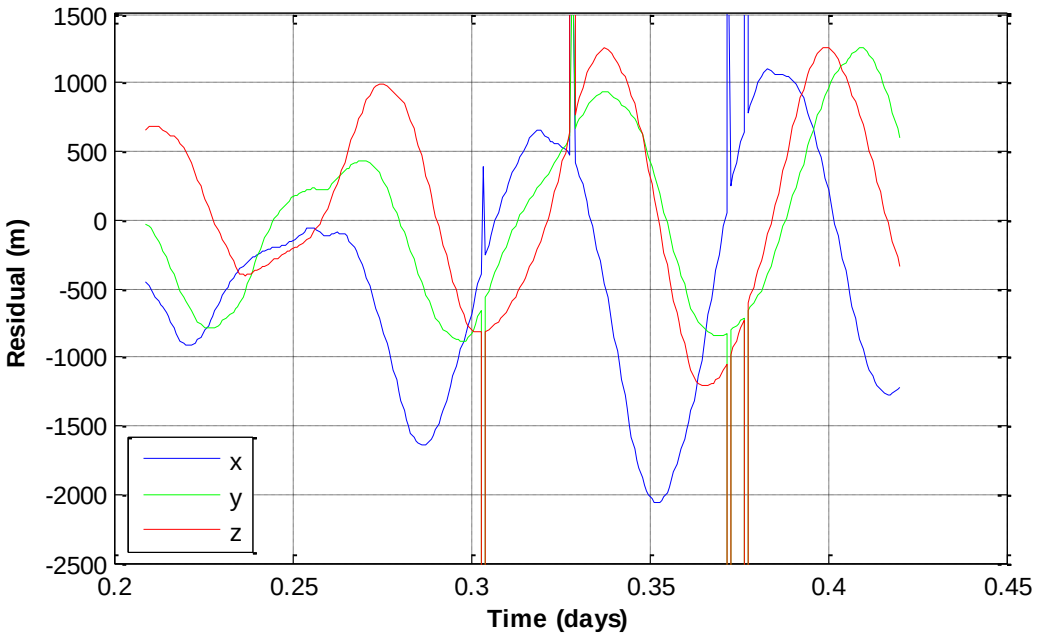

Figure 54. Residuals from second set of 300 observations prior to pre-filter and Bayes.

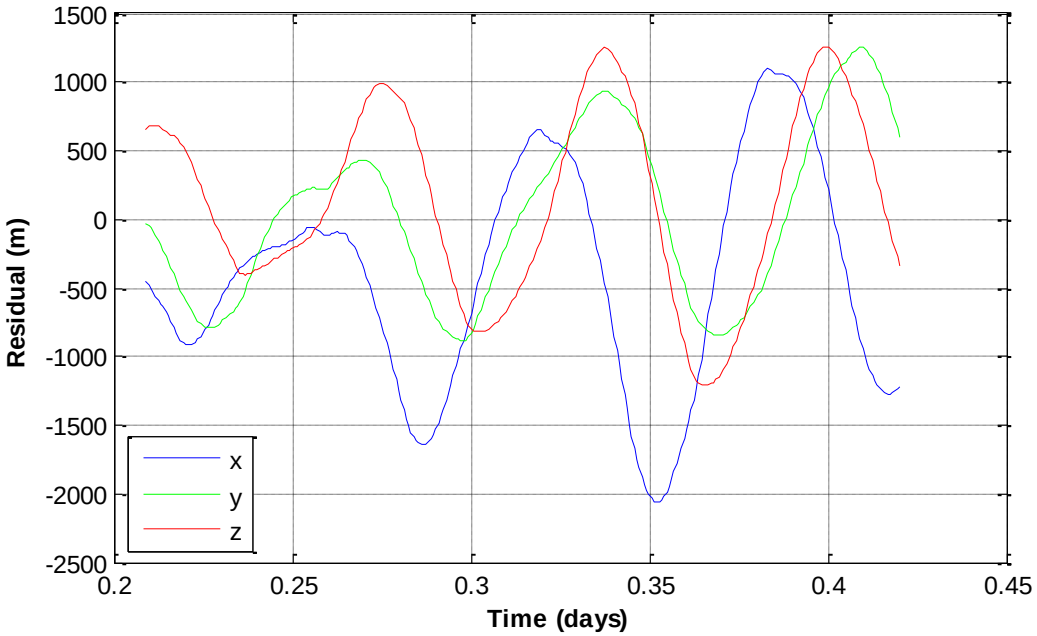

Figure 55. Pre-filtered residuals from second set of 300 observations prior to Bayes.

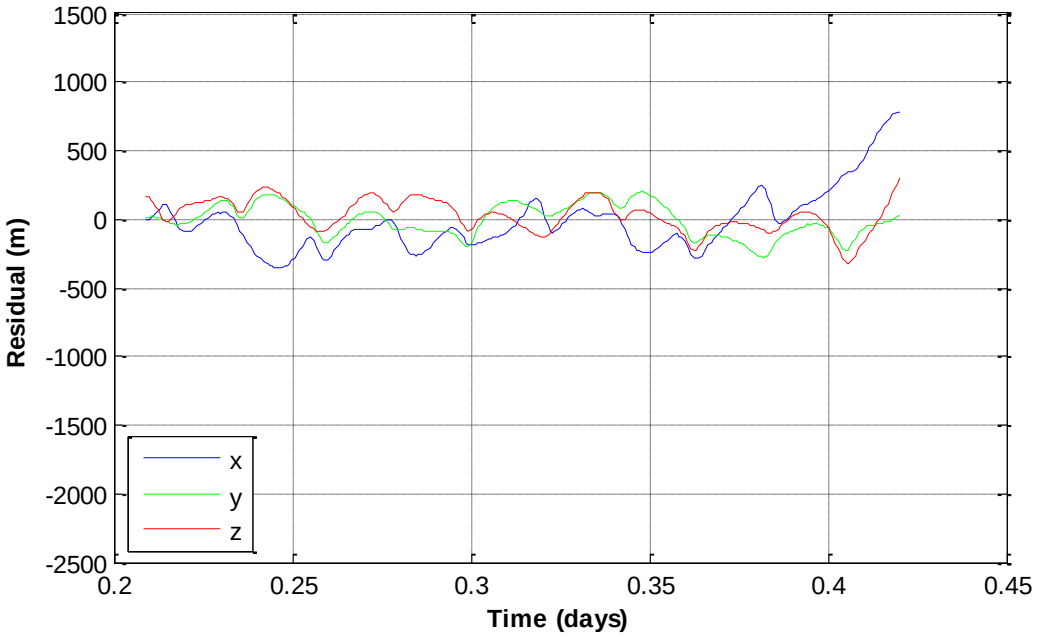

Figure 56. Bayes filtered residuals from second set of 300 observations.

A concatenation of the final residuals after 10 iterations from all 70 batches is shown in Figure 57. The RMS residuals for coordinates x, y and z are 255.14, 243.40, and 224.80 meters, respectively. The same is done for the reference torus corrections in Figure 58 - Figure 60 to show the change in the initial phase angles and momenta that best fit the data. The plots reveal a linear trend in the momenta and a periodicity in the phase angles as observed and discussed previously in §4.3.2.1.

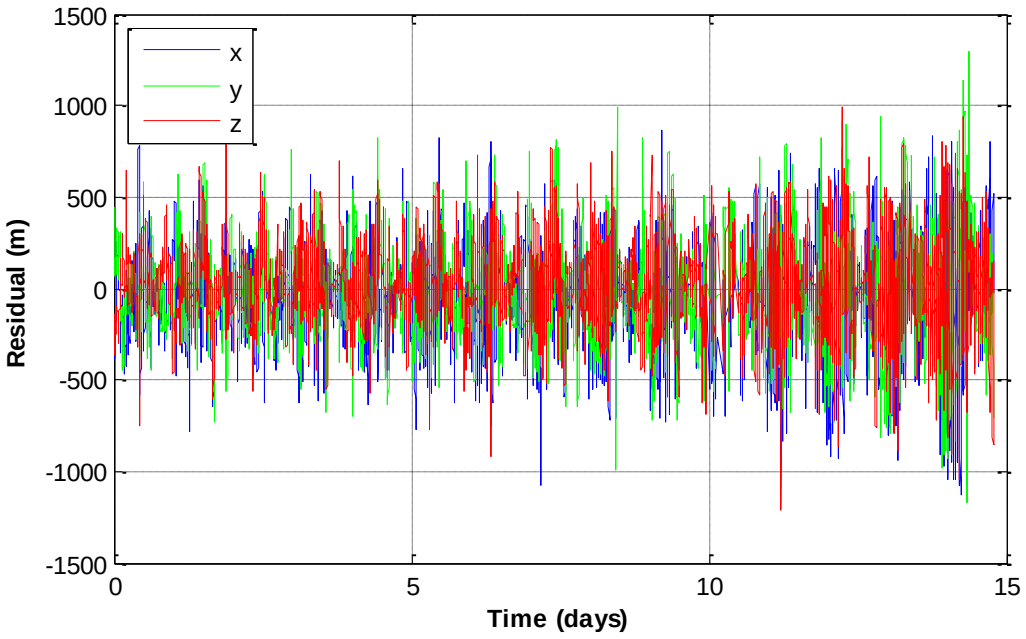

Figure 57. Bayes filtered residuals from batches of 300 observations.

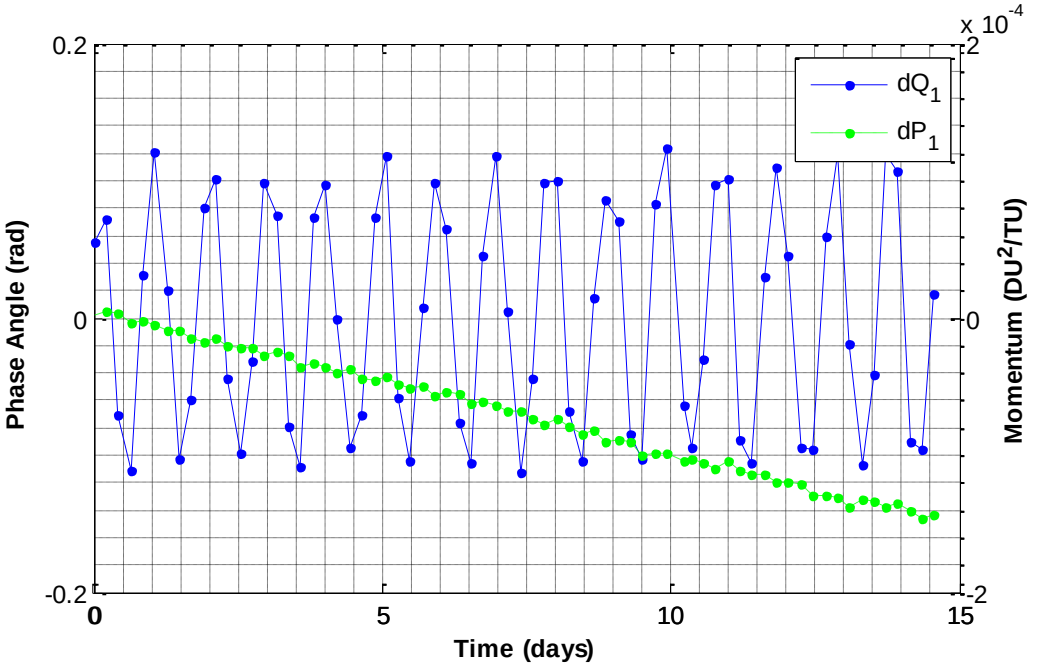

Figure 58. dQ_1 and dP_1 torus corrections from Bayes filtered batches of 300 observations.

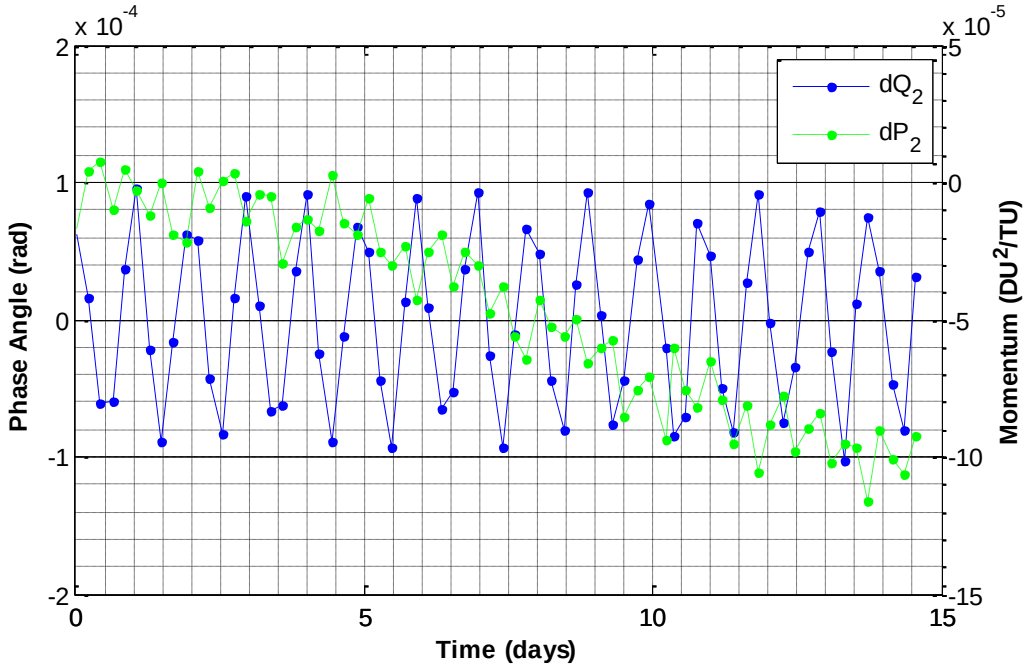

Figure 59. dQ_2 and dP_2 torus corrections from Bayes filtered batches of 300 observations.

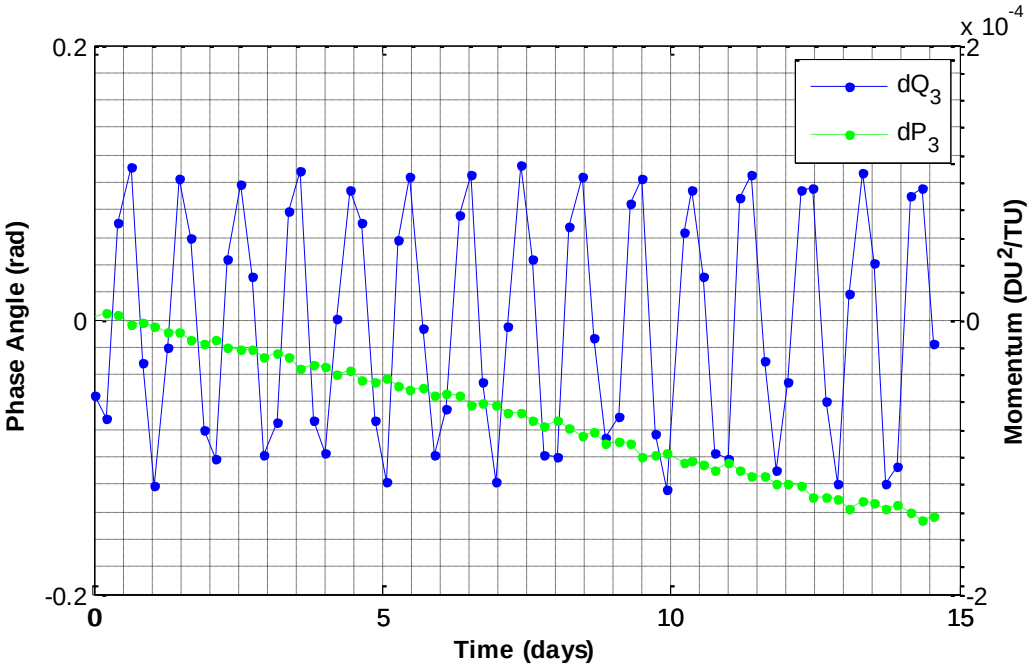

Figure 60. dQ_3 and dP_3 torus corrections from Bayes filtered batches of 300 observations.

After accumulating the updates to $\overrightarrow{\boldsymbol{Q_0}}$ from (172), a polynomial of degree two was fit to the data. Similarly, a polynomial of degree one was fit to $\overrightarrow{\boldsymbol{\delta P}}$ as shown in Figure 61 - Figure 63.

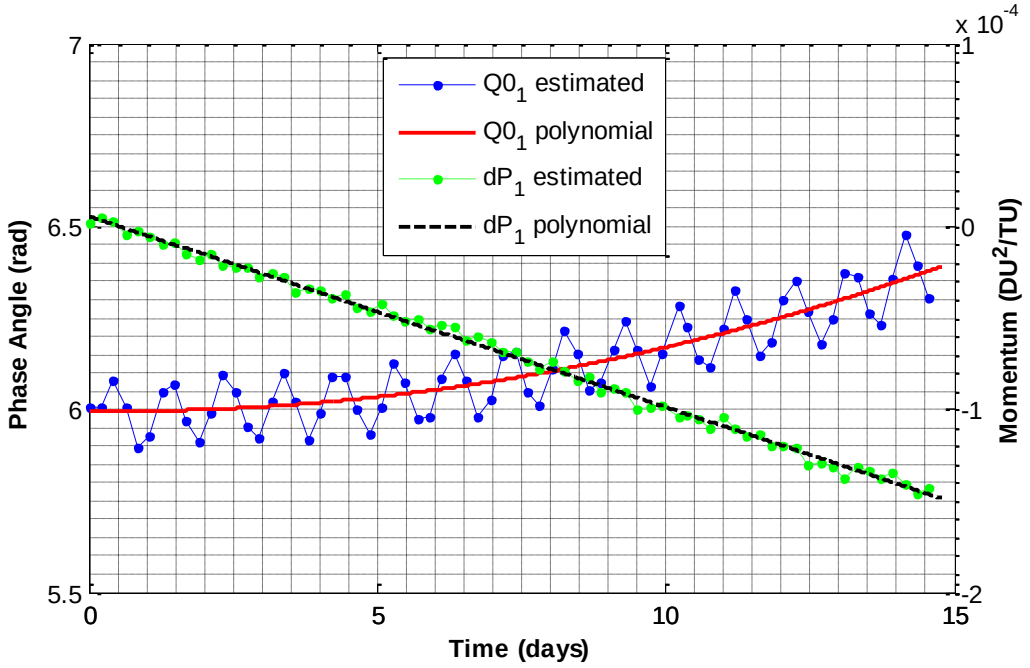

Figure 61. Polynomial approximations of $Q0_1$ and dP_1 from Bayes filtered batches of 300 observations.

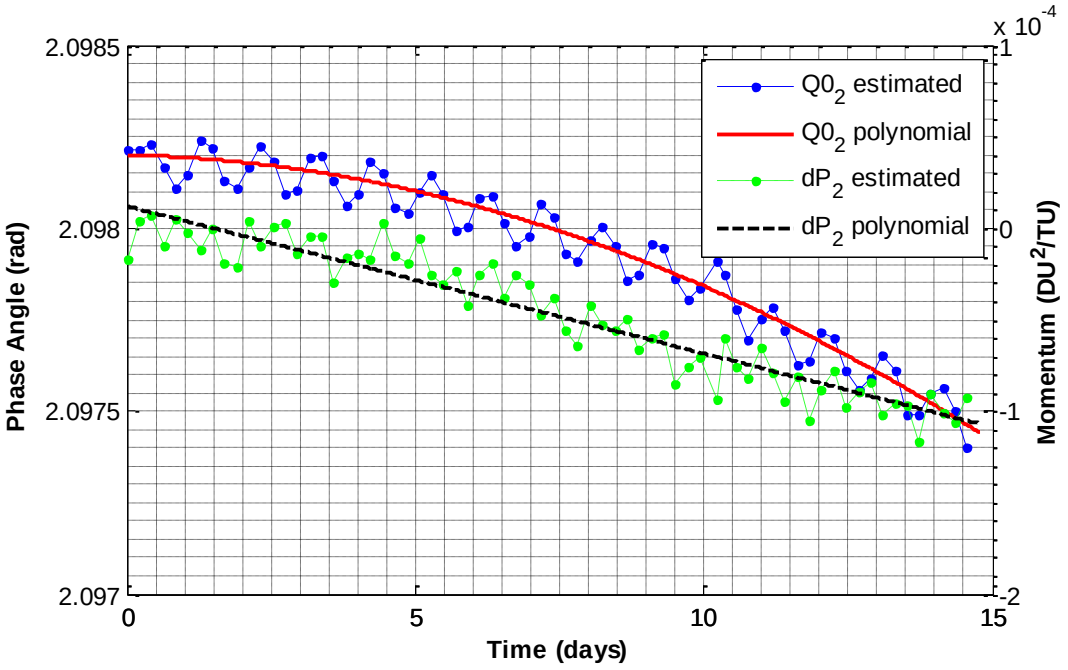

Figure 62. Polynomial approximations of $Q0_2$ and dP_2 from Bayes filtered batches of 300 observations.

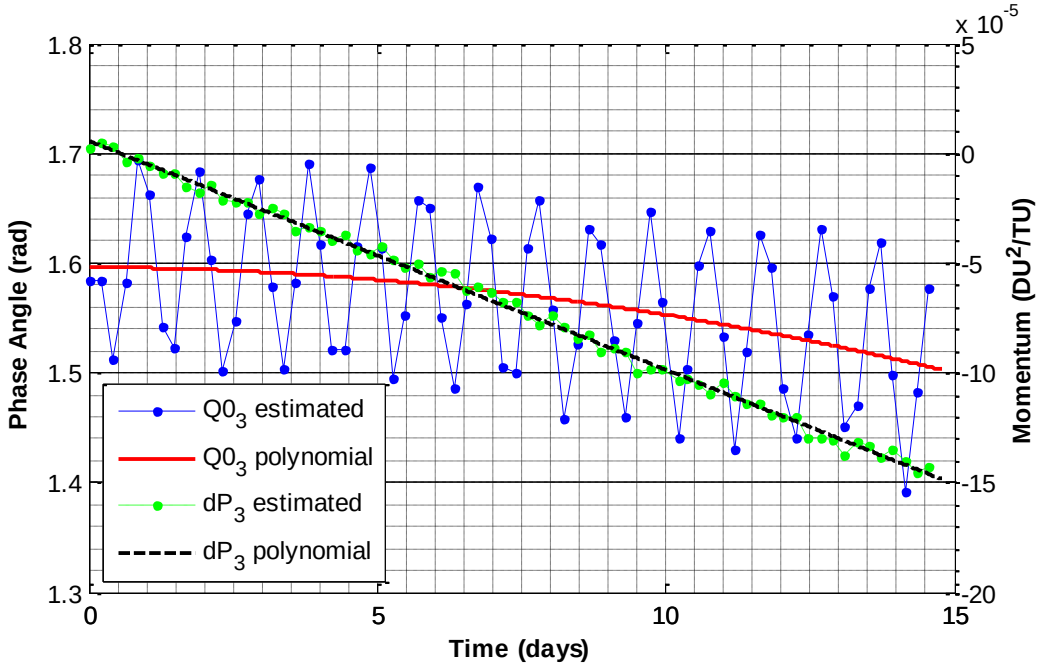

Figure 63. Polynomial approximations of $Q0_3$ and dP_3 from Bayes filtered batches of 300 observations.

As before, the pseudo-stochastic parameters were used to generate stochastic predictions from the reference torus. All 42,000 observations, including the first 21,000 that were used during the estimation process, were compared to the torus prediction. The last 21,000 observations are used to simulate the torus' ability to predict in real time since the data were not processed previously by the Bayes filter. Figure 64 shows the residuals for the full 42,000 observations with the exact same deterioration characteristics as seen previously. Prior to the degradation in the prediction at 18.5 days, the RMS residuals for coordinates x, y and z are 2.606, 2.617, and 2.456 kilometers, respectively. These are only slightly worse than those found with batches of 1,000 observations.

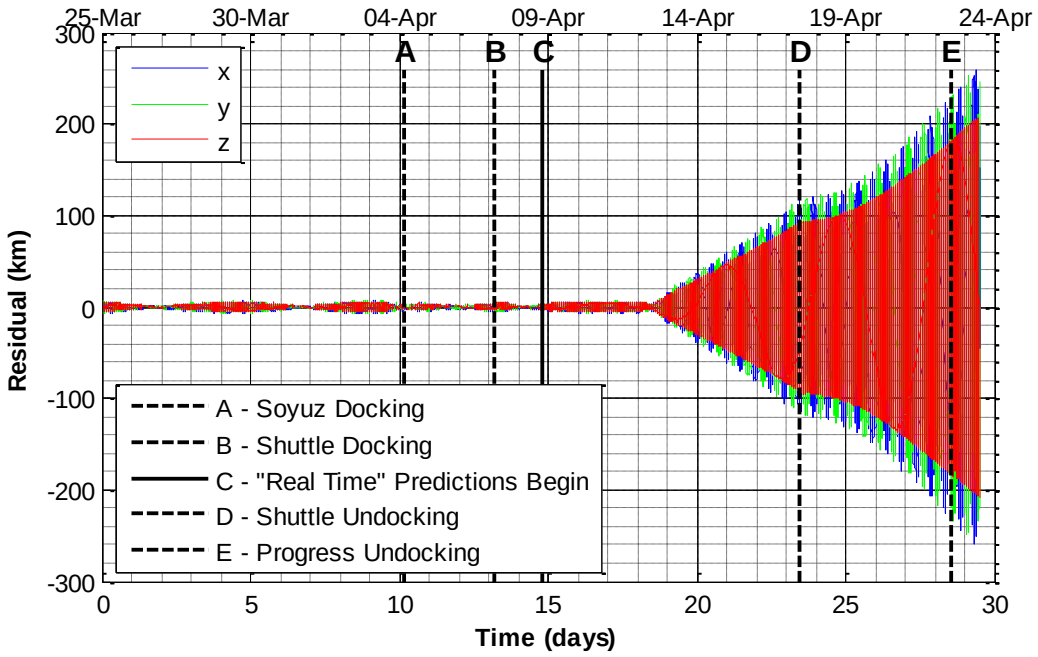

Figure 64. Residuals generated using pseudo-stochastic parameters estimated from batches of 300 observations.

For thoroughness, the last set of 21,000 observations were also run through the Bayes filter to estimate what the pseudo-stochastic parameters should have been and compare those to the curves generated from the first set of 21,000 observations. In doing so, the same trends appear as before with 1,000 observations per batch. Figure 65 - Figure 67 show that the polynomials fit the estimates fairly well until April 12 when the predictions degenerated. A clear jump is observed in the momenta offsets at the times of interest, indicating that the batch size likely has nothing to do with the anomalies. This further supports the hypothesis that drag changes shifted the ISS onto an adjacent torus trajectory that was not modeled.

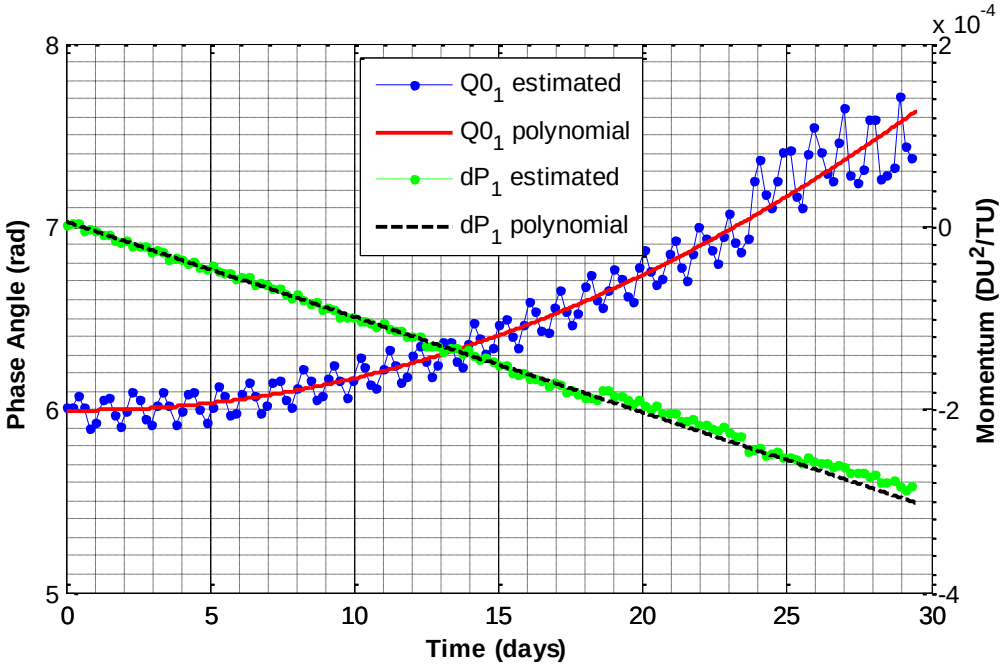

Figure 65. Estimates of dP_1 from Bayes filtered batches of 300 observations show a slight offset from the polynomial approximations at times of interest.

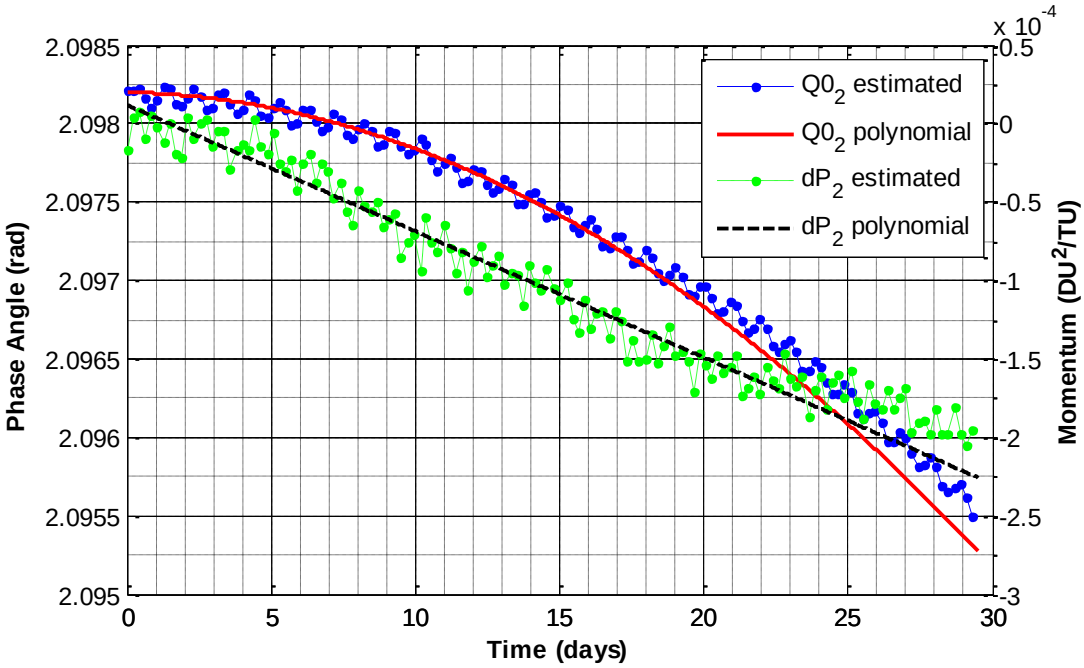

Figure 66. Estimates of dP_2 from Bayes filtered batches of 300 observations show a slight offset from the polynomial approximations at times of interest.

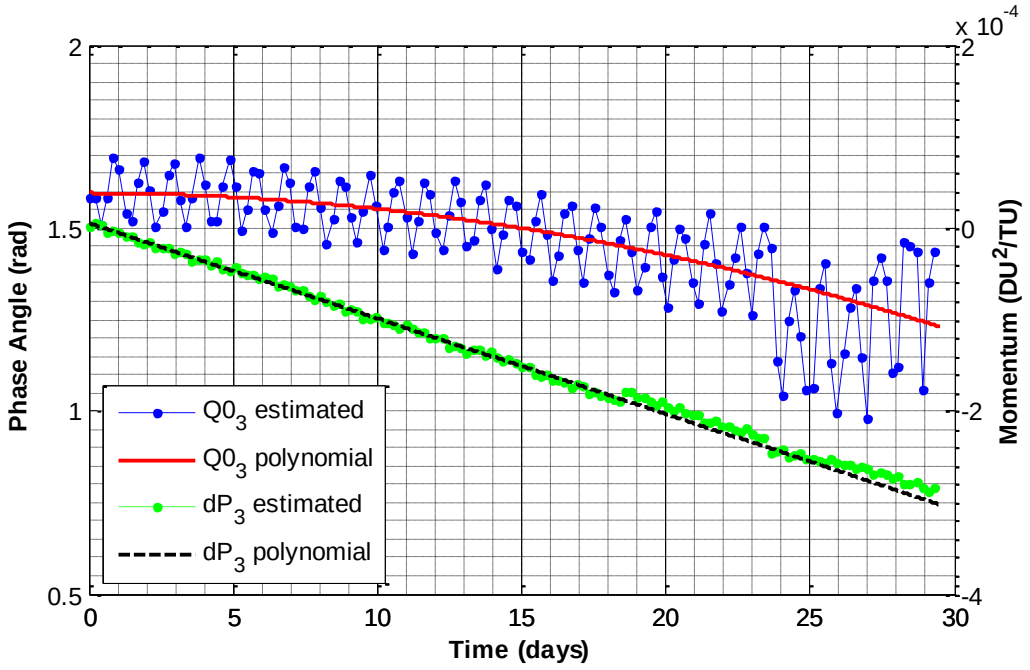

Figure 67. Estimates of dP_3 from Bayes filtered batches of 300 observations show a slight offset from the polynomial approximations at times of interest.

4.3.2.3 Estimations and Predictions: Batches of 100 Observations

The ensuing results are produced from batches of 100 observations which translate to a little more than a full orbit. As an assurance that the data was processed correctly by the pre-filter, NLS and Bayes filter, results from the first two batches will be presented in addition to the full string of 210 batches required to process the nearly 2-weeks of ISS data at 100 observations per batch.

The first batch of data was processed by the NLS since a priori data was not available. Prior to the first iteration of NLS, the residuals from the raw data are plotted in Figure 68 for monitoring the accuracy of the pre-filter. Figure 69 shows the residuals

after pre-filtration and Figure 70 shows the residuals after 10 iterations of NLS. The final RMS residuals for coordinates x, y and z are 104.95, 51.44, and 99.25 meters, respectively.

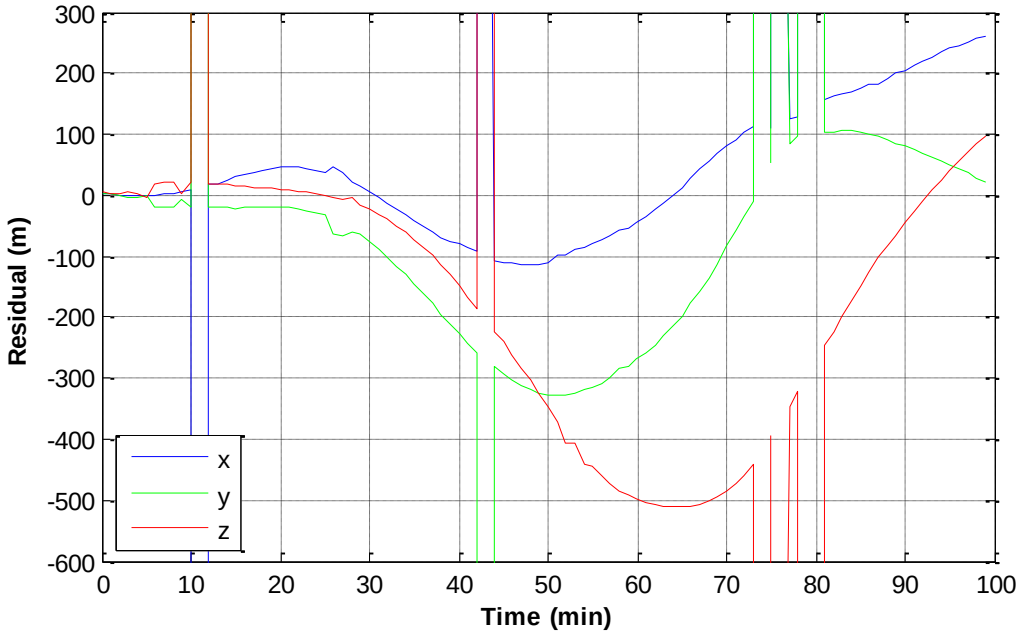

Figure 68. Residuals from first set of 100 observations prior to pre-filter and NLS.

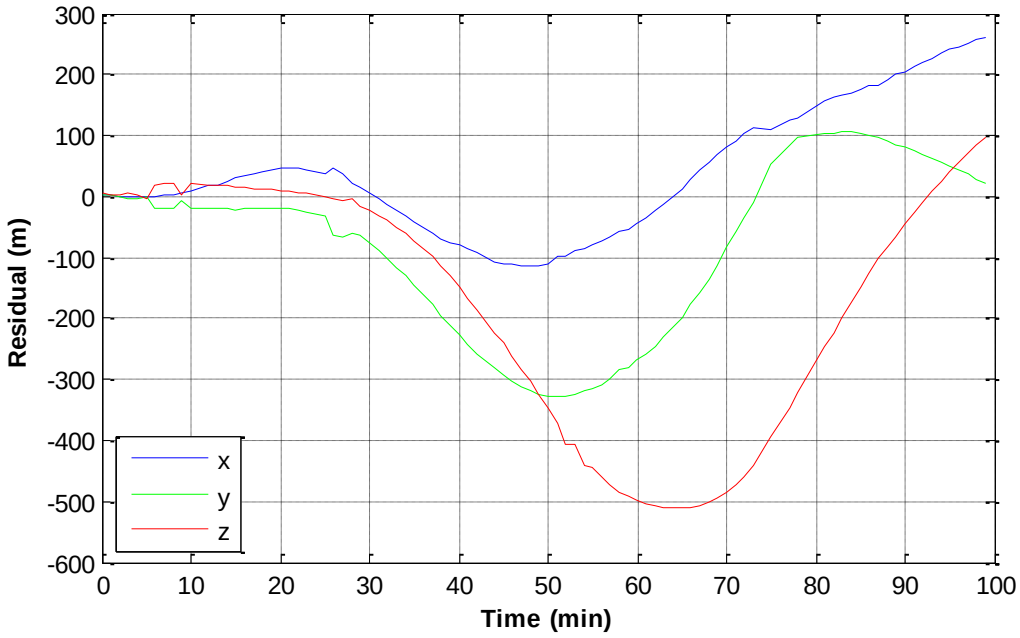

Figure 69. Pre-filtered residuals from first set of 100 observations prior to NLS.

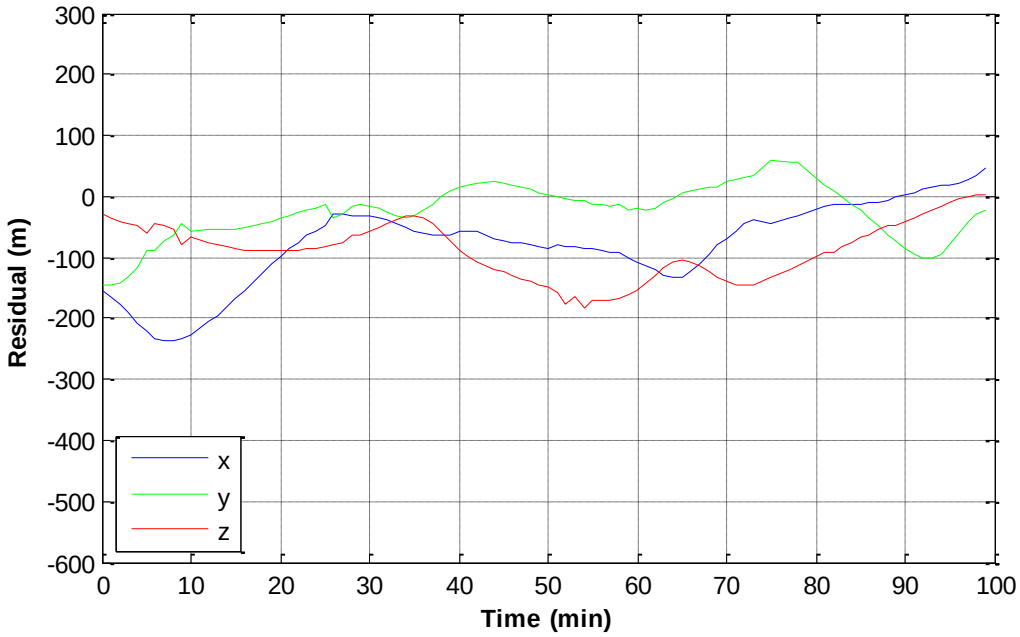

Figure 70. NLS filtered residuals from first set of 100 observations.

Subsequent batches (after the NLS batch) are processed by the Bayes filter. The residuals from the second batch of raw data are plotted in Figure 71 for monitoring the accuracy of the pre-filter prior to the first iteration of the Bayes filter. Figure 72 shows the residuals after pre-filtration and Figure 73 shows the residuals after 10 iterations of NLS. The final RMS residuals for coordinates x, y and z are 80.63, 68.75, and 97.30 meters, respectively.

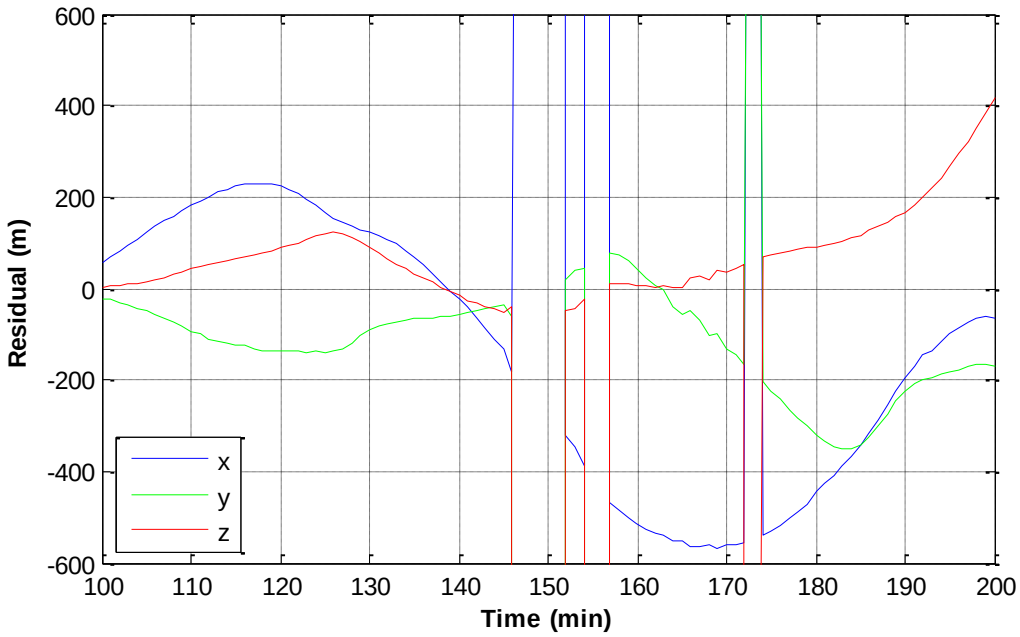

Figure 71. Residuals from second set of 100 observations prior to pre-filter and Bayes.

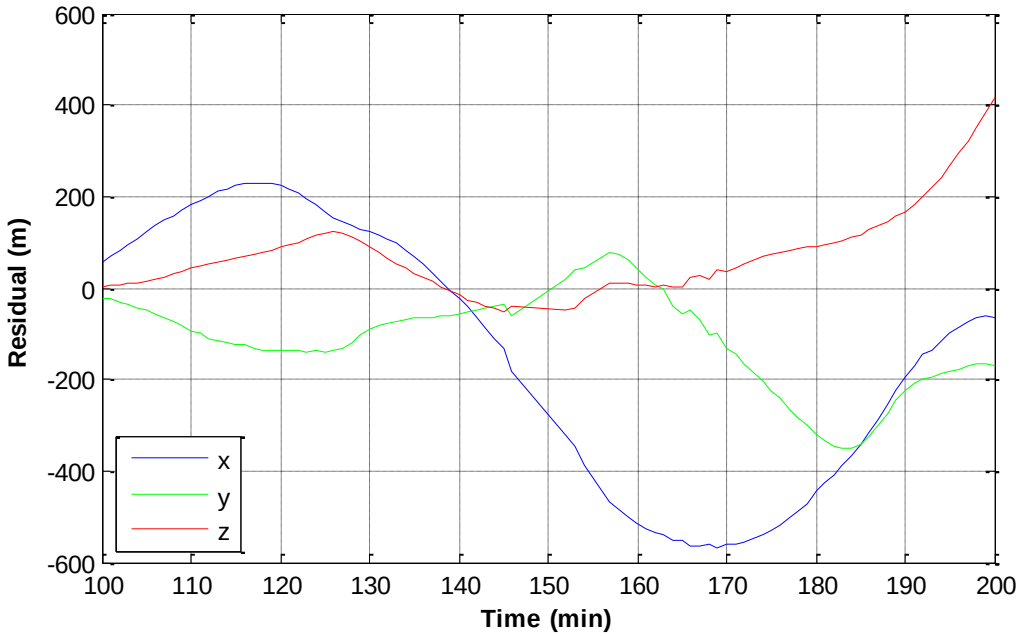

Figure 72. Pre-filtered residuals from second set of 100 observations prior to Bayes.

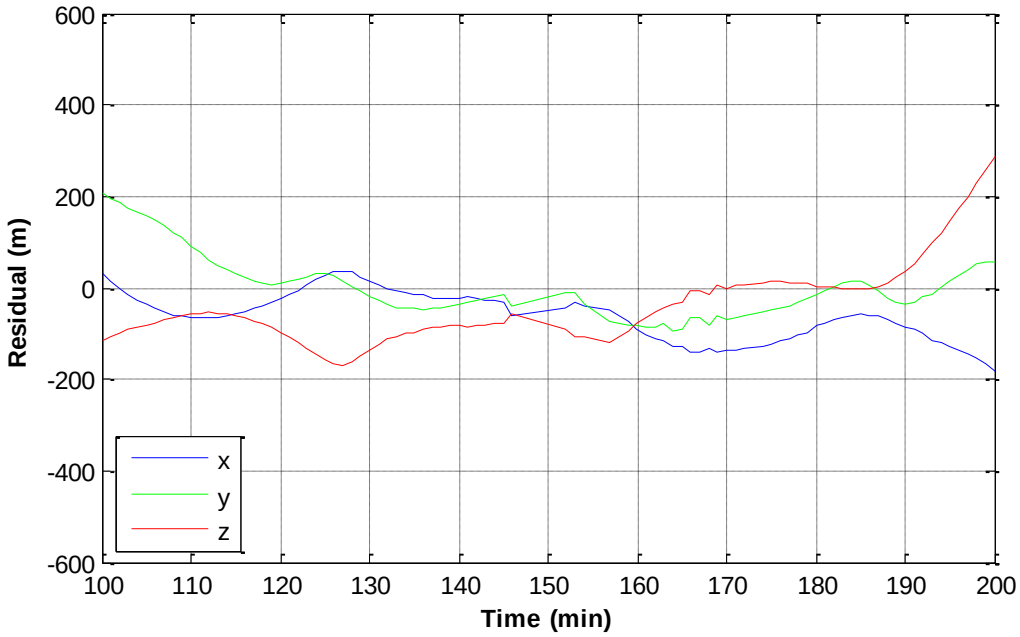

Figure 73. Bayes filtered residuals from second set of 100 observations.

A concatenation of the final residuals after 10 iterations from all 210 batches is shown in Figure 74. The RMS residuals for coordinates x, y and z are 180.42, 181.70, and 169.74 meters, respectively. The same is done for the reference torus corrections in Figure 75 - Figure 77 to show the change in the initial phase angles and momenta that best fit the data. The plots reveal a linear trend in the momenta and a periodicity in the phase angles as observed and discussed previously in §4.3.2.1.

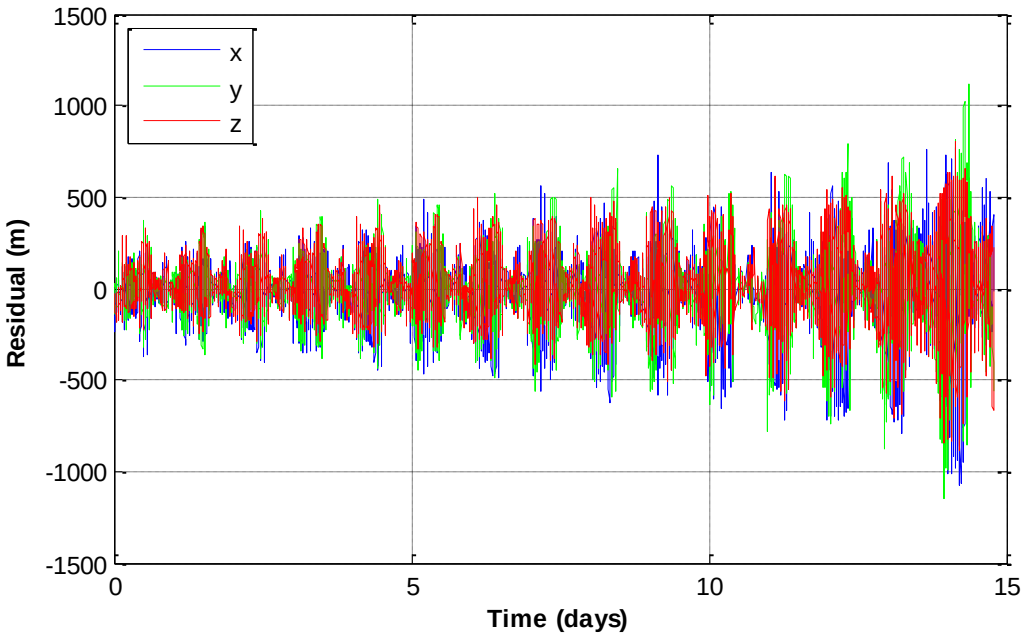

Figure 74. Bayes filtered residuals from batches of 100 observations.

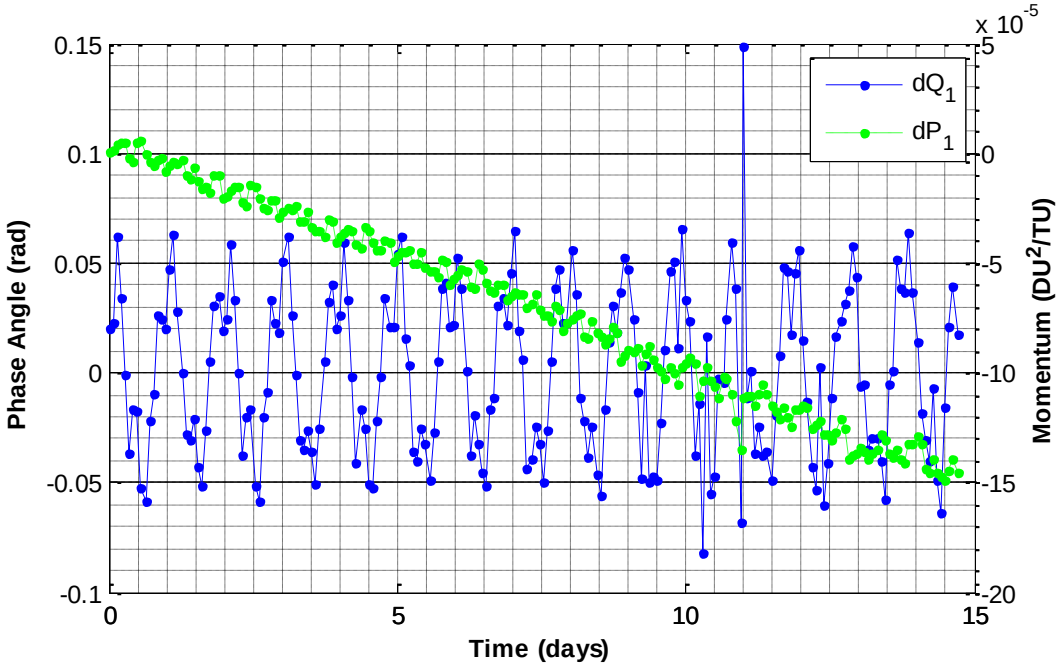

Figure 75. dQ_1 and dP_1 torus corrections from Bayes filtered batches of 100 observations.

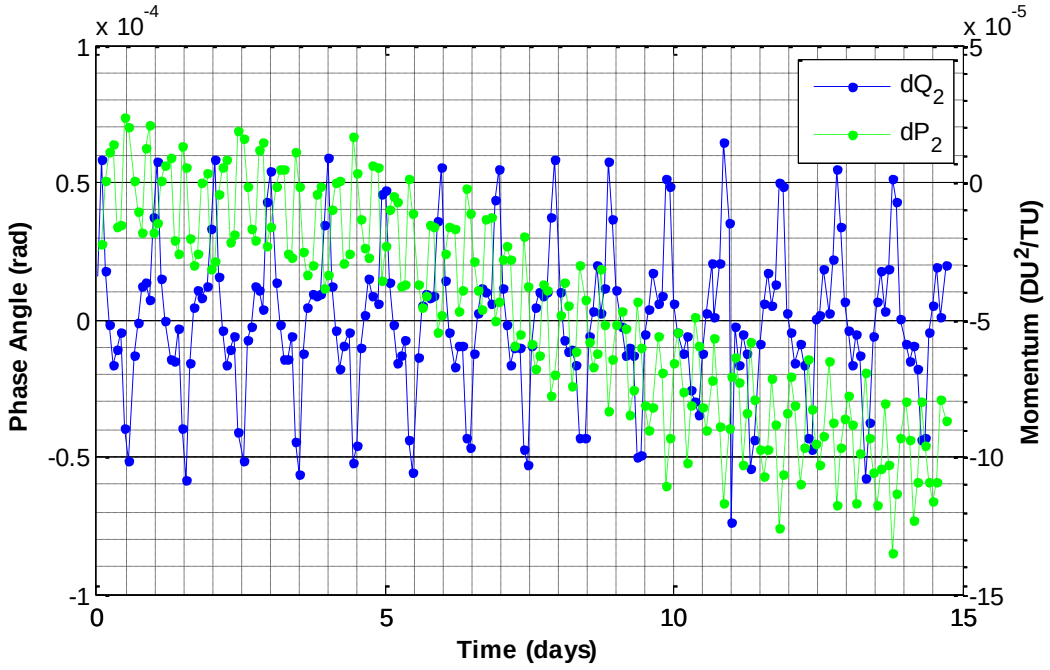

Figure 76. dQ_2 and dP_2 torus corrections from Bayes filtered batches of 100 observations.

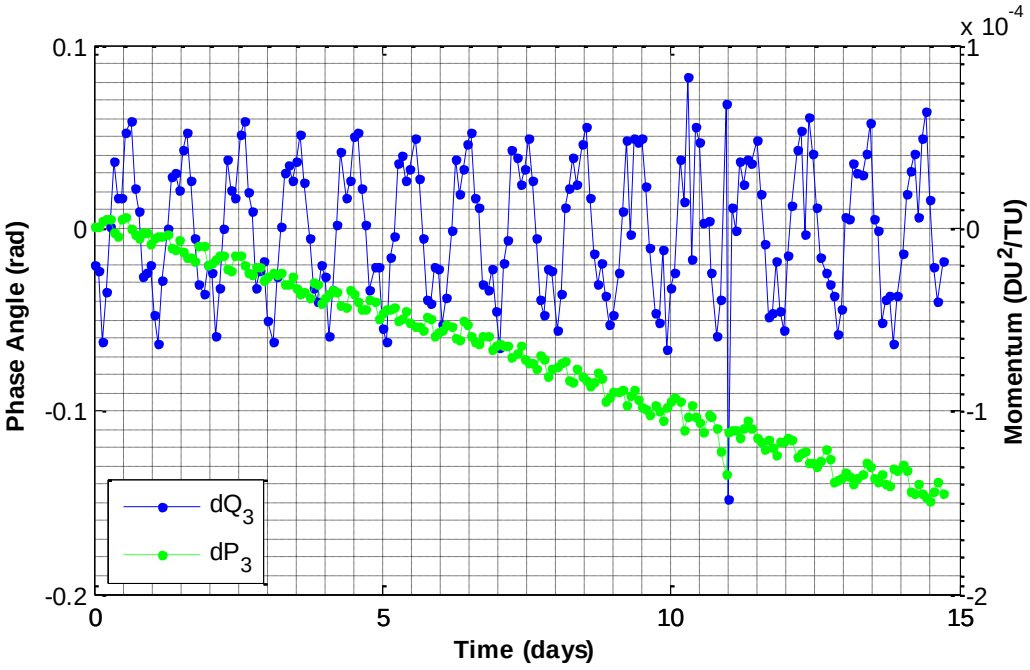

Figure 77. dQ_3 and dP_3 torus corrections from Bayes filtered batches of 100 observations.

After accumulating the updates to $\overrightarrow{\boldsymbol{Q_0}}$ from (172), a polynomial of degree two was fit to the data. Similarly, a polynomial of degree one was fit to $\overrightarrow{\boldsymbol{\delta P}}$ as shown in Figure 78 - Figure 80.

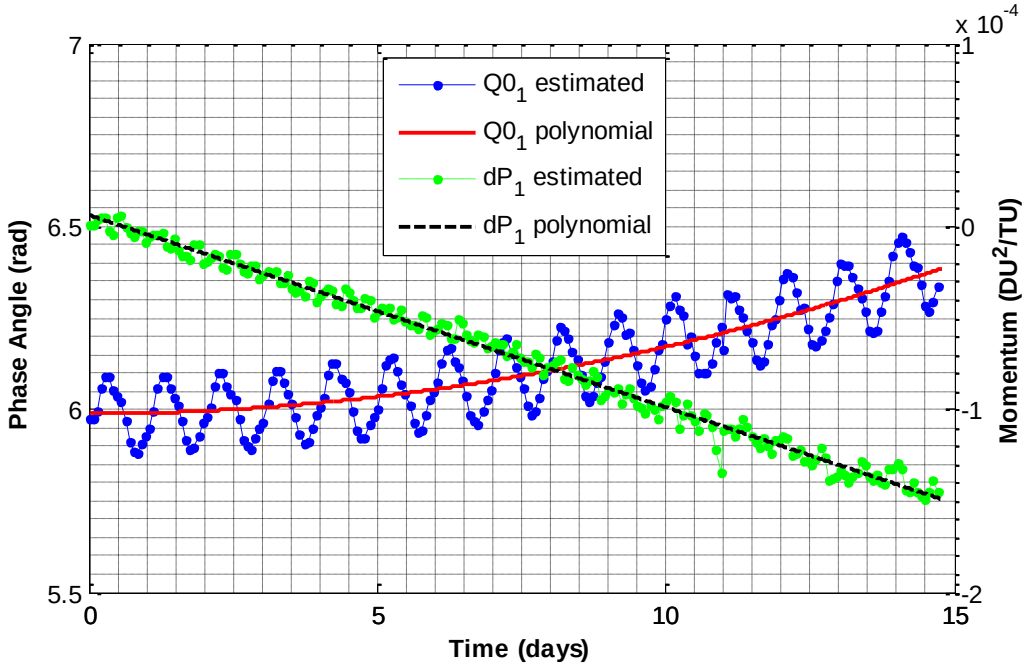

Figure 78. Polynomial approximations of $Q0_1$ and dP_1 from Bayes filtered batches of 100 observations.

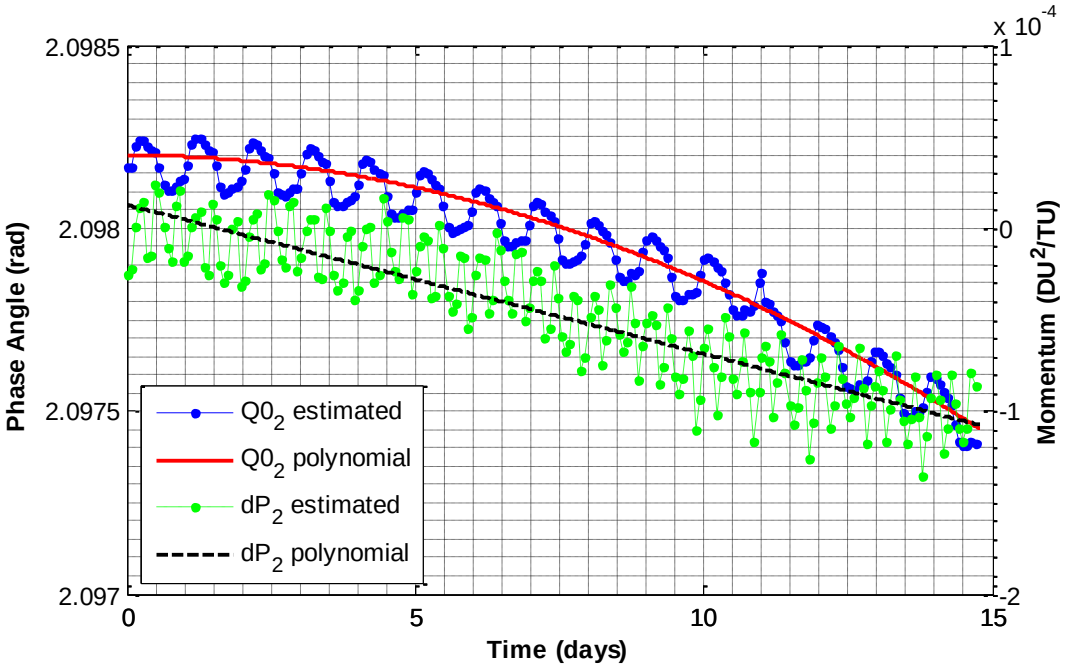

Figure 79. Polynomial approximations of $Q0_2$ and dP_2 from Bayes filtered batches of 100 observations.

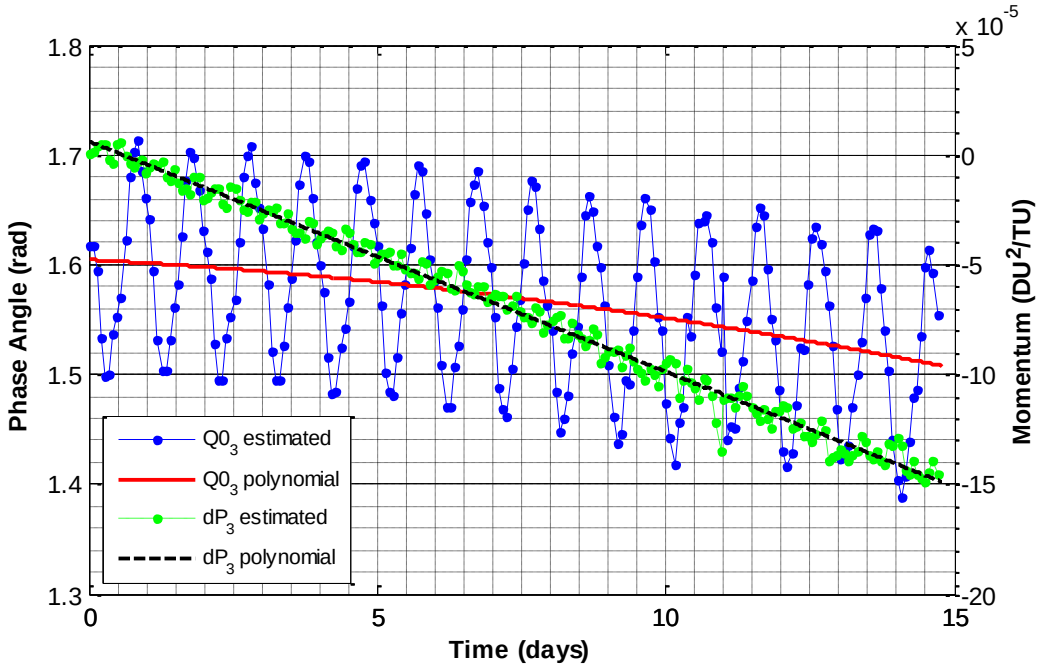

Figure 80. Polynomial approximations of $Q0_3$ and dP_3 from Bayes filtered batches of 100 observations.

As before, the pseudo-stochastic parameters were used to generate stochastic predictions from the reference torus. All 42,000 observations, including the first 21,000 that were used during the estimation process, were compared to the torus prediction. The last 21,000 observations are used to simulate the torus' ability to predict in real time since the data were not processed previously by the Bayes filter. Figure 81 shows the residuals for the full 42,000 observations with the exact same deterioration characteristics as seen previously. Prior to the degradation in the prediction at 18.5 days, the RMS residuals for coordinates x, y and z are 2.789, 2.800, and 2.643 kilometers, respectively. These are slightly worse than those found with batches of 300 and 1,000 observations.

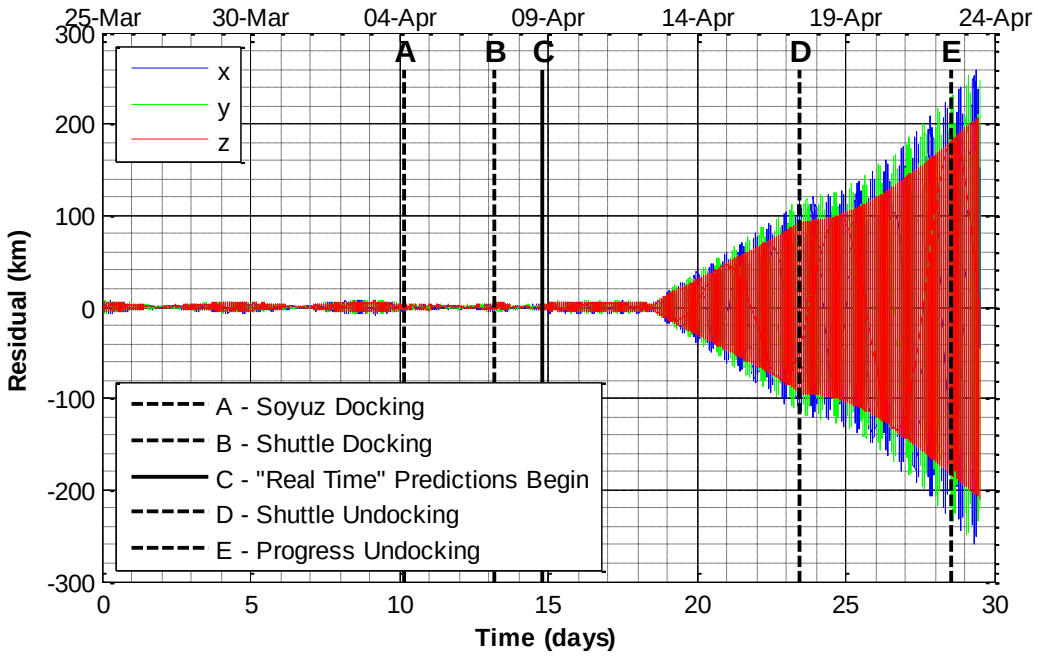

Figure 81. Residuals generated using pseudo-stochastic parameters estimated from batches of 100 observations.

For thoroughness, the last set of 21,000 observations were also run through the Bayes filter to estimate what the pseudo-stochastic parameters should have been and compare those to the curves generated from the first set of 21,000 observations. In doing so, the same trends appear as before with 300 and 1,000 observations per batch. Figure 82 - Figure 84 show that the polynomials fit the estimates fairly well until April 12 when the predictions degenerated. A clear jump is observed in the momenta offsets at the times of interest, further supporting the hypothesis that drag changes shifted the ISS onto an adjacent torus trajectory that was not modeled.

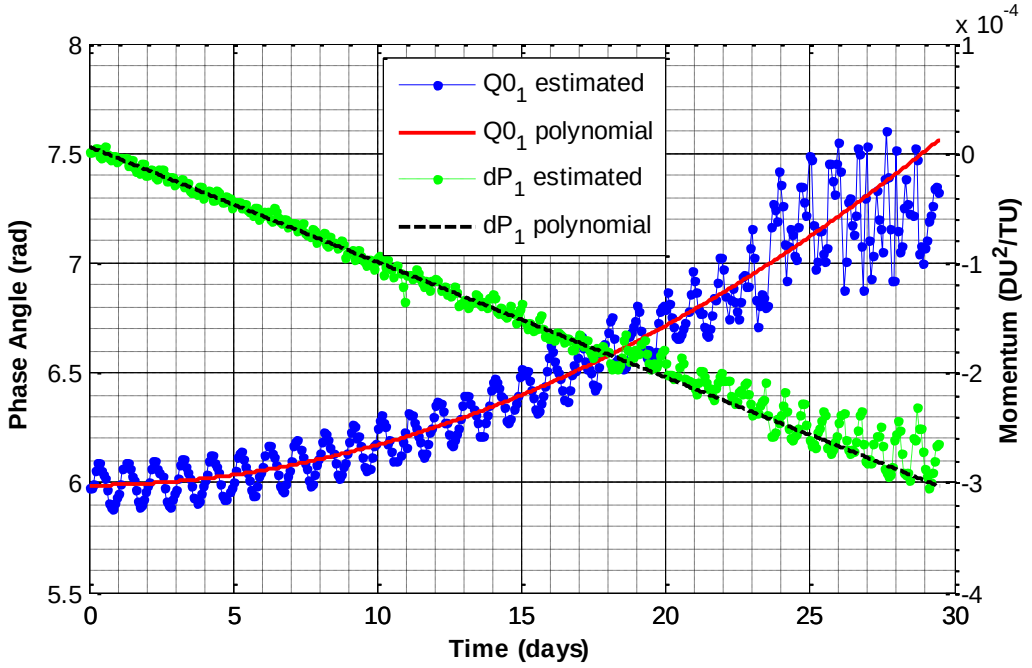

Figure 82. Estimates of dP_1 from Bayes filtered batches of 100 observations show a slight offset from the polynomial approximations at times of interest.

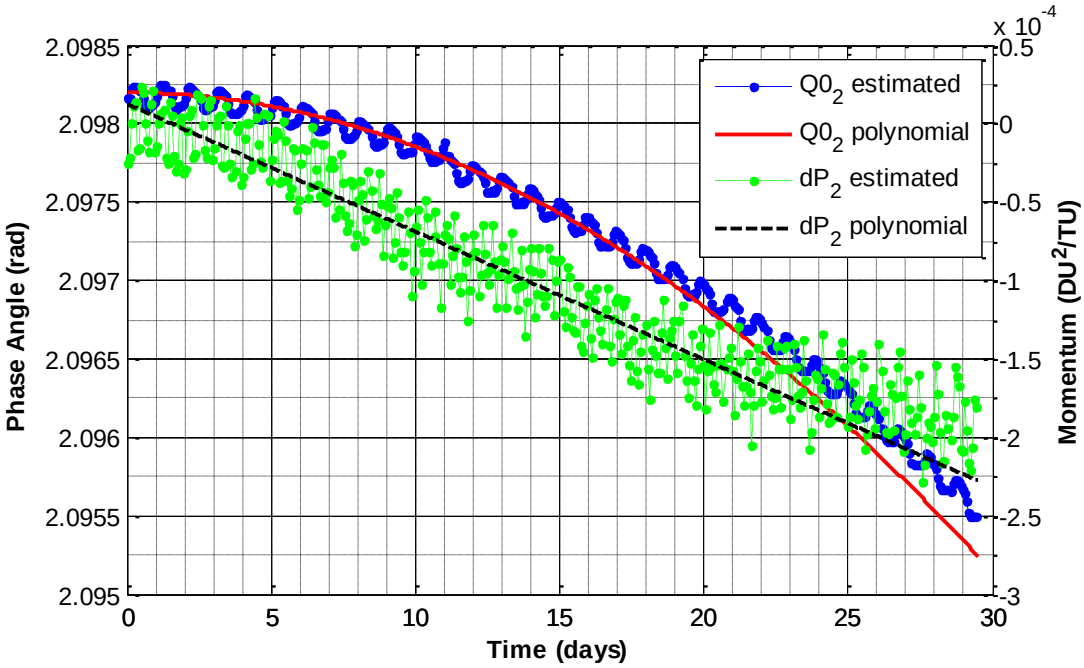

Figure 83. Estimates of dP_2 from Bayes filtered batches of 100 observations show a slight offset from the polynomial approximations at times of interest.

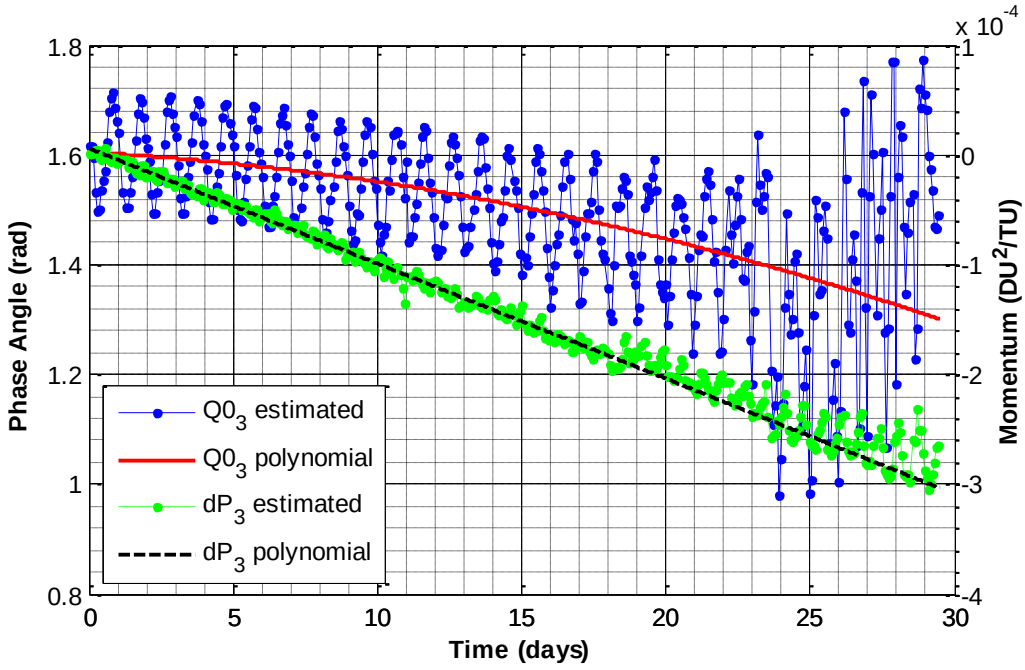

Figure 84. Estimates of dP_3 from Bayes filtered batches of 100 observations show a slight offset from the polynomial approximations at times of interest.

V. Conclusions and Recommendations

The underlying motivation for this research was to improve space situational awareness by extending KAM theorem's efficacy to stochastic orbit prediction. The results are conclusive. Most stochastic effects in LEO can be modeled to fit and predict a satellite's motion near a reference torus. The geometric construal of the satellite path suggests a flexing annulus of concentric, continuous tori about which the satellite may circumnavigate systematically.

5.1 Torus Construction

The Fourier decomposition of the integrated trajectory using Laskar's NAFF worked reasonably well to map $(x, v) \rightarrow (\mathrm{Q}, P)$; however, significant issues must be overcome to perfectly identify the fundamental frequencies. Even a faintly flawed basis set is enough to distort the Laskar process when picking off spectral amplitudes. This is believed to have been the cause of the inherent errors in the ISS reference that grew periodically to roughly 80 meters within the first six months.

As mentioned in §4.1, the most likely reason for the wrong frequencies is that the ten most prominent spectral lines used for the least squares solution were associated with the wrong j-index label. The most prominent peaks are not centered about $\omega_{n,0,1} = \vec{\boldsymbol{\Omega}} \cdot (\boldsymbol{n}, \mathbf{0}, \mathbf{1})^{\boldsymbol{T}}$ in the z coordinate, but instead are centered about $\omega_{n,0,n} = \vec{\boldsymbol{\Omega}} \cdot (\boldsymbol{n}, \mathbf{0}, \boldsymbol{n})^{\boldsymbol{T}}$. Nevertheless, these inconsistencies in the torus-construction machinery still provided a reference torus that was good enough to proceed with the stochastic estimation process – a testament of KAM theory's tractability even without an exact basis set.

If KAM theory is to find a place in the mainstream of orbital sciences, the procedures for generating tori must be improved so that they may be autonomously generated from space surveillance data with limited human involvement. The current state of the art requires extensive human massaging and tweaking that would make it impractical as an application for hundreds of thousands of earth orbiting objects. Nevertheless, it is the belief of this author along with all those who toil in this field, that it is possible, perhaps within this decade.

5.2 Stochastic Predictions

In this present work as in that by Little, low earth orbits have exhibited perturbations that cannot be modeled by a purely deterministic, static torus. If a non-chaotic earth orbit is occupied, the phase space will be filled with a dense continuum of flexing, persisting tori. The presence of large perturbations tends to distort local tori, forcing the satellite to migrate from one torus to another. Even still, the results from §4.3 showed that it is possible to forecast motion in the vicinity of a reference torus when the right conditions are met.

Modeling the non-periodic motion about the reference torus is largely contingent upon the pseudo-stochastic parameters. The low eccentricity of the ISS made it difficult to estimate the torus coordinate offsets since the Keplarian and apsidal coordinates opposed one another in a sinusoidal manner. Curve-fits of the parameters were still possible, but they suffered from immediate limitations in accuracy. The batch size had a slight impact on the accuracy; larger batches provide better results, but it is not clear to

what extent size matters. A more thorough review would be required with varied observation intervals.

Another cause for errors in the non-periodic motion is a rapid shift in the drag environment or surface area. These changes require larger offsets in the pseudo-stochastic parameters than are modeled during the estimation process.

In the end, the difficulties encountered are minor compared to the incredible feat of modeling the largest earth orbiting satellite in excess of 18 days with RMS residuals bounded near 2 km – quite the contrast from the results that showed the static torus' residuals grow unbounded to 3,000 km in the same time. The real value of these results cannot be known without a direct comparison to a "full-up" numerical propagator that includes the same high-order gravity field, a sophisticated atmosphere model with real solar characteristics, the complete solar and lunar ephemerides, and solar radiation pressure. This recommendation, left for the next section, would indicate if and how KAM theory improves the current state of the art. With the present low-eccentricity problem, it is expected that the full-up integrator will be more accurate in the short term (perhaps 10s or 100s of meters in total RMS from the true orbit), but the stochastic predictions from the KAM torus may rival the propagator in the long term as the full-up propagator diverges from reality.

Additional research will be required to confirm these findings and improvements in accuracy will be required before KAM theory can be relied upon for high priority assets such as the ISS. This does not preclude its immediate testing on debris orbits and low

priority assets which could extend the length of time between reacquisition by tracking systems.

5.3 Recommendations for Future Research

The first goal of future efforts should be an improvement to the automation process for finding fundamental frequencies from the trajectory-following method. Once it proves successful on a handful of numerically integrated orbits, a full 3-dimensional matrix of orbits with different eccentricities, altitudes, and inclinations ought to be assembled from real satellite ephemerides and batch processed to test the reliability of the Fourier analysis.

Another major hurdle that must be overcome is the low eccentricity problem encountered here and by Craft. As it relates to stochastic predictions, it may be possible to improve the polynomial functions and reduce sinusoidal behavior in the Keplarian and apsidal coordinates by iterating on the polynomial production process. After the first polynomial is generated, the Bayes filtration process could be repeated with initial torus offsets generated by the previous polynomial approximations. This procedure may be iterated upon until the polynomials are smooth.

The Bayes filter provided reasonable results using linearized two-body dynamics, but it may be worthwhile to explore an expansion of the equations of motion to include the moon, sun, and air drag. The current fitting process attempts to account for all of these nonconservative perturbations by lumping them into one set of all-inclusive pseudo-stochastic parameters. Better results may be obtained by isolating the parallel and perpendicular contributions from each source and proceeding to make stochastic

predictions from multiple sets of pseudo-stochastic parameters. This does not mean that the current dynamics model should be immediately discarded, though. It is quite possible that some orbits (such as those at higher LEO where air density is reduced) will fare very well with the simplified equations employed here.

As it relates to the first recommendation, observational data ought to be obtained from a vast assortment of satellite orbits and processed through a Bayesian filter—similar to the one established here or one improved by the previous recommendations. Predictions could then be generated for each of the satellites to determine the method's level of trustworthiness. Only then will it be certain that KAM theory can be applied effortlessly to the multitude of objects that must be tracked in earth orbits. The results from this study are simply not enough to guarantee the applicability of KAM theory for operational use. This study may also shed additional light on the impacts of solar events. Even though the present study showed deteriorations in predictions following a major solar storm, it may be possible to compensate for deleterious density changes by adjusting the pseudo-stochastic parameters in a predictable manner.

Finally, the results of this study indicate that the KAM torus can detect subtle changes in the thermosphere density. Since these changes are not easily observed in the osculating orbital elements or the native coordinates, KAM theory may offer an innovative approach for studying trends in the upper atmosphere from historical spacecraft ephemerides across a broader range of altitudes without the presence of specialized measurement devices.

Figure 85. A silhouette of the Space Shuttle Endeavor (STS-130) departing the ISS in which the backdrop depicts the lower layers of the earth's atmosphere. *Credit: NASA*

Appendix A

A.1 Identification of Power Spectral Frequency Combinations from 0 to 3 rad/TU

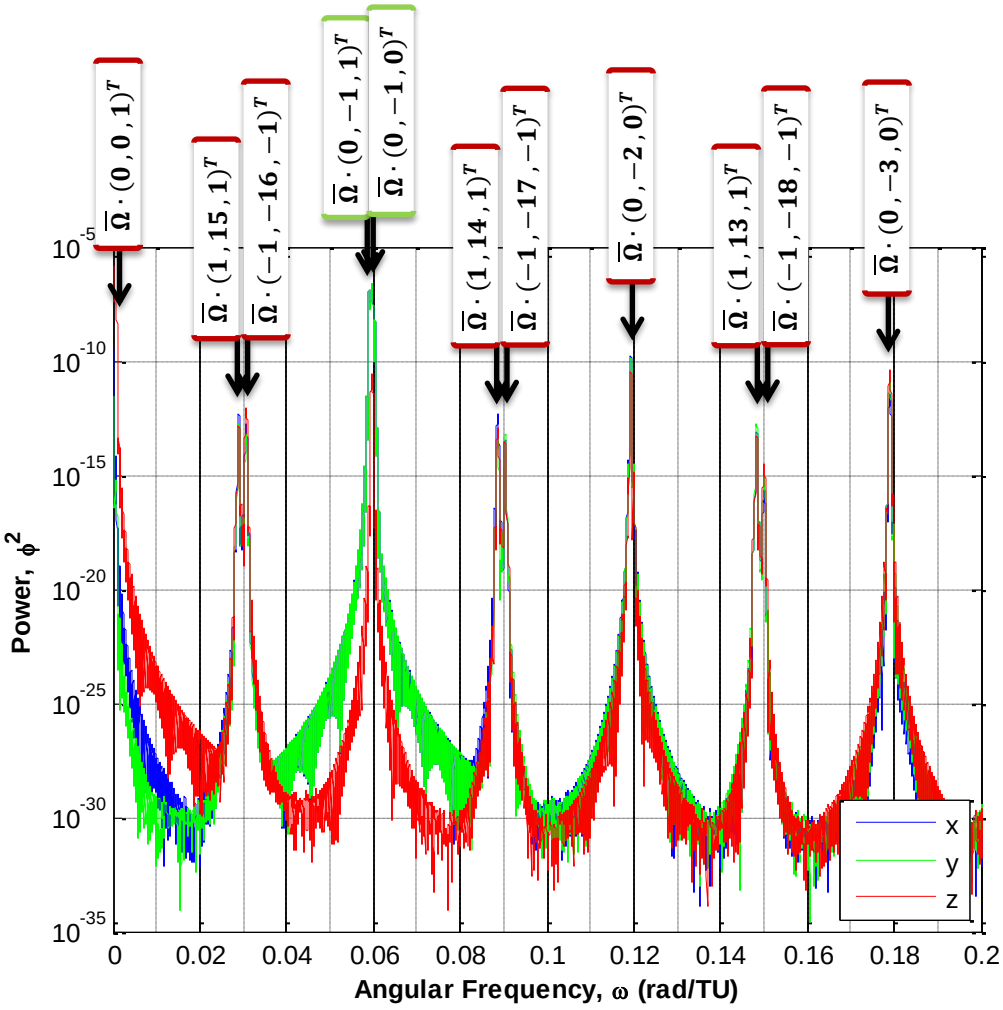

Figure 86. PSD plot identifying frequency combinations from [0, 0.2] rad/TU.

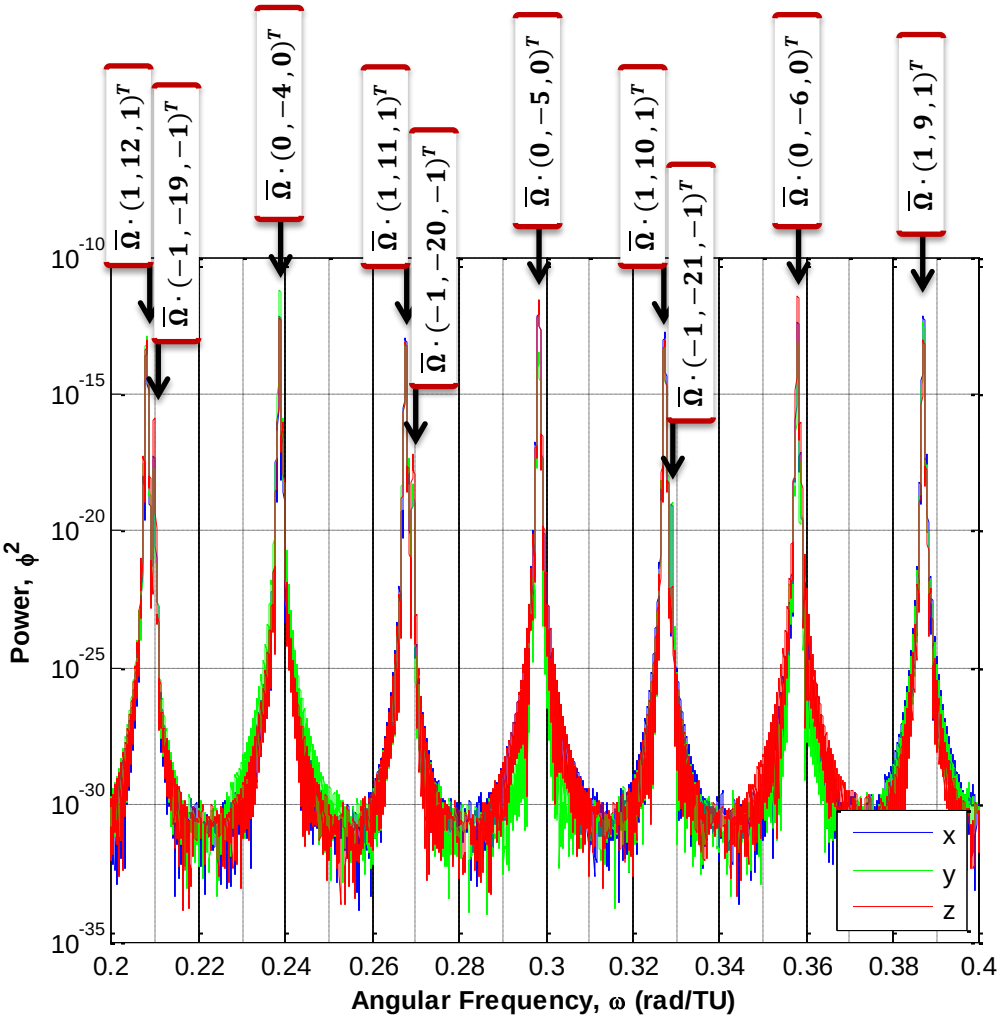

Figure 87. PSD plot identifying frequency combinations from [0.2, 0.4] rad/TU.

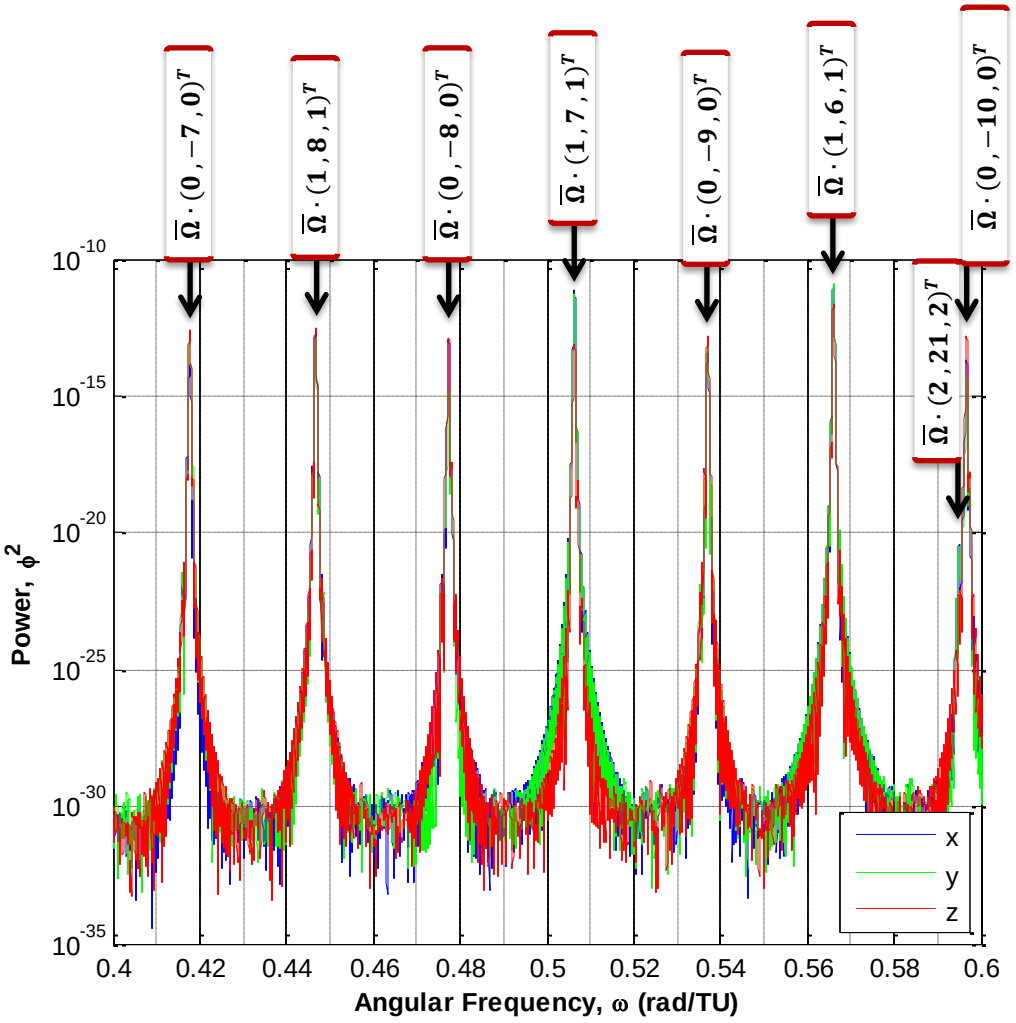

Figure 88. PSD plot identifying frequency combinations from [0.4, 0.6] rad/TU.

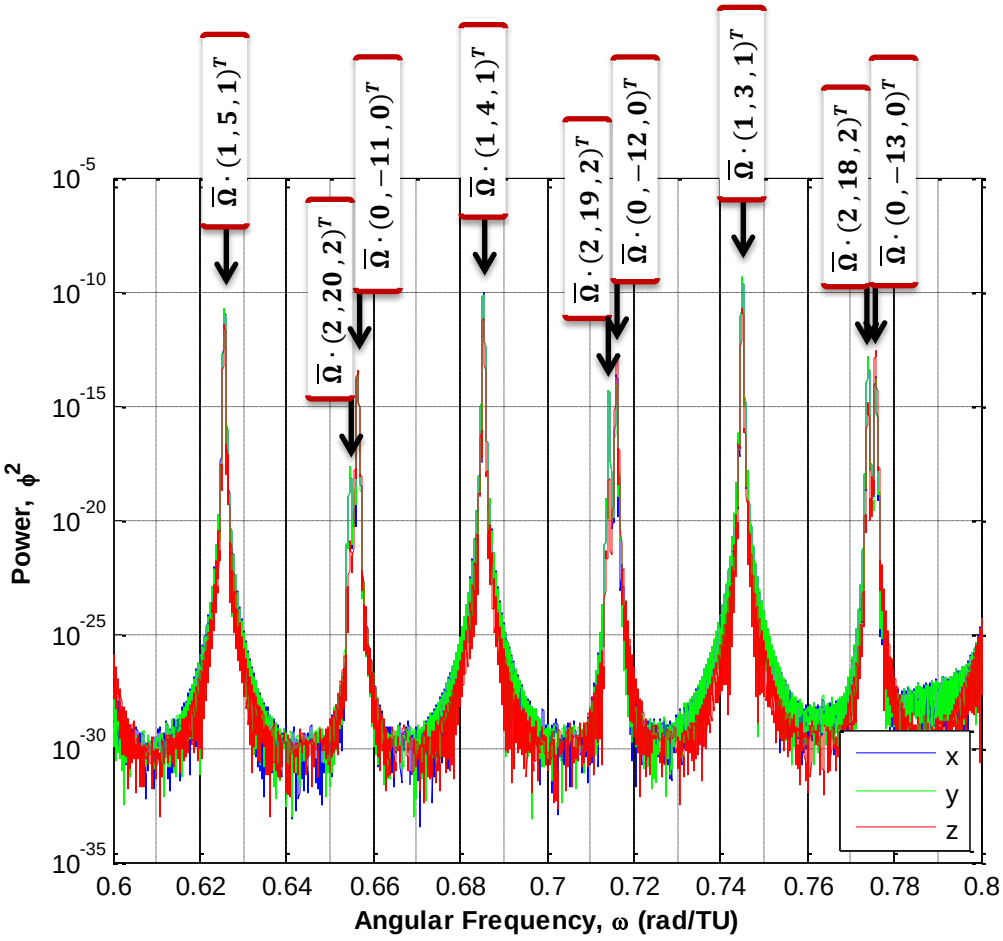

Figure 89. PSD plot identifying frequency combinations from [0.6, 0.8] rad/TU.

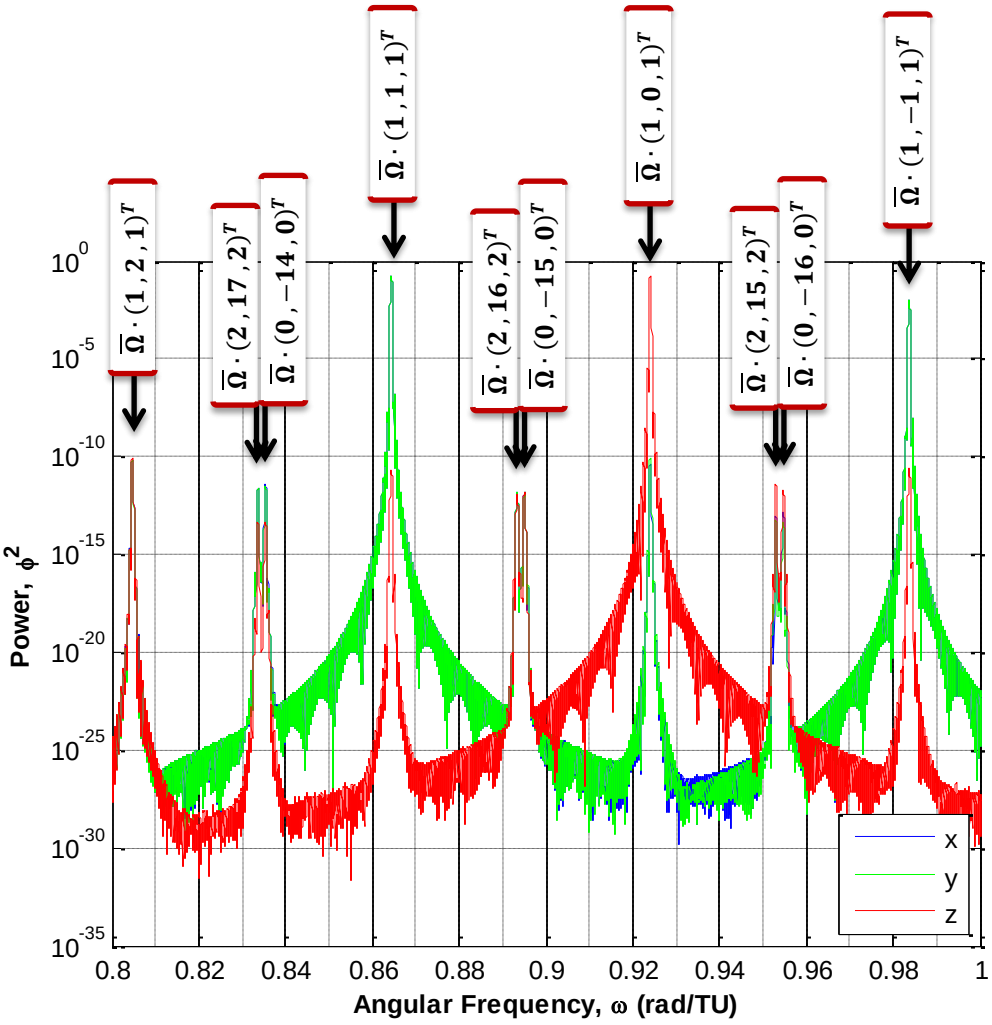

Figure 90. PSD plot identifying frequency combinations from [0.8, 1.0] rad/TU.

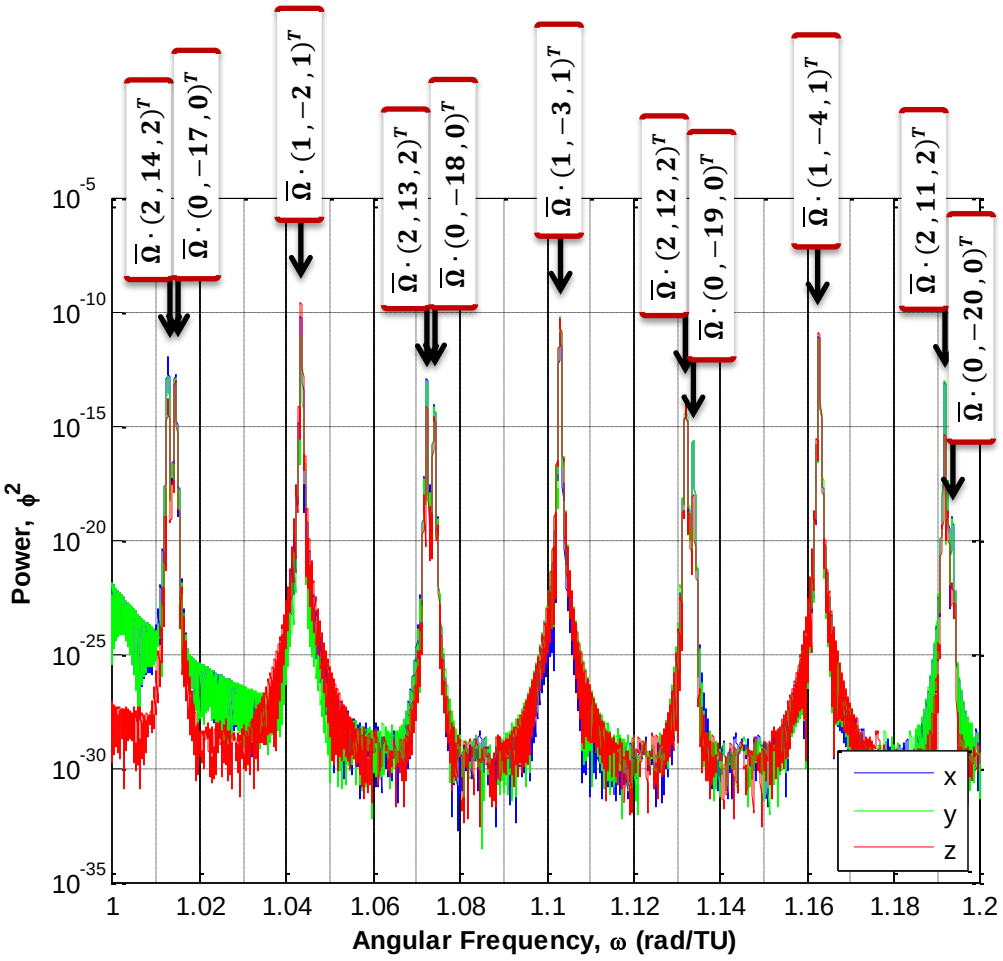

Figure 91. PSD plot identifying frequency combinations from [1.0, 1.2] rad/TU.

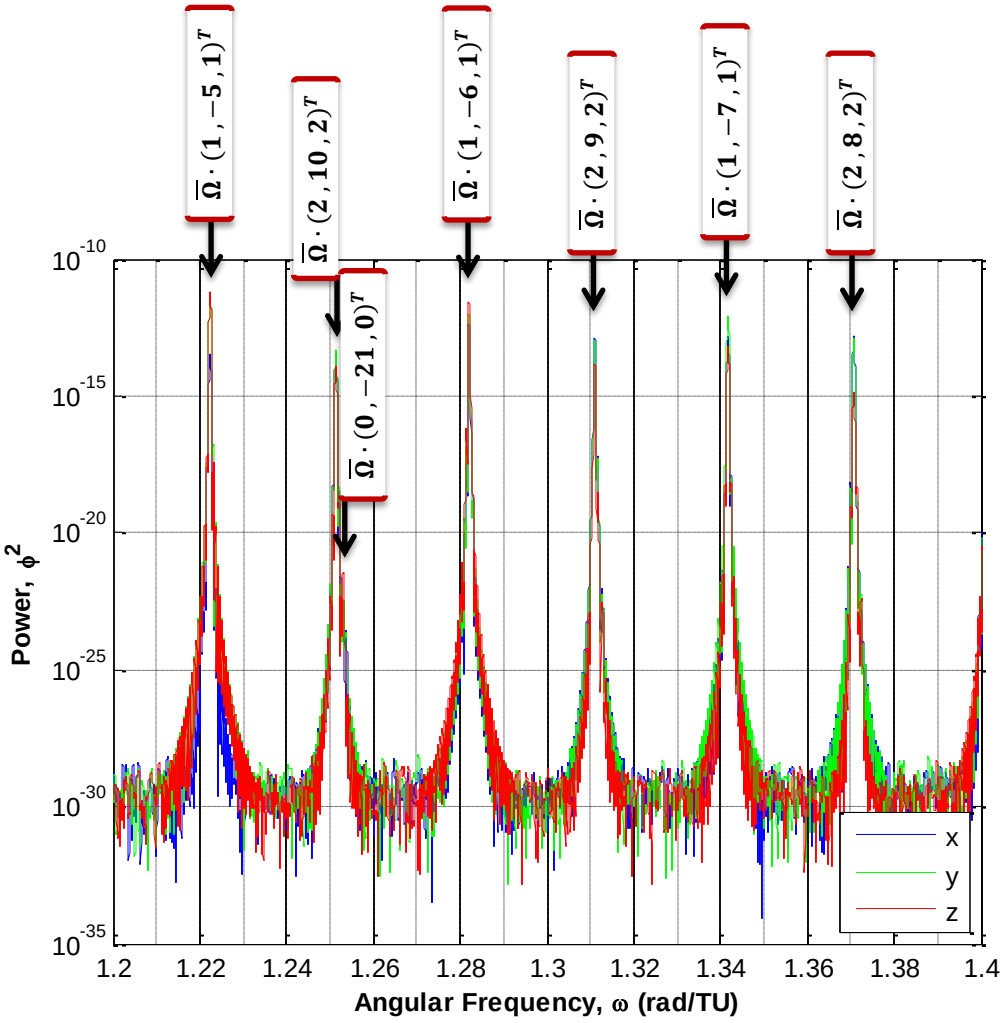

Figure 92. PSD plot identifying frequency combinations from [1.2, 1.4] rad/TU.

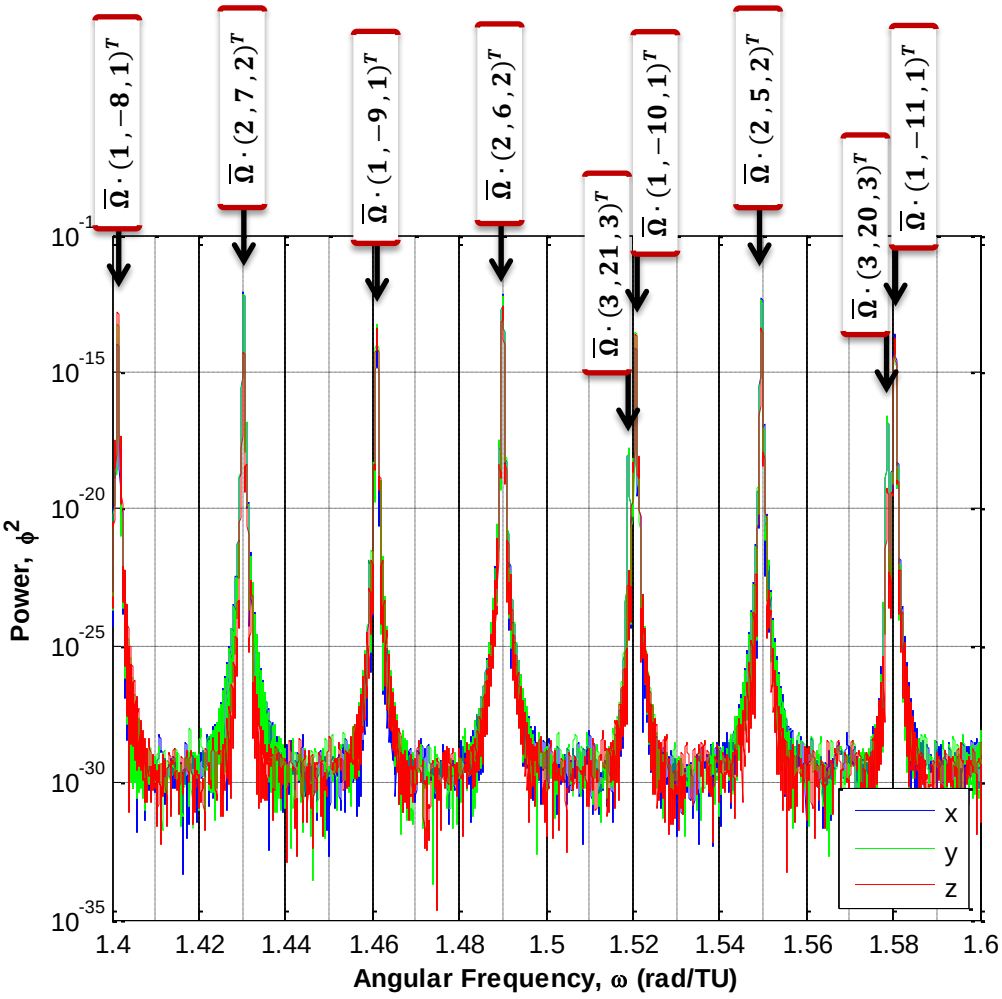

Figure 93. PSD plot identifying frequency combinations from [1.4, 1.6] rad/TU.

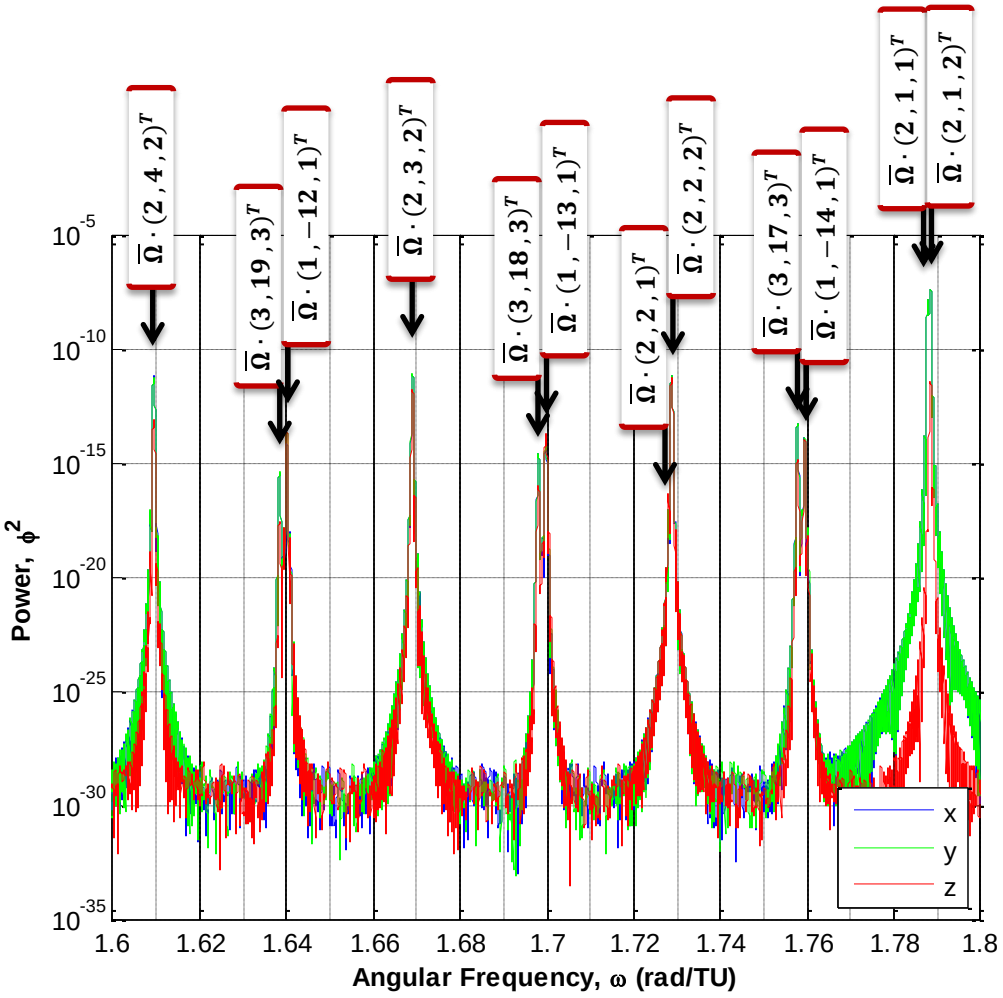

Figure 94. PSD plot identifying frequency combinations from [1.6, 1.8] rad/TU.

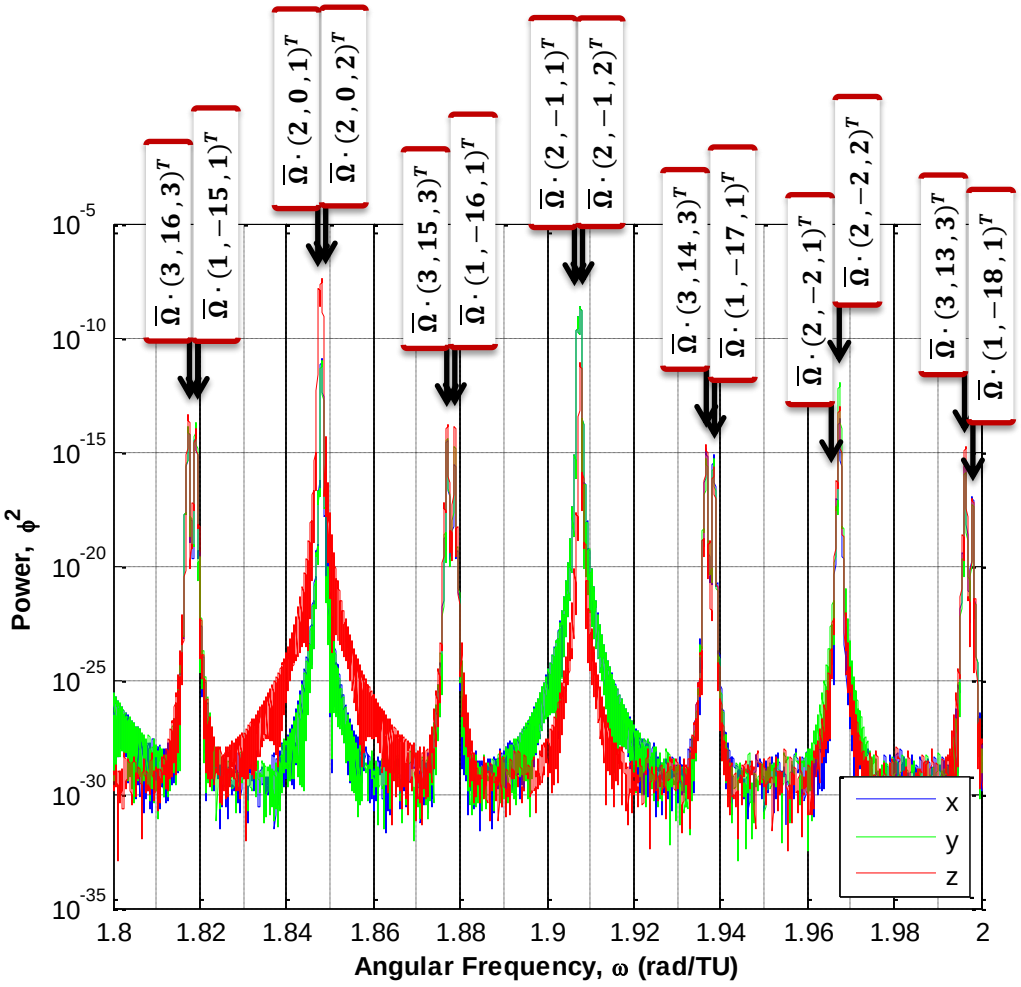

Figure 95. PSD plot identifying frequency combinations from [1.8, 2.0] rad/TU.

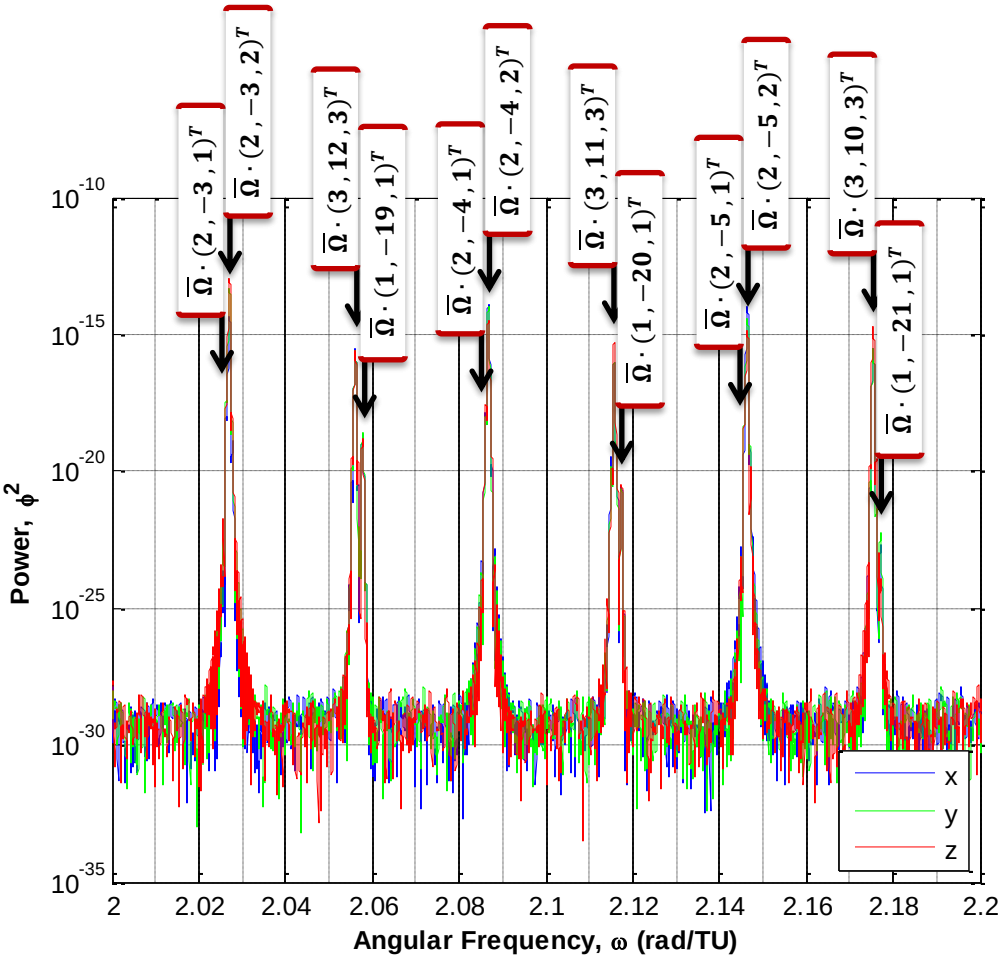

Figure 96. PSD plot identifying frequency combinations from [2.0, 2.2] rad/TU.

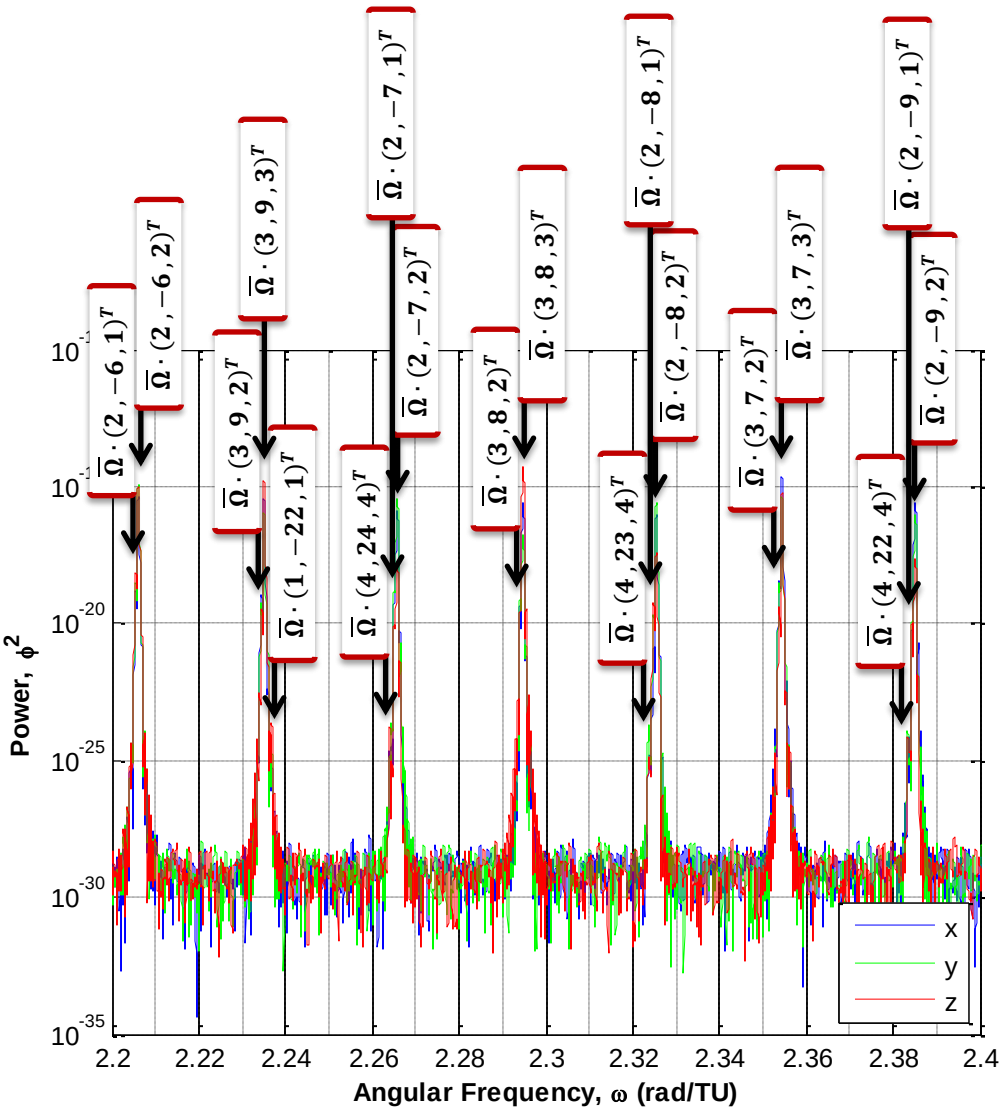

Figure 97. PSD plot identifying frequency combinations from [2.2, 2.4] rad/TU.

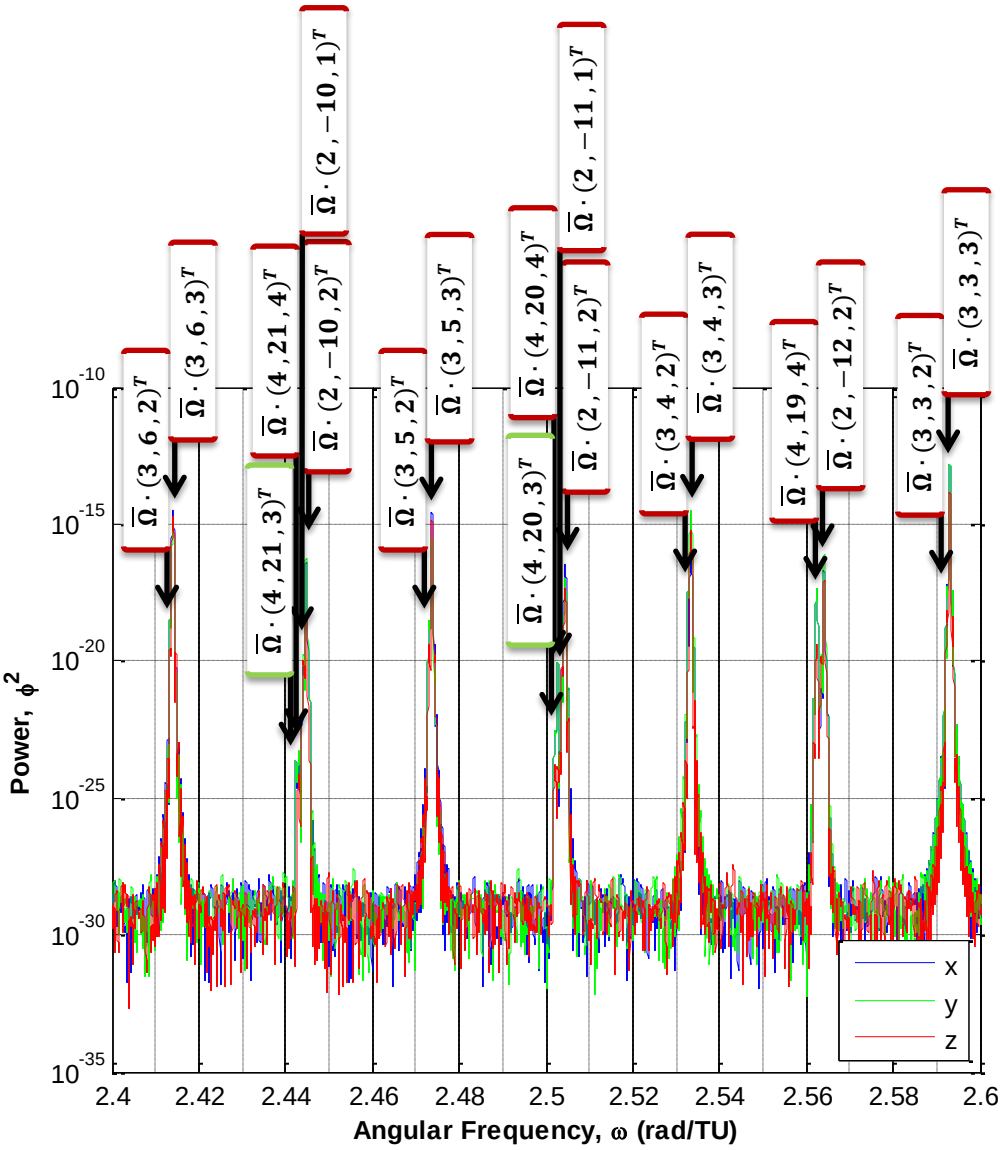

Figure 98. PSD plot identifying frequency combinations from [2.4, 2.6] rad/TU.

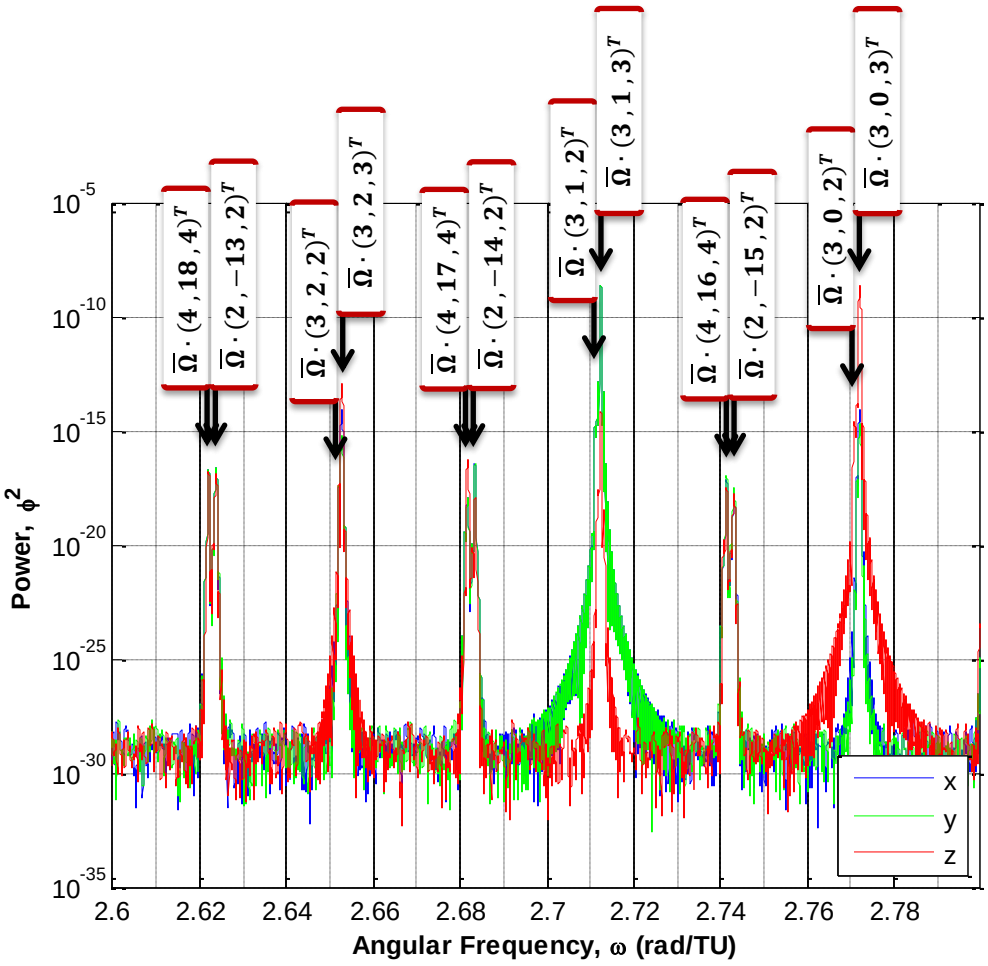

Figure 99. PSD plot identifying frequency combinations from [2.6, 2.8] rad/TU.

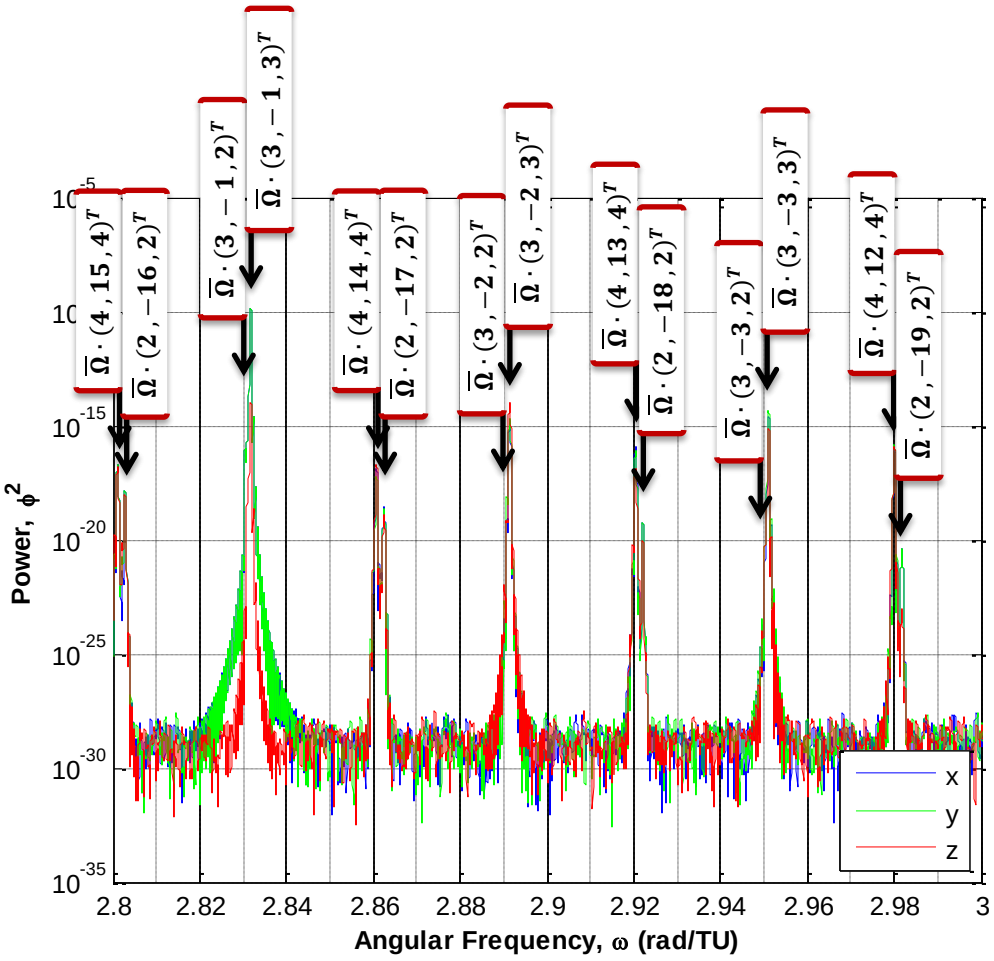

Figure 100. PSD plot identifying frequency combinations from [2.8, 3.0] rad/TU.

Bibliography

1 Semple, Mandi. Director of Community & Media Relations, Sewickley Academy, Sewickley PA. Telephone Interview. 19 August 2010.

2 "ISS On-Orbit Status 03/12/09." *NASA*. 12 March 2009. Available at http://www.nasa.gov/directorates/somd/reports/iss_reports/2009/03122009.html.

3 "Space Station Debris Threat Passes; STS-119 Rescheduled." *NASA*. 13 March 2009. Web. 19 August 2010. http://replay.waybackmachine.org/20090313173319/http://www.nasa.gov/mission_pages/station/main/index.html.

4 Bergin, Chris. "RED threshold late notice conjunction threat misses ISS – Crew egress Soyuz." *NASASpaceFlight.com*. 12 March 2009. Web. 19 August 2010. http://www.nasaspaceflight.com/2009/03/threat-to-iss-crew-soyuz/.

5 Borenstein, Seth. "Space station's close call: More to come." *Associated Press*. 12 March 2009. Available at http://www.msnbc.msn.com/id/29666148/.

6 "Astronauts forced to take refuge in escape pod after International Space Station comes under attack from junk." *Daily Mail Foreign Service*. 13 March 2009. Available at http://www.dailymail.co.uk/sciencetech/article-1161544/Astronauts-forced-refuge-escape-pod-International-Space-Station-comes-attack-junk.html.

7 "ISS On-Orbit Status 03/23/09." *NASA*. 23 March 2009. Available at http://www.nasa.gov/directorates/somd/reports/iss_reports/2009/03232009.html.

8 Gibson, Jano. "Jet's flaming space junk scare," *The Sydney Morning Herald*. 28 March 2007. Available at http://www.smh.com.au/news/world/jets-flaming-space-junk-scare/2007/03/28/1174761528947.html.

9 Kessler, Donald J. and Burton G. Cour-Palais. "Collision Frequency of Artificial Satellites: The Creation of a Debris Belt," *Journal of Geophysical Research*, 83(A6) 2637-2646 (1978).

10 Hannes Alfvén. "Apples in a Spacecraft," *Science, New Series*, 173(3996):522-525 (Aug. 6, 1971).

11 Kessler. Donald J. "Collisional Cascading: The Limits of Population Growth in Low Earth Orbit," *Advances in Space Research*, 11(12):63-66 (1991).

12 Kessler, Donald J. "Critical Density of Spacecraft in Low Earth Orbit: Using Fragmentation Data to Evaluate the Stability of the Orbital Debris Environment," JSC 28949, LMSMSS 33303, February 2000.

13 Kessler, Donald J., Nicholas L. Johnson, J.-C. Liou and Mark Matney. "The Kessler Syndrome: Implications to Future Space Operations." AAS 10-016, AAS Guidance and Control Conference, Breckenridge, CO, February 6-10, 2010.

14 Liou, J.-C. and N. L. Johnson, "Risks in Space from Orbiting Debris," *Science*, 311:340-341 (20 January 2006).

15 Rumsfeld, Donald H., et al. "Report of the Commission to Assess United States National Security Space Management and Organization." Pursuant to Public Law 106-65. January 11, 2001. Available at http://space.au.af.mil/space_commission/space20010111.pdf.

16 Knowles, S.H., "A Comparison of Geocentric Propagators for Operational Use." AAS 95-429, AAS/AIAA Astrodynamics Specialist Conference, Halifax, Nova Scotia, Canada, August 14-17, 1995.

17 Wiesel, William E., "Earth Satellite Orbits as KAM Tori," AAS 07-423, AAS/AIAA Astrodynamics Specialist Conference, Mackinac Island, Michigan, August 2007.

18 Wiesel, William E., "KAM Tori Construction Algorithms," Proceedings of the Advanced Maui Optical and Space Surveillance Technologies Conference, Wailea, Maui, Hawaii, September 17-19, 2008.

19 Wiesel, William E., "Earth Satellite Perturbation Theories as Approximate KAM Tori," AAS 10-122, AAS/AIAA Space Flight Mechanics Meeting, February 2010.

20 Wiesel, William E., "Earth Satellite Perturbation Theories as Approximate KAM Tori," *J. Astronautical Sciences*, In Press (2011).

21 Little, Bryan D. *Application of KAM Theorem to Earth Orbiting Satellites*. MS Thesis, AFIT/GA/ENY/09-M05. Graduate School of Engineering and Management, Air Force Institute of Technology (AU), Wright-Patterson AFB OH, March 2009.

22 Hughes, Peter C. *Spacecraft Attitude Dynamics*. Mineola NY: Dover Publications, 2004.

23 Bate, Roger R., Donald D. Mueller and Jerry E. White. *Fundamentals of Astrodynamics*. New York: Dover Publications, 1971.

24 Vallado, David A. and Wayne D. McClain. *Fundamentals of Astrodynamics and Applications* (2nd Edition). El Seundo CA: Microcosm Press, Dordrecht The Netherlands: Kluwer Academic Publishers, 2001.

25 Curtis, Howard D. *Orbital Mechanics for Engineering Students* (2nd Edition). Elsevier, 2009.

26 Battin, Richard H. *An Introduction to the Mathematics and Methods of Astrodynamics* (Revised Edition). Reston VA: AIAA Education Series, 1999.

27 Wiesel, William E. *Modern Astrodynamics*. Beavercreek OH: Aphelion Press, 2003.

28 Wertz, James R. and Wiley J. Larson (Editors). *Space Mission Analysis and Design* (3rd Edition). Hawthorn CA: Microcosm Press, New York: Springer, 1999.

29 Tascione, Thomas F. *Introduction to the Space Environment* (2nd Edition). Malabar FL: Krieger Publishing Company, 1994.

30 Meirovitch, Leonard. *Methods of Analytical Dynamics*. New York: McGraw-Hill, 1970.

31 Vinti, John P., Gim J. Der and Nino L. Bonavito. *Orbital and Celestial Mechanics*. Progress in Astronautics and Aeronautics, Vol. 177, AIAA, 1998.

32 Lagrange, Joseph-Louis. *Méchanique Analytique*. Paris: Vve. Desaint, 1788.

33 Kline, Morris. *Mathematical Thought from Ancient to Modern Times, Volume 2*. New York: Oxford University Press, 1990.

34 W.R. Hamilton, "On a General Method in Dynamics," *Philosophical Transaction of the Royal Society,* (Part I) 124:247-308 (1834); (Part II) 125:95-144 (1835).

35 Pars, L. A. *A Treatise on Analytical Dynamics*. Woodbridge CT: Ox Bow Press, 1979.

36 Kolmogorov, A. N. "On Conservation of Conditionally Periodic Motions for a Small Change in Hamilton's Function," *Dokl. Akad. Nauk SSR*, 98:527-530 (1954).

37 Arnol'd, V. I. "Proof of a Theorem of A. N. Kolmogorov on the Invariance of Quasi-Periodic Motions Under Small Perturbations of the Hamiltonian," *Russian Mathematical Surveys*, 18(5):9-36 (1963).

38 Moser, J. "On Invariant Curves of Area-Preserving Mappings of an Annulus," *Nachr. Akad. Wiss. Göttingen Math.-Phys.* Kl. II:1-20 (1962).

39 Celletti, A. and Chierchia L. "KAM Tori for N-body Problems: A Brief History," Celestial Mechanics and Dynamical Astronomy, 95(1):117-139 (2006).

40 Celletti, Alessandra, Claude Froeschlé and Elena Lega. "From Regular to Chaotic Motions through the Work of Kolmogorov," in *The Kolmogorov Legacy in Physics*. Ed. Roberto Livi and Angelo Vulpiani. New York: Springer-Verlag Berlin Heidelberg, 2003.

41 Poincaré, Henri. *New Methods of Celestial Mechanics*. Edited and introduced by Daniel L. Goroff. Woodbury NY: American Institute of Physics, 1993.

42 Tabor, Michael. *Chaos and Integrability in Nonlinear Dynamics: An Introduction*. New York: Wiley, 1989.

43 Merrit, David. "Non-integrable Galactic Dynamics," in *The Restless Universe: Applications of Gravitational n-Body Dynamics to Planetary, Stellar and Gallactic Systems*. Ed. Bonnie A. Steves and A. J. Maciejewski. Great Britain: J. W. Arrowsmith Ltd, Bristol.

44 Laskar, Jaques, "Frequency Map Analysis and Quasiperiodic Decompositions," Proceedings of Porquerolles School. pp 1-31. September 2001.

45 Laskar, Jaques. "Introduction to Frequency Map Analysis." *Hamiltonian Systems with Three or More Degrees of Freedom* edited by C. Simo. pp 134-150. Kluwer Academic Publishers, 1999.

46 Bordner, Ralph E. and William E. Wiesel. "Spectral Decomposition of Orbital Tori," *Journal of Guidance, Control, and Dynamics*, 34(2):504-512 (Mar-Apr 2011).

47 Briggs, William L. and Van Emden Henson. *The DFT: An Owner's Manual for the Discrete Fourier Transform*. Philadelphia: Society for Industrial and Applied Mathematics, 1995.

48 William E. Wiesel. "Motion Near an Earth Satellite KAM Torus." Unpublished, 2011.

49 Wiesel, William E., Modern Orbit Determination (3rd Edition). Beavercreek OH: Aphelion Press, 2011.

50 Scheid, Francis, *Theory and Problems of Numerical Analysis* (2nd Edition). Schaum's Outline Series, New York: McGraw-Hill, 1988.

51 "International Space Station Facts and Figures." *NASA*. Web. 1 February 2011. http://www.nasa.gov/mission_pages/station/main/onthestation/facts_and_figures.html

52 Craft, Christopher T. *Formation Flight of Earth Satellites on KAM Tori*. MS Thesis, AFIT/GA/ENY/09-S01. Graduate School of Engineering and Management, Air Force Institute of Technology (AU), Wright-Patterson AFB OH, September 2009.

53 "ISS Flight Attitudes." *NASA*. Web. 20 January 2011. http://spaceflight.nasa.gov/station/flash/iss_attitude.html.

54 Joint USAF/NOAA Report of Solar and Geophysical Activity SDF Numbers 084-114 Issued at 2200Z on 25 Mar 2010-24 Apr 2010.

55 "NOAA Space Weather Scales." *U.S. Dept. of Commerce, NOAA, Space Weather Prediction Center*. 1 March 2005. Web. 17 Jan. 2011. http://www.swpc.noaa.gov/NOAAscales/.

56 "The Weekly" -- Preliminary Report and Forecast of Solar Geophysical Data. SWO PRF 1804. *U.S. Dept. of Commerce, NOAA, Space Weather Prediction Center*. 30 March 2010.

57 "The Weekly" -- Preliminary Report and Forecast of Solar Geophysical Data. SWO PRF 1805. *U.S. Dept. of Commerce, NOAA, Space Weather Prediction Center*. 6 April 2010.

58 "The Weekly" -- Preliminary Report and Forecast of Solar Geophysical Data. SWO PRF 1806. *U.S. Dept. of Commerce, NOAA, Space Weather Prediction Center*. 13 April 2010.

59 "The Weekly" -- Preliminary Report and Forecast of Solar Geophysical Data. SWO PRF 1807. *U.S. Dept. of Commerce, NOAA, Space Weather Prediction Center*. 20 April 2010.

60 "The Weekly" -- Preliminary Report and Forecast of Solar Geophysical Data. SWO PRF 1808. *U.S. Dept. of Commerce, NOAA, Space Weather Prediction Center*. 27 April 2010.

REPORT DOCUMENTATION PAGE

Form Approved
OMB No. 074-0188

1. REPORT DATE *(DD-MM-YYYY)*	**2. REPORT TYPE**	**3. DATES COVERED** *(From – To)*
24-03-2011	Master's Thesis	Sep 2009 – Mar 2011

4. TITLE AND SUBTITLE

Stochastic Orbit Prediction Using KAM Tori

5a. CONTRACT NUMBER

5b. GRANT NUMBER

5c. PROGRAM ELEMENT NUMBER

6. AUTHOR(S)

Yates, Max W., Captain, USAF

5d. PROJECT NUMBER

5e. TASK NUMBER

5f. WORK UNIT NUMBER
#

7. PERFORMING ORGANIZATION NAMES(S) AND ADDRESS(S)
Air Force Institute of Technology
Graduate School of Engineering and Management (AFIT/ENY)
2950 Hobson Way, Building 640
WPAFB OH 45433-7765

8. PERFORMING ORGANIZATION REPORT NUMBER

AFIT/GA/ENY/11-M15

9. SPONSORING/MONITORING AGENCY NAME(S) AND ADDRESS(ES)

INTENTIONALLY LEFT BLANK

10.SPONSOR/MONITOR'S ACRONYM(S)

11. SPONSOR/MONITOR'S REPORT NUMBER(S)

12. DISTRIBUTION/AVAILABILITY STATEMENT
APPROVED FOR PUBLIC RELEASE; DISTRIBUTION UNLIMITED.

13. SUPPLEMENTARY NOTES
This material is declared a work of the U.S. government and is not subject to copyright protection in the United States.

14. ABSTRACT
Kolmogorov-Arnold-Moser (KAM) Theory states that a lightly perturbed, conservative, dynamical system will exhibit lasting quasi-periodic motion on an invariant torus. Its application to purely deterministic orbits has revealed exquisite accuracy limited only by machine precision. The theory is extended with new mathematical techniques for determining and predicting stochastic orbits for Earth satellite systems. The linearized equations of motion are developed and a least squares estimating environment is pioneered to fit observation data from the International Space Station to a phase space trajectory that exhibits drifting toroidal motion over a dense continuum of adjacent tori. The dynamics near the reference torus can be modeled with time-varying torus parameters that preserve both deterministic and stochastic effects. These parameters were shown to predict orbits for days into the future without tracking updates—a vast improvement over classical methods of orbit propagation that require routine updates.

15. SUBJECT TERMS
KAM, torus, tori, orbit, satellite, predictions, perturbations, stochastic, non-conservative

16. SECURITY CLASSIFICATION OF:			**17. LIMITATION OF ABSTRACT**	**18. NUMBER OF PAGES**	**19a. NAME OF RESPONSIBLE PERSON**
a. REPORT	**b. ABSTRACT**	**c. THIS PAGE**			William E. Wiesel, Ph.D.; Instructor, AFIT
U	U	U	UU	215	**19b. TELEPHONE NUMBER** *(Include area code)* (937) 255-3636, ext 4312 william.wiesel@afit.edu